On the Impact of Drying on Surface Tension Gradient Induced Marangoni Convection in Thin Polymer Solution Films

Zur Erlangung des akademischen Grades eines
DOKTORS DER INGENIEURWISSENSCHAFTEN (DR.-ING.)

von der KIT-Fakultät für Chemieingenieurwesen und Verfahrenstechnik des
Karlsruher Instituts für Technologie (KIT)
genehmigte

DISSERTATION

von
Dipl.-Ing. Max Tönsmann
aus Leopoldshöhe

Erstgutachter:	Prof. Dr.-Ing. Dr. h.c. Wilhelm Schabel
Zweitgutachter:	Prof. Dr. Norbert Willenbacher
Tag der mündlichen Prüfung:	05. Juli 2022

≫ *God made the bulk; surfaces were invented by the devil.* ≪

Presumably – Wolfgang Ernst Pauli –

Preface & Acknowledgement

This dissertation originates from my research conducted as PhD student between November 2015 and Mai 2021 at the Thin Film Technology (TFT) group at Karlsruhe Institute of Technology (KIT). During this time, many people have significantly contributed to the success of this dissertation, and I would like to express my sincere gratitude to every single one of them.

I would like to thank Prof. Dr.-Ing. Dr. h. c. Wilhelm Schabel and Dr.-Ing. Philip Scharfer, who employed me and supervised my work at the TFT group, for their support, the fruitful scientific discussions, and for the freedom they granted me during my research, which resulted in this dissertation. I am also grateful for the opportunity to present my results at numerous national and international conferences, due to their support. Furthermore, I would like to thank Prof. Dr. Norbert Willenbacher for providing the second review of this dissertation.

My eternal gratitude deserves Margit Morvay, who not only helped me with all administrative related work at TFT/KIT, but also always offered emotional support and encouragement during stressful and unnerving phases, bound to occur during five years of PhD studenthood. The former and current members of the Institute of Thermal Process Engineering (TVT)'s mechanical and electrical workshop, as well as lab staff, I would like to thank for their input on my design drawings, fabrication of various prototypes, and for conducting measurements. Among these are Michael Wachter, Andreas Roth, Stephan Fink, Steffen Haury, Max Renaud, Stefan Böttle, Sabrina Herberger, and Annette Schucker. My thanks also go to Prof. Dr.-Ing. Matthias Kind, Prof. Dr.-Ing. Thomas Wetzel, Dr.-Ing. Benjamin Dietrich, Sebastian Schwarz, Nicole Feger, and Vanessa Gamer for supervising and administrating my teaching obligations at the Institute of Thermal Process Engineering (TVT).

I cannot stress enough how thankful I am for the amazing former and current colleagues at TVT and TFT, who made my everyday work worthwhile and enjoyable, not only during scientific discussions, joint research projects, teaching obligations, and mutually visited scientific conferences, but also during numerous coffee and lunch breaks, private activities and festivities. Among others, I

would like to point out namely Andreas Altvater, Susanna Baesch, Dominic Becker, Tobias Börnhorst, Ralf Diehm, Konrad Dubil, Jochen Eser, Víctor Alfonso Gracia Medrano Bravo, Thilo Heckmann, Julian Klemens, Jana Kumberg, Sebastian Meinicke, Lisa Merklein, Sebastian Raupp, David Siebel, Sandro Spiegel, Philipp Quarz, Anna-Lena Walz, and Sonja Weise. Especially Tobi, Jochen, Lisa and Jana, who all joined the TFT group in the same year as me, and we therefore spent the better part of our five-year PhD studenthood together at TFT, were an immense help with their positivity, encouragement, feedback, and so many more things impossible to enumerate in full. Each one of them deserves my eternal gratitude. My best wishes also go to the new members of TFT, Alexander Hoffmann, Lukas Lödige, Kevin Ly, Jonas Mohacsi, Philip Quarz, and Nadine Zimmerer, with their ongoing research endeavor, who can consider themselves lucky if they experience a glimpse of the support among themselves I had from Tobi, Jochen, Lisa, and Jana.

I would also like to thank all students who contributed substantially to my research and worked under my supervision during my time at TFT: Etele Berszany, Stefan Hodapp, Christian Dallmann, Lars Herdan, Amelie Spix, Nico Korell, Fabian Kröhl, Sara Koß, Raphael Kräling, and Daniel Ewald.

Finally, I like to thank all my friends and family members, supporting and distracting me from work-related issues during all ups and downs accompanying my five years of PhD studenthood.

I acknowledge the financial support during my early years of research from the Federal Ministry of Education and Research (Bundesministerium für Bildung und Forschung, BMBF, project POESIE, grant number 13N12692), from the Helmholtz Association's program "Science and Technology of Nanosystems", and from the German Research Foundation (Deutsche Forschungsgemeinschaft, DFG, grant number 444945948) during my last year of research, as well as the KIT-Publication Fund of the Karlsruhe Institute of Technology (KIT) for the partial funding of several of my scientific publications.

Karlsruhe, March 2022

Max Tönsmann

Abstract

Thin functional polymer films are widely used in classic applications and novel (organic) electronic devices. Typically, such films are produced by polymer-solution coating and subsequent drying. Dry film thickness variations should not exceed 1 % of the average thickness in order to ensure device performance or functionality. Thin liquid films, however, may be subject to buoyancy- or surface-tension-gradient-driven convective instabilities, which bear the potential of causing free surface deformations that may persist in the solidified dry films. While stationary convective instabilities are well understood in single-component non-volatile liquid films, the intrinsic non-stationarity of polymer solution film drying, due to transient film shrinkage, concentration change, and viscosity increase, are subject of ongoing scientific research. The coupled transient heat- and mass-transfer in combination with the three-dimensional nature of convective instabilities makes the rigorous investigation a challenging task. The aim of this work is the investigation of the impact of drying conditions on the occurrence and lifetime of convective instabilities in thin drying polymer-solution films, by means of quantitative experimental investigations in combination with the calculation of characteristic dimensionless numbers, based on realistic concentration- and temperature-dependent material properties. Since concentration- and temperature-dependent surface tension data of polymer solutions are not readily available, special emphasis was laid on the measurement of such data and the evaluation of available mixing rule equations.

For the experimental investigation of the three-dimensional transient flow field in drying polymer solution films, microscopic particle tracking velocimetry (3D-µPTV) was utilized. The experimental setup was acquired prior to this work and requires only one optical access, which was realized from below the drying film utilizing a thin transparent glass substrate. The line-of-sight vertical position of tracer particles can be reconstructed from the diffraction ring diameter observed when a tracer particle resides not in the lateral focus plane of the observing optics. Since the vertical extent of this approach is limited by the deteriorating signal-to-noise ratio with increasing tracer particle distance to the focus plane, the available 3D-µPTV setup combines this approach with multifocal microscopy, using several cameras with different vertical focus plane positions, which results in several observation volumes. In this work, a rigorous calibration, automation and postprocessing routine was developed, which allows for quantitative, transient, and three-dimensional flow field measurements of fluorescent tracer particle trajectories in thin liquid films. It was found that the multifocal approach affects the tracer particle's line-of-sight position reconstruction, and a simplified routine for the vertical stitching of individual observation volumes derived with several cameras was proposed. In comparison to a rigorously correct vertical stitching routine, the simplified approach requires less calibration samples and data, and is computationally less demanding. Due to the optical access from below the film, different experimental drying conditions can be employed. Any form of forced convective airflow for drying induces laterally inhomogeneous heat- and mass-transfer coefficients. Hence, film drying experiments are presented without forced convective airflow under ambient conditions, and with a deliberate lateral inhomogeneity in experimental drying conditions, realized by partially covering the drying films. The material system poly(vinyl acetate)-methanol serves as model system.

It was found that during drying experiments without deliberate laterally inhomogeneous drying conditions, short-scale Marangoni convection cells may occur in the drying film, emerging at the onset of drying and stopping during the constant-rate period of drying. A higher initial viscosity (lower initial solvent content) and a smaller initial film thickness result in convectively stable films during the entire course of drying. The flow field results were combined with one-dimensional non-isothermal drying simulations matched to experimental results, which grant access to transient vertical concentration and temperature profiles, and allow for the calculation of dimensionless Marangoni numbers, which are widely used in literature to describe the (in)stability of liquid films subject to surface tension gradient induced instabilities. The presented results indicate that the effect of concentration changes during drying is dominating the instability mechanism over thermal effects. Furthermore, an empiric power-law correlation for the critical solutal Marangoni number, denoting (in)stability, was found, unifying the conditions at onset of drying and at the stability threshold during drying.

Film drying experiments with deliberate laterally inhomogeneous drying conditions exhibited a lateral flow from the covered area of the film towards the uncovered area, which is in accordance with expectations and with preliminary published drying experiments, due to concentration-gradient induced surface tension

differences. The lateral flow during all conducted experiments stopped close to the end of the constant rate period of drying. At lower initial solvent concentrations, solely a lateral flow was found, whereas at higher initial solvent concentrations, a lateral flow and perpendicular convection cells occurred simultaneously. The convection cells stopped at an earlier drying time than the long scale flow, indicating a lower stability threshold for lateral long-scale convective instabilities. The lateral flow was accompanied by strong deformations of the free film's surface, persisting in the dry film.

An assessment of characteristic leveling times of lateral short-scale and long-scale surface deformations indicate that free surface deformations are unlikely to occur while a convective instability in the form of vertical convection cells is still active. Deformations may arise only after the instability stopped, due to the lateral polymer transport during the instability. The lateral flow in partially covered experiments, however, induces deformations at early stages of drying, which are unlikely to level because of the strong viscosity increase during polymer film drying. Hence, it was concluded that any strategy to avoid deformations, should be based on inhibiting convective instabilities altogether during drying, for example by using different material combinations or multi-solvent solutions. The material system poly(ethylene glycol)-methanol-water appears to be a promising candidate for future investigations because it comprises two binary subsystems with complementary surface tension concentration-dependency.

The presented results show that the 3D-µPTV measurement technique is well suited for the quantitative investigation of convective instabilities during drying of thin polymer films. The proposed empiric correlation for surface tension gradient induced convection cells indicates that predicting (in)stability may well be possible by simple empiric correlations of the critical Marangoni number.

Kurzfassung

Dünne funktionale Polymerfilme sind in klassischen Anwendungen und neuartigen (organisch-)elektronischen Produkten weit verbreitet. Typischerweise werden solche Filme durch Beschichtung mit einer Polymerlösung und anschließendem Trocknen hergestellt. Die Schwankungen der trockenen Filmdicke sollten 1 % der durchschnittlichen Trockenfilmdicke nicht überschreiten, um die Effizienz oder Funktionalität der Produkte zu gewährleisten. Dünne Flüssigkeitsfilme können jedoch auftriebs- oder oberflächenspannungsgradientengetriebenen konvektiven Instabilitäten unterliegen, die potenziell zu Deformationen der freien Filmoberflächen führen, welche in den verfestigten Trockenfilmen bestehen bleiben. Während stationäre konvektive Instabilitäten bei einkomponentigen, nichtflüchtigen Flüssigkeitsfilmen gut verstanden sind, ist die intrinsische Instationarität der Trocknung von Polymerlösungsfilmen, aufgrund von transienter Filmschrumpfung, Konzentrationsänderung und Viskositätserhöhung, Gegenstand laufender wissenschaftlicher Forschung. Der gekoppelte instationäre Wärme- und Stofftransport in Kombination mit der dreidimensionalen Natur der konvektiven Instabilitäten macht die Untersuchung zu einer anspruchsvollen Aufgabe. Ziel dieser Arbeit ist die Untersuchung des Einflusses der Trocknungsbedingungen auf das Auftreten und die Lebensdauer konvektiver Instabilitäten in dünnen, trocknenden Polymerlösungsfilmen, mittels quantitativer experimenteller Untersuchungen in Kombination mit der Berechnung charakteristischer dimensionsloser Kennzahlen, basierend auf realistischen konzentrations- und temperaturabhängigen Materialeigenschaften. Da konzentrations- und temperaturabhängige Oberflächenspannungsdaten von Polymerlösungen nicht ohne weiteres verfügbar sind, wurde besonderer Wert auf die Messung solcher Daten und die Evaluierung verfügbarer Mischungsregeln gelegt.

Für die experimentelle Untersuchung des dreidimensionalen instationären Strömungsfeldes in trocknenden Polymerlösungsfilmen wurde mikroskopische Particle Tracking Velocimetry (3D-µPTV) eingesetzt. Der Versuchsaufbau wurde im Vorfeld dieser Arbeit angeschafft und benötigt nur einen einzigen optischen Zugang, der von der Unterseite des Trocknungsfilms unter Verwendung eines dünnen transparenten Glassubstrats realisiert wurde. Die vertikale Position der

Tracerpartikel senkrecht zur Filmebene kann aus dem Durchmesser der Beugungsringe rekonstruiert werden, die beobachtet werden, wenn sich ein Tracerpartikel außerhalb der lateralen Fokusebene der Beobachtungsoptik befindet. Da die vertikale Ausdehnung des Beobachtungsvolumens dieses Ansatzes durch ein sich verschlechterndes Signal-Rausch-Verhältnis mit zunehmendem Abstand der Tracerpartikel zur Fokusebene begrenzt ist, kombiniert der verfügbare 3D-µPTV-Aufbau diesen Ansatz mit multifokaler Mikroskopie. Dabei werden mehrere Kameras mit unterschiedlichen Positionen der vertikalen Fokusebene verwendet, was zu mehreren Beobachtungsvolumina führt. In dieser Arbeit wurden umfassende Kalibrierungs-, Automatisierungs- und Nachbearbeitungsroutinen entwickelt, die quantitative, transiente und dreidimensionale Strömungsmessungen in dünnen Flüssigkeitsfilmen ermöglichen. Es wurde festgestellt, dass der multifokale Ansatz die Rekonstruktion der vertikalen Tracerpartikelposition beeinflusst, und es wurde eine vereinfachte Routine für die vertikale Kombination einzelner Beobachtungsvolumina vorgeschlagen. Im Vergleich zu einer vollständig vertikalen Stitching-Routine erfordert der vereinfachte Ansatz weniger Kalibrierungsproben und -daten und ist weniger rechenintensiv. Durch den optischen Zugang von unterhalb des Filmes können unterschiedliche experimentelle Trocknungsbedingungen eingesetzt werden. Jede Form der erzwungenen konvektiven Luftströmung zur Trocknung induziert lateral inhomogene Wärme- und Stoffübergangskoeffizienten. Daher werden Filmtrocknungsversuche ohne erzwungene konvektive Luftströmung unter Umgebungsbedingungen und mit einer gezielten lateralen Inhomogenität der experimentellen Trocknungsbedingungen vorgestellt. Dies wird durch eine teilweise Abdeckung der Trocknungsfolien realisiert. Als Modellsystem dient das Stoffsystem Polyvinylacetat-Methanol.

Es wurde festgestellt, dass bei Trocknungsexperimenten ohne gezielt lateral inhomogene Trocknungsbedingungen kurzskalige Marangoni-Konvektionszellen im Trocknungsfilm auftreten können, die zu Beginn der Trocknung entstehen und während der Dauer der Trocknung im ersten Trocknungsabschnitt enden. Eine höhere Anfangsviskosität (geringerer Anfangslösemittelgehalt) und eine geringere Anfangsfilmdicke führen zu konvektiv stabilen Filmen während des gesamten Trocknungsverlaufs. Die Ergebnisse der Strömungsuntersuchungen wurden mit eindimensionalen nicht-isothermen Trocknungssimulationen kombiniert, die mit experimentellen Ergebnissen validiert wurden. Diese ermöglichen den Zugang zu instationären vertikalen Konzentrations- und Temperaturprofilen

und erlauben die Berechnung dimensionsloser Marangoni-Zahlen, die in der Literatur weit verbreitet sind, um die (In)Stabilität von Flüssigkeitsfilmen zu beschreiben, die durch Oberflächenspannungsgradienten hervorgerufen werden. Die vorgestellten Ergebnisse zeigen, dass der Effekt von Konzentrationsänderungen während der Trocknung den Instabilitätsmechanismus gegenüber thermischen Effekten dominiert. Darüber hinaus wurde eine empirische Potenzgesetz-Korrelation für die kritische Marangoni-Zahl, welche (In)Stabilität kennzeichnet, gefunden, die sowohl die Bedingungen zu Beginn der Trocknung als auch an der Stabilitätsgrenze während der Trocknung beschreibt.

Filmtrocknungsexperimente mit gezielt lateral inhomogenen Trocknungsbedingungen zeigten eine laterale Strömung vom abgedeckten Bereich des Films in Richtung des unbedeckten Bereichs aufgrund von konzentrationsgradienteninduzierten Oberflächenspannungsunterschieden, was mit den Erwartungen und mit zuvor veröffentlichten Trocknungsexperimenten übereinstimmt. Bei allen durchgeführten Experimenten endet die laterale Strömung nahe dem Ende des ersten Trocknungsabschnitts. Bei niedrigeren anfänglichen Lösungsmittelkonzentrationen wurde ausschließlich eine laterale Strömung beobachtet, während bei höheren anfänglichen Lösungsmittelkonzentrationen eine laterale Strömung und senkrecht dazu auftretende Konvektionszellen gleichzeitig auftraten. Dabei endeten die Konvektionszellen zu einem früheren Trocknungszeitpunkt als die langskalige laterale Strömung, was auf eine niedrigere Stabilitätsschwelle für laterale langskalige konvektive Instabilitäten hinweist. Die laterale Strömung wurde von starken Verformungen der freien Filmoberfläche begleitet, die im trockenen Film fortbestehen.

Eine Analyse der charakteristischen Nivellierungszeiten von lateralen kurz- und langskaligen Oberflächendeformationen zeigt, dass freie Oberflächendeformationen unwahrscheinlich sind solange eine konvektive Instabilität in Form von vertikalen Konvektionszellen aktiv ist. Diese treten erst nach dem Abklingen der Instabilität aufgrund des lateralen Polymertransports während der Instabilität auf. Die laterale Strömung in teilweise abgedeckten Experimenten induziert jedoch Verformungen in frühen Stadien der Trocknung, die sich aufgrund des starken Viskositätsanstiegs während der Trocknung des Polymerfilms nicht nivellieren können. Daraus wurde gefolgert, dass eine Strategie zur Vermeidung von Deformationen darauf beruhen sollte, konvektive Instabilitäten während der Trocknung gänzlich zu unterbinden. Dies kann beispielsweise durch die Verwendung

anderer Materialkombinationen oder von Multi-Lösemittel-Systemen erreicht werden. Das Materialsystem Polyethylenglykol-Methanol-Wasser scheint ein vielversprechender Kandidat für zukünftige Untersuchungen zu sein, da die binären Subsysteme eine komplementäre Konzentrationsabhängigkeit der Oberflächenspannung aufweisen.

Die vorgestellten Ergebnisse zeigen, dass die 3D-µPTV-Messtechnik für die quantitative Untersuchung konvektiver Instabilitäten während der Trocknung dünner Polymerfilme gut geeignet ist. Die gefundene empirische Korrelation für Konvektionszellen, induziert durch Oberflächenspannungsgradienten, deutet darauf hin, dass eine Vorhersage der (In)Stabilität durch einfache empirische Korrelationen der kritischen Marangoni-Zahl möglich ist.

Table of Contents

Symbols & Abbreviations

Latin Symbols

Symbol	Unit	
a_i	$-$	Solvent activity of component i
A		Fit constant
AAD	%	Averaged absolute deviation
B		Fit constant
Bi	$-$	Biot number
Bo	$-$	Bond number
c	kg/m^3	Concentration
$c_{M,0}$	$-$	Fit constant magnification intercept
$c_{M,1}$	mm^{-1}	Fit constant magnification slope
c_p	$J/(kg \cdot K)$	Heat capacity
C		Fit constant
Ca	$-$	Capillary number
d_{cells}	μm	Lateral convection cell size
$d_{opening}$	mm	Diameter of lens opening
d_p	μm	Tracer particle diameter
f_r	$-$	Diffraction-ring radius correction factor
f_z	$-$	Particle z-position correction factor
g	m/s^2	Earth's gravitational acceleration
Ga	$-$	Galileo number
k	μm^{-1}	Wavenumber
h	μm	Film height
h_{cover}	mm	Partial cover distance to substrate

Symbol	**Unit**	
h_{gap}	μm	Coating gap height
h_{glass}	μm	Glass substrate thickness
Δh_v	J/kg	Heat of vaporization
I	a. u.	Signal intensity
$l_{capillary}$	mm	Capillary length
ΔL	mm	Lateral length scale
m_{fd}	$-$	Slope of focal displacement due to refractive index mismatch
M	$-$	Lateral magnification
M_w	kg/mol	Molar mass
Ma_s	$-$	Solutal Marangoni number
Ma_T	$-$	Thermal Marangoni number
n_g	$-$	Refractive index of glass substrate
n_i	$-$	Refractive index of immersion medium
n_s	$-$	Refractive index of sample
N	$-$	Number of components / data points
NA	$-$	Numerical aperture
p_i^*	$mbar$	Vapor pressure of component i
P_4		4th degree polynomial
Pe	$-$	Péclet number
r	μm	Radius
r_{ring}	μm	Diffraction ring radius
Ra	$-$	Rayleigh number
s_{axis}	mm	Motorized lens position
Sc	$-$	Schmidt number
t	s	Drying time
$t_{crit,CRP}$	s	Critical drying time for end of constant rate period during drying

Symbol	Unit	
$t_{crit,Ma}$	s	Critical drying time for end of Marangoni instability during drying
t_g	μm	Glass substrate thickness in PSF-simulation
T	$°C$	Temperature
T_g	$°C$	Glass transition temperature
u	$\mu m/s$	Flow Velocity
v_{int}	$\mu m/s$	Film interface velocity (shrinkage)
x	μm	Cartesian coordinate
x_i	$-$	Mass fraction of component i
X_i	$g_{solvent}/g_{polymer}$	Solvent load of component i
y	μm	Cartesian coordinate
z	μm	Cartesian coordinate in film thickness direction
$\tilde{z}_{focus}$	μm	Vertical focus plane position in lens coordinates

Greek Symbols

Symbol	Unit	
α_{bottom}	$W/(m^2 \cdot K)$	Heat transfer coefficient at film surface
α_{top}	$W/(m^2 \cdot K)$	Heat transfer coefficient at substrate bottom
$\beta_{i,g}$	m/s	Mass transfer coefficient of component i in the gas phase
$\dot{\gamma}$	s^{-1}	Shear rate
δ_{ij}	m^2/s	Fickian diffusion coefficient of component i in j
Γ	$-$	Aspect ratio lateral / height
ε	$-$	Supercriticality
η	$Pa \cdot s$	Dynamic viscosity

Symbol	**Unit**	
η_0	$Pa \cdot s$	Zero-shear viscosity
κ	m^2/s	Thermal diffusivity
λ	$W/(m \cdot K)$	Heat conductivity
λ	μm	Lateral wavelength of instability
ρ	kg/m^3	Density
σ	mN/m	Surface tension
σ^E	mN/m	Excess surface tension in mixtures
τ	s	Characteristic time constant
φ_i	$-$	Volume fraction of component i
χ_{ij}	$-$	Flory-Huggins interaction parameter

Subscripts

0	Property at onset of drying ($t = 0\ s$)
b	Value at bottom of the film
$capillary$	Capillary wave related property
$cells$	Short-scale instability related property
$crit$	Critical threshold value
dry	Property of dry film
$focus$	Focus plane position
$gravity$	Gravity wave related property
i,j	Component index
$lateral$	Long-scale instability related property
max	Maximum value
$mean$	Averaged value
p	Tracer particle
s	Value at the surface of the film
$vertical$	Short-scale instability related property

x	Value in Cartesian x direction
y	Value in Cartesian y direction
z	Value in Cartesian z direction

Superscripts

$+$	Slightly elevated value
$-$	Slightly reduced value
$*$	Optical design condition for PSF simulation

Accents

$\bar{}$	Value averaged over the film height
$\tilde{}$	Property in lens coordinates
$\smile$	Value calculated with extrapolated viscosity, likely to be smaller
$\frown$	Value calculated with extrapolated viscosity, likely to be larger

Abbreviations

BM	Bénard-Marangoni (convection)
CRP	Constant rate period
GPU	Graphics processing unit
IMRS	Inverse Micro Raman Spectroscopy
MeOH	Methanol
OLED	Organic light-emitting diode
PCIe	Peripheral Component Interconnect Express
PEG	Polyethylene glycol
PIV	Particle image velocimetry
PMMA	Poly(methyl methacrylate)
PSF	Point spread function
PTV	Particle tracking velocimetry

μPTV	Micro particle tracking velocimetry
PVA	Poly(vinyl alcohol)
PVAc	Poly(vinyl acetate)
RB	Rayleigh-Bénard (convection)
RBM	Rayleigh-Bénard-Marangoni (convection)
SFE	Surface free energy
SG	Savitsky-Golay (filter)
TTL	Transistor-transistor logic (digital voltage signal)

1 Introduction and State of the Art

Thin functional polymer films are widely used in various applications and devices. Among these are classic applications such as varnish coatings, adhesive tapes and displays, and novel (organic) electronic devices such as OLEDs, solar cells, biosensors, battery separators and membranes for fuel cells (Ohring 2002; Buckley 2013; Koide 2014; Wengeler 2014; Langhe and Ponting 2016). Typically thickness variations should not exceed 1 % in order to ensure device functionality and efficiency in films with a thickness in the order of 10 to 100 μm (Schweizer 1997). Such polymer films are commonly produced from solvent solution via coating and subsequent film drying due to the good scalability of said processes for industrial applications (Kistler and Schweizer 1997). For engineering purposes, the film drying and the accompanying film shrinkage is often described as a one-dimensional process perpendicular to the film plane (Schabel 2004a; Siebel 2017b), whereas it is well-known that three-dimensional convective instabilities in thin liquid films, driven by buoyancy or surface tension effects, may arise (Bénard 1900; Rayleigh 1916; Pearson 1958; Gutoff et al. 2010). The occurrence of such instabilities strongly depends on the liquid film's material properties as well as the experimental boundary conditions. Observed instabilities manifest in various different forms and patterns (e.g. vertical convection cells with a regular pattern or lateral waves) (Cross and Hohenberg 1993). If such instabilities occur during the drying of a thin film, deformations of the free film surface may arise, persisting in the dry film after solidification. A well-known observation in paint and varnish coatings is the so-called "orange-peel effect" when the dry film surface exhibits wrinkles resembling the skin of an orange (Gutoff et al. 2010; Saranjam et al. 2016; Abbasian et al. 2004; Curak et al. 2018).

In the following sections, the state of the art regarding one-dimensional description of polymer film drying as well as convective (in)stability mechanisms is summarized.

1.1 Fundamentals of Polymer Film Drying

Polymer film drying is a complex interplay between heat and mass transfer. It is common practice to describe it as one-dimensional process, ignoring possible edge effects due to the large lateral extent of the film compared to the film thickness as well as convective fluid flow (e.g. Romdhane et al. 2001; Schabel 2004a; Siebel 2017b; Sharma et al. 2019). The schematic transient course of the film height and solvent load as well as the film temperature during the drying of a diluted polymer solution are given in Figure 1.1. The 1D description of mass transfer accounts for the solvent diffusion in the film, the phase equilibrium at the free surface and the solvent vapor transport in the gas phase. The latter is commonly accounted for by a constant mass transfer coefficient in the gas phase, depending on the forced convective airflow conditions during drying, whereas the diffusion in the film and the phase equilibrium depend on material properties of the coating solution. The transient course of the film height as well as solvent load, referred to as drying curves, consists of three characteristic regimes. Initially, the curves show a constant negative slope, known as the constant-rate period (CRP, I in Figure 1.1). During this period, the polymer-solution film exhibits a constant drying rate since the mass transfer is limited by the solvent transport in the gas phase. This is a result of the material properties of the coating solution. Exemplarily, the solvent activity, denoting the phase equilibrium and the diffusion coefficient in the liquid polymer solution are given in Figure 1.2 for a poly(vinyl acetate)-methanol (PVAc-MeOH) solution. The solvent activity (green line) is close to unity for a wide concentration range, exhibiting a steep decrease at low solvent concentrations. The diffusion coefficient (orange line) is also strongly dependent on the solvent concentration, decreasing by several orders of magnitude during drying. It is, however, fairly close to the pure solvent's self-diffusion coefficient (orange dashed line) over a wide concentration range. The end of the constant rate period coincides with the low solvent concentration range, where the solvent activity as well as the diffusion coefficient strongly decrease. Subsequently, the drying rate decreases noticeably, therefore this regime is known as the falling-rate period (II in Figure 1.1). During this regime, the solvent-mass transport becomes additionally affected by the phase equilibrium and the diffusion in the film. Subsequently, the film drying becomes solely limited by the solvent diffusion in the film, resulting in a diffusional plateau (III in Figure 1.1). Due to the low diffusion coefficient (orange line in Figure 1.2), the film height (solvent load) asymptotically approaches the dry-film thickness (zero solvent load).

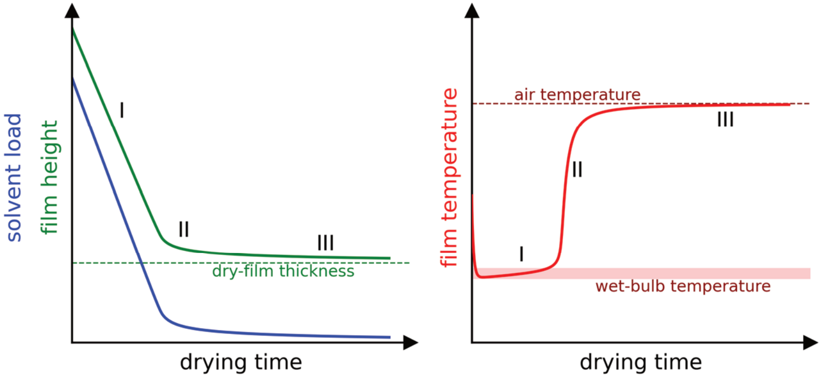

Figure 1.1: Schematic course of the transient solvent load and film height (left) as well as the film temperature (right) during polymer film drying at ambient conditions.

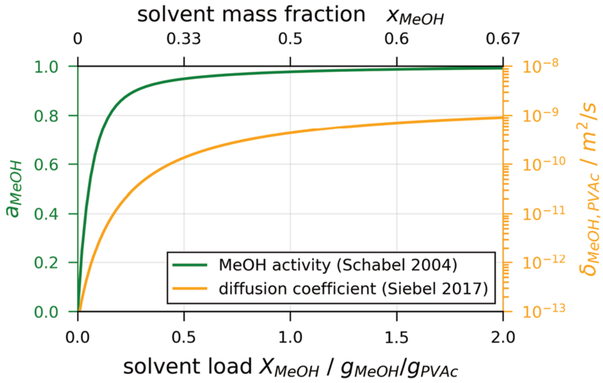

Figure 1.2: Concentration-dependent solvent activity and diffusion coefficient of poly(vinyl acetate)-methanol (PVAc-MeOH) solutions at 20 °C.

The film exhibits a close to constant steady-state temperature (wet-bulb temperature) during the constant rate period, due to evaporative cooling. Subsequently, the temperature asymptotically approaches the set drying temperature (substrate and drying air temperature), as schematically shown in Figure 1.1, right.

If the pure polymer exhibits glass transition, the added solvent acts as a plasticizer, reducing the glass transition temperature of the solution (Chow 1980; Hiemenz et al. 2007; Naseri et al. 2019). When the film temperature during drying resides below the pure polymers glass transition temperature, the film may undergo transition from rubbery to glassy state starting at the solvent depleted surface of the film (Romdhane et al. 2001; Arya et al. 2016; Merklein et al. 2021). This would result in a strong viscosity increase at the free surface and may inhibit lateral surface flows from convective instabilities (see section 1.2) (Berry and Fox 1968; Baumgärtel and Willenbacher 1996; Schnell and Wolf 2001). The solvent transport in a polymer solution above the glass transition temperature can be described accounting for Fickian diffusion, whereas below the glass transition temperature additional (e.g. visco-elastic) effects contributing to diffusion become relevant (Ramesh and Duda 2000; Mueller et al. 2012; Sharma et al. 2019).

The heat and mass transfer coefficients in the gas phase above the film can often be calculated from appropriate dimensionless Nusselt- or Sherwood-number correlations, respectively, specific to the type of forced convective airflow utilized during drying. Due to the analogy of heat and mass transfer, the transfer coefficients are linked by the Lewis's law. A comprehensive compilation of such correlations can be found in "VDI Heat Atlas" (VDI e.V. 2013). It is important to consider that these correlations exist for laterally averaged transfer coefficients as well as for local transfer coefficients. Considering an array of impinging jets, the transfer coefficients are largest at the stagnation point of the airflow. For a lateral flow, they are largest at the leading edge. This results in locally constant, but laterally inhomogeneous transfer coefficients during drying, which manifests in a laterally inhomogeneous drying rate. Similar inhomogeneities may arise when the substrate has defects (e.g. a weldseam), exhibiting laterally inhomogeneous heat conductivity (e.g. Gambaryan-Roisman 2010) or when an uncoated part of a thermally well-conducting substrate acts as a heat fin. Due to such lateral inhomogeneities in drying conditions, a lateral surface tension gradient may arise during drying, which induces a lateral Marangoni flow, solute transport and free surface deformations as schematically shown in Figure 1.3. The state of the art on convective instabilities in thin liquid films will be further discussed in section 1.2.

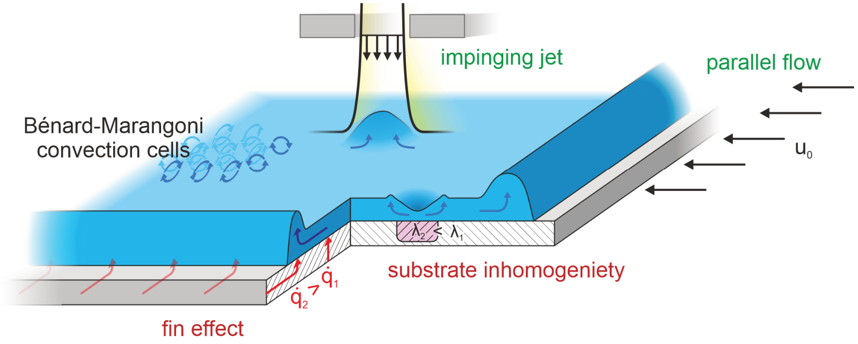

Figure 1.3: Schematic drawing of possible surface deformations due to laterally inhomogeneous drying conditions and surface gradient induced Marangoni flows in the drying film.

Experimental methods for the determination of temperature- and concentration-dependent phase equilibria and diffusion coefficients of polymer solutions have been developed in the past (e.g. Mamaliga et al. 2004; Schabel et al. 2007; Siebel et al. 2015). Other authors use various forms of gravimetric measurement techniques, NMR measurements, fluorescence spectroscopy, or theoretically derived diffusion coefficients based on the free volume theory (Grabowski and Mukhopadhyay 2008; Kriesten et al. 2009; Bernardo 2013; Sharma et al. 2017). In addition, a measurement technique based on Raman spectroscopy was established, which allows for the transient measurement of vertical concentration profiles during polymer film drying. Based on the experimental results and on the one-dimensional approach, a simulation model was developed. The Raman measurement technique as well as the simulation model are briefly summarized in the following subsections.

1.1.1 Inverse Micro Raman Spectroscopy

The Raman spectrum of a multicomponent solution can be accurately calculated by a weighted superposition of the individual component's pure Raman spectra (Schabel et al. 2004b; Schabel 2005). Considering a polymer solution, the weight factor after Schabel et al. (2004b) is proportional to the solvent load X, denoting the solvent mass per non-volatile polymer mass ($m_{solvent}/m_{polymer}$). The calibration factor (slope of the linear dependency) can be acquired by measuring the pure component's spectra and the spectra of several calibration solutions with known composition. Based on this approach, a microscopic measurement technique, named Inverse Micro Raman Spectroscopy (IMRS), was developed by Schabel et al. (2004b) and is explained in detail in Schabel (2004a) and Scharfer (2009). The optical access by an inverse confocal microscope was realized from below the film using a thin glass substrate. Vertical concentration profiles are derived by consecutively changing the vertical lens position with a piezo actuator, and a measurement resolution in the order of $\approx 1\ \mu m$ was achieved by using an oil immersion lens with high numeric aperture. Due to a possible mismatch between the refractive index of the utilized immersion oil and the polymer film, a vertical movement of the lens, for example $\Delta\tilde{z}_{lens} = 10\ \mu m$, does not necessarily coincide with the vertical position change of the focal point in the film. This focal displacement can be corrected, if the refractive index of the sample is known, which may change with changing solvent concentration during drying. The refractive index of a polymer solution, however, can be calculated from the pure component's refractive index using an ideal volumetric mixing rule (Schabel 2004a). Accordingly, the evaluation of IMRS measurements requires not only the Raman spectra of all utilized pure substances and corresponding calibration solutions with known composition, but also the refractive indices of all pure substances and their respective densities in order to calculate the concentration-dependent refractive index. For additional details regarding the experimental setup and the evaluation routine, the readers are referred to Schabel (2004a) and Scharfer (2009). The IMRS measurement technique is well established and was successfully applied in the past to acquire transient vertical concentration profiles in drying polymer solution films with up to three solvents (Schabel 2004a; Müller 2013; Siebel et al. 2016; Siebel et al. 2017a) under various drying conditions, as well as in polymer membranes (Scharfer et al. 2008; Scharfer 2009), and in interdiffusing polymer-polymer double layers (Raupp et al. 2017).

1.1.2 Numerical Simulation of Film Drying

In the Thin Film Technology group, a one-dimensional simulation model for isothermal polymer film drying was developed and validated for many different polymer-solvent combinations including poly(vinyl acetate)-methanol using experimental IMRS results (Schabel 2004a; Müller 2013; Siebel 2017b; Merklein et al. 2021). The model accounts for 1D Fickian solvent diffusion in the liquid film, the solvent's phase equilibrium and a constant mass transfer coefficient in the gas phase as upper boundary condition. For impermeable substrates, the lower boundary condition is a zero solvent flux condition. Additional details regarding the implementation can be found in Schabel (2004a) and Scharfer et al. (2008). A non-isothermal extension of the model, accounting for up to three substrate layers and evaporative cooling, was published by Erz (2014). The measurement of vertical temperature profiles in liquid films with a thickness in the order of 10 to 100 μm is a challenging task, yet to be resolved. Therefore, the simulated vertical temperature profiles in the drying film have not been validated quantitatively. However, a recent comparison between a similar implementation of the same governing equations with temperature measurements at the bottom of a free hanging substrate were in excellent agreement (Kumberg et al. 2020).

1.2 Convection in Thin Liquid Films

During film drying, several types of convective instabilities may arise in thin liquid films. Such instabilities manifest in three-dimensional convective flow within the liquid film. Whenever the non-volatile solute (polymer) is transported laterally, the dry film may be subject to surface deformation. In this section and the included subsections, the state of the art regarding possible sources of convective instabilities in thin liquid films is summarized.

1.2.1 Pure Liquid without Evaporation

More than a century ago, French physicist Henri Bénard (1900, 1901) was the first to report spontaneous pattern formation in thin liquid layers, uniformly heated from below. He observed polygonal convection cells with a very regular length scale in liquid layers of thicknesses in the range of 0.5 to 1 mm, and an upward flow at the cell centers as well as a downward flow at the borders (Figure 1.4). Bénard erroneously attributed this observation to buoyancy-driven instabilities.

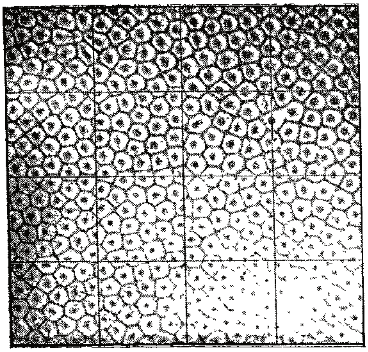

Figure 1.4: Top view on regular convection cell pattern observed in a thin (non-volatile) liquid ($h \approx 0.8\ mm$) heated from below. *Reprint from Bénard (1900) with permission from EDP Sciences.*

Inspired by this observation, Lord Rayleigh derived a theoretic stability analysis, accounting for buoyancy and density changes due to the heated bottom of the film (Rayleigh 1916). The analysis revealed a stability criterion, which must be exceeded for a liquid film to become convectively unstable. The instability criterion was later grouped into a dimensionless (subsequently named) critical Rayleigh number Ra_{crit}, depending on the vertical temperature difference and thermal expansion coefficient of the liquid. Furthermore, it was found that the least stable condition can be associated with a characteristic lateral wavenumber k (or wavelength λ) denoting the size of convection cells.[1] A schematic illustration of the instability mechanism is shown in Figure 1.5. The necessary condition is a liquid layer with a lower density at the bottom compared to the surface $\rho_b < \rho_s$. It starts with a fluid element near the bottom of the film, which flows upwards driven by buoyancy. In the case of a subcritical Rayleigh number $Ra < Ra_{crit}$, the upward flow dissipates and the liquid layer remains convectively stable.

---

[1] It has to be noted that according to Jeffreys (1926) the boundary conditions employed by Rayleigh imply a liquid film with a free surface at the surface <u>and</u> the bottom, which is unrealistic for real systems. Jeffreys provided solutions for various boundary conditions, including thermally conducting and insulating boundaries as well as a rigid or free upper surface.

When the Rayleigh number exceeds the critical threshold value Ra_{crit}, cellular convection emerges.

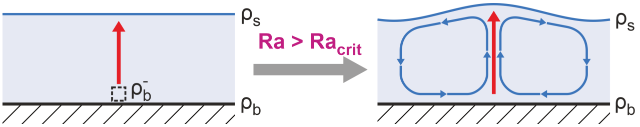

Figure 1.5: Schematic visualization of the Rayleigh-Bénard (RB) instability mechanism. The driving force of this convective instability is a buoyancy-driven upward flow in thin liquid layers, when the density is lower at the bottom of the film (e.g. higher temperature at the bottom). The instability arises when the Rayleigh number exceeds a critical threshold value Ra_{crit}.

The general case of buoyancy driven convection is known as natural convection, whereas the specific case in a thin liquid layer is named Rayleigh-Bénard (RB) convection[2].

Decades later and unsatisfied with the explanations provided by Bénard and Rayleigh, Block (1956) performed similar experiments observing hexagonal cells down to 50 μm film thickness in a hydrocarbon liquid. The observed hexagonal convection cells could be stopped by covering the liquid film with a thin insoluble silicone oil layer. With subsequent film thickness increase of the same sample, convective motion started again at 2 mm film thickness but without a regular pattern. Furthermore, Block observed cellular patterns in a liquid film with 0.8 mm thickness cooled from below, which should not exhibit any buoyancy effects. He concluded that surface tension fluctuations rather than buoyancy are causing hexagonal convection cells in thin films, because the added oil layer was unlikely to change the density of the underneath liquid. From the observation that a less regular convective instability emerged upon film thickness increase, Block further deduced that buoyancy driven convection is relevant only for thicker films.

---

[2] Critical Rayleigh numbers and Nusselt correlations for various boundary conditions as well as geometries are available (VDI e.V. 2013).

In a highly recognized publication, Pearson (1958) comes to a similar conclusion. He performed a linear stability analysis, assuming a thin non-volatile liquid film with a non-deformable free upper surface heated from below, and the liquid's surface tension linearly decreasing with temperature. Introducing a dimensionless (later to-be-named) Marangoni number

$$Ma = \frac{\partial\sigma}{\partial T}\Delta T_{vertical}\frac{h}{\eta\kappa}\ , \tag{1.1}$$

Pearson postulated a stability threshold Ma_{crit} for two limiting cases regarding the heat conductivity of the substrate. His analysis also included a dimensionless wavenumber k, being a reciprocal characteristic length for the lateral convection cell size. For an "insulating case", where the heat conductivity of the substrate is small compared to that of the liquid (constant heat flux boundary condition), he calculated a lower limit of $Ma_{crit} = 48$ (with a Biot number at the free surface of the film $Bi = \alpha_{top}h/\lambda \rightarrow 0$) for the onset of surface-tension-induced convection cells (Bénard-Marangoni (BM) convection). In a "conducting case", where the heat conductivity of the substrate is high compared to that of the liquid (constant temperature boundary condition), his analysis resulted in a critical threshold of $Ma_{crit} = 80$ ($Bi \rightarrow 0$, black line in Figure 1.7). The critical threshold value for both cases increased with increasing Biot number. The instability mechanism inferred from Pearson's analysis is depicted in Figure 1.6. It starts with a point at the free surface where the surface tension is slightly lower than its lateral surrounding (σ_s^-) induced by naturally occurring fluctuations. This causes a tangential surface flow due to the lateral surface tension gradient, which is known as Marangoni convection[3]. The liquid at the point of low surface tension is replenished by an upward vertical flow. According to Pearson's theory, the convective instability can only be maintained when the fluid element flowing upward has a lower surface tension than the surface[4] and therefore maintains the tangential Marangoni flow. Considering a pure liquid (as done by Pearson), this implies

---

[3] Carlo Giuseppe Matteo Marangoni was an Italian physicist (1840 – 1925) whose lifelong research efforts were focused on the investigation of free liquid surfaces.

[4] Note that a liquid's bulk has no free surface and therefore no surface tension. However, it possesses a certain temperature associated with a "fictive" surface tension value and as soon as the upward moving liquid reaches the film's free surface, the surface tension emerges.

that the film must be heated from below, since the surface tension of liquids decreases with increasing temperature (e.g. Poling et al. 2001, see Figure 3.4 (a)). The initial trigger of such instabilities is a tangential surface tension gradient, which is induced by a lateral Marangoni flow, but the instability is maintained by the upward vertical flow. This explains why Pearson's definition of the Marangoni number (equation (1.1)) contains a vertical temperature difference $\Delta T_{vertical}$ and not a lateral one. The limiting case of $Bi \rightarrow 0$ in Pearson's analyses can be regarded as a thermally insulated free film surface and therefore initial lateral temperature perturbations persist at the film's surface making it least stable, whereas for $Bi > 0$ lateral temperature perturbations are mitigated due to the heat transfer to the gas phase. Hence, the stability threshold increases (Pearson 1958).

In analogy to Rayleigh's analysis, the liquid layer's Marangoni number has to exceed the critical threshold values Ma_{crit} in order to become convectively unstable (Pearson 1958). It has to be noted that, according to the original theoretic models, neither Rayleigh-Bénard (RB, Rayleigh 1916) nor Bénard-Marangoni (BM, Pearson 1958) convection analyses account for a deformable free surface, whereas such are shown in Figure 1.5 and Figure 1.6. Nevertheless, several authors point out that it is a possible indicator to identify experimentally which mechanism is the cause of observed convection cells in liquid films. A surface elevation at the cell centers indicates buoyancy driven convection (RB), whereas an indentation at the cell centers indicates surface tension driven (BM) convection (e.g. Scriven and Sternling 1964; Berg et al. 1966).

Comparing his findings with the critical Rayleigh number $Ra_{crit} = 571$ (Jeffreys 1926) for the onset of buoyancy-driven convection, Pearson further concluded that for film thicknesses above 1 cm, buoyancy (Rayleigh-Bénard mechanism) is the dominant cause for convection cells, while for a thickness below 1 mm, surface tension fluctuations (Bénard-Marangoni mechanism) are the sole cause for convection. In the present, it is established to refer to the dimensionless Bond number Bo (see section 3.5, equation (3.1)) to assess which mechanism dominates. $Bo \ll 1$ implies the prevalence of surface tension driven instabilities, whereas $Bo \gg 1$ implies buoyancy (e.g. Schatz and Neitzel 2001; Rahal et al. 2007; Craster and Matar 2009). Nevertheless, Pearson's conclusion regarding the film thickness limits remains valid.

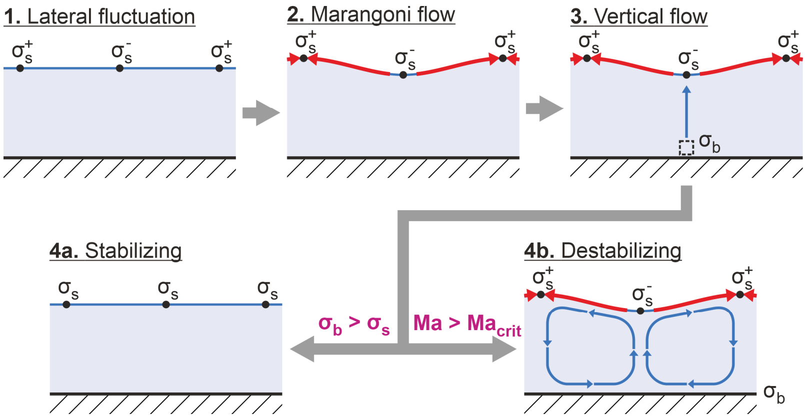

Figure 1.6: Schematic representation of the convective instability mechanism (Bénard-Marangoni convection cells) inferred from Pearson's (1958) linear stability analysis. A lateral Marangoni flow induced by naturally occurring lateral perturbations in the surface tension triggers the instability, whereas the vertical surface tension difference continuously drives the instability.

Additional theoretical work has been performed by Nield (1964) who combined Rayleigh's and Pearson's theories and found that both instability mechanisms may reinforce one another, reducing the individual stability thresholds when simultaneous RB and BM convection, known as Rayleigh-Bénard-Marangoni (RBM) convection, was considered. Davis (1969) introduced a method of energy, complementary to Pearson's linear stability analysis, and postulated "subcritical" disturbances for the conducting case starting at $Ma \approx 57$. Both, Nield and Davis assumed a non-deformable free surface.

On the contrary, Scriven and Sternling (1964) extended Pearson's analysis by allowing a deformation of the free upper film surface in their mathematical model. The deformability was described with a dimensionless Capillary number describing the ratio of viscous to surface tension forces $Ca{\sim}\eta/\sigma$ (see section 3.5, equation (3.6)). The film stability was assessed by mathematically superimposing a small initial lateral disturbance with a given wavenumber. Subsequently, it was analyzed under which conditions the disturbance amplifies or weakens. The authors found that for small wavenumbers k (large disturbance's lateral wavelength) Ma_{crit} decreases, and that for the limiting case of zero wavenumber (infinite wavelength) thin liquid films are always unstable. This can be seen in Figure 1.7 where the black line denotes Ma_{crit} as a function of the dimensionless wavenumber k (and dimensionless wavelength λ/h, upper horizontal axis) as derived by the Pearson model with a non-deformable free surface ($Ca \rightarrow 0$), resulting in a global minimum of the Marangoni number $Ma_{crit} = 80$ (black circle). The blue line accounts for a surface deformability, increasing with increasing Capillary number, and show no global minimum in the Marangoni number. These findings led to an important distinction between two different forms of Marangoni convection: Short-scale instabilities, known as the already discussed Bénard-Marangoni convection cells, with a characteristic lateral length scale in the order of the film thickness (λ/h in the order of 1), and long-scale instabilities, having a characteristic lateral length scale significantly larger than the film thickness ($\lambda/h \gg 1$) and resulting in a lateral flow alongside with a free surface deformation (e.g. Takashima 1981; Gambaryan-Roisman 2015). Smith (1966) additionally accounted for the leveling effect of long-scale surface deformations due to gravity. This can be accounted for by a dimensionless Galileo number Ga (see section 3.5, equation (3.7)), representing the ratio of gravitational to viscous forces, and improves the stability for long-scale deformations (small k), as shown by the red line in Figure 1.7 (increased y-axis intercept of red line to $Ma_{crit} > 0$ in comparison with blue line without gravity wave leveling).

These early theoretic findings imply that short-scale Bénard-Marangoni convection may occur without a free surface deformation, whereas the deformability is a necessary requirement for long-scale Marangoni instabilities. It appears logical that there must be a critical threshold limit for convection cells (short-scale instability) to appear, as the lateral Marangoni flow must be strong enough to initiate cellular convection. The long-scale instability, however, implies that the characteristic lateral length scale of the convection is significantly larger than the film thickness and therefore has to manifest solely in a lateral flow, whereas a critical stability threshold for such a flow is less apparent. This can be understood when acknowledging that the long-scale instability is always accompanied by surface deformations, as implied by the previously discussed theoretical results.

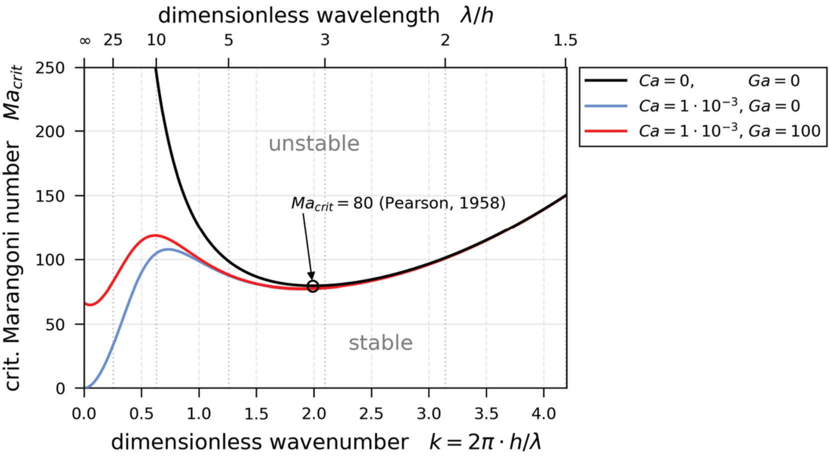

Figure 1.7: Critical Marangoni number as function of the dimensionless wavelength for the "conducting" case with a constant temperature at the bottom of the film and a Biot number $Bi \rightarrow 0$ at the surface. The black line is the result of the Pearson model (Pearson 1958) with a non-deformable free surface ($Ca \rightarrow 0$, surface tension forces dominate over viscous forces). The blue line include a deformable surface accounted for by an increasing Capillary number $Ca = \eta\kappa/(\sigma_s h) > 0$ (Scriven and Sternling 1964). The deformability significantly reduces the stability threshold at low dimensionless wavenumbers (long-scale) with a limiting value of $Ma_{crit} = 0$ at $k = 0$. The red line additionally accounts for the stabilizing effect of gravity-wave leveling, especially at low wavenumbers (Smith 1966), quantified by a dimensionless Galileo number $Ga = \rho g h^3/(\eta\kappa)$. *Own calculations based on equations by Pearson (1958), Scriven and Sternling (1964), and Smith (1966).*

Assuming a thin liquid film with a periodically deformed free surface, De Gennes et al. (2010) summarized the two possible leveling mechanisms counteracting the deformations inferred by the discussed results of Scriven and Sternling (1964) and Smith (1966): *First*, a periodically deformed liquid surface has a higher surface area compared to the flat surface. Accordingly, the sheer presence of surface tension (no gradients required) acts as contracting tangential force. Fundamental principles of thermodynamics imply that any system desires to reach the lowest possible state of free energy. For systems with a free liquid surface and surface tension, this manifests in the desire to minimize its free surface area.[5] This leveling mechanism is sometimes referred to as capillarity or "capillary waves" and is commonly described with the dimensionless Capillary number[6] Ca being the quotient of viscous forces resisting leveling and surface tension enhancing leveling. When the lateral length-scale of periodic deformations is very large, the surface area increase compared to a flat surface is small. Consequently, the capillary leveling mechanism is only relevant for small to moderate lateral length scales of perturbations. This explains why theoretical models accounting for capillarity still show no critical Marangoni threshold for the limiting case of zero wavenumber (infinite wavelength) as discussed and indicated by the blue line in Figure 1.7. The *second* leveling mechanism summarized by De Gennes et al. (2010) accounts for hydrostatic pressure differences. Due to gravity, the hydrostatic pressure under an elevated portion of a deformed liquid film (larger film thickness) is higher than under a depression (smaller film thickness). The leveling occurs because of the desire of the system to balance this lateral hydrostatic pressure difference. It can be quantified in the form of a dimensionless Galileo number[7] $Ga \sim \rho g h^3/\eta$ and is often referred to as "gravity waves".

---

[5] Two popular scientific observations illustrate this effect: First, droplets of water, having a high surface tension of $\approx 72\ mN/m$, adopt a spherical form in zero-gravity environments, since a sphere has the smallest surface area for a given volume. Second, a small coin carefully placed on the free surface of a pool of water can float on the free surface despite having a higher density. The weight force of the coin deforms the surface of water whereas the desire to minimize the free surface due to the high surface tension keeps the coin afloat.

[6] Several definitions can be found in literature focused on Marangoni convection, differing in the definition of the characteristic velocity v_c in $Ca = \eta v_c/\sigma$. For Marangoni convection induced by temperature effects $v_c = \kappa/h$ is commonly employed (e.g. Golovin et al. 1995; Bestehorn et al. 2003; Doumenc et al. 2010) whereas for concentration gradient induced (solutal) Marangoni convection (see section 1.2.3) $v_c = \delta_{ij}/h$ is widely used (e.g. Trouette et al. 2012; Hennessy and Munch 2014). Considering evaporating films (see section 1.2.2) $v_c = v_{int}$, being the surface shrinkage velocity, can also be found (e.g. Sultan et al. 2005; Babaie and Stoeber 2015). Note that several authors also use the name Crispation number for the Capillary number or it's inverse (e.g. Bestehorn et al. 2003; Doumenc et al. 2010).

[7] For Marangoni convection induced by temperature $Ga = \rho g h^3/\eta\kappa$ is prevalent (e.g. Golovin et al. 1995; Doumenc et al. 2010), whereas for solutally induced Marangoni convection (see section 1.2.3) $Ga = \rho g h^3/(\eta\delta_{ij})$ is used (e.g. Trouette et al. 2012; Hennessy and Munch 2014). Other authors use the Bond number instead of the Galileo number.

According to De Gennes et al. (2010) the dominating leveling mechanism can be found by comparing the lateral length scale of surface deformations with a capillary length

$$l_{capillary} = \sqrt{\sigma/(\rho g)}\ , \tag{1.2}$$

which is in the order of a few millimeters for most liquids. In the case of $\lambda \ll l_{capillary}$, capillary wave leveling dominates, whereas for $\lambda \gg l_{capillary}$ gravity wave leveling is dominant (De Gennes et al. 2010). This explains why the consideration of gravity waves increases the stability of long-scale (large wavelength, short wavenumber) instabilities (reintroducing a global minimum of Ma_{crit}, see Figure 1.7 red line compared to blue line), whereas it has little effect on short-scale (short wavelength, large wavenumber) instabilities.

Regarding thin drying polymer-solvent films under consideration in this dissertation, it is to be expected that, due to a strong viscosity increase during drying and the small film thickness (in the order of μm), neither capillary nor gravity wave leveling are of relevant importance.

Despite the long ongoing research efforts in this field, experimental findings regarding the validation of classic stability threshold theories of short- and long-scale Bénard-Marangoni convection are scarce. Koschmieder and Biggerstaff (1986) observed the onset of hexagonal convection cells in silicone oil films with 2 to 5 mm thickness, agreeing with Pearson's conducting case ($Ma_{crit} \approx 80$), but they also observed subcritical irregular instabilities starting at $Ma \approx 7$, which is below any theoretically found stability threshold. Schatz et al. (1995) found a critical Marangoni number of $Ma_{crit} = 84$ with a hysteresis of 3 % during experiments with silicone oil layers of $0.4\ mm$ thickness, observed with shadowgraphy. Palmer and Berg (1971) experimentally investigated combined Rayleigh-Bénard-Marangoni (RBM) convection. The resulting stability threshold was in reasonable agreement with the theoretical results by Nield (1964). Considering long-scale Marangoni convection, VanHook et al. (1995) found instabilities 35 % below the onset predicted by linear theory. In a follow-up work, VanHook et al. (1997) assessed from experiments in combination with a theoretic analysis including the dynamics of the gas phase that short-scale BM convection cells are predominant in relatively thick films ($h > 0.24\ mm$), whereas a long-scale deformational instability was only observed under special conditions (e.g. small Galileo number and a helium as gas phase) in sufficiently thin films ($h < 0.17\,mm$).

Thermally induced Marangoni convection caused by a *deliberate lateral temperature gradient* was theoretically investigated by Smith and Davis (1983). Their definition of the Marangoni number merely differs from equation (1.1) in the direction of the temperature difference. The authors differentiate between two flow states within the liquid film: A laterally infinite film with a linear velocity profile over the film height and a film laterally bounded by rigid walls with a return flow in the liquid bulk. They conclude that for $Ma \geq 21$ for an infinite film and $Ma \geq 399$ for bounded films with return flow, the films are always convectively unstable. No experimental validation of the critical thresholds reported by Smith and Davis (1983) could be found in literature for thin liquid layers. Villers and Platten (1992), Daviaud and Vince (1993), as well as Riley and Neitzel (1998) experimentally investigated convective instabilities due to a deliberate lateral temperature gradient in a liquid layer but they all investigated cases were a combination of thermocapillary- and buoyancy-driven convection occurred (RBM convection) simultaneously. Furthermore, they focused on transitions between different convective modes rather than the onset of convection.

Additional aspects subject to investigations are the lateral cell size beyond the critical stability threshold (Cerisier et al. 1987; Koschmieder and Switzer 1992; Eckert et al. 1998), the form and transition between different cell geometries (Cerisier et al. 1987; Eckert et al. 1998; Cross and Hohenberg 1993), the film aspect ratio (Cerisier et al. 1987; Rahal et al. 2007), as well as floating zone process geometries (Schwabe and Scharmann 1979; Cröll et al. 1989).

In summary, convective instabilities in thin films are caused either by buoyancy driven Rayleigh-Bénard (RB) convection or by surface tension gradient induced Bénard-Marangoni (BM) convection. The dominance of either mechanism can be discriminated with the dimensionless Bond number. For thin films below $1\,mm$ thickness, being the focus of this dissertation, Marangoni convection is prevalent. In the case of short scale perturbations the convective instability manifests in the form of convection cells and the stability threshold can be characterized by a critical Marangoni number Ma_{crit}, which is not a constant value but depends on the boundary conditions. In the case of long scale perturbations, the instability manifests in a lateral flow always associated with surface deformations. The stability threshold may be lower or non-existent, depending on the strength of gravity wave or capillary wave leveling, which decreases with increasing viscosity. Experimental validation of theoretically predicted stability thresholds are scarce and ambiguous. Several reviews focusing on thermally induced Marangoni convection in non-volatile liquids have been published in the past. Davis (1987) focuses on theoretical work while Schatz and Neitzel (2001) exclusively account for experimental findings. Nepomnyashchy et al. (2001) covers both but focuses on theory. Additional reviews on flow dynamics in liquid films, not limited to Marangoni convection, are also available (Oron et al. 1997; Craster and Matar 2009; Gambaryan-Roisman 2015).

1.2.2 Pure Liquid Subject to Evaporation

Heretofore, only non-volatile liquid films with a forced temperature gradient (external temperature control) have been considered, giving rise to Rayleigh-Bénard or Bénard-Marangoni convection in thin liquid films. Considering a volatile liquid subject to evaporation, it is possible that evaporative cooling of the free film surface induces thermally driven Marangoni convection. This was already insinuated in Pearson's pioneering work (Pearson 1958). In an early review, Berg et al. (1966) summarized past developments regarding linear stability analyses and compiled recent observations of various convective patterns in evaporating liquids not limited to thin films.

Decades later, Chai and Zhang (1998) argued that all past theories on RB and BM convection rely on a negative vertical temperature gradient (hot bottom and cool free surface) and cannot account for the cellular patterns observed by Block (1956) in a film cooled from below. They performed evaporation experiments with alcohol and R-113 films, having a thickness in the range of 1 to 2 mm and being either heated or cooled uniformly from below and evaporating into ambient air. The convection was visualized with a small amount of aluminum powder carefully applied on top of the liquid films and the liquid motion was recorded with a camera from above. The vertical temperature gradient was measured with thermocouples placed at different heights within the film. They observed short-scale cellular motion even at zero or positive (cool bottom, hot free surface,

$Ma < 0$) vertical temperature gradients. The authors concluded that lateral perturbations in the evaporation rate may induce lateral temperature fluctuations at the free surface due to local evaporative cooling and may cause the observed cellular convective patterns in volatile liquids, even in the absence of a negative vertical temperature gradient. Furthermore, they suggest a modified Marangoni number as a function of evaporation rate and heat of vaporization. In a follow-up work, Zhang and Chao (1999) report similar experiments and short-scale cellular convection was observed at classical Marangoni numbers (equation (1.1)) as low as $Ma = -109$ but no critical threshold values for their modified Marangoni number were provided, since all investigated films were convectively unstable.

Mancini and Maza (2004) performed experiments, investigating evaporating hexamethyldisiloxane films without external temperature control. A low but constant drying rate was realized by placing the evaporating film in a sealed box, which was slowly evacuated, removing the solvent loaded air while replenishing it with solvent free air. During evaporation, starting at a film thickness of $2\ mm$, irregular turbulent convection was observed in the film, which transformed into ordered cell patterns when the film thickness fell below $0.8\ mm$ and the wavelength monotonically decreased with film shrinkage. Below a critical film height of $0.3 \pm 0.02\ mm$, the motion stopped altogether, and the film became convectively stable. The authors assessed that this stability threshold is in reasonable agreement with theoretic values for non-volatile films. It has to be noted, however, that the vertical temperature difference during the experiment, necessary for the comparison with theory, was close to the resolution limit of the used sensors. Nevertheless, the results imply that critical stability thresholds derived for non-volatile liquid films are applicable to volatile films for very low drying rates and a homogeneous gas phase.

Regarding theoretic stability analyses accounting for evaporation, a distinction between one-layer models, where the gas layer was not considered explicitly but only in the form of the upper Biot number (like the Pearson model), and two-layer models, explicitly accounting for a gas layer above the liquid film, emerged (e.g. Merkt and Bestehorn 2003; Sultan et al. 2005). The relative importance of the gas phase above an evaporating liquid film was investigated by Sultan et al. (2005), considering only long-scale convective instabilities in the film. The authors summarized past theoretical work on evaporating films, which all were one-layer models. All of the reviewed works imply that evaporation always acts destabilizing on long-scale convection in liquid films. Sultan et al. (2005) extended these studies by deriving a two-layer model, accounting for vapor diffusion and discussing two limiting cases of evaporation. For the case that the evaporation is limited by the mass transfer across the liquid-gas interface, the impact of vapor diffusion was negligible, and evaporation was assessed to always act destabilizing on the liquid film, in accordance with the one-layer models. In the second case, however, the evaporation was limited by vapor diffusion in the gas phase which had a stabilizing effect on long-scale convective instabilities (Sultan et al. 2005).

In summary, the dynamics of the gas phase in contact with an evaporating liquid film may affect the stability threshold of convective instabilities. For more information regarding long-scale convective instabilities, the readers are referred to two comprehensive reviews on the matter. Oron et al. (1997) summarized the governing equations and gave an overview of available one-layer models whereas Craster and Matar (2009) focused on two-layer models as well as experimental findings. The review by Karbalaei et al. (2016) on thermally induced Marangoni convection also considers short-scale instabilities, yet it is not limited to liquid film geometries, but also considers sessile droplets.

1.2.3 Multi-component Mixtures

Complexity increases, when the liquid film under consideration is not a pure substance but a liquid mixture or solution. In this case, the surface tension of the liquid is not only a function of the temperature but additionally depends on the composition (e.g. Poling et al. 2001). Vertical as well as lateral concentration gradients may therefore lead to solutally induced Marangoni convection. This was also indicated in the early work of Pearson (1958).

One of the earliest reports of this phenomenon was published by Thomson (1855) explaining the tears of wine phenomenon. The effect can be observed in a glass filled with e.g. strong wine or liquor. At ambient conditions, the liquid at the three-phase contact line (where the free liquid surface is in contact with the inner glass surface) continuously flows upwards the inner side of the glass until several millimeters above the initial contact line, the film then breaks up into droplets, which flow back into the liquid bulk. Thomson assumed a binary liquid mixture of ethanol and water, where ethanol has the higher vapor pressure but a significantly lower surface tension. Due to the preferred selective evaporation of ethanol, the concentration of water increases at the contact line, giving rise to a local increase in surface tension, which ultimately results in solutal Marangoni convection from the center of the free surface in the middle of the glass towards the contact line. The convection is strong enough to form the observed thin liquid film rising up the inner side of the glass defying gravity. A secondary instability causes the breakup into droplets. A more recent investigation of the tears of wine phenomenon suggests that, in addition to solutal effects, evaporative cooling significantly contributes to this effect due to the temperature dependency of the surface tension (Venerus and Nieto Simavilla 2015).

Regarding thin liquid films, several authors theoretically studied the stability of binary mixtures without evaporation and a solutal Marangoni number was introduced (e.g. Bahloul et al. 2003):

$$Ma_s = \frac{\partial \sigma}{\partial c} \Delta c_{vertical} \frac{h}{\eta \delta_{ij}} \tag{1.3}$$

McTaggart (1983) generalized the linear stability analysis by Pearson (1958), considering both thermally and solutally induced short-scale Marangoni convection. Similar to the RBM coupling performed by Nield (1964), McTaggart found that both effects may reinforce one another, reducing the individual stability threshold. This is shown in Figure 1.8 where the stability thresholds of combined thermal and solutal Marangoni convection according to McTaggart (1983) are depicted. The limiting case of purely thermal instabilities ($Ma_s = 0$) coincides with Pearson's conducting case with a constant temperature at the bottom of the film. Considering only solutal effects ($Ma_T = 0$), the analogy to the thermal conducting case would imply a constant concentration at the bottom of the film (a permeable substrate). Instead, Figure 1.8 shows the solutal analogy of the insulating case, with a zero mass-flux condition at the bottom of the film. Again, in analogy to Pearson, an increase in the thermal or solutal Biot number increases the stability threshold.

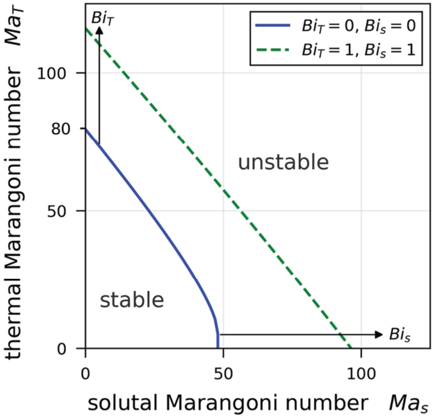

Figure 1.8: Neutral stability curves of simultaneous thermally and solutally induced short-scale Bénard-Marangoni convection as derived by McTaggart (1983) for the conducting thermal case (constant bottom temperature) in combination with the insulating solutal case (zero vertical mass flux at the bottom).

In the last two decades, film drying of polymer solutions has received much attention. Due to the exponential viscosity increase with decreasing solvent content during drying and subsequent solidification, potential surface deformations may be preserved in the solid polymer film. However, the focus of published research was not solely focused on identifying stability thresholds of convective instabilities but more on the deliberate pattern formation through (sometimes surface tension driven) self-assembly (motivated by e.g. structural colors, superhydrophobic surfaces, biological microarrays or photonic waveguides; Janes et al. 2013). Several experimental findings, occasionally attributed to Marangoni convection, were reported. Ordered patterns in polymer solutions subject to phase separation during drying have been found (e.g. Kumacheva et al. 1997; Xu et al. 2003; Xue et al. 2012; Foglarová et al. 2016). Varying surface roughness of dry polymer films with varying evaporation rate were reported experimentally (Strawhecker et al. 2001; Luo et al. 2005). In a series of theoretic considerations, Birnie et al. attribute this observation to solutally induced Marangoni convection (Birnie 2001; Haas and Birnie 2002; Birnie 2013). Regular patterns observed in drying polymer films not subject to phase separation were also observed (e.g. Sakurai et al. 2002; Torres et al. 2005; Wu et al. 2008).

Meanwhile, De Gennes (2001, 2002) derived a mathematical model of polymer film drying subject to short-scale convective instabilities. He proposed a new solutal mechanism but the description strongly resembles the mechanism already implied by Pearson, as shown in Figure 1.6 but with concentration gradients being the source of surface tension differences. In addition, De Gennes argued that a polymer-rich skin might undergo mechanical tension and rupture at an advanced drying stage, leading to surface deformations. Additional theoretic models accounting for solutal Marangoni convection in drying polymer-solution films are available, but all make simplifying assumptions such as a constant viscosity, a constant diffusion coefficient or surface tension linear with concentration (Bahloul et al. 2003; Machrafi et al. 2010; Serpetsi and Yiantsios 2012; Hennessy and Munch 2014).

A few authors investigated the impact of a *deliberate lateral gradient* as cause for Marangoni convection. Chen and Lin (2000) derived a mathematical model studying RBM convection in polymer solution with a Gaussian radiant heat profile at the free surface. They accounted for a viscosity increase and film shrinkage, but limited Marangoni effects to thermal contributions. Weh (2005) experimentally introduced a point heat source under evaporating films and observed regular honeycomb patterns without local heating and more complex patterns upon heating. An interesting observation was reported by Bormashenko et al. (2010). They dried a film of polystyrene and polycarbonate in a mixture of chloroform and dichloromethane on a flat substrate, locally heated from below with a single wire, under otherwise ambient conditions. Curiously, the film area above the wire was free of patterns, while the adjacent regions developed regular cells. The authors argue that this observation contradicts the idea of thermal Marangoni instabilities being the cause of patterning, since $Ma_T \approx 2 - 20$. Additionally, they elaborate that swift solidification due to rapid evaporation can neither be the cause for the pattern-free area, because the patterns generally appeared within the first second of evaporation while drying time was approximately 10 s. They conclude that concentration gradients and solutal Marangoni effects must be the cause for large-scale patterns.

In order to assess whether mechanical instabilities due to a polymer-rich skin proposed by De Gennes (2002) or convective instabilities are the reason for surface deformations, Bassou and Rharbi (2009) performed film drying experiments with polystyrene-toluene solutions. The initial polymer concentration was

$5\ vol\%$ to $20\ vol\%$, the film thickness was in the range of $55\ \mu m$ to $1.5\ mm$ and the drying rate was controlled using perforated covers with differently sized holes, resulting in drying rates between $0.03\ g/(m^2 s)$ and $0.35\ g/(m^2 s)$. The evolving patterns were observed from above using 2D in-situ particle image velocimetry and shadowgraphy of the dry films. The concentration-dependent viscosity as well as the concentration- and temperature-dependent surface tension were measured in order to calculate the thermal and solutal Marangoni numbers and the Rayleigh number. Ordered patterns were observed in solutions $\geq 10\ vol\%$ polystyrene, whereas at $5\ vol\%$ the resulting patterns in the dry film were less ordered. The cell wavelength increased linearly with initial film thickness showing no clear dependency on the initial concentration. The ratio of deformation amplitude to average dry film thickness, on the other hand, increased linearly with evaporation rate, while being constant for all initial concentrations. Regarding the transient evolution of the lateral pattern size, a constant lateral length scale over $75\ \%$ of the drying time was found. The authors argued that the linear dependency of the wavelength on the initial film thickness implies RB or BM instabilities. They estimated a maximum Rayleigh number of $Ra < 5 \ll Ra_{crit}$, concluding that buoyancy effects can be excluded. The thermal Marangoni number was calculated to be in the range of $Ma_T = 721 - 15.6$ with increasing polymer concentration. Comparing these values with $Ma_T \approx 80$ from Pearson (1958), they assess that for higher initial polymer concentrations, patterns were not induced by thermal BM convection either. Finally, the authors estimated a solutal Marangoni number in the range of $Ma_s = 73 - 14319$ increasing with initial film thickness. In the absence of available critical solutal Marangoni numbers, Bassou and Rharbi concluded that pattern formation was either due to thermal or solutal Bénard-Marangoni convection while the amplitude of deformations increasing with evaporation rate could be attributed to a faster local viscosity increase at the cell borders.

The discussed publications up to this point show that regular pattern formation and surface deformations are common phenomena found during polymer film drying. Several authors attribute these observations to convective Marangoni instabilities and some of them conclude that solutal Marangoni convection is dominating over thermal effects (De Gennes 2001; Bassou and Rharbi 2009; Machrafi et al. 2010; Bormashenko et al. 2010; Cavadini et al. 2013). However, little experimental work could be found, which quantitatively investigates the stability threshold of convective instabilities in thin drying polymer films. This has been acknowledged by several authors in the past. Only recently, Wang et al. (2016) published a comprehensive review on multiphase non-equilibrium Marangoni convection and explicitly emphasized the need for new quantitative experiments in polymer film drying subject to convective instabilities, as done in this work.

A noteworthy exception was published by Toussaint et al. (2008). They experimentally investigated convection cells in polyisobutylene-toluene films with an initial thickness between 0.3 and $14.3\ mm$ and an initial polymer cocentration between 0 to 15 $wt\%$. They observed Bénard-like convection cells in films with an initial thickness $\leq 4\ mm$, and for thicker films they found roll cells, persisting even after a solvent-depleted viscous surface layer emerged during drying. These modes of instability were attributed to BM and RB convection, respectively. The experimental results indicate that skin formation during drying strongly affects BM convection but only weakly impacts RB convection. The authors conclude that a skin may dampen Marangoni convection even above the stability threshold but do not explicitly consider the possibility of glass transition (see section 1.1).

Below 5 mm, the initial cell wavelength increased almost linearly with the initial film thickness, being in reasonable agreement with classical BM theory ($k_{crit} \approx 2$, Pearson 1958, see Figure 1.7) and in qualitative agreement with the observations by Bassou and Rharbi (2009). Based on these experiments, Touazi et al. (2010) developed a two-dimensional mathematical model accounting for thermal RBM convection but neglected solutal effects. Further simplifications were a flat non-deforming surface and a constant film thickness. The focus was on a realistic viscosity increase during solvent evaporation. The model accounted well for the increasing cell wavelength with initial film thickness. In addition, the critical stability threshold at the onset of drying was in reasonable agreement with the experimental findings by Toussaint et al. (2008). The end of convective instabilities during the drying experiments, however, was not discussed. The mathematical model revealed that for the limiting case of pure Marangoni instabilities (no gravity), $Ma_{T,crit}$ solely and non-monotonically depends on the Biot number with a minimum value at $Bi_T \approx 2$. The reported values for the critical thermal Marangoni numbers were in the order of 10^2 to 10^5.

A slightly different model, accounting for film-shrinkage, a realistic viscosity increase, and solutal Marangoni convection but neglecting thermal effects, was reported by Trouette et al. (2012). Several simplifying assumptions were made: The concentration dependency of the diffusion coefficient in the film was neglected, using a constant value of $\delta_{ij} = 10^{-10}\ m^2/s$(which typically changes orders of magnitude with concentration, see Figure 1.2) and the concentration dependency of the surface tension was assumed linear. Unfortunately, no experimental validation was provided. Nevertheless, two interesting relations regarding the critical solutal Marangoni number were found. $Ma_{s,crit}$ increased with increasing Pécet number $Pe = v_{int}h/\delta_{ij}$, where v_{int}, h and δ_{ij} denote the film shrinkage velocity, the film thickness and the diffusion coefficient in the film, respectively. In addition, the model revealed that $Ma_{s,crit}$ initially decreased with increasing Schmidt number Sc, asymptotically approaching a constant value for very large Schmidt numbers. The found critical solutal Marangoni number ranged in the order of 10^2 to 10^5, similar to the experimentally validated model by Touazi et al. (2010), which accounts only for thermal effects.

1.2.4 Measurement Techniques

Several measurement techniques are widespread in available publications, visualizing short-scale convection cells. Providing (microscopic) pictures of the dry film, recorded with a regular camera or microscope, or pictures acquired using shadowgraphy/schlieren photography methods (e.g. Berg et al. 1966) are the most prevalent visualization methods (e.g. Li et al. 2000b; Mancini and Maza 2004; Bormashenko et al. 2006; Bassou and Rharbi 2009). Regular camera recordings rely on the optical visibility of cell features and are therefore only applicable to films with non-volatile intransparent components, whereas shadowgraphy and schlieren photography methods rely on the distortion of transmitted light, which can be achieved by surface deformations or components with varying refractive index. As the latter techniques require transmitted light, they are rarely used on its own for in-situ measurements. In addition, films under investigation often do not meet the aforementioned requirements. Therefore, several authors have applied an early form of particle image velocimetry (PIV), adding a small amount of visible powders or tracer particles which follow the convective motion of the liquid and can be observed in-situ or in the dry film (e.g. Bénard 1901; Koschmieder 1974; Chai and Zhang 1998; Toussaint et al. 2008). Such early works, however, use the particles only as means for (microscopic) visualization without assessing flow velocities or 3D images. A complementary measurement option for thermally induced convection is the recording with a thermal imaging (IR) camera (e.g. Toussaint et al. 2008; Chauvet et al. 2012; Doumenc et al. 2013; Sankaran and Yarin 2018). All these methods provide a two-dimensional top view of the films under investigation. Furthermore, and despite the long ongoing research on convective instabilities in thin liquid films, high quality images of cell patterns are surprisingly scarce. This was acknowledged by Chmelař et al. (2019) and motivated them to provide high-resolution pictures of cellular patterns in acrylated hyaluronan films.

Preceding this dissertation, Krenn et al. (2011) developed an experimental method to measure the transient long-scale surface deformations of polymer-solvent films during drying[8]. They placed a random dot pattern below the film and reconstructed the free surface position in three dimensions by cross correlating the distorted pattern observed from top view with the undistorted original. The applicability was demonstrated using a thermally conducting aluminum block with a small hole in the center below a thin glass substrate. The lateral inhomogeneity in heat transfer due to the hole resulted in a local surface depression in the film, developing during drying, which was attributed to long-scale Marangoni convection and successfully observed in-situ (Krenn et al. 2011). The same measurement technique was used to observe surface deformations with deliberate laterally inhomogeneous drying conditions, using an aluminum substrate (high thermal conductivity) with a partial Teflon inlay (low thermal conductivity) (Figure 1.9, Cavadini et al. 2013). In this configuration, a poly(vinyl acetate)-methanol film with an initial film thickness of $150\ \mu m$ and an initial polymer concentration of $33\ wt\%$ was dried with a constant lateral air velocity of $0.5\ m/s$ and the aluminum block kept at a constant temperature of $30\ °C$.

---

[8] Joachim (Krenn) Erz and Philip Cavadini are the predecessors of this work's author, who also conducted research on Marangoni instabilities in drying polymer films in the Thin Film Technology group of KIT.

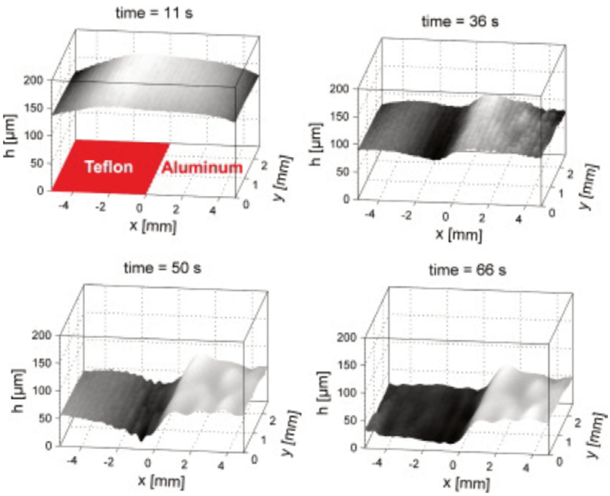

Figure 1.9: Transient evolution of a surface deformation in a drying poly(vinyl acetate)-methanol film subject to deliberate laterally inhomogeneous experimental conditions using an aluminum substrate with a Teflon inlay *Reprint from Cavadini et al. (2013) with permission from Elsevier.*

The authors argue that two competing Marangoni mechanisms may occur: *Assuming only thermally induced convection*, the reduced heat flux at the position of the Teflon inlay would result in a lower surface temperature compared to the adjacent area without inlay. Since a lower temperature implies a higher surface tension, a lateral thermally induced Marangoni flow *towards the area of the Teflon inlay* would be expected. On the other hand, *assuming only solutally induced convection*, a reduced surface temperature would lead to a lower vapor pressure of the volatile methanol and therefore a lower drying rate and a higher solvent content above the inlay. Since surface tension increases with decreasing methanol content, a solutal Marangoni flow should manifest *away from the inlay*. The experimental observations revealed that a surface wave developed during drying, with material transport away from the Teflon inlay, showing that solutal Marangoni convection dominated over thermal effects (see Figure 1.9). Additionally, secondary short-scale deformations were observed above the inlay-free aluminum substrate. Neither the air velocity nor the substrate temperature affected the dry surface profile significantly. Accompanying 1D non-isothermal drying simulations supported the conclusion that solutal Marangoni effects dominate over thermal effects (Cavadini et al. 2013).

Valuable additional information regarding the Marangoni-induced flow velocity can be acquired using particle image velocimetry (PIV) or particle tracking velocimetry (PTV). A few authors reported lateral flow velocities in thin liquid films subject to convective instabilities using tracer particles with a diameter in the order of $10\ \mu m$ and a camera in top view position (Bassou and Rharbi 2009; Saranjam et al. 2016; Curak et al. 2018). Cellular motion with lateral flow velocities up to $80\ \mu m/s$ could be observed. This configuration, observing the tracer particles from top view through the free film surface, may suffer from distortions due to light refraction at the potentially deformed surface. Kang et al. (2003) used PIV to investigate the velocity field in a vertical cross section of a two-layer system of immiscible liquids, subject to interfacial Rayleigh-Marangoni convection and a large film height of approximately $5\ mm$. The optical access was realized through a transparent sidewall, requiring a laterally bounded film in a rectangular pool. The authors reported the vector field of a vertical cross section, revealing the direction of flow but no velocity values were provided. Toussaint et al. (2008) also reported experimental results utilizing PIV/PTV on selected films of drying polyisobutylene-toluene with an initial film thickness of $8\ mm$. In contrast to Kang et al. (2003), they used laser sheet illumination and the observing camera was tilted, observing the illuminated vertical cross section at an angle of $20°$ through the free film surface. The refraction-induced distortion was corrected using a regular grid and a pure toluene film as reference. The authors reported two different measurement approaches: First, selected recordings were made using a long exposure time, resulting in images where the tracer particle movement manifested in visible particle trajectories. Second, selected individual particles were manually tracked in a series of recordings with short exposure times. Only a single velocity value, denoting the maximal lateral velocity ($0.25\ mm/s$), was provided. The results gave unprecedented insights into the dynamics of convective instabilities, but were limited to a two-dimensional observation plane and those results obtained from vertical cross sections were obtained only in relatively thick films with a thickness of several millimeters.

The conventional approaches to extend particle tracking velocimetry to three-dimensional measurements is either realized by consecutively scanning through different observation planes, or by utilizing several cameras from different observation directions. The former approach is limited by the scanning speed and is therefore better suited for stationary flow fields, whereas polymer film drying is inherently instationary. The latter requires optical access from different angles, which is geometrically challenging for thin liquid films with a thickness in the order of micrometers. For more information on state-of-the-art (microscopic) PIV/PTV techniques, the readers are referred to several comprehensive reviews (Lindken et al. 2009; Wereley and Meinhart 2010; Cierpka and Kähler 2012).

An interesting microscopic approach to acquire three-dimensional flow field data based on particle tracking velocimetry, was proposed by Speidel et al. (2003). Instead of using sheet illumination, scanning methods or multi-camera systems, the authors proposed to extract information on the tracer particle's position in the line-of-sight third dimension by analyzing the diffraction ring pattern, occurring when a tracer particle has a certain distance to the focus plane of the observing microscope optics. Speidel et al. (2003) found that the diameter of such diffraction rings monotonically increases with increasing particle distance to the focal plane. This technique was named "off-focus imaging" and enables three-dimensional microscopic particle tracking with a single camera. Furthermore, it requires only a single observing camera, which can be realized using a glass substrate and observation from below. The illumination can be realized using fluorescent tracer particles and an epi-fluorescence microscope (illumination as well as observation through the same microscope lens). This allows for an undisturbed gas phase above the film and an unoccupied space at the top for additional equipment realizing different forms of forced convective drying. Depending on the numerical aperture of the microscope lens, the brightness of the light source, and the sensitivity and exposure time of the utilized camera, the line-of-sight extent of the observation volume can be extended (Park et al. 2005; Park and Kihm 2006).

Arguing that their recent findings (reported earlier in this section, Figure 1.9) could account for the long-wave deformation but not for the short-wave humps, Cavadini et al. (2015) investigated the flow field within the drying polymer film, using "off-focus imaging". Due to the new measurement setup, a lateral inhomogeneity in experimental drying conditions could not be achieved by a Teflon inlay in the substrate, but by partially covering the film, reducing the evaporation rate in this region. It was possible to track vertical tracer particle movements in a limited range of $\approx 4\ \mu m$ in the line-of-sight direction, but vertical velocity profiles were measured performing z-scans. It was found that in the covered area of the film, the vertical velocity profile was almost linear with a flow towards the uncovered area, which decelerated, presumably due to the viscosity increase during drying. In the uncovered area, however, the flow field was dominated by 3D convection cells, which could account for the short-scale deformations observed earlier but could not be fully resolved due to the limited extent of the vertical observation volume and the transient features of the flow field.

1.3 Starting Point and Aim of this Work

In the last sections, it was elaborated that three-dimensional convective Marangoni instabilities in thin drying polymer-solution films are subject of ongoing research efforts. The occurrence of such instabilities is a complex interplay between heat and mass transfer, as well as material properties and fluid dynamics. It may be affected by naturally occurring perturbations of temperature and concentration, evaporative cooling, the dynamics of the gas phase, as well as the viscosity increase and concentration change during drying. In addition, different modes of instability (short-scale and long-scale) exist and the combined occurrence of thermosolutal convective instabilities may reinforce one another, thereby lowering the stability threshold of the drying film. All of these effects make the assessment of stability thresholds in drying polymer films a very challenging task. With regards to industrial process design, guidelines to predict the convective (in)stability of drying polymer films and associated surface deformations are desirable.

The *aim of this dissertation* is to gain a better understanding of the impact of different drying conditions on short- and long-scale Marangoni convection in drying polymer films with new experimental methods. Hence, two research hypotheses have been investigated with special emphasis on quantitative experiments over the entire drying time.

The investigation of the hypotheses, provided in the next paragraphs, rely on a sophisticated measurement setup: Based on the preliminary flow field measurements reported by Cavadini et al. (2015), utilizing the “off-focus imaging” approach, a new setup based on microscopic particle tracking velocimetry (µPTV) was developed. In order to circumvent the limited line-of-sight extent of the observation volume, the “off-focus imaging” approach was combined with multifocal microscopy, which utilizes multiple cameras, sharing the same optical access, but having a different vertical focus position in the drying film. Prior to this dissertation, the physical measurement setup was acquired and an algorithm for the automatic detection of diffraction rings in large video data was developed (Cavadini et al. 2018). The setup, however, lacked proper calibration, especially regarding the correlation between diffraction ring sizes and vertical tracer particle positions, as well as the stitching of several observation volumes derived from multiple camera recordings with different vertical focus positions. Hence, a *vital part of this work* was to develop a rigorous calibration and automatization procedure for the new setup, with the aim to measure transient three-dimensional flow fields in convectively instable polymer-solution films during the entire drying time and over the entire film height. The entire setup including the new calibration and evaluation method is called 3D-μPTV in this work.

The available literature indicates that short-scale Marangoni instabilities possess a stability threshold in the form of a critical Marangoni number, below which the drying films remain convectively stable. Experimentally derived stability thresholds during polymer film drying, however, are scarce and limited to the initial conditions at the onset of drying (Bassou and Rharbi 2009; Toussaint et al. 2008; Touazi et al. 2010). Due to the viscosity increase during drying, initial instabilities were reported to stop during the drying process. The *first research hypothesis* is that the onset and end of short-scale convective instabilities during drying can be described by a unified critical threshold in Marangoni numbers. Therefore, film drying experiments were conducted without deliberate laterally inhomogeneous drying conditions using the new 3D-μPTV setup, quantitatively investigating the occurrence of short-scale Marangoni instabilities. During polymer film drying, all properties in the definitions of the thermal and solutal Marangoni number are transient, resulting in transient Marangoni numbers. Therefore, the evolution of the vertical temperature and concentration profiles is required, as well as concentration- and temperature-dependent material properties of the polymer solution. The concentration profiles are accessible through the spectroscopy based IMRS measurements during drying, using the same experimental boundary conditions as for the 3D-μPTV experiments, whereas the temperature profiles can be acquired utilizing the non-isothermal 1D simulation model. A special emphasis was laid on realistic material properties, especially the surface tension, being the driving force of Marangoni instabilities.

Regarding long-scale lateral Marangoni instabilities, the stability threshold is significantly lower, if there is any, balanced only by the leveling mechanism of capillary waves or gravity waves, because a long-scale Marangoni instability appears to be always accompanied by free surface deformations. Since the leveling affinity decreases with increasing viscosity and polymer film drying is always accompanied by a strong viscosity increase, it is unlikely that the leveling occurs during polymer film drying. Hence, the *second research hypothesis* is that long-scale Marangoni instabilities, induced by laterally inhomogeneous drying conditions, have no stability threshold. Therefore, polymer film drying experiments with deliberate laterally inhomogeneous drying conditions have been conducted. The flow field in such films has been investigated using the new 3D-µPTV method and the evolution of the lateral surface tension gradient has been assessed by IMRS derived experiments at different lateral positions.

This dissertation is structured as follows: In chapter 2, the developed rigorous calibration routine for the new 3D-µPTV setup, equipment automatization during experiments, and the post-processing routine are presented. The experimental details of drying experiments, additional methods, and material properties with a special emphasis on concentration- and temperature-dependent surface tension of polymer solutions are provided in chapter 3. Experiments exhibiting short-scale Marangoni instabilities and an assessment of the stability threshold are presented and discussed in chapter 4, and experiments with long-scale Marangoni instabilities induced by a deliberate lateral inhomogeneity in drying conditions are provided in chapter 5.

2 Micro Particle Tracking Velocimetry (3D-µPTV)

In order to measure the flow field in drying polymeric films, a new setup for microscopic particle tracking velocimetry was previously developed in this work's research group based on preliminary findings reported by Cavadini et al. (2015). It is based on microscopic tracking of fluorescent nanoscale tracer particles in a liquid film from below the film through a glass substrate. The "off-focus imaging" technique, first proposed by Speidel et al. (2003), allows for the detection of line-of-sight vertical particle positions by analyzing the diffraction rings occurring when tracer particles are not in focus (see section 1.2.4). The diffraction ring diameter increases with increasing particle distance to the focal plane, as can be seen in Figure 2.1 left. This allows for three-dimensional measurements with a single camera. However, since the signal-to-noise ratio of the diffraction rings deteriorates with increasing distance to the focal plane (decreasing intensity with increasing ring size, Figure 2.1 left), the vertical extent of the observation volume is limited. Therefore, this approach was combined with multifocal microscopy. The tracer particle's fluorescence signal is distributed to multiple cameras via beam splitters, as shown in Figure 2.2. The cameras are supplemented with motorized lens systems, which allow individual adjustment of the vertical focal plane position of each camera. Figure 2.1 (right) shows a schematic drawing of the desired vertical focal plane positions (colored planes) including the limited vertical extent of the resulting individual observation volumes.

The 3D-µPTV setup was acquired prior to this dissertation, but it was lacking rigorous calibration, especially regarding the "off-focus imaging" approach. Additional challenges, which had to be addressed, were the synchronized control of lens positioning and camera recordings during experiments and the handling of large amounts of video data, because at full resolution and utilizing all available cameras, the setup generates video data in the order of $1\ GB/s$, which corresponds to $600\ GB$ of video data for a single drying experiment lasting 10 minutes. Furthermore, the lateral as well as vertical stitching of the individual observation volume data were addressed. All of these challenges will be presented in the following sections.

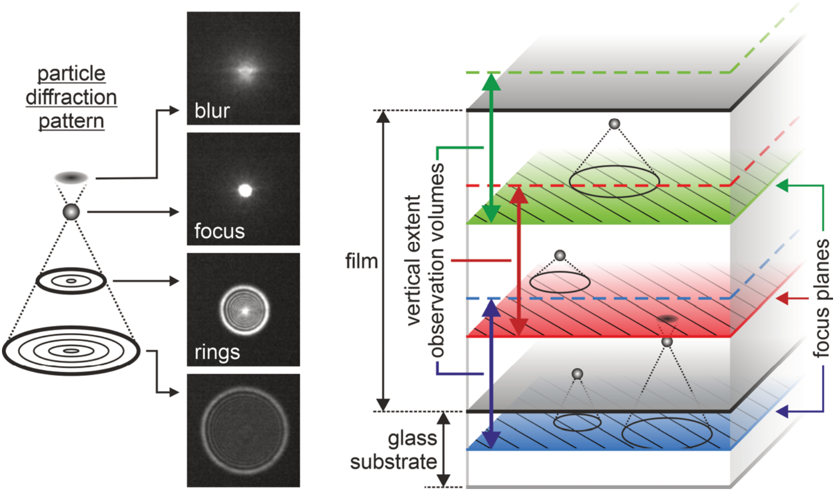

Figure 2.1: Left: Schematic drawing and selected images of the three-dimensional diffraction pattern of a tracer particle. The diffraction ring size increases with increasing distance to the focus plane while the signal intensity decreases. Right: Schematic drawing of the vertical positioning of three focus planes (colored planes) and the corresponding observation volumes (upper end denoted by dashed lines) in a thin liquid film utilizing multifocal microscopy.

2.1 Physical Setup[9]

The 3D-µPTV measurement setup (Figure 2.2) comprises an inverse epifluorescence microscope (Nikon Ti) with a lens (Plan Apo λ $60\times/0.95$, Nikon), a LED light source (pE-100, CoolLED Ltd.), a MultiCam beamsplitter unit (Cairn Research Ltd.) and five cameras (Andor Zyla 5.5 sCMOS, $2560\times2160\,px^2$, $6.5\,\mu m/px$, $50\,fps$). The prefix "epi" denotes that the sample illumination as

---

[9] The setup's hardware specifications were originally published in a peer-reviewed journal article: Cavadini, P.; Weinhold, H.; **Tönsmann**, M.; Chilingaryan, S.; Kopmann, A.; Lewkowicz, A.; Miao, C.; Scharfer, P.; Schabel, W. (**2018**): *Investigation of the flow structure in thin polymer films using 3D µPTV enhanced by GPU*. In *Exp Fluids* 59 (4), p. 370. DOI: 10.1007/s00348-017-2482-z.

well as observed fluorescence signal travel through the microscope lens. The vertical lens position $\tilde{z}_{lens}$ can be controlled manually and with a piezo actuator (P-725.2CD, Physik Instrumente PI GmbH). One of the cameras is directly attached to the backport of the microscope body while four cameras are supplemented with motorized lens systems for the individual adjustment of the vertical focal plane position, illustrated in Figure 2.3. Due to the large amount of video data, each camera is connected to an individual computer with two Camera Link ports. The camera recordings can be externally triggered using an additional TTL signal cable, connected to a PCIe extension board (PCIM-DDA06/16, Measurement Computing Corporation) installed in one of the computers.

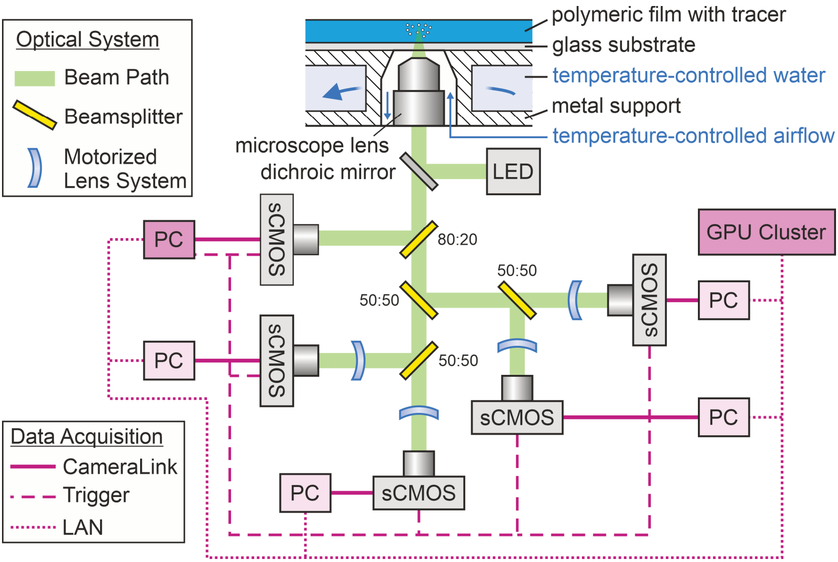

Figure 2.2: Schematic drawing of the 3D-µPTV measurement setup including all cameras and motorized lens systems as well as the data acquisition connections and the substrate temperature control.

The samples under investigation are applied on top of a thin microscope-grade glass substrate ($h_{glass} = 145 \pm 5\ \mu m$), which is attached to a metal support for temperature control. For optical access, the metal support has an opening for the microscope lens. The diffraction-ring detection in camera recordings was performed on a Supermicro server (SYS-7049GP-TRT) with four graphic cards

(NVIDIA GeForce GTX 1080Ti) using a GPU-accelerated algorithm published by Cavadini et al. (2018).

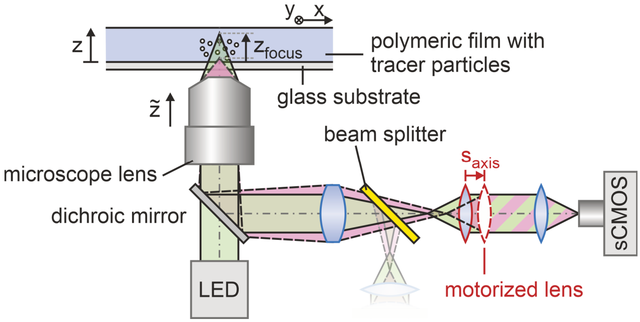

Figure 2.3: Schematic drawing of a single motorized lens system for the individual adjustment of the vertical focal plane position. At a motorized lens position $s_{axis} = 0\ mm$, the focus plane is at its maximum position (green beam path), whereas for $s_{axis} > 0\ mm$ (purple beam path) the focus plane is closer to the substrate.

2.2 Calibration[10]

For quantitative three-dimensional flow-field measurements, the lateral magnification and camera alignment, as well as the dependency of the tracer particle diffraction-ring size on the distance to the focal plane have to be known. All following evaluations were implemented as *python* scripts in this work, utilizing the *numpy* and *scipy* libraries (Oliphant 2006; Virtanen et al. 2020).

---

[10] Results presented in this section have been previously published in a peer-reviewed journal article:
Tönsmann, M.; Kröhl, F.; Cavadini, P.; Scharfer, P.; Schabel, W. (**2019**): *Calibration Routine for Quantitative Three-Dimensional Flow Field Measurements in Drying Polymer Solutions Subject to Marangoni Convection*. In *Colloids and Interfaces* 3 (1), p. 39. DOI: 10.3390/colloids3010039.
Figures have been reprinted under the license CC-BY-4.0.

2.2.1 Lateral Magnification and Camera Alignment

The lateral magnification M changes with motorized lens position s_{axis} and was measured by manually focusing on a micrometer scale under variation of s_{axis}. Figure 2.4 shows an overlay of three camera images taken with the same camera and $s_{axis} = 0\,mm$ (red), $80\,mm$ (green) and $160\,mm$ (blue). It can be seen that the magnification decreases with increasing s_{axis}. It was found that the magnification can be calculated with regard to the motorized lens position s_{axis} using the relation:

$$M = c_{M,0} - c_{M,1} \cdot s_{axis} \ , \tag{2.1}$$

with $c_{M,0} \approx 58.3 \pm 0.2$ and $c_{M,1} \approx 0.055 \pm 0.010\,mm^{-1}$, slightly varying for each camera and different beam splitter configurations.

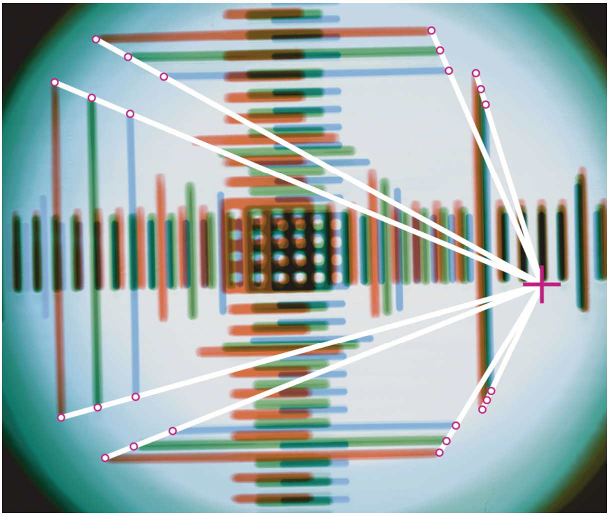

Figure 2.4: Superimposed images of lateral calibration scale from a single camera with motorized lens system at $s_{axis} = 0\,mm$ (red), $80\,mm$ (green) and $160\,mm$ (blue). The lateral magnification M decreases with increasing s_{axis} and the image laterally shifts with s_{axis}. The purple cross indicates the vanishing point for $s_{axis} \rightarrow \infty$, characteristic for each camera and beam splitter configuration. The physical distance between the dashes of the micrometer scale is $5\,\mu m$.

The fixed magnification of the backport camera without motorized lens system was found to be $M = 54.1$. Figure 2.4 also reveals that the image laterally shifts with varying s_{axis}, showing a vanishing point (purple cross) when extrapolating characteristic points to $s_{axis} \to \infty$. The position of the vanishing point is different for each camera and may change whenever any optical component of the measurement setup was physically adjusted. The lateral offset between multiple camera recordings of the same experiment can be corrected by comparing an arbitrary reference point on the micrometer scale in the calibration images of all utilized cameras. The detection of the magnification and lateral position of the micrometer scale in calibration images was implemented in *python* using a template-matching algorithm detailed in Appendix A.1.

2.2.2 Point Spread Function Simulation

The three-dimensional diffraction pattern of a point light source (e.g. a fluorescent tracer particle) is called point spread function (PSF) and can be simulated using the well-established Gibson-Lanni model (Gibson and Lanni 1992). The model requires the optical properties of the microscope lens, the immersion medium, the glass substrate, and the sample, as well as the true vertical particle position z_p as input parameters. Being able to simulate the PSF, and therefore the diffraction rings, has the potential to reduce the amount of calibration samples needed to correlate the diffraction ring size to the vertical particle position significantly. The model's limitation is the computational speed, which is in the order of minutes for a single vertical particle position z_p and varying microscope lens focus position $\tilde{z}_{focus}$. The utilization for 3D-µPTV calibration, however, requires a fixed lens position and varying vertical particle positions, resulting in numerous individual simulations with z_p variation.

A fast and yet accurate approximation of the Gibson and Lanni model was recently proposed, accelerating a single simulation by a factor in the order of 10^2 (Li et al. 2017). The authors provided the source code for Matlab, and Douglas and Babcock (2018) implemented it in python. A detailed list of all input parameters is given in Appendix A.2. Figure 2.5a exemplarily shows the simulated vertical cross-section of the PSF for a single set of optical parameters and fixed vertical particle position z_p. The origin of z_p and $\tilde{z}_{focus}$ is the bottom of the sample, if not noted otherwise. The lens position at which the particle is in focus

$\tilde{z}_{focus,p}$ was extracted by finding the intensity maximum in the vertical intensity profile (horizontal dashed line in Figure 2.5b). The observable diffraction-ring radius was extracted using the brightest (largest) of several concentric diffraction rings, indicated by the dash-dotted line (Figure 2.5a), which was fitted by a fourth degree polynomial $\tilde{P}_4$.

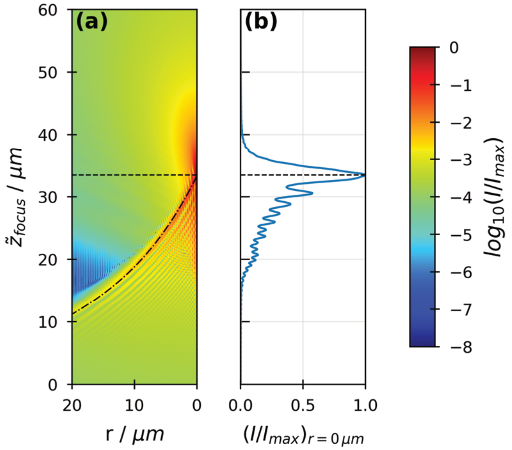

Figure 2.5: Asymmetric point spread function (PSF) simulated with fast Gibson-Lanni model implementation proposed by Li et al. (2017). Parameters: $z_p = 54\ \mu m$, $n_s = 1.472$, $NA = 0.95$, $t_g^* = 150\ \mu m$, $t_g = 144\ \mu m$. (**a**) Vertical cross-section of PSF. The dash-dotted line indicates the brightest (outmost) diffraction ring. (**b**) Vertical intensity profile at $r = 0\ \mu m$. The dashed line indicates the particle at $\tilde{z}_{focus,p} = 33.5\ \mu m$. (Tönsmann et al. 2019)[10]

Several aspects regarding the PSF have to be considered: First, the microscope lens utilized uses no immersion medium between lens and glass substrate (air immersion, refractive index $n_i = 1.0$) while the refractive index of liquid films typically resides in the range of $n_s = 1.3$ to 1.6. This results in a deliberately asymmetric PSF where diffraction rings only occur below the tracer particle and the particle image blurs out quickly above the particle (see Figure 2.5a and Figure 2.1 left). The use of an immersion medium (water $n_i = 1.34$, or oil $n_i = 1.56$) would result in diffraction rings observable below and above the tracer particle, rendering the reconstruction of the particle position ambiguous (e.g. Gibson and Lanni 1992, see also section 2.2.5). Due to this deliberate refractive-index mismatch between sample and immersion medium, the true vertical focus plane position differs from the lens position (similar to IMRS setup, see section 1.1.1). This can be seen in Figure 2.5, where the true vertical particle position was set to $z_p = 54\ \mu m$ but was observed at a vertical lens position of $\tilde{z}_{focus,p} = 33.5\ \mu m$ (62 % of the true vertical position). Hence, the "~" accent denotes physical lens positions while no accent denotes true vertical positions. Second, the intensity of the diffraction ring deteriorates with increasing radius (color along dash-dotted line in Figure 2.5a, Figure 2.1 left). To maximize the vertical extent of the observation volume of a single camera, it has to be assessed which tunable optical properties increase the slope of $\tilde{P}_4$ (dash-dotted line). Third, the impact of the motorized lens systems on the PSF has to be evaluated. All of these aspects will be addressed in the following sections.

2.2.3 Diffraction-Ring Calibration Samples

In order to validate the PSF simulation results, calibration samples with known vertical particle position and known sample refractive index are required. Cavadini et al. (2018) proposed a stack of transparent tape strips with tracer particles deposited inbetween the layers. Similar samples were prepared using tesa-film crystal clear ($n_s = 1.472$, $\Delta z = 54 \pm 3\ \mu m$, tesa SE). These samples are limited to a single sample refractive index. Additional samples, depositing tracer particles on two glass slides with spacers of known thickness between them and the gap filled with different fluids, allow for a wide range of n_s variation. The fluids used are air ($n_s = 1.000$), bidistilled water ($n_s = 1.336$, Carl Roth GmbH, 3478.1) and oil ($n_s = 1.557$, Bellingham + Stanley Ltd., 90-235). In contrast to the tesa stacks, multiple vertical particle positions had to be realized in separate calibration samples. Figure 2.6 shows a schematic drawing of the different calibration sample types.

The samples were measured using the 3D-µPTV setup, recording image series of a vertical $\tilde{z}$-scan with $\Delta\tilde{z}_{focus} = 1\ \mu m$. The true vertical particle positions are known from sample preparation and the recorded particle position $\tilde{z}_{focus,p}$ of each particle layer was determined by extracting the maximum of the vertical intensity distribution identical to Figure 2.5b with *ImageJ*. The observed diffraction rings were detected using the GPU-accelerated algorithm published by Cavadini et al. (2018) and converted from image pixels to μm using the lateral magnification reported in section 2.2.1. False-positive detections were sorted out manually.

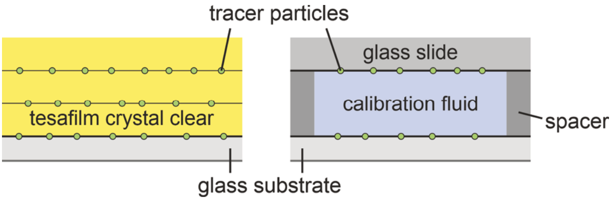

Figure 2.6: Schematic drawings of the two types of calibration samples. Left: Tesa stack. Right: Glass slides with spacer and calibration fluid. (Tönsmann et al. 2019)[10]

2.2.4 Focal Displacement Validation

Figure 2.7 shows the resulting vertical particle positions $\tilde{z}_{focus,p}$ for different sample refractive indices n_s as function of the motorized lens position s_{axis}. Each sample has two or more particle layers, indicated by the same marker shape and color shade. Each sample also has an arbitrary origin of $\tilde{z}_{focus}$ which was kept constant within individual samples. The change in vertical focus position with s_{axis} (slope of grey dashed lines) is independent of the sample refractive index as well as the vertical particle position.

A linear fit to each particle layer reveals the vertical focus position change due to the motorized lens systems,

$$\Delta\tilde{z}_{focus} = 0.301\ \mu m/mm \cdot s_{axis}\,, \quad R^2 = 1.00\,. \tag{2.2}$$

The corrected vertical focus position during drying experiments due to the motorized lens refocusing can then be calculated using

$$\tilde{z}_{focus}(s_{axis}) = \tilde{z}_{focus}(s_{axis} = 0\ mm) - \Delta\tilde{z}_{focus}\ . \tag{2.3}$$

In addition, the focal displacement due to the refractive index mismatch between immersion (air, $n_i = 1.000$) and sample medium n_s can be extracted by vertically shifting the data presented in Figure 2.7 so that the origin equals $\tilde{z}_{focus,p}$ of the lowest particle layer of each sample. These data are plotted over the true vertical particle position z_p, known from sample preparation, in Figure 2.8. It can be seen that the slope is unity ($z_p = \tilde{z}_{focus,p}$) only when $n_i = n_s$ (red line and markers). With increasing sample refractive index, the true vertical particle position z_p is larger than the vertical lens focus position $\tilde{z}_{focus}$ (slope < 1). This is in excellent agreement with PSF-simulation results, given as lines in the plot, and with preliminary calibration results reported by Cavadini et al. (2018) (empty squares).

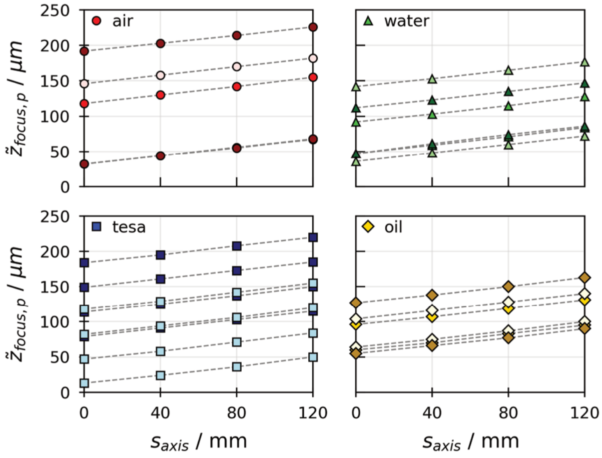

Figure 2.7: Change in lens focus position as function of sample refractive index and motorized lens position, derived from $\tilde{z}$-scans of calibration samples. Different color shades indicate individual samples. Grey dashed lines connect data of each particle layer. Each sample has an arbitrary $\tilde{z}_{focus}$ origin, remaining constant within individual sample datasets. (Tönsmann et al. 2019)[10]

The slope of the lines in Figure 2.8 denoting focal displacement was found in this work to be

$$m_{fd} = \frac{\Delta\tilde{z}_{focus}}{\Delta z_{focus}} = 0.996 \cdot n_s^{-1.056} \tag{2.4}$$

for a sample refractive index in the range $n_s = 1.0$ to 1.7. The maximum of the motorized lens position of the 3D-µPTV setup is $s_{axis} = 160\,mm$. With equation (2.2) this corresponds to a maximal vertical focus plane distance in lens coordinates of $\Delta\tilde{z}_{focus,max} = 48\ \mu m$. Assuming $n_s = 1.4$ and using equation (2.4), this results in a true maximal vertical focus plane distance of $\Delta z_{focus,max} = 69\ \mu m$ in the sample[11].

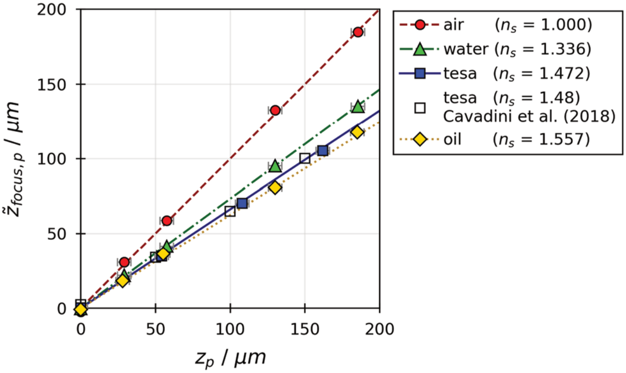

Figure 2.8: Focal displacement due to refractive index mismatch between immersion (air, $n_i = 1.000$) and sample n_s. Markers indicate experimental data from calibration samples and lines indicate PSF-simulation results. (Tönsmann et al. 2019)[10]

2.2.5 Diffraction Ring Validation

In the last section, the vertical focus positions of the PSF simulation model were validated experimentally. The vertical line-of-sight position of the “off-focus imaging” approach, however, relies on the accurate determination of diffraction ring sizes. Figure 2.9 exemplarily compares the vertical cross-section of a point spread function. Figure 2.9b shows the simulated PSF and Figure 2.9a shows

---

[11] Since each focus plane denotes the lower limit of the individual observation volume of a single camera (see Figure 2.1 right), the maximal vertical extent of the combined observation volumes of all cameras is $\Delta z_{focus,max}$ plus the vertical extent of the upmost observation volume. It will be seen later (e.g. vertical extent of green trajectories in Figure 2.19) that for the experiments presented in this work, the vertical extent of the upmost camera was $\approx 50\ \mu m$, resulting in a combined observation volume with an extent of $\Delta z_{ov,max} \approx 120\ \mu m$. This, however, depends on the respective sample refractive index as well as the exposure time of the cameras.

experimental results, stitched from a $\tilde{z}$-scan image stack with *ImageJ* and converted from pixel to micrometer using the lateral magnification derived in section 2.2.1. It can be seen that experimental and simulated vertical cross-sections are in good agreement.

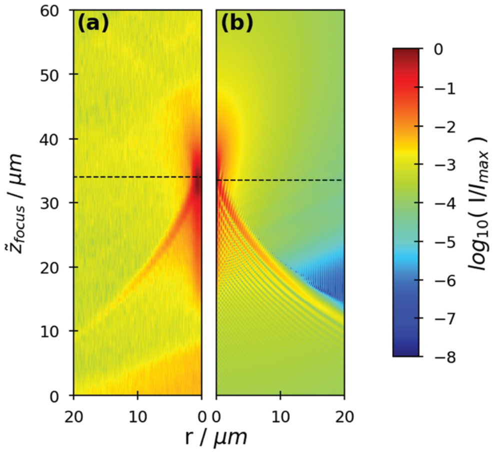

Figure 2.9: Vertical point spread function (PSF) cross-section of a single particle in a tesa stack. Parameters: $z_p = 54\ \mu m$ (true vertical particle position), $n_s = 1.472$. Horizontal lines indicate the extracted vertical focus position. (a) Experimental result from a $\tilde{z}$-scan stitched with *ImageJ* ($\tilde{z}_{focus,p,exp.} = 34\ \mu m$, $s_{axis} = 0\ mm$). (b) Simulation results from fast Gibson-Lanni model implementation (Li et al. 2017) and resulting $\tilde{z}_{focus,p,sim.} = 33.5\ \mu m$. (Tönsmann et al. 2019)[10]

The diffraction rings, detected with the GPU-enhanced algorithm, are plotted in comparison with PSF simulation results in Figure 2.10. The red lines denote the brightest (outmost) ring diameter from simulations and the markers indicate the detected rings from $\tilde{z}$-scans of a single tesa stack calibration samples with four vertically stacked particle layers. It can be seen that the experimentally derived valid rings (grey circles) are in good agreement with simulation results (red lines). However, it can also be seen that multiple ring detections had to be sorted out manually (blue crosses and yellow diamonds). The yellow diamonds denote tracer particle agglomerates, which only occur during calibration-sample preparation because the pure tracer-particle suspension was used for preparation. Such agglomerates were not observed in experiments with tracers mixed to polymer-solution samples. Consequently, they can be ignored and are given for transparency reasons only. The blue crosses, however, denote false-positive ring detections. They occur for very small radii only. An example frame from the tesa calibration stack is shown in Figure 2.11. It shows that the false-positive small rings are caused either by blurred particle images, occurring when the vertical focus position is above the true particle position (see Figure 2.1 left), or when the central bright point instead of the outmost diffraction ring was detected. In actual drying experiments, reported later, the average number of ring detections is in the order of 10^5. Therefore, manually removing these false-positives is unfeasible. Instead, all detected rings below a threshold radius r_{min} are discarded. The exact value of r_{min} depends on the utilized camera resolution, it is approximately $8\ px$.

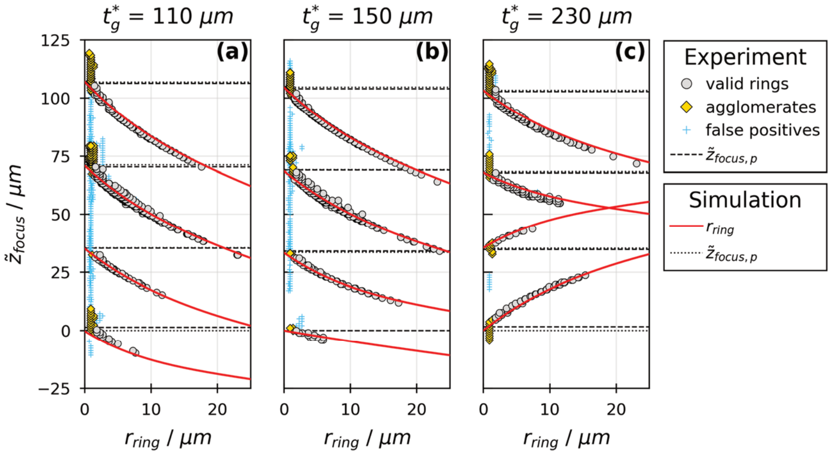

Figure 2.10: Comparison of simulated and experimentally detected diffraction-ring radii in a single tesa stack with four vertically stacked particle layers and with different correction-collar settings t_g^*. Parameters: $z_p = 54, 108, 162,$ and $216\ \mu m$, $n_s = 1.472$, $t_g = 144\ \mu m$, $s_{axis} = 0\ mm$. (Tönsmann et al. 2019)[10]

The utilized microscope lens has a variable correction collar setting t_g^* in order to adjust the lens to the respective glass substrate thickness t_g. The utilized glass substrates have a thickness of $t_g \approx 150\ \mu m$ while the correction can be set between $t_g^* = 110\ \mu m$ and $230\ \mu m$. The standard lens usage is to match the correction collar setting to the actual glass substrate thickness ($t_g^* = t_g$). This is commonly referred to as "design conditions". The PSF-simulation model can account for a discrepancy between these values (see Appendix A.2 for full list of input parameters). Figure 2.10 also shows the impact of correction collar setting t_g^* variation on the observed diffraction rings. When the correction collar is set to its maximum position ($t_g^* = 230\,\mu m > t_g$, Figure 2.10c), diffraction rings from tracer particles closer to the bottom of the sample occur above the particle (lower two red lines with upward slope). This results in a vertical region where detected diffraction rings may denote an ambiguous vertical particle position (crossing red lines), unwanted in 3D-µPTV measurements. This does not occur when $t_g^* \leq t_g$ (Figure 2.10a and b). Setting the correction collar to its minimum results in a steeper slope of diffraction ring radii without ambiguity ($t_g^* = 110\,\mu m < t_g$, Figure 2.10a). This is favorable compared to the "design condition" (Figure 2.10b), since the vertical extent of the observation volume of a single camera can be extended. Consequently, the correction collar was set to $t_g^* = 110\,\mu m$ non-design condition for all drying experiments, reported later.

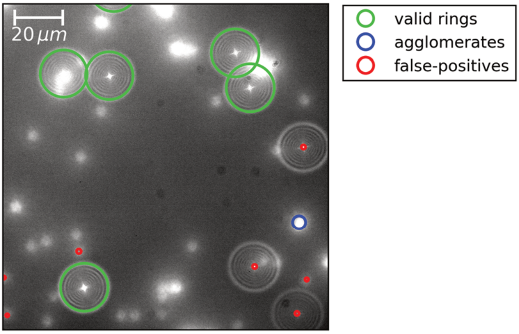

Figure 2.11: Single cropped camera image from tesa calibration stack (Figure 2.6 left and Figure 2.10a) with superimposed rings detected by the GPU-algorithm. Vertical lens focus position $\tilde{z}_{focus} = 82\,\mu m$. The blurred particles are from the lower particle layer at $\tilde{z}_{focus,p} = 70\,\mu m$ while the valid rings are from particles at $\tilde{z}_{focus,p} = 106\,\mu m$.

Heretofore, all results presented in this subsection regarding the diffraction rings where experimentally derived with a motorized lens position $s_{axis} = 0\,mm$, which is equivalent to the backport camera without motorized lens system. The Gibson-Lanni PSF model does not account for such additional lens systems, because they are not standard microscope equipment, but specific to the 3D-µPTV setup presented in this work. While s_{axis} does not affect the vertical focus position due to refractive index mismatch, as demonstrated in section 2.2.4, it may well have an impact on the observed diffraction-ring sizes. Figure 2.12 shows the comparison of simulated (red lines) and experimental (markers) diffraction rings for varying sample refractive indices n_s (left to right), different vertical particle layer positions (vertical data groups) and varying motorized lens positions s_{axis} (different shaped and colored markers). The experimentally derived diffraction rings start to deviate from the simulated results with increasing $s_{axis} > 0\,mm$. In addition, it can be seen that the deviation decreases with increasing sample refractive index (upper data groups left to right) and vertical particle layer position (bottom to top, except for $n_s = n_i = 1.0$, where the deviation is independent of z_p).

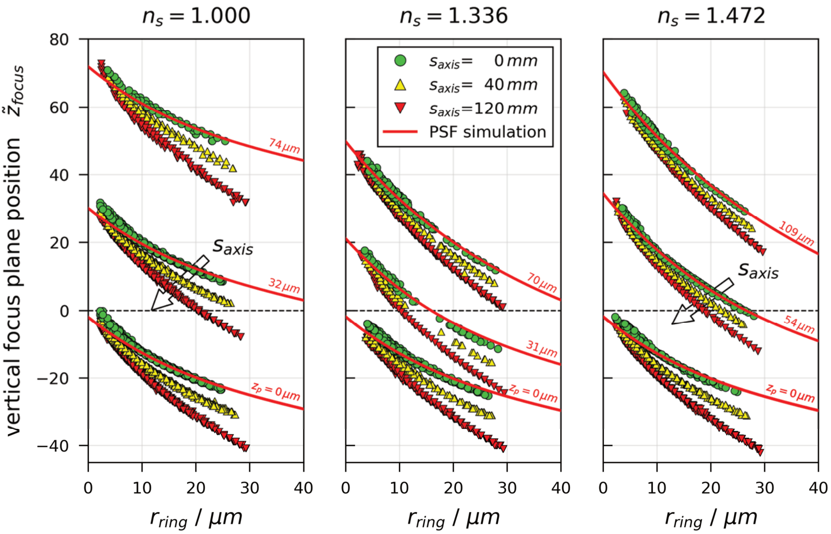

Figure 2.12: Comparison of simulated diffraction ring radii (red lines) and experimentally derived radii from calibration samples (markers) under variation of the sample refractive index n_s (left to right), the vertical particle position (vertical data groups) and motorized lens positions s_{axis} (differently shaped and colored markers). The horizontal dashed lines ($\tilde{z}_{focus} = 0$) indicate the focus plane being at the interface between glass substrate ($\tilde{z}_{focus} < 0$) and sample ($\tilde{z}_{focus} > 0$).

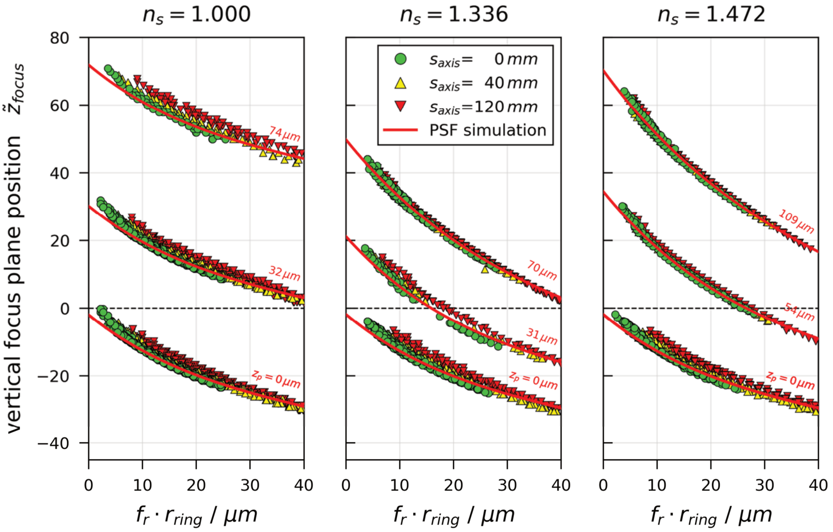

Figure 2.13: Comparison of simulated diffraction ring radii (red lines) and experimentally derived radii from calibration samples (markers) as in Figure 2.12, but corrected with a factor $f_r(s_{axis}, n_s, z_p)$. The horizontal dashed lines ($\tilde{z}_{focus} = 0$) indicate the focus plane being at the interface between glass substrate ($\tilde{z}_{focus} < 0$) and sample ($\tilde{z}_{focus} > 0$).

This observation can be interpreted as follows: In order to compare the experimentally detected diffraction rings with the simulated ones, the experimental radii have to be converted from pixel to micrometer, using the lateral magnification derived in section 2.2.1. The good agreement between experimentally derived rings and simulation for $s_{axis} = 0\,mm$ means that the lateral magnification is independent of the vertical focus position $\tilde{z}_{focus}$. This appears not to be the case when $s_{axis} > 0\,mm$. Figure 2.13 shows that it is possible to introduce a correction factor $f_r(s_{axis}, n_s, z_p)$ resulting in the experimental ring radii (markers) aligning with the simulated ones (red lines). f_r can be interpreted as a correction of the change in lateral magnification of the ring radii with vertical focus position when $s_{axis} > 0\,mm$. It varies between $f_r(s_{axis} = 0\,mm) = 1$ and $f_r(s_{axis} = 160\,mm) \leq 2.3$. In addition f_r decreases with increasing sample refractive index and increasing vertical particle position. No closed function for this relation was found, as it would require a significantly larger amount of calibration samples with fine increments of the sample refractive index n_s and vertical particle positions z_p (see Appendix A.3 for details). Furthermore, an additional challenge regarding this correction arises for drying experiment evaluation. This challenge, as well as an alternative approach of correction, will be discussed in section 2.3.3.

2.2.6 Summary Calibration Routine

In the last sections, it was shown that simulated point spread (PSF) functions are in good agreement with experimentally derived data regarding the vertical focus position as well as the diffraction ring radii. The sole exception was a discrepancy between ring radii when the motorized lens position was $s_{axis} > 0\,mm$, which will be addressed in section 2.3.3. Consequently, the PSF simulation can be used to derive a relation between ring radii and vertical particle positions, instead of preparing numerous additional calibration samples with fine increments of z_p and n_s, which would be unfeasible.

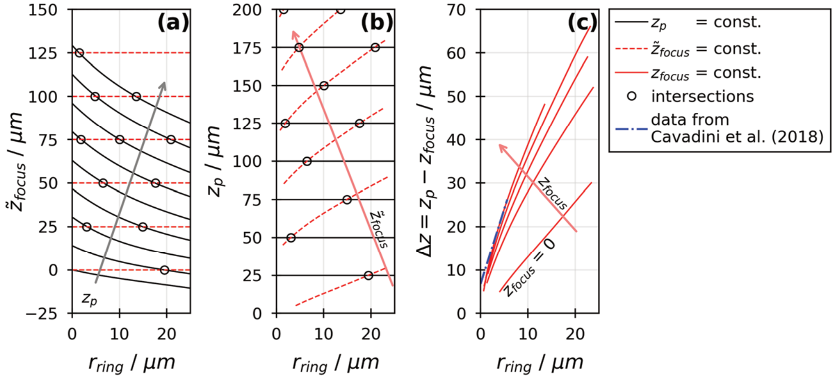

Figure 2.14: Conversion steps to obtain particle-position lookup polynomials from PSF simulations with fixed particle positions. (a) Diffraction-ring sizes for various particle positions z_p and intersections for constant vertical lens focus positions $\tilde{z}_{focus}$. (b) Converted data for fixed lens positions and variable vertical particle positions as required for experiment evaluation. (c) Relative distance of particle positions to vertical focal plane positions in comparison with preliminary calibration by Cavadini et al. (2018). (Tönsmann et al. 2019)[10]

There is, however, one final conversion step necessary: While the PSF simulation assumes a constant vertical particle position z_p and a varying vertical lens focus position $\tilde{z}_{focus}$, in a drying experiment $\tilde{z}_{focus}$ remains constant while z_p changes according to the flow field in the film. Therefore, a parameter variation of z_p in steps of $\Delta z_p = 5\ \mu m$ was simulated, resulting in the relation $\tilde{z}_{focus} = \tilde{P}_4(r_{ring})_{z_p=const.}$ given in Figure 2.14a as black lines[12]. For reasons of clarity, only every fifth curve is shown.

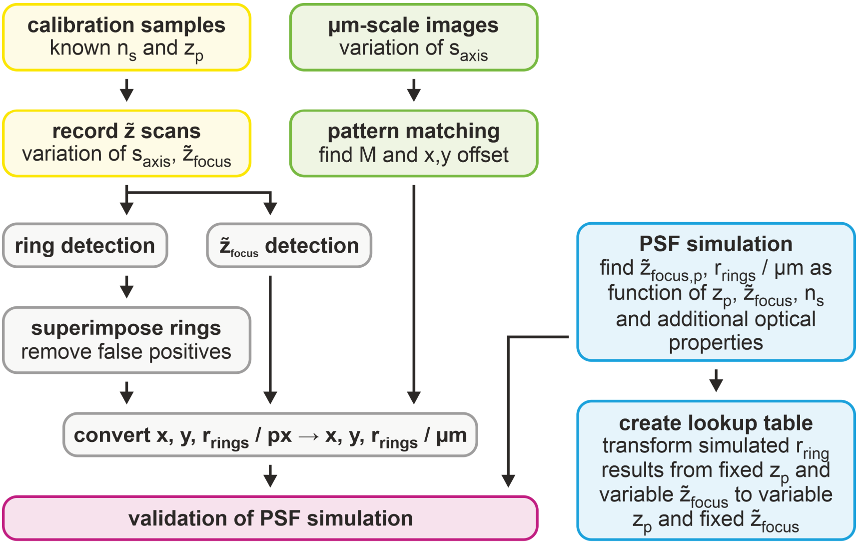

Figure 2.15: Flow chart summarizing the developed procedure to validate the simulated point spread function (PSF) results with experimental results of calibration samples. Details regarding the yellow, green, blue, and purple steps are provided in sections 2.2.3, 2.2.1, 2.2.2, and 2.2.5, respectively.

By extracting the intersections (circle markers) of these curves at constant values of $\tilde{z}_{focus}$ (horizontal red dashed lines), these relations can be converted to $z_p = P_4(r_{ring})_{\tilde{z}_{focus}=const.}$ as fourth degree polynomials, depicted in in Figure 2.14b as red dashed lines. The list of polynomial coefficients for each of the vertical

---

[12] $\tilde{P}_4$ denotes a polynomial of fourth degree, fitted to the brightest (outmost) diffraction ring, as shown as black dash-dotted line in Figure 2.5.

focus positions $\tilde{z}_{focus}$ is referred to as “lookup table” for experiment evaluation. In order to compare these results with an early simple linear calibration for a single sample refractive index reported by Cavadini et al. (2018), Figure 2.14c shows the same results, but as relative distance to the vertical focal plane position $\Delta z = z_p - z_{focus}$. It can be seen that the preliminary linear calibration (blue dash dotted line) is in reasonable agreement with the newly derived calibration data, but only for a single large value of the true vertical focus position z_{focus}. The calibration routine developed during this dissertation also accounts for a variation of vertical focus positions as well as variation of the sample refractive index, which was neglected during the early preliminary calibration.

The overall procedure developed to validate the PSF simulation model with calibration samples and to derive the calibration lookup table for experiment evaluation is summarized in Figure 2.15.

2.3 Automatization and Experiment Evaluation

2.3.1 Equipment Control during Experiments

Before and during a drying experiment recorded with 3D-µPTV, several components have to be controlled simultaneously. Among these are the piezo positioning of the microscope lens, the control of the motorized lens system of each camera as well as triggering several camera recordings simultaneously. To facilitate this process, a graphical user interface was developed in *LabVIEW*. Its main features are:

- Equidistant positioning of vertical focus positions of all utilized cameras via control of the piezo actuator for microscope lens movements and the motorized lenses for individual focal plane adjustments.
- Logging of all lens positions over time.
- Simultaneous triggering of all utilized cameras using the PCIe expansion board connected to the camera trigger inputs, and log trigger time.
- Facilitate simultaneous adjustment of all vertical focus positions during experiments.

Figure 2.16 shows a screenshot of the main user interface with colored boxes, highlighting different regions of interest. In the orange box, metadata required for experiment evaluation as well as the number of cameras can be selected prior to experiments. The blue boxes indicate all lens positions in raw (s_{axis}) as well as converted to microscope lens coordinates $\tilde{z}_{focus}$ or to corrected true vertical coordinates z_{focus}, depending on the settings in the green box. Triggering all utilized cameras simultaneously as well as controlling the vertical focus positions during experiments was implemented in the red box.

The resulting log file comprises all entered metadata and the time-dependent position of all lenses as well as the camera trigger times. This allows for synchronization of the lens positions with camera recordings, which is especially important when the lens positions have been changed during an experiment.

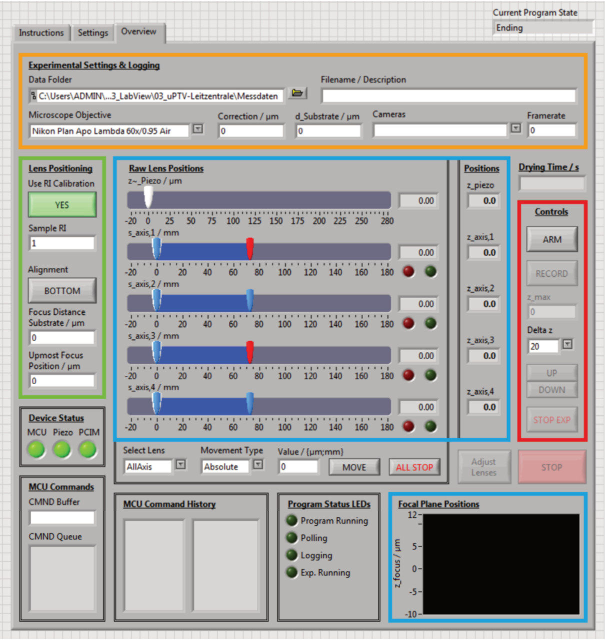

Current Program State: Ending

Data Folder: C:\Users\ADMIN\...3_LabView\03_uPTV-Leitzentrale\Messdaten

Microscope Objective: Nikon Plan Apo Lambda 60x/0.95 Air

Correction / µm: 0

d_Substrate / µm: 0

Framerate: 0

Use RI Calibration: YES

Sample RI: 1

Alignment: BOTTOM

Focus Distance Substrate / µm: 0

Upmost Focus Position / µm: 0

z~_Piezo / µm: 0.00

s_axis,1 / mm: 0.00

s_axis,2 / mm: 0.00

s_axis,3 / mm: 0.00

s_axis,4 / mm: 0.00

Positions

z_piezo: 0.0

z_axis,1: 0.0

z_axis,2: 0.0

z_axis,3: 0.0

z_axis,4: 0.0

z_max: 0

Delta z: 20

Select Lens: AllAxis

Movement Type: Absolute

Value / {µm;mm}: 0

set metadata and camera selection

refractive index input vertical focus alignment

trigger cameras and change vertical focus positions during drying

visualize vertical lens/focus positions

Figure 2.16: Screenshot of the main graphical user interface for 3D-µPTV experiments implemented in *LabVIEW*. The function of the most relevant regions, highlighted with colored boxes, are summarized in the text annotations.

2.3.2 Postprocessing of Raw Data

After an experiment, the recorded video data of all cameras were manually converted from a proprietary video format to universally readable tif format using the camera software *Andor Solis*. The resulting tif files were then copied from the individual camera computers to the GPU server for postprocessing. A single experiment, recorded with three cameras at a 16th of their maximum resolution (4×4 pixel binning), a framerate of $30\ fps$, and a duration of 10 minutes results in a total of approximately $15\ GB$ of video data. The remainder of postprocessing routines was conducted on the GPU server with several *python* scripts.

The diffraction rings were detected using the algorithm already published by Cavadini et al. (2018). Since this algorithm is based on fast Fourier transformation, it crops originally rectangular image data to a quadratic subregion with an edge width of power of two. In order to avoid information loss due to the cropping, the recorded videos were divided into four quadratic subregions and each of the subregions was processed using the ring-detection algorithm. The resulting data sets were merged by filtering out duplicate detections due to subregion overlap. This detection process took approximately $2\ h$ for a single experiment.

The detected rings could be superimposed over the original camera images using the same *python* script used for the calibration samples (see Figure 2.11 for example frame). Since an average drying experiment results in individual detections in the order of 10^5 ring, manually sorting out false positives, as done for the calibration samples, is unfeasible for drying experiments. Consequently, this step was only used to assess the detection accuracy qualitatively. As already pointed out in section 2.2.5, very small ring radii are prone to false-positive detections. Therefore, all detected rings with a radius of $8\ px$ ($\approx 4\ \mu m$ when converted to physical dimensions) and smaller were sorted out automatically.

The lateral ring center positions as well as radii were converted from pixel to micrometer using the lateral magnification, derived as presented in section 2.2.1. Afterwards, the ring radii were converted to vertical particle positions using the calibration “lookup table” from PSF simulations, as described in section 2.2.6. For this conversion, the vertical focus position $\tilde{z}_{focus}$ of each camera had to be known, which was calculated from $\tilde{z}_{focus}(s_{axis} = 0\ mm)$ and s_{axis} from the

LabVIEW log file using equation (2.3). It has to be noted that the data in the calibration lookup table are designed to have the origin of $\tilde{z}_{focus}$ and z_p at the bottom of the film, which is equivalent to the top surface of the glass substrate. This origin, however, is not precisely known prior to an experiment because no procedure was found to precisely detect it before the polymer solution with tracer particles is coated on the substrate (see Appendix A.4 for a discussion). Therefore, the first of a series of drying experiments was solely performed to manually adjust the vertical microscope lens position to get a coarse estimate of the vertical origin. This was achieved by setting all motorized lens positions s_{axis} to the desired measurement position. Then, the live image of the camera with the lowest vertical focus position ($s_{axis,max}$) was observed while the vertical lens position was adjusted manually until the smallest observable diffraction rings were noticeably larger than the 8 pixel cutoff. The found vertical lens position was set to be the preliminary vertical origin, used for the following experiments. After the conversion from diffraction radii to vertical particle positions, as described at the beginning of this paragraph, the lowest resulting particle position was assessed. Assuming a sufficient amount of tracer particles in the film and particle distribution over the entire film height, the lowest particle position should occur immediately above the glass substrate surface. Therefore, a corrected vertical origin was found by changing the value of the preliminary origin until the lowest particle position was $z_p \approx 0.5\,\mu m$. This procedure was done iteratively, since each change in the vertical origin also changes the corresponding polynomial in the lookup table used for z_p calculation.

The individual particle detections, converted to three dimensional positions, were stitched to particle trajectories using an algorithm presented by Afik and Steinberg (2017) for data of each utilized camera individually. The trajectories were smoothened by a Savitzky-Golay filter, using a second degree polynomial and a window length of $\Delta t = 2\,s$ (Savitzky and Golay 1964). The particle velocities were calculated using the first derivative in Savitzky-Golay filtering.

2.3.3 Vertical Camera Stitching

Up to this point, the necessary correction factor, accounting for the discrepancy between diffraction ring radii of calibration samples and PSF simulations when $s_{axis} > 0\,mm$ (section 2.2.5), was not accounted for. In this section, the impact of such a correction on the vertical alignment of the individual camera measurement volumes will be discussed. Figure 2.17 shows exemplarily the uncorrected vertical tracer particle positions over drying time, recorded during a film drying experiment. Note that the experimental details will be presented later. The upmost camera (green trajectories) had a motorized lens position of $s_{axis} = 0\ mm$, needing no correction, whereas for the middle (red) and lower (blue) camera the lens position was $s_{axis} = 75\ mm$ and $151\ mm$, respectively.

The plotted data without correction factor suggest that there is no vertical overlap between the lower and middle camera (blue and red) and only little vertical overlap between the middle and upper camera (red and green). In addition, a discontinuity between upper and middle camera can be observed when the upmost camera stops to provide valid data due to film shrinkage during drying.

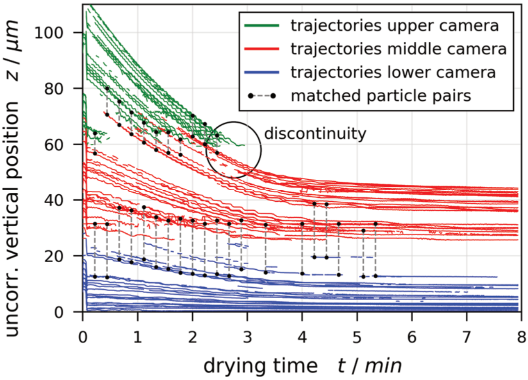

Figure 2.17: Transient vertical position of tracer particles during a drying experiment and evaluated without a correction factor, which is required to compensate the impact of s_{axis} on the diffraction ring sizes, as pointed out in section 2.2.5.

Consideration of the correction factor f_r in experiment evaluation poses two challenges: First, no closed function $f_r(s_{axis} > 0, n_s, z_p)$ was found during calibration, as it would require a significant amount of additional calibration samples, as pointed out in section 2.2.5. Second, in contrast to the calibration samples, the vertical particle position z_p is not known prior to the experiment evaluation, whereas f_r depends on it. This results in the implicit equation

$$0 \overset{!}{=} z_p - P_4\left(r_{ring} \cdot f_r(z_p)\right) , \tag{2.5}$$

where P_4 denotes the polynomial relation between z_p and r_{ring} from the calibration lookup table as described in section 2.2.6. With a known function for the correction factor f_r, this implicit equation could easily be solved using *fsolve* function of the *python* package *scipy* (Virtanen et al. 2020). The challenge of this approach, however, is computational. An average drying experiment results in several individual detections in the order of 10^5 rings, and equation (2.5) would have to be solved for each of the ring detections individually. Combined with the iterative finding of the vertical origin, discussed before, this would result in very long evaluation times for each experiment in addition to the ring detection duration.

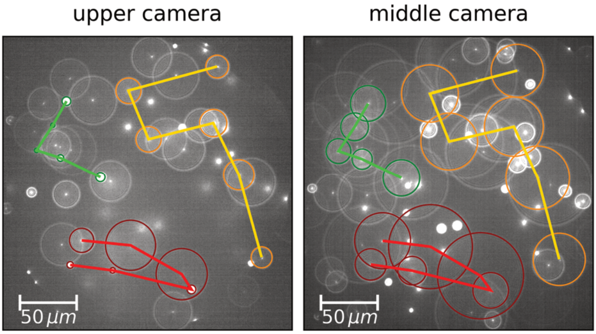

Figure 2.18: Frames of the upper two out of three utilized cameras with adjacent vertical focus plane positions, recorded at the same time (resulting in green and red data in Figure 2.17). The same lateral positions of arbitrarily selected particle constellations can be found in both frames, clearly showing that these must be identical particles. The different diffraction-ring sizes are due to the different vertical focus plane positions.

Instead, a different approach was chosen for the vertical stitching of the individual observation volumes from multiple cameras. Figure 2.18 shows two camera frames, simultaneously recorded with the upper and middle camera during the film drying experiment. Several arbitrarily selected lateral particle positions and their respective diffraction rings are highlighted. The same constellations can be found in both camera recordings, differing only in the respective diffraction ring sizes. This shows that these are indeed the same tracer particles, which therefore must have the same vertical positions. Such particle matches between vertically adjacent cameras were found by comparing camera frames, recorded at the same time, and matching ring detections with the same lateral position in both frames. Several of the found matches are highlighted in Figure 2.17 as black circles and connecting gray dashed lines.

In order to ensure that these pairs have the same vertical position, a modified correction factor f_z was introduced in this work, using the relation

$$z_p = \left(P_4\left(r_{ring}\right) - z_{focus}\right) \cdot f_z + z_{focus} \ , \tag{2.6}$$

with z_{focus} being the true vertical focus position of each camera (intercept of P_4 polynomial at $r_{ring} = 0\ \mu m$). For the upmost camera, the modified correction factor was kept constant $f_z(s_{axis} = 0\ mm) = 1$, since the calibration data show no discrepancy between experimentally derived diffraction rings and the PSF simulations when $s_{axis} = 0\ mm$ (see Figure 2.12). The remaining modified correction factors for the two cameras with $s_{axis} > 0\ mm$ were found by sum of least squares minimization of the vertical distance between the matched particle recordings from vertically adjacent cameras. Applying this procedure to the data from the drying experiment, the resulting transient vertical particle positions are given in Figure 2.19. The corrected trajectories show an excellent transition between the vertically adjacent observation volumes.

This simplified approach to vertical stitching of the observation volume requires that during any 3D-µPTV experiment, the upmost camera must have a motorized lens position of $s_{axis} = 0$ as reference. The approach may introduce some residual error in vertical particle position reconstruction (see Appendix A.5), but it ensures a continuous tracking of tracer particles moving from one observation volume to another. It also requires only a single minimization step, whereas the first approach would require solving approximately 10^5 implicit equations. Consequently, the latter approach using a modified correction factor f_z was used for the evaluation of all 3D-µPTV experiments in this work.

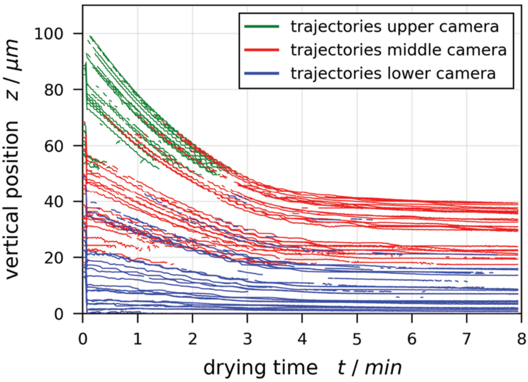

Figure 2.19: Transient vertical position of tracer particles during a drying experiment and evaluated with simplified correction factor f_z, which ensures that identical tracer particles, recorded with cameras having vertically adjacent focus plane positions, have the same vertical position after evaluation.

2.3.4 Summary Experiment Evaluation

The flowchart in Figure 2.20 summarizes the evaluation routine for 3D-µPTV experiments. The logged lens positions from the *LabVIEW* program, the simulated ring lookup table, accounting for optical properties, and the lateral magnification calibration comprise all necessary information for the conversion of the detected diffraction rings from pixel to three-dimensional tracer particle positions for all camera recordings. The subsequent simplified vertical stitching approach is computationally efficient and ensures a continuous tracking of particles moving from one observation volume to another. From the resulting particle trajectories, the velocities were calculated using the first derivative in Savitsky-Golay filtering with a window length of $\Delta t = 2\ s$ and a second-degree polynomial. For better visualization of velocity vector plots, the resulting discrete data were interpolated on a regular grid. An assessment of experimental errors associated with the 3D-µPTV evaluation is provided in Appendix A.6.

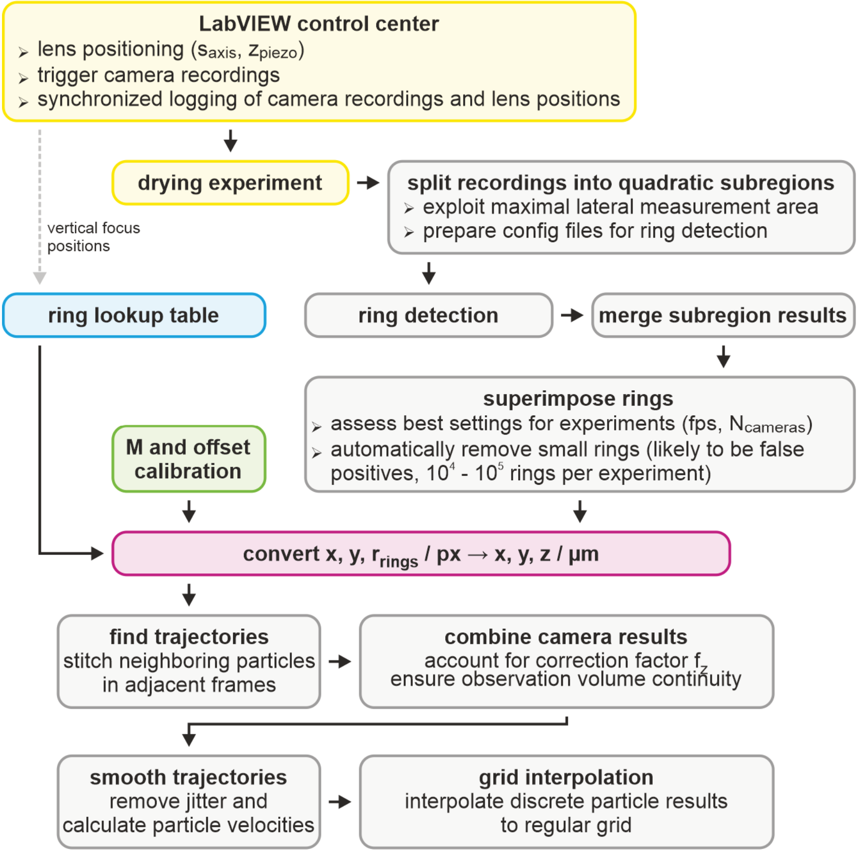

Figure 2.20: Flow chart summarizing the developed evaluation routine for 3D-µPTV recordings.

3 Materials, Properties and Methods

Besides drying experiments using the already presented 3D-µPTV setup (chapter 2), additional experiments have been performed using the Raman-based IMRS setup developed by Schabel (2004a; 2005) and presented in section 1.1.1, and one-dimensional film drying simulations were conducted using the isothermal and non-isothermal model summarized in section 1.1.2. Furthermore, several dimensionless numbers were calculated in order to assess the stability threshold of found convective instabilities in drying thin polymer films. All methods and required temperature- and concentration-dependent material properties are presented in this chapter, with a special emphasis on the surface tension of polymer solutions, being the driving force of Marangoni-induced instabilities (section 3.7).

3.1 Solution Preparation, Coating and Drying

All drying experiments have been performed using poly(vinyl acetate)-methanol solutions with an initial solvent load of $X_0 = 1$, 1.5, or 2 g_{MeOH}/g_{PVAc}. Binary polymer solutions have been prepared using poly(vinyl acetate) (PVAc, 9154.1, Carl Roth,) and methanol (MeOH, 4627.1, Carl Roth) by weight. The solutions were mixed on a roll mixer for at least one week. Thin films were prepared using custom made blade coaters with a coating gap of $h_{gap} = 50,\ 100,\ 150$, and $200\ \mu m$ on microscope-grade glass substrates with a thickness of $150\ \mu m$. The resulting films had lateral dimensions of approximately $5 - 8\ cm$ in coating direction and $2\ cm$ in cross-coating direction. The glass substrates were attached on top of metallic supports, temperature-controlled by water thermostats set to $T_{substrate} = 20\ °C$. For 3D-µPTV and IMRS measurements, the metallic supports have a necessary opening in the center for optical access with the respective microscope lens. The temperature at the underside of the glass substrate above the opening was also controlled using a temperature-controlled airflow around the tip of the microscope lens. A schematic drawing of the temperature control during 3D-µPTV and IMRS experiments is shown in Figure 3.1.

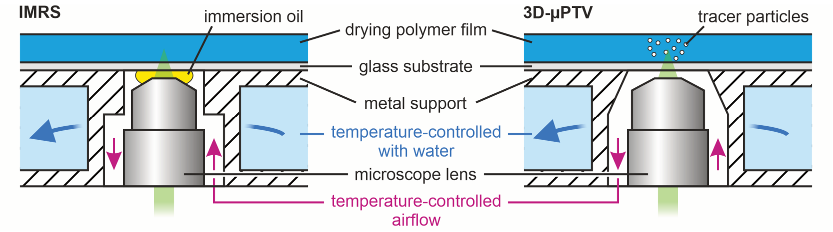

Figure 3.1: Schematic drawing of the substrate temperature control during IMRS (left) and 3D-µPTV (right) experiments. The setups slightly differ in the geometry of the lens opening and IMRS uses oil immersion while 3D-µPTV uses air immersion. (Tönsmann et al. 2021b, License: CC-BY 4.0)

Drying of the thin PVAc-MeOH films was performed under ambient lab conditions. The films were covered with a box having approximately 15 cm edge length and an open top in order to mitigate the effect of lab ventilation on drying.

3.2 3D-µPTV Drying Experiments

Three dimensional flow field measurements were conducted using the 3D-µPTV setup and the evaluation routines presented in chapter 2. Monodisperse fluorescent particles (FSDG003, Bangs Laboratories Inc.) with a diameter of $d_p = 0.5\ \mu m$ were used as tracers. They were added to the PVAc-MeOH solutions, using 1 μl of the original tracer particle suspension (1 $wt\%$ particles) added to 20 ml of polymer solution[13]. After adding the particles, the solutions were mixed for another hour on a roll mixer before the coating and drying procedure described in the previous section. In order to reduce the large amount of resulting video data and the time for the computationally intensive ring detection, only three of the five cameras were used with a low resolution of $640\ px \times 540\ px$

---

[13] This results in a particle volume fraction of approximately $0.5\ ppm$ or $5 \cdot 10^{-5}\ vol\%$ in the polymer solution. With a particle diameter of $d_p = 0.5\ \mu m$, an lateral extent of the observation volume of approximately $250\ \mu m$, and an initial film height $h_0 = 100\ \mu m$, the total amount of particles observable in the combined observation volume of all used cameras is approximately 45 particles.

(4×4 pixel binning, 1/16th of maximum resolution) and a recording speed of $10 - 30\ fps$. The resulting observation volume had an extent of approximately $250\ \mu m$ in lateral diameter and the entire film height of all films under investigation which was $h_{0,max} \approx 100\ \mu m$.

The evaluation of the vertical tracer particle position depends on the refractive index of the polymer film (section 2.2), which continuously changes during drying with decreasing solvent content (see section 3.6 and Appendix B). Therefore, the experiments were evaluated using the refractive index of the coating solution n_0, the refractive index of the dry polymer n_{dry} and the mean refractive index of these two limiting values n_{mean}. All provided flow fields and velocity distributions were derived using the mean refractive index, whereas the extracted transient film height was determined using the limiting values n_0 and n_{dry}.

3.3 Drying Experiments with IMRS

All 3D-µPTV drying experiments have been repeated using the IMRS setup presented in section 1.1.1. For details regarding the setup and the evaluation routine, the readers are referred to Schabel (2004a; 2005) and other references provided. The substrate temperature control is very similar to 3D-µPTV experiments, with the sole exception that immersion oil between the microscope lens and the underside of the glass substrate is required to ensure a high spatial resolution (Schabel 2004a). Similar to 3D-µPTV evaluation, the IMRS measurement technique also requires the knowledge of the refractive index of the film under investigation. Since the IMRS measurements give direct access to vertical concentration profiles, the transient concentration-dependent refractive index is used for the correction of the vertical measurement positions. Additionally, the evaluation requires the component's pure Raman spectra and a concentration calibration using solutions with known composition. These data are provided in Appendix B.5.

3.4 Film Drying Simulations

The one-dimensional film drying simulation model presented in section 1.1.2 was used in this dissertation, giving access to transient vertical concentration and temperature profiles, needed for the calculation of several dimensionless numbers, with the intention to assess the stability threshold of found convective instabilities. The input parameters required for film drying simulations are the concentration- and temperature-dependent diffusion coefficient $\delta_{s,p}$ of solvent s in the polymer p, the phase equilibrium in the form of a Flory-Huggins interaction parameter $\chi_{i,p}$, the solvent's vapor pressure p_s^*, as well as a constant heat-transfer coefficient α_{top} representing the vapor transport in the gas phase above the drying film. The corresponding mass-transfer coefficient $\beta_{s,air}$ was calculated using the analogy of heat- and mass transfer (Lewis law, e.g. VDI e.V. 2013). The lower mass boundary condition is a zero flux condition at the substrate, since the glass substrate is impermeable. Additionally, the density of the polymer solution ρ is required. For non-isothermal simulations the thermal properties (heat conductivity λ, heat capacity c_p) of the solution and the glass substrate, the solvent's heat of vaporization $\Delta h_{v,s}$, and the heat transfer coefficient at the bottom of the substrate α_{bottom} are required as well. Additional details regarding the governing equations and implementation can be found in the respective references provided in section 1.1.2.

3.5 Calculation of Dimensionless Numbers

Several dimensionless numbers reported in literature (chapter 1) are being used to assess the dominant driving force of convective instabilities, the stability threshold of such instabilities as well as the free surface deformability. The following definitions have been used in this dissertation and all numbers have been calculated using material properties that changes during film drying experiments.

In order to assess whether buoyancy or surface tension effects are dominating, the dimensionless Bond number Bo was used and calculated using

$$Bo = \frac{\rho g h^2}{\sigma} \, , \tag{3.1}$$

with $g = 9.81\, m/s^2$ being earth's gravitational constant, σ being the surface tension, and h the film thickness. In the case of $Bo \gg 1$, buoyancy driven effects are dominating whereas in the case of $Bo \ll 1$ surface tension effects dominate.

The stability threshold of surface-tension induced convection was quantified using the dimensionless Marangoni number. Since the necessary surface tension gradient may arise due to a temperature gradient or a concentration gradient (see section 3.7) across the film height (see section 1.2.1), the following definitions for the thermal and solutal Marangoni number have been used for short-scale (cellular) instabilities, respectively. The general idea of the Marangoni number is that the driving force for convection, namely the surface tension gradient, is represented in the numerator whereas balancing forces are given in the denominator. As either temperature or concentration gradients may give rise to a surface tension gradient, the thermal diffusivity κ and diffusion coefficient $\delta_{s,p}$ represent the ability to mitigate these gradients and appear in the respective denominators. In addition, the dynamic viscosity η dampens any flow and therefore appears in both definitions:

$$Ma_T = \Delta\sigma(\bar{x}, T) \cdot \frac{h}{\eta(\bar{x}, \bar{T}) \cdot \kappa(\bar{x}, \bar{T})} \tag{3.2}$$

$$Ma_s = \Delta\sigma(x, \bar{T}) \cdot \frac{h}{\eta(\bar{x}, \bar{T}) \cdot \delta_{s,p}(\bar{x}, \bar{T})} \tag{3.3}$$

The subscripts T and s denote whether the Marangoni convection is induced by thermal or solutal effects. $\Delta\sigma$ denotes the vertical surface-tension difference between the free surface and bottom of the film, induced by either temperature or concentration differences. Note that these definitions are equivalent to previously published work but $\Delta\sigma$ is sometimes given as $\partial\sigma/\partial R \cdot \Delta R_{vertical}$, with R being either temperature or concentration. Since the material properties continuously change during film drying, the Marangoni numbers are calculated with transient properties using the height-averaged film temperature $\bar{T}$ and solvent mass fraction $\bar{x}$, indicated by bars above the respective symbols.

Considering long-scale (lateral) Marangoni convection induced by a lateral gradient in surface tension, the used definitions are

$$Ma_{T,lateral} = \frac{\Delta\sigma(\bar{x}, T)_{lateral}}{\Delta L} \cdot \frac{h^2}{\eta(\bar{x}, \bar{T}) \cdot \kappa(\bar{x}, \bar{T})} \tag{3.4}$$

and

$$Ma_{s,lateral} = \frac{\Delta\sigma(x,\bar{T})_{lateral}}{\Delta L} \cdot \frac{h^2}{\eta(\bar{x},\bar{T}) \cdot \delta_{s,p}(\bar{x},\bar{T})} , \qquad (3.5)$$

respectively. $\Delta\sigma_{lateral}/\Delta L$ now denotes the linearized lateral surface tension gradient induced by either temperature or concentration.

In order to assess the impact of capillary and gravity wave leveling effects, the dimensionless Capillary number Ca and Galileo number Ga are defined as

$$Ca = \frac{\bar{\eta}\overline{\delta_{s,p}}}{\sigma_s h} \qquad (3.6)$$

and

$$Ga = \frac{\bar{\rho} g h^3}{\bar{\eta}\overline{\delta_{s,p}}} , \qquad (3.7)$$

respectively, with a bar denoting height-averaged properties. Note that different definitions can be found in literature, depending on whether thermal or solutal effects are dominating (see footnotes 6 and 7 in section 1.2.1).

According to De Gennes et al. (2010), the dominant leveling mechanism can be discriminated using the capillary length $l_{capillary}$ (equation (1.2)). The authors provide equations for the characteristic time constant τ of leveling, assuming a two-dimensional periodically deformed free surface. For capillary waves ($\lambda \ll l_{capillary}$), the time constant is

$$\tau_{capillary} = \frac{3\bar{\eta}}{\sigma_s h^3 k^4} , \qquad (3.8)$$

with $k = 2\pi/\lambda$ being the wavenumber (reciprocal wavelength) of the lateral perturbations. The characteristic time constant for gravity waves ($\lambda \gg l_{capillary}$) is

$$\tau_{gravity} = \frac{3\bar{\eta}}{\bar{\rho} g h^3 k^2} . \qquad (3.9)$$

3.6 Material Properties

From the last sections 3.2 to 3.5, it can be seen that many material properties are required for the rigoruous evaluation of drying experiments, simulations, and dimensionless number calculations. In this dissertation, special emphasis is laid on using realistic concentration- and temperature-dependent values for these properties. Several of them, for example the solution density ρ, refractive index n or the heat conductivity λ, do not vary much with concentration. Therefore, ideal mixing rule equations were used to calculate the solution properties. All values, mixing rules and their respective sources are provided in Appendix B. Hereafter, only the material properties showing a strong non-ideal concentration-dependency are presented in detail.

The dynamic viscosity η of a polymer solution strongly increases with decreasing solvent content. The values for binary PVAc-MeOH solutions were measured using a rotary type rheometer (MCR 101, Anton Paar) in cone-plate configuration ($60\,mm$ diameter, $2°$ cone angle) with a shear rate between 0.01 and $1000\ s^{-1}$ and a temperature between 10 to $40\ °C$. The experimental data did not show any shear rate dependency in the measurement range down to a methanol mass fraction of $x_{MeOH} \geq 0.67$, indicating Newtownian behavior. At lower solvent mass fractions between $0.37 \leq x_{MeOH} \leq 0.50$ shear tinning behavior started at lower shear rates with decreasing temperature and decreasing methanol mass fraction but were independent of the shear rate for $\dot{\gamma} \leq 100\ s^{-1}$ (Appendix B.3, Figure A.9 to Figure A.12). The zero-shear viscosity η_0 data were fitted using

$$\eta_0 = A \cdot \exp\left\{\frac{B}{T} + (C_0 + T \cdot C_1) \cdot x_{MeOH}\right\}\ , \tag{3.10}$$

with T being the temperature in Kelvin, x_{MeOH} the mass fraction of methanol and A, B, C_0 and C_1 being fit parameters. The relation was originally reported by Al-Fariss and Al-Zahrani (1993) but without the temperature-dependency of parameter C. The experimental data and the fit are shown in Figure 3.2. The averaged relative deviation between experimental data and fit is 7.4 %. A qualitative discussion for expected behavior at lower methanol concentrations is provided in Appendix B.9.

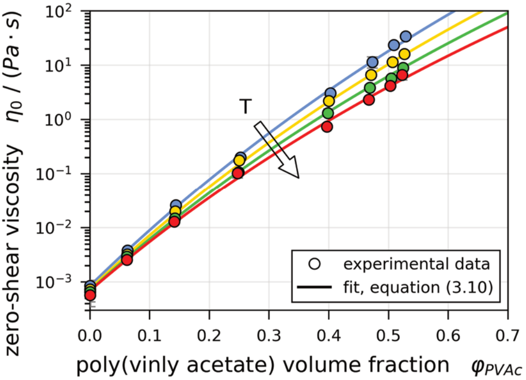

Figure 3.2: Concentration- and temperature-dependent dynamic viscosity of poly(vinyl acetate)-methanol solutions. $T = 10, 20, 30, \text{and } 40\ °C$. The fit parameters found for equation (3.10) are given in Appendix B.3. *Data and fit were previously published in Tönsmann et al. (2021c).*

The diffusion coefficient $\delta_{s,p}$ as well as the solvent activity a_i have already been discussed in section 1.1 and Figure 1.2. The data were taken from Siebel (2017b) and Schabel (2004a), respectively. Regarding the surface tension of polymer solutions, it was found almost no data are available in the literature, especially for low solvent concentrations. In addition, most published data are limited to diluted solutions (e.g. Ober et al. 1983; Bhattacharya and Ray 2004) or to polymers with a low molecular mass which are in the liquid state at ambient conditions (e.g. Gaines 1969; Siow and Patterson 1973). Films during drying, however, undergo a wide concentration change from the initial coating solution to the dry polymer. Hence, special consideration was given to the experimental determination as well as the continuous description of the surface tension data in form of mixing rule equations. The findings are presented in the following separate section.

3.7 Surface Tension of Polymer Solutions[14]

The driving force of Marangoni convection is an interfacial-tension gradient along a phase boundary between two fluids and, regarding polymer film drying, a surface-tension gradient along the film's free surface in contact with the surrounding gas. Consequently, accurate data of the temperature- and concentration-dependent surface tension of the material system under investigation are crucial to determine the impact of drying conditions on Marangoni-induced convective instabilities during film drying. While surface-tension data are readily available for many liquid-liquid mixtures (Wohlfarth and Lechner 2016), data of polymer solutions are scarce, addressed in detail in Tönsmann et al. (2021a). The solvent concentration during polymer film drying decreases continuously. Therefore, surface tension data are required over a wide concentration range, from the initially diluted coating solution to the dry solidified pure polymer. Within the framework of this dissertation, the surface tension of several binary and ternary polymer-solvent(-solvent) solutions was investigated. In order to close the data gap at low solvent concentrations, available mixing rule equations for liquid-liquid mixtures were evaluated regarding their applicability to polymer-solvent mixtures. The presented results have been previously published and are discussed in the following sections (Tönsmann et al. 2021a).

3.7.1 Measurement Technique

The surface tension was measured using a drop volume tensiometer (Tropfenvolumentensiometer TVT2, Lauda Scientific GmbH) using a $2.5\,ml$ or $5\,ml$ glass syringe, a steel capillary (SK 1) and an attached thermostat for temperature control (Ministat 125, Peter Huber Kältemaschinenbau AG). The measurement

---

[14] Results presented in this section have been previously published in a peer-reviewed journal article:
Tönsmann, M.; Ewald, D. T.; Scharfer, P.; Schabel, W. (**2021a**): *Surface tension of binary and ternary polymer solutions: Experimental data of poly(vinyl acetate), poly(vinyl alcohol) and polyethylene glycol solutions and mixing rule evaluation over the entire concentration range*. In *Surfaces and Interfaces* 26, p. 101352. DOI: 10.1016/j.surfin.2021.101352.
Figures have been reprinted with permission from Elsevier.

principle relies on the detection of detaching drops at the capillary for a set volume flow. Ten or more individual measurements have been averaged for further analysis (Tönsmann et al. 2021a). Details regarding the components and preparation of the additional liquid mixtures and polymer solutions reported in this section are provided in Appendix B.6.

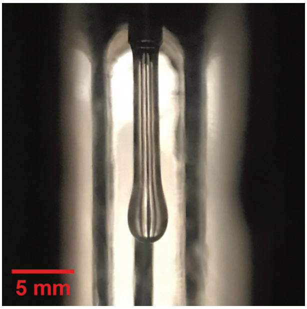

Figure 3.3: Liquid thread at capillary rendering surface tension measurements with drop volume method impossible since no drop detachment could be detected. Properties: PVA-water, $x_{water} = 0.5$, $T = 20\ °C$. *Reprint from Tönsmann et al. (2021a)*[14] *with permission from Elsevier.*

For polymer-solvent solution measurements, a lower solvent concentration limit was observed when individual drops stopped to detach from the capillary due to the high viscosity. This is exemplarily depicted in Figure 3.3 for poly(vinyl alcohol)-water. The concentration limit may vary with different measurement techniques and material systems, but it was not within the scope of this work to identify the exact limit.

3.7.2 Temperature and Concentration Dependency

The surface tension of a pure liquid decreases with increasing temperature until it reaches zero close to the liquid's critical temperature. This relation was first described with the well-known Eötvös equation (Eötvös 1886). Within a limited temperature range, $\partial\sigma/\partial T$ is close to constant, and the temperature-dependent surface tension is commonly represented by a linear relation (e.g. Poling et al. 2001).

The surface tension of a mixture, however, is not a simple relation of the pure component data since the component with lower surface tension is prone to accumulate at the free surface. This may result in a difference between bulk and surface concentration (Poling et al. 2001). While a mixture of components with similar pure surface tensions may show a close to ideal behavior in the form of a linear concentration dependency thereof (see methanol-toluene in Figure 3.4 right), the non-ideality increases when the pure component's surface tension differs noticeably. Due to the affinity of the component with lower surface tension to accumulate at the free surface, the excess surface tension, expressing non-ideality, is negative for most mixtures (Poling et al. 2001).

Initially, the temperature- and concentration-dependency of several pure solvents as well as binary liquid-liquid mixtures were examined, with the intention to compare the results to available data and thereby assessing the measurement accuracy. Figure 3.4 (a) and (b) show the temperature-dependent surface tension of several solvents and the concentration-dependent data of liquid-liquid mixtures, respectively. The colored markers indicate own measurements while the empty markers denote available data from *SpringerMaterials* database (Wohlfarth and Lechner 2016). Regarding the pure solvent's temperature-dependent data (Figure 3.4 (a)), it can be seen that the temperature dependency is indeed linear. In addition, the results are in excellent agreement with available data. Solely the data of water are slightly lower (≤ 2 % deviation) than the reference values. Since water is known to be prone to surface contaminations due to its high surface tension (Palmer and Berg 1971; Berg et al. 1966; Cammenga et al. 1984; De Gennes et al. 2010), the mild deviation may be caused by using double distilled water "as is" in this work without further purification. Considering this fact, the small discrepancy appears acceptable. Adding $1\,\mu l$ tracer particle suspension to $20\,ml$ pure methanol, as required for the 3D-µPTV measurements, did not affect the surface tension. Tracer particles in pure water lowered the measured surface tension by less than 2 %. Hence, it can be concluded that the addition of tracer particles for the 3D-µPTV experiments has no effect on the surface tension of the coating solution (poly(vinyl acetate)-methanol) and only little effect on water-based systems.

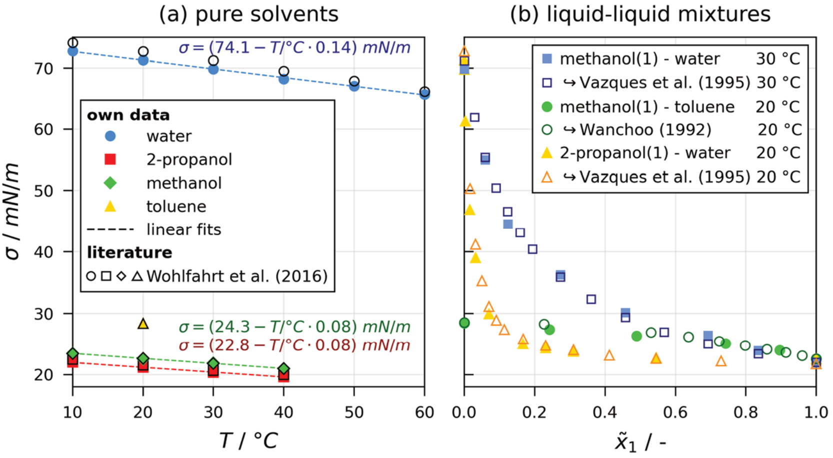

Figure 3.4: Surface tension data of pure solvents (a) and binary liquid-liquid mixtures (b) measured with drop volume method (colored markers) and in comparison with available data (empty markers). *Data and linear temperature fits were previously published in Tönsmann et al. (2021a)*[14].

The measured concentration-dependent surface tension data of binary liquid-liquid mixtures, given in Figure 3.4 (b), are also in good agreement with available reference values (Wanchoo and Narayan 1992; Vazquez et al. 1995). It can further be seen that the methanol-toluene mixture, with both components having a similar pure surface tension value, shows a close to linear concentration dependency. Methanol-water and 2-propanol-water mixtures, on the other hand, differ significantly in their respective pure surface tension values. Thus, the concentration dependency is noticeably non-linear.

3.7.3 Surface Energy of Polymers

The surface tension of a liquid is given in units of N/m, whereas the surface property of a solid is the surface free energy (SFE) in $J/m^2 (= (Nm/m^2))$. Both variables have the same dimension and can be compared with each other. The surface free energy of a solid can be acquired by contact angle measurements with test liquids, having a known surface tension (i.e. Zisman or Owen-Wendt-Rabel-Kaeble methods) (Uyama et al. 1991; Zisman 1964; Owens and Wendt

1969; Rabel 1971; Kaelble 1970). Alternatively, it can be found by extrapolating the surface tension of the pure polymer melt to room temperature (Roe 1968; Wu 1969). Both methods imply that a liquid's surface tension and a solid's surface free energy are equivalent properties, which is also reflected in the equivalent units. Consequently, it is possible to use the surface free energy (SFE) as an additional data point when assessing the concentration dependent surface tension of polymer solutions. Temperature-dependent SFE data of pure polymers used in solutions in this work were taken from literature (Wu 1969; Rastogi and St. Pierre 1971; Van Oss et al. 1987) and are summarized in Appendix B.7.

3.7.4 Mixing Rule Equations

Due to the non-ideality of mixtures, mixing rule equations, describing the concentration-dependent surface tension, require not only the pure component's surface tension values but also additional parameters accounting for the non-ideality (Poling et al. 2001). Available equations in literature, describing the surface tension of liquid-liquid mixtures, can be divided into empiric and thermodynamic-based mixing rules. While empiric rules are commonly fitted to experimental data, thermodynamic-based mixing rules were originally intended to predict the non-ideality of surface tension, but they require additional thermodynamic properties not readily available for polymers. Alternatively, the thermodynamic-based equations can be used for fitting to experimental data (Tönsmann et al. 2021a).

Approximately twenty different liquid-liquid mixing rule equations were found in literature. However, most of them use the component's molar fraction as concentration unit. For polymer-solvent systems, the polymer's molar mass is orders of magnitude larger than the solvent's.[15] Accordingly, utilizing molar fractions as concentration unit for polymer solutions is unfeasible. Instead, the concentration unit in all found equations was substituted with the mass fraction, as done by Di Nicola and Pierantozzi (2013). In Tönsmann et al. (2021a) a total of twelve different equations have been evaluated on three binary liquid-liquid mixtures and five binary polymer-solvent solutions. Some equations contain a temperature

---

[15] In addition, the polymer's molar mass is a distribution not a single value.

dependency. For all others, fit parameters linear in temperature were used (see Table 3.1). Several found mixing rules have been intentionally omitted, since they either do not comprise all pure component values (e.g. equations for diluted solutions) (Crawford and Van Winkle 1959; Li and Lu 2001b, 2001a), are mathematically complex (e.g. implicit definitions or systems of multiple equations) (Gaines 1969; Sprow and Prausnitz 1966; Boyer et al. 2017; Topping et al. 2007) and are therefore not suitable for fitting to experimental data, or are mathematically similar to tested equations (Macleod 1923; Sugden 1924).

In addition, two ternary polymer-solvent-solvent solutions have been investigated, and it was assessed whether the surface tension of a ternary solution could be predicted with data from the respective binary subsystems (Appendix B.8). Here, only the main findings will be reported. For further details, the reader is referred to Tönsmann et al. (2021a).

Mathematically, the available equations can be divided into non-excess equations and excess equations following

$$\sigma_{m(ixture)} = \sum_{i=1}^{N} x_i \sigma_i + \sigma^E(x_i) \ . \tag{3.11}$$

The sum reflects an mixture of N components with their respective pure surface tension σ_i and mass fraction x_i, while $\sigma^E(x_i)$ is the excess surface tension accounting for non-ideality. Exemplarily, equations (3.12) and (3.13) denote modified mixing equations originally proposed by Li et al. (2000a) and Santos et al. (2003), respectively, but utilizing mass fractions x_i instead of originally proposed mole fractions (Tönsmann et al. 2021a).

$$\sigma_m = \sum_{i=1}^{N} x_i \sigma_i + \sum_{i=1}^{N} \frac{x_i}{\sum_{j=1}^{N} x_j \mathbf{C}_{ij}} \sum_{i=1}^{N} x_j \boldsymbol{C}_{ij} \boldsymbol{A}_{ij} \tag{3.12}$$

$$\sigma_{\mathrm{ij}}^{\mathrm{E}} = x_i x_j \left(\boldsymbol{A} + \boldsymbol{B} \left[1 - \left(x_i - x_j \right) \right]^{\boldsymbol{C}} \right) \tag{3.13}$$

A, B and C denote fit parameters, adapted to experimental data by least-square minimization, and N in equation (3.12) is the number of components. In Tönsmann et al. (2021a), ten additional mixing rules have been tested.

The best matching fit to binary and ternary polymer solution data was found by least-square minimization. The fit quality was assessed by calculating the averaged absolute deviation (AAD) between fitted and experimental data, using equation (3.14), with N being the number of binary and ternary data points.

$$AAD/\,\% = 100 \cdot \frac{1}{N}\sum_{i}^{N}\left|\frac{\sigma_{exp} - \sigma_{fit}}{\sigma_{exp}}\right| \tag{3.14}$$

3.7.5 Results Binary Polymer-Solvent Solutions

The experimentally determined surface tension data of five different binary polymer-solvent solutions are given in Figure 3.5. It can be seen that all data sets have gaps at low solvent concentrations, where the surface tension was experimentally inaccessible due to the high viscosity (see section 3.7.1). While all three solutions with methanol and toluene show a non-ideal but continuous surface tension change with composition, the two solutions with water exhibit a step-like decrease of surface tension at very low polymer concentrations. This indicates that the added polymer acts as a strong surface-active agent in water, which is known for its affinity for surface contaminations.

Cavadini et al. (2018) found no convective instability in drying films of poly(vinyl alcohol)-water and explained this observation by a stable stratification regarding surface tension $\partial\sigma/\partial x_{water} > 0$ (see BM mechanism in Figure 1.5). The new data (red triangles) suggest, however, that the surface tension of this solution exhibits a plateau of constant surface tension over a wide concentration range, which also explains the lack of convective instabilities observed by Cavadini et al. (2018).

Equation (3.12) was found to reasonably match all three tested binary liquid-liquid mixtures as well as all five polymer-solvent solutions with an AAD as little as ≤ 1.64 %, including the step-like change of surface tension in polymer-water solutions. The fit of equation (3.13) fails to follow the strong non-ideality of PVA-water data (dashed red line), but resulted in a good AAD of ≤ 1.60 % for the remaining binary polymer solutions (Tönsmann et al. 2021a).

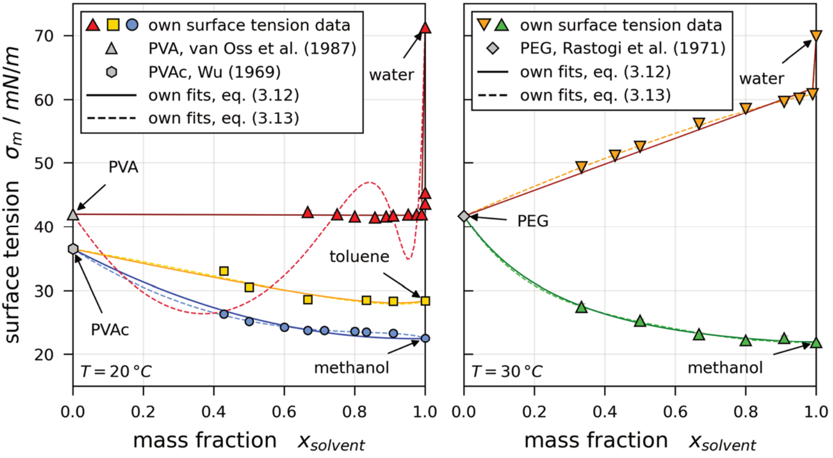

Figure 3.5: Concentration-dependent surface tension of five different binary polymer-solvent solutions measured with drop volume tensiometry (colored markers). The fits were performed using the solid polymer's surface free energy as additional data point (gray markers), closing the data gap at low solvent concentrations. *Data and fits were published independently in Tönsmann et al. (2021a)*[14].

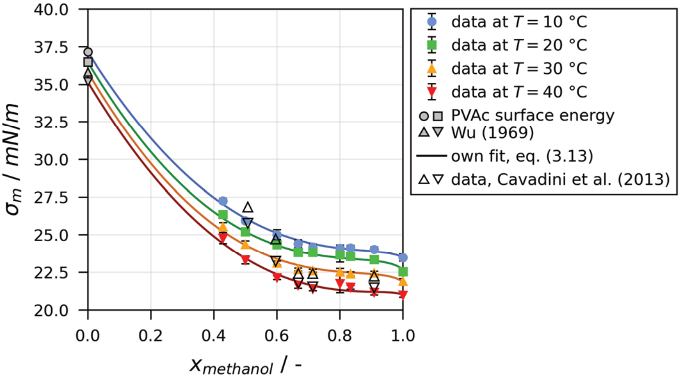

Figure 3.6: Concentration- and temperature-dependent surface tension data of poly(vinyl acetate)-methanol solution. Colored markers denote experimental values from drop volume tensiometer measurements, empty markers denote available reference values and the lines denote the best fit using equation (3.13) derived in this work. *Data and fit were published independently in Tönsmann et al. (2021a).*

Regarding the binary poly(vinyl acetate)-methanol solution, used for drying experiments reported in chapter 4 and 5, equation (3.13) was used with fit coefficients linear in temperature. The concentration- and temperature-dependent data and the fitted equation are shown in Figure 3.6 in comparison with previously reported data from Cavadini et al. (2013). The current and previously reported data are in excellent agreement for $x_{methanol} > 0.6$. For smaller methanol concentrations, however, the previous values are larger than this work's data. It was found that the equilibration time increases with decreasing methanol content (Tönsmann et al. 2021a). Cavadini et al., however, did not provide any details if they considered this in their work. Hence, it is reasonable to assume that the increasing discrepancy between the experimental data for lower methanol concentrations may be a result of insufficient equilibration times during measurements by Cavadini et al. (2013). The resulting fit coefficients from this work's data are given in Table 3.1 with a resulting $AAD = 0.59\ \%$.

Table 3.1: Parameters for binary PVAc-methanol solution fitted with equation (3.13) and resulting in $AAD = 0.59\ \%$ (Tönsmann et al. 2021a)[14].

Parameters	Fitted Value
$A\ /\ mN/m$	$1234 + 1089 \cdot T/°C$
$B\ /\ mN/m$	$-1256 - 1089 \cdot T/°C$
C	$4.272 \cdot 10^{-4} - 8.888 \cdot 10^{-6} \cdot T/°C$

3.7.6 Summary

In order to assess the driving force of Marangoni convection, surface tension data of five binary polymer-solvent solutions were investigated experimentally. An inevitable data gap for low solvent concentrations (high viscosity) could be circumvented by fitting available liquid-liquid mixing rule equations to experimental data and the pure polymer's surface free energy as an additional data point. The approach to substitute molar fraction as concentration unit (as originally reported for said mixing rules) by mass fraction resulted in good agreement between several of the tested equations with experimental data. An additional evaluation of ternary polymer-solvent-solvent solutions (Appendix B.8) revealed that an additional fit to ternary data is better suited than a predictive approach using fitted equations to the respective binary subsystems only (Tönsmann et al. 2021a).

The found concentration- and temperature-dependent fit for poly(vinyl acetate)-methanol using equations (3.11) and (3.13) was used in this work for surface tension calculations (Figure 3.6).

4 Short-Scale Instabilities in Drying Polymer-Solvent Films[16]

In order to evaluate the hypothesis that the onset and stop of short-scale convective instabilities (convection cells) in drying polymer-solvent films can be described by a unified critical Marangoni number threshold, a series of film drying experiments have been conducted. The results are presented in this chapter. The flow field in drying polymer films was measured using the 3D-µPTV setup presented in chapter 2. The experimental procedure and drying conditions as well as material properties can be found in chapter 3. It will be shown that some films are convectively stable during the entire drying time, whereas some films initially exhibit short-scale convection cells, which stop during drying and before the end of the constant rate period (section 4.1). In order to derive realistic transient Marangoni numbers accounting for concentration- and temperature-dependent material properties, simulations have been used as an elaborated fit to the 3D-µPTV experiments, giving access to transient vertical concentration and temperature profiles during drying (section 4.4 and 4.5). The concentration profiles have been validated by means of IMRS drying experiments (section 4.2). In addition, several aspects regarding the comparability of simulation results and 3D-µPTV experiments will be discussed (section 4.3). Finally, the impact of the found instabilities on free surface deformation and leveling is assessed in section 4.6.

---

[16] Results presented in this section have been previously published in two peer-reviewed journal articles:
Tönsmann, M.; Scharfer, P.; Schabel, W. (**2021b**): *Critical Solutal Marangoni Number Correlation for Short-Scale Convective Instabilities in Drying Poly(vinyl acetate)-Methanol Thin Films*. In *Polymers* 13 (17). DOI: 10.3390/polym13172955.
Tönsmann, M.; Scharfer, P.; Schabel, W. (**2021c**): *Transient Three-Dimensional Flow Field Measurements by Means of 3D µPTV in Drying Poly(Vinyl Acetate)-Methanol Thin Films Subject to Short-Scale Marangoni Instabilities*. In *Polymers* 13 (8), p. 1223. DOI: 10.3390/polym13081223.
Figures have been reprinted under the license CC-BY-4.0.

4.1 Transient 3D Flow Fields

4.1.1 Convective (In)stability

The three-dimensional particle trajectories in evaporating films of PVAc-MeOH with an initial solvent load $X_0 = 1\ g_{MeOH}/g_{PVAc}$ as well as $X_0 = 1.5\ g_{MeOH}/g_{PVAc}$ and a coating gap of $h_{gap} = 200\ \mu m$ measured with 3D-µPTV are given in Figure 4.1. The different colors denote particle trajectories recorded with three cameras at different vertical positions in the film over the entire drying time. The results for $X_0 = 1\ g_{MeOH}/g_{PVAc}$ (left) clearly show that the particle trajectories are solely vertical, showing no convective instability.

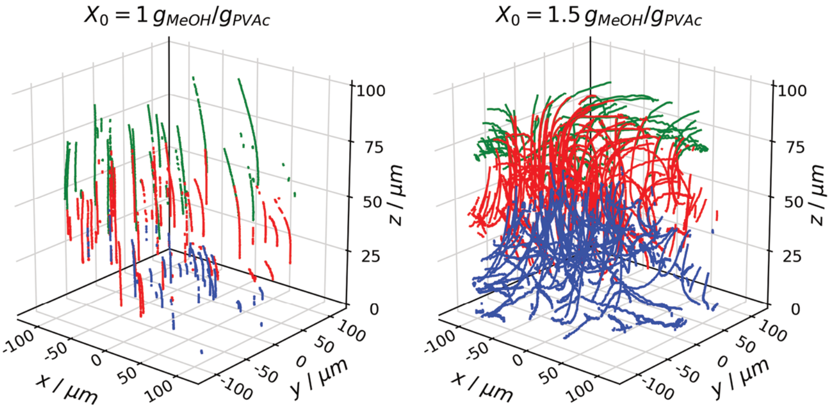

Figure 4.1: Three-dimensional tracer particle trajectories in two poly(vinyl acetate)-methanol films, with drying conducted at $T_{substrate} = 20\ °C$ and otherwise ambient conditions, measured with 3D-µPTV and evaluated with mean refractive index n_{mean}. The different colors denote the recording camera. Left: $X_0 = 1\ g_{PVAc}/g_{MeOH}$ and $h_{gap} = 200\ \mu m$; the flow field is solely dominated by film shrinkage. Right: $X_0 = 1.5\ g_{PVAc}/g_{MeOH}$ and $h_{gap} = 200\ \mu m$; the flow field clearly shows convective instabilities. (Tönsmann et al. 2021c)[16]

The vertical position in the film z of the same trajectories, plotted over the drying time t, is given in Figure 4.2. The particles move solely in negative z-direction, following the film shrinkage due to methanol evaporation. In order to extract the transient film height (drying curve), an upper hullcurve denoting the highest vertical particle positions was extracted, plotted as black solid line. The 3D-µPTV evaluation depends on the refractive index of the sample, which changes with decreasing methanol concentration during drying. Accordingly, the solid black line denotes the drying curve evaluated for the mean refractive index n_{mean}. The evaluation was repeated with the initial refractive index of the coating solution n_0 and the refractive index of the dry solid polymern_{dry}. The resulting drying curves are given as black dotted and black dash-dotted line in Figure 4.2, respectively.

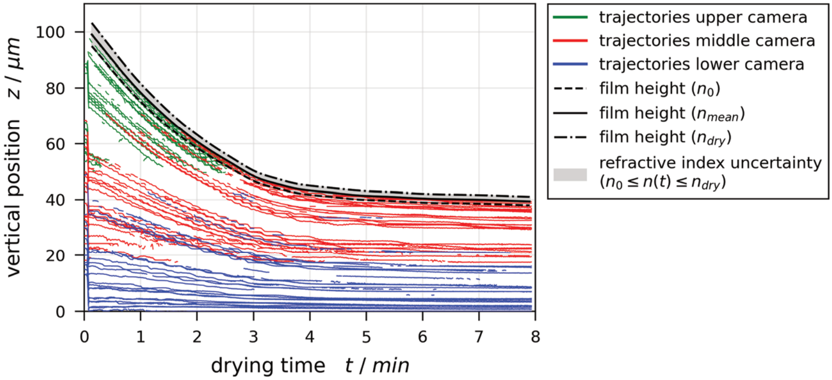

Figure 4.2: Transient vertical tracer particle positions in the drying poly(vinyl acetate)-methanol film, exhibiting film shrinkage only ($X_0 = 1\ g_{PVAc}/g_{MeOH}$ and $h_{gap} = 200\ \mu m$, Figure 4.1 left), evaluated using the mean refractive index n_{mean}. The extracted drying curves are additionally given for an evaluation with the refractive index of the coating solution n_0 and the dry polymer n_{dry}, respectively (black curves). (Tönsmann et al. 2021c)[16]

A significant change in the flow field can be observed when increasing the initial solvent load to $X_0 = 1.5\ g_{MeOH}/g_{PVAc}$ (Figure 4.1 right). The trajectories move vertically as well as laterally, showing convective instabilities. Figure 4.3 shows again the vertical particle positions z over drying time t for this case. It can be seen that the drying film exhibits a simultaneous upward and downward flow in the first two minutes. At a critical drying time $t_{crit,Ma} = 144\ s$, the last upward moving particle reaches its highest position. Thereafter, the convective instability stops and the particles solely follow the film shrinkage.

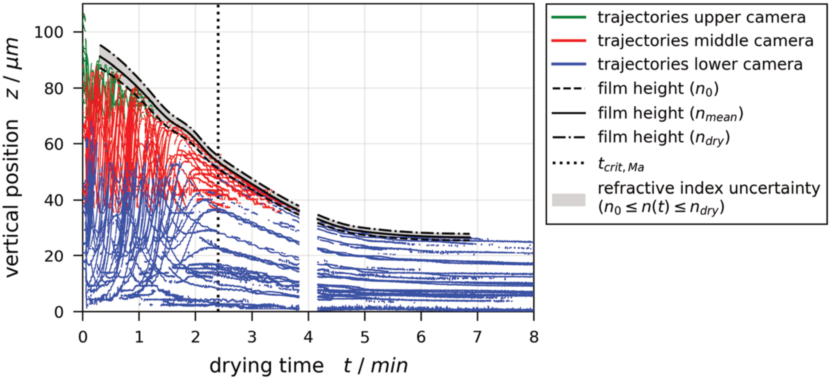

Figure 4.3: Transient vertical tracer particle positions in the drying poly(vinyl acetate)-methanol film, exhibiting initial convective instabilities ($X_0 = 1.5\ g_{PVAc}/g_{MeOH}$ and $h_{gap} = 200\ \mu m$, Figure 4.1 right), evaluated using the mean refractive index n_{mean}. The convective instability stops during drying at $t_{crit,Ma} = 144\ s$. The extracted drying curves are additionally given for an evaluation with the refractive index of the coating solution n_0 and the dry polymer n_{dry}, respectively (black curves). (Tönsmann et al. 2021c)[16]

The corresponding velocity distributions over the film height were calculated by averaging the particle velocities laterally and in slices of $\Delta z = 5\ \mu m$. Figure 4.4 shows the resulting magnitude of lateral as well as vertical velocity at different drying times from the convectively stable film ($X_0 = 1\ g_{MeOH}/g_{PVAc}$). The vertical velocity (right) is highest at the film surface ($|u_z| \leq 0.5\ \mu m/s$)[17]. It decreases linearly towards the bottom of the film during the constant rate period of drying (red, blue and yellow markers). After the constant rate period, the vertical velocity is very small ($|u_z| \leq 0.1\ \mu m/s$) and constant over the film height (green markers). The lateral velocity (left) shows a similar behavior, but the lateral flow

---

[17] The film shrinkage velocity derived from non-isothermal drying simulations matched to the 3D-µPTV experiments (section 4.3) is $v_{int} = 0.2$ to $0.3\ \mu m/s$ during the constant rate period of drying (see Table 4.1 in section 4.5.3). Note that v_{int} is slightly smaller compared to $|u_z| \leq 0.5\ \mu m/s$ presented here. This is due to the simplified vertical stitching routine introducing a small systematic deviation in early stages of drying as discussed in detail in section 4.3.

decelerates faster, exhibiting a very small velocity magnitude and uniform velocity profile over the film height earlier during drying (yellow and green markers).

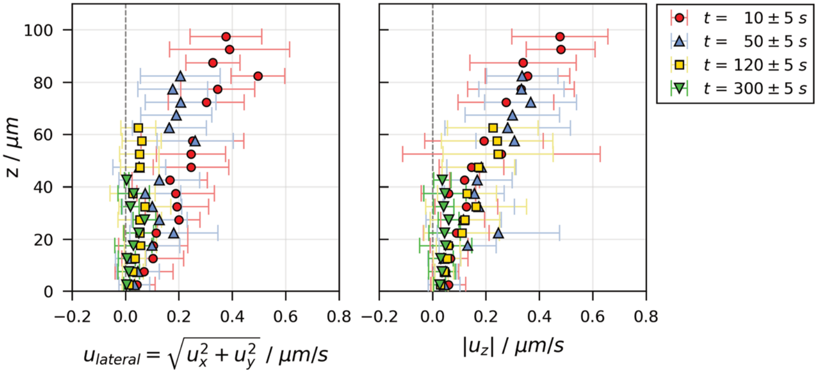

Figure 4.4: Velocity distribution in the poly(vinyl acetate)-methanol film exhibiting only film shrinkage ($X_0 = 1\ g_{PVAc}/g_{MeOH}$ and $h_{gap} = 200\ \mu m$, Figure 4.1 left, Figure 4.2), measured with 3D-μPTV and evaluated with mean refractive index n_{mean}. The discrete data were averaged laterally and in vertical slices of $\Delta z = 5\ \mu m$. Left: Lateral (x, y) velocity over film height. Right: Absolute vertical (z) velocity over film height. (Tönsmann et al. 2021c)[16]

The identical plot for the initially convectively unstable film ($X_0 = 1.5\ g_{MeOH}/g_{PVAc}$) is given in Figure 4.5. Before the critical drying time $t_{crit,Ma} = 144\ s$ is reached, the lateral velocity (Figure 4.5 left, red and blue markers) shows a pronounced maximum at the film's surface, a local minimum at approximately two-thirds of the film height and a local maximum at approximately one-third of the film height. Thereafter, the lateral velocity is uniform over the film height and significantly smaller than during the initial convective instability (yellow and green markers). The vertical velocity magnitude (right), however, shows only one pronounced maximum at approximately two-thirds of the film height but also becomes small and uniform over the film height after the convective instability stopped. The highest convection velocities in the film occur after a drying time of $t = 10\ s$ (red markers) with a lateral (x, y) and vertical (z) velocity magnitude of $\approx 17\ \mu m/s$ and $\approx 7\ \mu m/s$, respectively. The observation that the highest velocity occurs laterally at the film's surface is a clear indicator for surface tension gradients being the driving force of the observed instability. In addition, the velocity distribution shows that the instability has the form of vertical convection cells, with a driving lateral surface flow, a vertical flow in the upper third of the film height and a lateral backflow in the lower third of the film. The form of convective instability is further discussed in section 4.1.2.

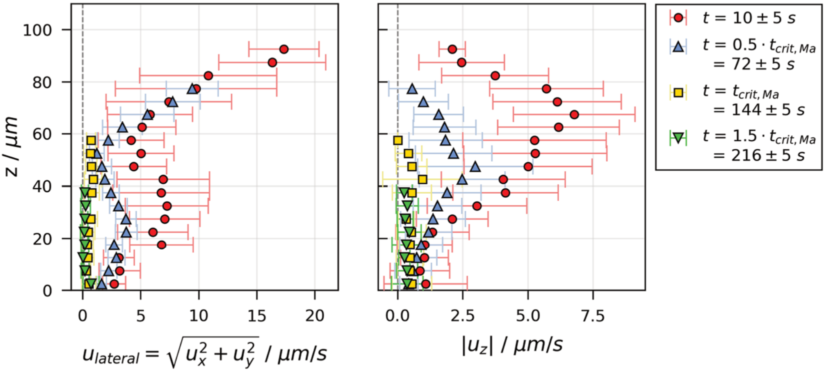

Figure 4.5: Velocity distribution in the poly(vinyl acetate)-methanol film exhibiting initial convective instability until $t_{crit,Ma} = 144\ s$ ($X_0 = 1.5\ g_{PVAc}/g_{MeOH}$ and $h_{gap} = 200\ \mu m$, Figure 4.1 right, Figure 4.3), measured with 3D-µPTV and evaluated with mean refractive index n_{mean}. The discrete data were averaged laterally and in vertical slices of $\Delta z = 5\ \mu m$. Left: Lateral (x, y) velocity over film height. Right: Absolute vertical (z) velocity over film height. (Tönsmann et al. 2021c)[16]

These two types of flow fields are a good representation of all drying experiments reported in this chapter. All drying experiments with an initial solvent load of $X_0 = 1\ g_{MeOH}/g_{PVAc}$ ($h_{gap} = 100$ and $200\ \mu m$) were convectively stable during the entire course of drying, while drying experiments with an initial solvent load of $X_0 = 1.5\ g_{MeOH}/g_{PVAc}$ and a coating gap of $h_{gap} = 100$ to $200\ \mu m$, as well as $X_0 = 2\ g_{MeOH}/g_{PVAc}$ and $h_{gap} = 50$ to $200\ \mu m$, initially exhibited convective instabilities with varying threshold times $t_{crit,Ma}$ at which the flow field transitioned to vertical (z) film shrinkage only. Three repetitions of drying experiments with $X_0 = 1.5\ g_{MeOH}/g_{PVAc}$ and a coating gap of $h_{gap} = 50\ \mu m$ showed mixed results with two repetitions being initially unstable with $t_{crit,Ma} \leq$

$20\ s$ while one repetition was stable during the entire course of drying. This indicates that said experiments were very close to a stability threshold. The critical drying times $t_{crit,Ma}$ are further discussed in section 4.5.1.

The highest decile fraction of lateral as well as vertical particle velocities for films with a coating gap of $h_{gap} = 100$ and $200\ \mu m$ over the drying time are given in Figure 4.6. It can be seen that the lateral surface velocity magnitude (left) is larger than the vertical velocity magnitude (right) for all initially convectively unstable films, indicating that the instabilities are driven by surface tension gradients during their entire lifetime. In addition, the velocity magnitude decreases with decreasing initial solvent content (different colors). This is likely the result of the strong concentration dependency of the solution viscosity.

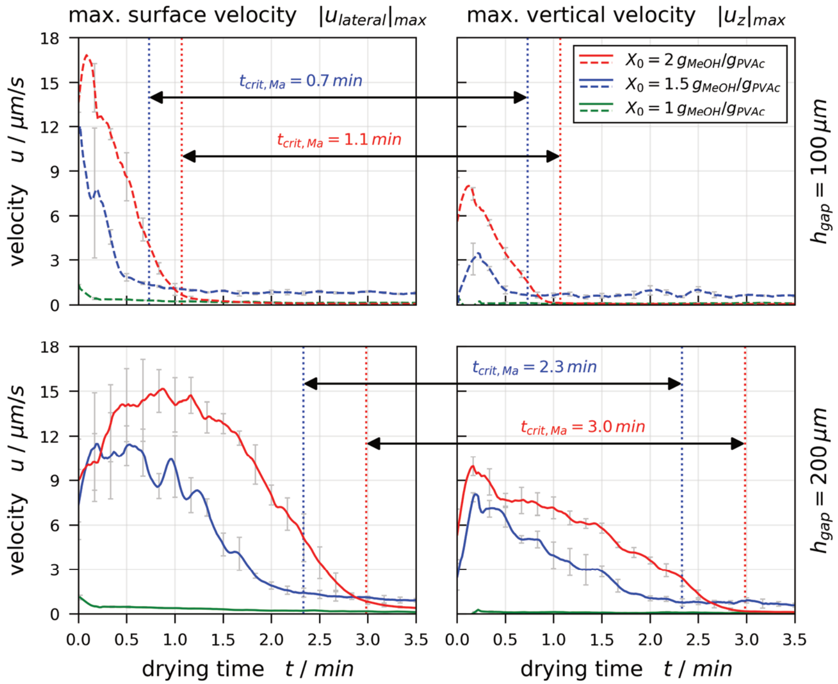

Figure 4.6: Transient evolution of lateral (left column) and vertical (right column) flow velocities, accounting for the highest decile fraction of 3D-µPTV derived tracer particle data in drying poly(vinyl acetate)-methanol films with varying initial solvent content X_0 (colors) and coating gap h_{gap} (plot rows).

4.1.2 Convection Cell Pattern and Size

From the velocity distributions of an initially unstable film, reported in detail in the last section, it was deduced that the convective instability has the form of vertical convection cells. This can be confirmed by extracting vertical cross sections of the velocity vector field from several initially unstable films shortly after the start of drying ($t = 10\ s$, Figure 4.7). It can be seen that the convective instability has the form of vertical cells. Therefore, it can be concluded that the observed instabilities are short-scale Bénard-Marangoni convection cells. In addition, the vertical cross sections indicate that the convection cells are more regular in drying films with $X_0 = 2\ g_{MeOH}/g_{PVAc}$ (right column).

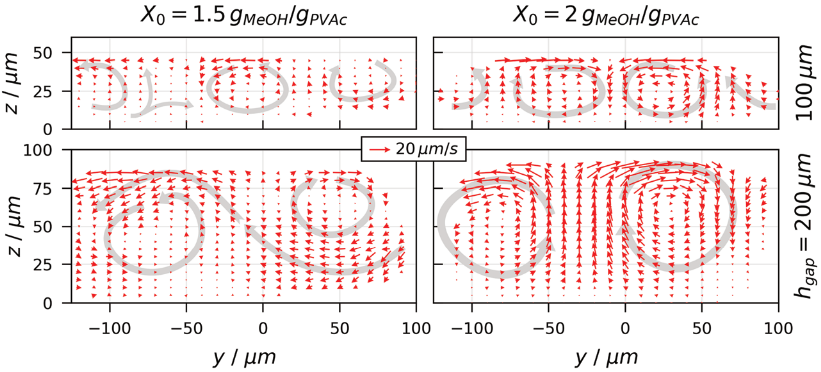

Figure 4.7: Vertical cross section of the velocity field in drying poly(vinyl acetate) films at early stages of drying ($t = 10\ s$) under variation of the initial solvent load (columns) and initial coating gap $h_{gap} = 100$ and $200\ \mu m$ (rows, resulting in a wet film thickness of ≈ 45 and $90\ \mu m$, respectively). The red arrows indicate velocity data interpolated from discrete tracer particle data derived by 3D-μPTV and transferred to a regular grid for better visualization. The grey arrows qualitatively denote the flow directions.

Figure 4.8 shows the top-view of several initially unstable drying films at $t = 10\ s$. The colored background indicates the height-averaged vertical velocities, with green areas denoting an upward flow and brown areas denoting a downward flow. In addition, the lateral surface velocities are given as black arrows.

The vertical cross sections, as well as the top view, clearly show that the lateral surface velocity is directed away from areas with upward flow and towards areas with downward flow. The vertical cross sections confirm the lateral backflow in the lower third of the films assessed from the velocity distributions and the top-view confirms that the lateral cell pattern is less regular for $X_0 = 1.5\ g_{MeOH}/g_{PVAc}$ while showing close to circular convection cells for $X_0 = 2\ g_{MeOH}/g_{PVAc}$.

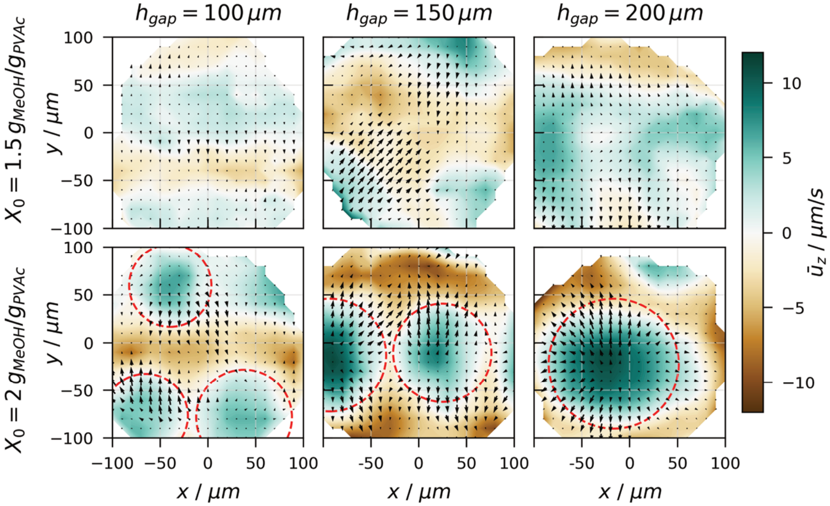

Figure 4.8: Top-view of the flow field in initially convectively unstable poly(vinyl acetate)-methanol films at early stages of drying ($t = 10\ s$). The colored background denotes the height-averaged vertical velocity. The black arrows denote the lateral surface flow. The discrete tracer data were interpolated on a regular grid for better visualization. The red circles were fitted to the white areas, indicating regions with zero height-averaged vertical flow velocity ($\bar{u}_z = 0\ \mu m/s$), as a measure for the lateral cell size. (Tönsmann et al. 2021c)[16]

In order to extract the lateral cell sizes of the regular cells, observed in films with $X_0 = 2\ g_{MeOH}/g_{PVAc}$, circles were matched to white areas of the top view, denoting areas of zero height-averaged velocity ($\bar{u}_z = 0\ \mu m/s$, red circles in Figure 4.8). Note that this approach differs from results published by other authors, who averaged the center-to-center (dark green spots) or edge-to-edge (dark brown edges) distance of multiple convection cells over a large lateral field-of-view. As the lateral observation volume of 3D-μPTV is limited (e.g. lower left plot shows only one cell without defined boundaries), this approach is unfeasible for the presented results. The limited data on lateral cell size, extractable from the experiments, are plotted in Figure 4.9 over the normalized drying time $t/t_{crit,Ma}$. It can be seen that the lateral cell size increases with increasing initial film thickness (coating gap) and stays close to constant during the course of drying. An increasing cell size with increasing initial film thickness is in line with classic stability analyses (e.g. Pearson 1958, see section 1.2.1), because, as a result from linear stability analysis, the least stable mode is always associated with a specific constant dimensionless wavelength $\lambda/h \sim d_{cells}/h \approx const.$ (minimum in Figure 1.7 black line). Following this argumentation, the film shrinkage during drying should also result in a decrease of the lateral cell size d_{cells}, which is, however, not supported by the results. Instead, the observation of a constant lateral cell size during drying is in good qualitative agreement with results from Bassou and Rharbi (2009), who reported lateral convection cell sizes in drying polyisobutylene-toluene solutions (see section 1.2.3). This underlines the limitations of classic linear stability analyses, which were derived for stationary states only.

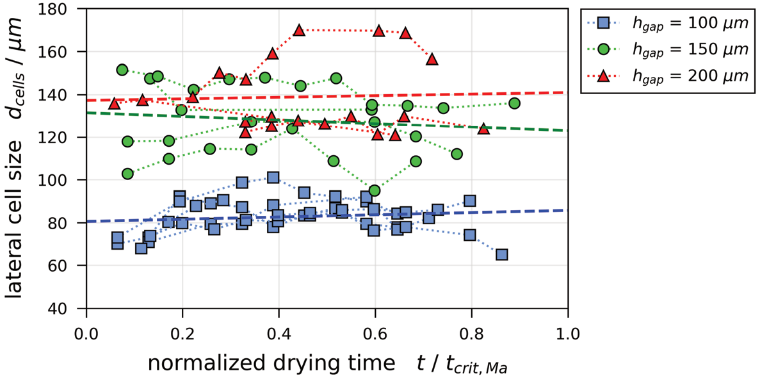

Figure 4.9: Lateral convection cell size from poly(vinyl acetate)-methanol fims with an initial solvent load of $X_0 = 2\ g_{PVAc}/g_{MeOH}$ and different coating gaps. Each marker set denotes experimental results of a single cell (see Figure 4.8, red circles) and the dashed lines represent the respective linear fits. (Tönsmann et al. 2021c)[16]

4.2 Validation of Simulated Concentration Profiles

In order to gain access to transient concentration profiles for Marangoni number calculation, all drying experiments which were performed using the 3D-µPTV setup (section 4.1) were repeated measuring the transient vertical concentration profiles with IMRS (sections 1.1.1 and 3.3). One-dimensional isothermal drying simulations (sections 1.1.2 and 3.4) were performed for each of the experiments using the experimentally derived dry film thickness and the initial solvent load X_0 as fixed input parameters. Since ambient drying conditions without forced convective airflow were employed, the mass transfer coefficient was unknown. Therefore, the corresponding heat transfer coefficient (linked by Lewis' law) as input for the simulations was adapted to $\alpha_{top} = 1.4\, W/(m^2K)$.

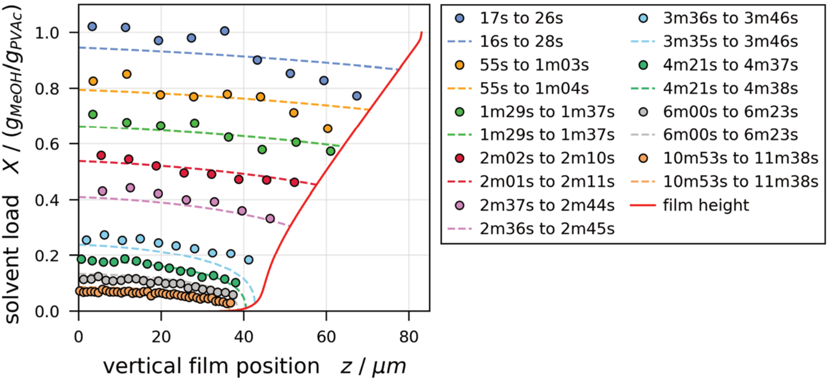

Figure 4.10: Comparison of transient vertical concentration profiles in a PVAc-MeOH film ($X_0 = 1\, g_{MeOH}/g_{PVAc}$ and $h_{gap} = 200\, \mu m$), drying at $T_{substrate} = 20\, °C$. Markers denote experimental results from IMRS experiments and lines denote the simulation results. The simulation was performed with the initial film thickness $h_0 = 83\, \mu m$ as well as an effective upper heat-transfer coefficient $\alpha_{top} = 1.4\, W/(m^2K)$. The corresponding 3D-µPTV drying experiment was convectively stable during the entire drying time. (Tönsmann et al. 2021b)[16]

Figure 4.10 and Figure 4.11 show the resulting comparison of vertical concentration profiles and transient film height, respectively, for a drying film with $X_0 = 1\, g_{MeOH}/g_{PVAc}$ and $h_{gap} = 200\, \mu m$ ($h_0 = 83\, \mu m$), which exhibited no convective instabilities during 3D-µPTV experiments (Figure 4.1 left and Figure 4.2). The drying simulation is in good agreement with the experimental values. It has to be noted that IMRS experiments are performed via vertical scanning. The measured vertical concentration profiles therefore do not occur at a fixed drying time but at a given range of drying time starting at the bottom of the film. This has been accounted for in the simulation evaluation. The vertical scanning implies that the presented vertical concentration profiles are likely to show a more pronounced curvature because drying progresses during acquisition. Nevertheless, it can be seen from the simulated concentration profiles in Figure 4.10 that they are close to linear. This observation justifies the use of the linearized surface tension gradient in the definition of the short-scale Marangoni numbers (equations (3.2) and (3.3)). This is likely to change for an increasing drying rate.

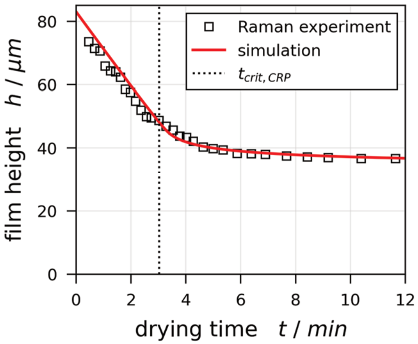

Figure 4.11: Comparison of the transient film height from IMRS experiment (PVAc-MeOH, $X_0 = 1\ g_{MeOH}/g_{PVAc}$, $h_{gap} = 200\ \mu m$, $T_{substrate} = 20\ °C$) and drying simulation ($h_0 = 83\ \mu m$, $\alpha_{top} = 1.4\ W/(m^2K)$) as reported in Figure 4.10. The vertical dotted line denotes the approximate end of the constant rate period derived from the simulation results. (Tönsmann et al. 2021b)[16]

The same comparison for a film with $X_0 = 1.5\ g_{MeOH}/g_{PVAc}$ and $h_{gap} = 200\ \mu m$ ($h_0 = 78\ \mu m$), which initially exhibited short-scale Marangoni convection cells until $t_{crit,Ma} = 144\ s$ during 3D-µPTV measurements (see Figure 4.1 and Figure 4.3), is shown in Figure 4.12 and Figure 4.13. The IMRS and simulation results are again in good agreement, even though the simulation model is one-dimensional whereas the drying film exhibits three-dimensional convection cells during 3D-µPTV experiments under close to identical drying conditions.

The 1D simulation fits well because the mass transfer resistance is in the gas phase during the constant rate period.

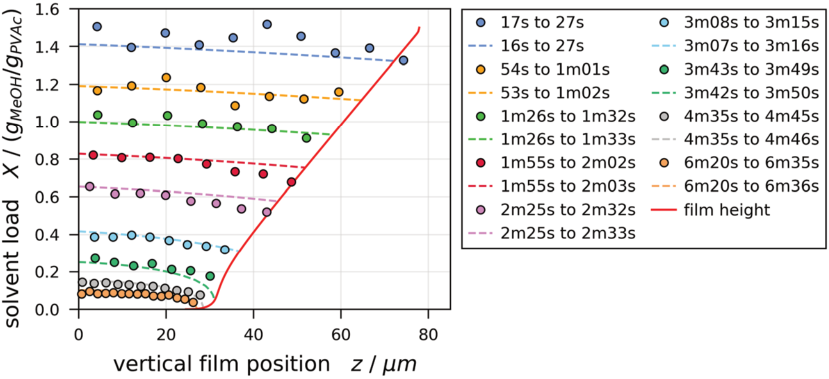

Figure 4.12: Comparison of transient vertical concentration profiles in a PVAc-MeOH film ($X_0 = 1.5\ g_{MeOH}/g_{PVAc}$ and $h_{gap} = 200\ \mu m$), drying at $T_{substrate} = 20\ °C$. Markers denote experimental results from IMRS experiments and lines denote the simulation results. The simulation was performed with the initial film thickness $h_0 = 78\ \mu m$ as well as an effective upper heat-transfer coefficient $\alpha_{top} = 1.5\ W/(m^2K)$. The corresponding 3D-µPTV drying experiment exhibited initial convective instabilities in the form of short-scale convection cells. (Tönsmann et al. 2021b)[16]

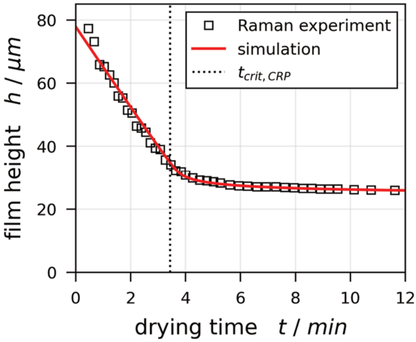

Figure 4.13: Comparison of the transient film height from IMRS experiment (PVAc-MeOH, $X_0 = 1.5\ g_{MeOH}/g_{PVAc}$, $h_{gap} = 200\ \mu m$, $T_{substrate} = 20\ °C$) and drying simulation ($h_0 = 78\ \mu m$, $\alpha_{top} = 1.5\ W/(m^2K)$) as reported in Figure 4.12. The vertical dotted line denotes the approximate end of the constant rate period derived from the simulation results. (Tönsmann et al. 2021b)[16]

The good agreement between experimental results and isothermal drying simulation holds true for all conducted drying experiments measured with IMRS. The best-matching heat transfer coefficient averaged over all experiments is $\alpha_{top} = 1.4 \pm 0.2\ W/(m^2K)$. Within the given uncertainty, no trend was found between the results from convectively stable films and films initially exhibiting short-scale Marangoni cells. Consequently, the 1D simulation model can be used to calculate accurate transient dimensionless numbers despite 3D short-scale instabilities.

4.3 Comparability of 3D-µPTV Experimental Results with Numerical Simulations

The only property, allowing a direct comparison between numerical drying simulations and 3D-µPTV results, is the transiently shrinking film height. It was extracted from 3D-µPTV results by deriving upper envelope curves denoting the largest vertical particle positions, as shown in section 4.1.1. Due to the impact of the film's refractive index on 3D-µPTV evaluation, the resulting transient film heights are given in Figure 4.14 as grey-green areas. The true drying curves should align with the lower bounds of these areas at the onset of drying $t = 0\ s$ and with the upper bounds when the films are dry.

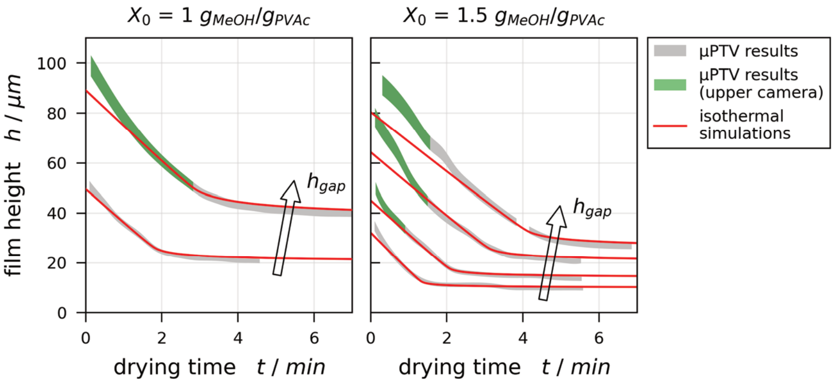

Figure 4.14: Comparison of the transient film height during drying of PVAc-MeOH films derived by 3D-µPTV experiments and by best matching drying simulations, pinned to the experimentally derived dry film thickness. *Data previously published in Tönsmann et al. (2021c, 2021b)*[16].

Isothermal drying simulations matching the 3D-µPTV results were found as described in section 4.2, using the dry film thickness and initial solvent load X_0 as fixed input for the simulations and varying α_{top} until the simulated drying curve coincided best with the grey area of uncertainty from 3D-µPTV experiments. In Figure 4.14, it can be seen that the drying curves of 3D-µPTV experiments and simulations coincide well for a large range of the drying time. There is, however, a noticeable systematic discrepancy for larger film thicknesses and early drying times. This discrepancy occurs almost exclusively when the 3D-µPTV enveloping curve was derived from tracer particle positions recorded with the camera having the upmost focus plane position (green areas).

Several reasons may account for this observation: *First*, the assumption that the tracer particles during 3D-µPTV experiments are distributed over the entire film height may be false. This would affect the extracted enveloping drying curves. *Second*, while IMRS measurements require immersion oil between the lens and the bottom of the glass substrate, no immersion medium was used during 3D-µPTV experiments (see Figure 3.1). This might result in a lateral temperature difference between the portion of the film above the lens opening and the temperature-controlled metallic support, and therefore might induce a long-scale lateral Marangoni flow away from the opening, which the one-dimensional simulation cannot account for. *Third*, the simplified procedure to stitch the individual observation volumes during 3D-µPTV evaluation (section 2.3.3) may cause the systematic discrepancy between 1D simulated and experimentally derived drying curves. A detailed discussion addressing all of these possibilities is provided in Appendix C. It was found that the simplified stitching approach during 3D-µPTV evaluation can be assumed to be the sole cause for the discrepancy in 3D-µPTV-derived and simulated drying curves in Figure 4.14 and that the simulations are indeed a good quantitative representation of the drying experiments. The average effective heat transfer coefficient found from the best-matching drying simulations is $\alpha_{top} = 1.6 \pm 0.2\ W/(m^2K)$ with again no trend regarding the convective (in)stability. The value is slightly larger than the average value found from IMRS drying experiments and matching simulations thereof ($\alpha_{top} = 1.4 \pm 0.2\ W/(m^2K)$, see section 4.2). The small discrepancy occurs most likely due to small fluctuations in ambient drying conditions. Since the IMRS and the 3D-µPTV setup were located in different labs, different forms of lab air ventilation may account for this deviation. The covering box with open top was to minimize this impact. This does not affect the results, since the following calculations of dimensionless numbers are based on the drying simulation results directly matched to the 3D-µPTV experiments.

4.4 Non-isothermal Drying Simulations

All drying simulation results presented up to this point were isothermal, not accounting for evaporative cooling. Marangoni instabilities may also be induced by temperature gradients (see sections 1.2.1 and 1.2.2). In order to assess whether the short-scale Marangoni instability was thermally or solutally induced, additional non-isothermal simulations have been conducted. Since measuring vertical temperature profiles in thin liquid films in the order of 10 to $100\ \mu m$ film height is a challenging task, the non-isothermal simulations grant access to transient vertical temperature profiles. The non-isothermal simulation model accounts for thermal properties of the film and the glass substrate, as well as evaporative cooling (see section 3.4). It requires the heat transfer coefficient at the bottom of the glass substrate α_{bottom} as additional input. Due to the complex geometry of the gap between glass substrate, metallic substrate support and microscope lens (see Figure 3.1), a corresponding Nusselt correlation is not available. Therefore, a parameter variation using $\alpha_{bottom} = 25,\ 50,$ and $150\ W/(m^2K)$ was conducted. For each of the α_{bottom} values, the heat-transfer coefficient in the gas phase above the film α_{top} was again varied in steps of $0.1\ W/(m^2K)$ until a best match between the resulting drying curves and the matching 3D-µPTV experiments was found. Figure 4.15 shows exemplarily results of a non-isothermal simulation. In Figure 4.15 left, the black line denotes the drying curve of the isothermal drying simulation matching the 3D-µPTV experiment with $X_0 = 1.5\ g_{MeOH}/g_{PVAc}$ and $h_{gap} = 200\ \mu m$ as well as the drying curves of three matched non-isothermal simulations with different α_{bottom} values (different colors). The lines coincide perfectly, as intended. Figure 4.15 left also shows the resulting transient temperature at the bottom (dash-dotted colored lines) and at the free surface (dashed colored lines) of the drying film. It can be seen that the steady-state temperature during the constant-rate period significantly differs with different values of α_{bottom}. From the three values tested, the steady-state temperature during the constant rate period resulting from the non-isothermal drying simulation with $\alpha_{bottom} = 50\ W/(m^2K)$ (orange lines) is closest to the film temperature measured with thermal imaging, presented in Appendix C.2. Figure

4.15 right shows that the vertical temperature difference is close to identical for all three values of α_{bottom}, which is a an important value for determining the transient thermal Marangoni number. The impact will be further discussed in the next sections.

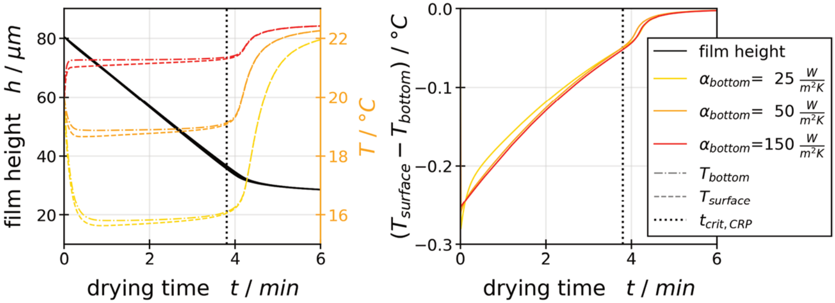

Figure 4.15: Impact of the lower heat transfer coefficient below the glass substrate α_{bottom} on the non-isothermal simulation results of a PVAc-MeOH film with $X_0 = 1.5\ g_{MeOH}/g_{PVAc}$ and $h_0 = 80\ \mu m$. Left: Transient film height and temperature at the bottom (colored dash-dotted lines) and surface (colored dashed lines) of the film. The black lines, denoting the film height, coincide perfectly for all α_{bottom} values and the isothermal simulation matched to 3D-µPTV experiments, as intended. Right: Vertical temperature difference being similar for all α_{bottom} values. (Tönsmann et al. 2021b)[16]

4.5 Marangoni Stability Threshold

Up to this point, the convective (in)stability of drying PVAc-MeOH films was investigated with 3D-µPTV experiments denoting the start and stop of convective instabilities in the form of a critical drying time $t_{crit,Ma}$ (section 4.2). The transient vertical concentration profiles as well as transient film thicknesses of the available isothermal simulation were validated using independent IMRS drying experiments (section 4.2). It was elaborated that the transient film height derived from drying simulations matches the one determined from the 3D-µPTV experiments with the dry film thickness and transient film height being a good quantitative representation of the 3D-µPTV drying experiments (section 4.3). Furthermore, non-isothermal drying simulations matching the 3D-µPTV experiments give access to experimentally inaccessible vertical temperature differences.

In the following, the 3D-µPTV and non-isothermal simulation results will be combined, allowing for a quantitative assessment of the conditions at the stability threshold $t_{crit,Ma}$.

4.5.1 Critical Initial Wet-Film Thickness

In Figure 4.16 left, the critical threshold time of convective instabilities $t_{crit,Ma}$ is plotted over the initial wet film thickness h_0, derived from the matching drying simulations. Initially convectively stable films are plotted with $t_{crit,Ma} = 0\ s$. It can be seen that the critical threshold time, denoting the end of convective instabilities, increases linearly with increasing initial wet film thickness. The linear fits (dashed lines) for different initial solvent loads intersect with $t_{crit,Ma} = 0\ s$ at $h_0(X_0 = 1.5\ g_{MeOH}/g_{PVAc}) \approx 27\ \mu m$ and $h_0(X_0 = 2\ g_{MeOH}/g_{PVAc}) \approx 15\ \mu m$, respectively, indicating a critical initial wet film thickness, which has to be exceeded for instabilities to occur. Figure 4.16 right shows the height-averaged solvent load at the stability threshold $\bar{X}_{crit,Ma} = \bar{X}(t_{crit,Ma})$. It was found that values of $\bar{X}_{crit,Ma}$ for thick films (highlighted with black arrows) are noticeably lower than $1\ g_{MeOH}/g_{PVAc}$, albeit the finding that films with an initial solvent load of $X_0 = 1\ g_{MeOH}/g_{PVAc}$ were convectively stable during the entire drying time. This implies a hysteresis between the onset of instabilities at the start of drying and the stop of instabilities during drying. This will be further discussed in section 4.5.3.

The threshold time for short-scale instabilities $t_{crit,Ma}$ was normalized with $t_{crit,CRP}$ indicating the end of the constant rate period of drying. The normalized threshold time $t_{crit,Ma}/t_{crit,CRP}$ for initially convectively instable films was found to be in the range of $0.2 - 0.7$, increasing with increasing initial film thickness. Clearly all instabilities ceased before the end of the constant rate period $t_{crit,CRP}$. The lowest found value for the local solvent load at the surface of the films was $X_{crit,Ma,surface} \geq 0.7\ g_{MeOH}/g_{PVAc}$, whereas the glass transition temperature is still below the drying temperature for a significantly lower methanol concentration ($T_g(X = 0.046\ g_{MeOH}/g_{PVAc}) = 15 \pm 6\ °C$, Schabel 2004a). This clearly shows that a possible glass transition, starting at the solvent depleted surface of the films, may only occur well after the convective instabilities have already stopped, and it is not the reason for convection cells to end. However, this may be different for other polymer systems (e.g. PMMA, $T_g \approx 105\ °C$, Merklein et al. 2021), when the glass transition temperature of the pure polymer significantly exceeds the drying temperature.

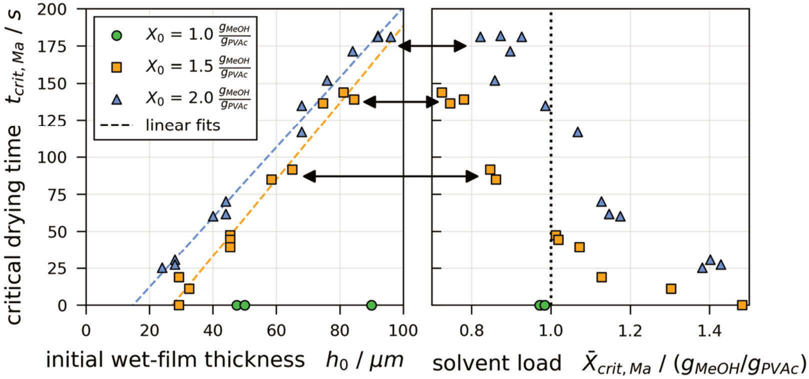

Figure 4.16: Combined results regarding the stability threshold of convective instabilities from 3D-µPTV experiments ($t_{crit,Ma}$) and matched drying simulations (h_0 (left) and $X_{crit,Ma}$ (right)). The black arrows denote experiment groups, which exhibited $X_{crit,Ma} < 1\ g_{MeOH}/g_{PVAc}$ despite the finding that films with $X_0 = 1\ g_{MeOH}/g_{PVAc}$ were convectively stable during the entire course of drying. (Tönsmann et al. 2021b)[16]

4.5.2 Transient Marangoni Numbers during Drying

The non-isothermal drying simulations matched to 3D-µPTV experiments and the concentration- and temperature-dependent material properties summarized in section 3.6 were used to calculate the transient thermal and solutal Marangoni numbers using equations (3.2) and (3.3), respectively. Figure 4.17 exemplarily shows the course of Marangoni numbers during drying. The colored lines are based on the simulation results using $\alpha_{bottom} = 50\ W/(m^2K)$, whereas the colored areas denote the uncertainty accounting for α_{bottom} variation as well as using not the height averaged solution properties in the denominator of equations (3.2) and (3.3) but local values at the bottom and surface of the film. The thermal Marangoni number (red) is two orders of magnitude smaller than the solutal Marangoni number. In addition, the thermal values calculated here are at least three orders of magnitude smaller than any reported critical values found in literature (see chapter 1). This clearly proves that the convective instabilities reported in this chapter are dominated by solutal effects on the surface tension. Hence, the following discussion will be limited to the solutal values. In Figure 4.17, it can also be seen that the solutal Marangoni number exhibits a local maximum at the onset of drying. Thereafter, Ma_s decreases and the critical solutal Marangoni number was extracted at the threshold time found from 3D-µPTV experiments $Ma_{s,crit} = Ma_s(t_{crit,Ma})$. Nearing the end of the constant rate period, Ma_s strongly increases due to the strong decrease of the diffusion coefficient with decreasing residual solvent content. In this regime, the experimentally validated viscosity values are not experimentally validated (see Figure 3.2). The calculated values of the green dashed portion of Ma_s were therefore not considered for further analysis. A qualitative discussion regarding the viscosity at low solvent concentrations is provided in Appendix B.9. The discussed findings were found qualitatively for all non-isothermal simulations. The discrete values of Ma_s at the local maximum as well as at $Ma_{s,crit}$, denoted by black markers, will be used for further analysis in the following subsection.

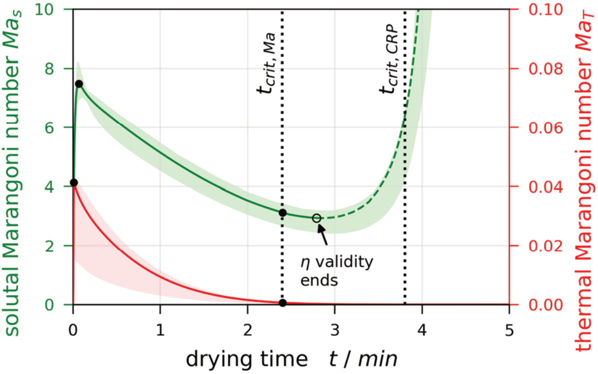

Figure 4.17: Transient course of the thermal (red) and solutal (green) Marangoni numbers, calculated from non-isothermal simulation matched to a 3D-µPTV experiment ($X_0 = 1.5\ g_{MeOH}/g_{PVAc}$,$h_{gap} = 200\ \mu m$, $h_{dry} = 25\ \mu m$, $\alpha_{bottom} = 50\ W/(m^2K)$). The colored areas denote the uncertainty due to α_{bottom} variation, as well as the choice of reference concentration and temperature for η, κ, and $\delta_{s,p}$ calculation. The dashed portion of Ma_s is deemed uncertain due to viscosity data extrapolation. (Tönsmann et al. 2021b)[16]

4.5.3 Critical Marangoni Numbers

Several extracted properties are summarized in Table 4.1, grouped with regards to initial (in)stability ($t \approx 0\ s$) and at the stability threshold $t_{crit,Ma}$ for initially convectively unstable films. The values of the found critical Marangoni numbers (last column) are significantly smaller than theoretically derived values found in literature (see section 1.2.3). This is most likely a result of simplifications made during the theoretical analyses. The values of the diffusion coefficient calculated in this work vary in the range of $(2.6 - 9.0) \cdot 10^{-10}\ m^2/s$, whereas in past theoretic work $\delta_{s,p}$ was assumed constant (e.g. Trouette et al. 2012). Comparing the solutal and thermal Marangoni numbers (last row) calculated in this dissertation confirms that the solutal Marangoni number Ma_s is two to three orders of magnitude larger than the thermal Marangoni number Ma_T, whereas many literature sources suggests that the critical values should be in the same order of magnitude (e.g. McTaggart 1983; Touazi et al. 2010; Trouette et al. 2012). Therefore, it can be concluded that the convective instability reported in this chapter in drying PVAc-MeOH films is dominated by solutal effects.

Table 4.1: Summary of selected properties regarding Marangoni instabilities calculated from non-isothermal simulations matched to 3D-µPTV experiments. The black circles in Figure 4.17 denote the source of the data.

Property	Unit	Entirely Stable ($t \approx 0\ s$)	Initially Unstable ($t \approx 0\ s$)	Stability Threshold ($t_{crit,Ma}$)
v_{int}	$\mu m/s$	$0.2 - 0.3$	$0.2 - 0.3$	$0.2 - 0.3$
Ma_T	10^{-3}	$2.4 - 10.0$	$7.0 - 206.6$	$0.6 - 3.3$
$\delta_{s,p}(\bar{X},\bar{T})$	$10^{-10}\ m^2/s$	$4.1 - 6.9$	$6.8 - 9.0$	$2.6 - 6.5$
$\boldsymbol{Ma_s}$	$-$	$\mathbf{1.1 - 10.3}$	$\mathbf{0.8 - 11.5}$	$\mathbf{0.4 - 3.7}$
Pe	10^{-2}	$1.0 - 5.5$	$0.6 - 2.6$	$0.6 - 3.8$
Sc	10^{6}	$0.7 - 6.6$	$0.2 - 0.8$	$0.9 - 31.6$
$\boldsymbol{Ma_s/Ma_T}$	$\mathbf{10^{2}}$	$\mathbf{1.9 - 10.8}$	$\mathbf{0.6 - 1.9}$	$\mathbf{2.4 - 49.3}$

When comparing the extracted values of Ma_s from entirely stable with initially unstable films, there is no distinction in the value range, indicating that a unified constant critical solutal Marangoni number accounting for all experimental results was not found. Instead, the critical solutal Marangoni number has to be regarded as a function of the Péclet number $Pe = v_{int}h/\delta_{s,p}$ (with v_{int} being the film shrinkage velocity) and the Schmidt number $Sc = \eta/\delta_{s,p}$, as found by the theoretic analysis presented by Trouette et al. (2012). Figure 4.18 depicts the values of the solutal Marangoni number over Pe (left) and Sc (right), respectively. The green markers denote the maximum of $Ma_s(t \approx 0\ s)$ from entirely convectively stable films, whereas the red markers denote the maximum of $Ma_s(t \approx 0\ s)$ at the beginning of drying from initially convectively unstable films. The yellow markers denote values at the stability threshold $Ma_s\left(t_{crit,Ma}\right)$ from the initially unstable films. Figure 4.18 left shows that a critical solutal Marangoni number increasing with Pe (dashed blue line) allows for the distinction between initially unstable films (red markers) and the values at the stability threshold as well as from the initially stable films (green and yellow markers). However, the blue circles highlight values where the initial solutal Marangoni number of entirely stable films is larger than the threshold values from initially unstable films at comparable Péclet numbers. These values can be distinguished regarding the corresponding Schmidt number, as seen in Figure 4.18 right.

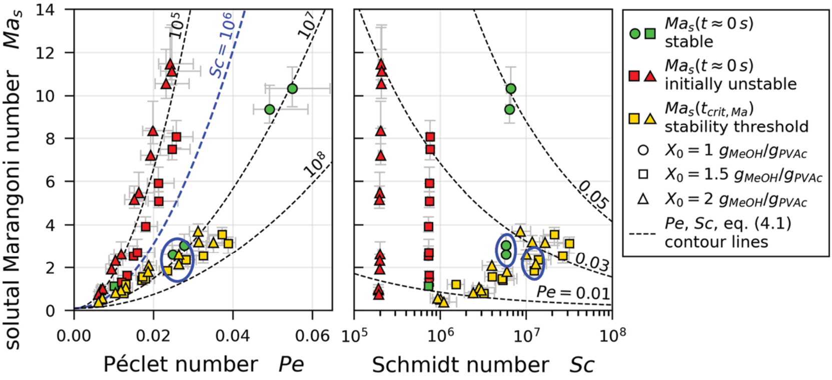

Figure 4.18: Solutal Marangoni numbers derived from drying simulations matched to 3D-µPTV experiments plotted over the Péclet number (left) and the Schmidt number (right). (Tönsmann et al. 2021b)[16]

An empiric power-law correlation $Ma_s = f(Pe, Sc)$ was found in this work, accounting for the impact of the Péclet and Schmidt numbers on the critical solutal Marangoni number:

$$Ma_{s,crit} = 7.5 \cdot 10^5 \cdot Pe^2 \cdot Sc^{-1/3} + 0.1 \tag{4.1}$$

This dimensionless correlation qualitatively follows the trends found from the theoretic model of Trouette et al. (2012). Contour lines of this correlation are plotted in Figure 4.18 as dashed lines.

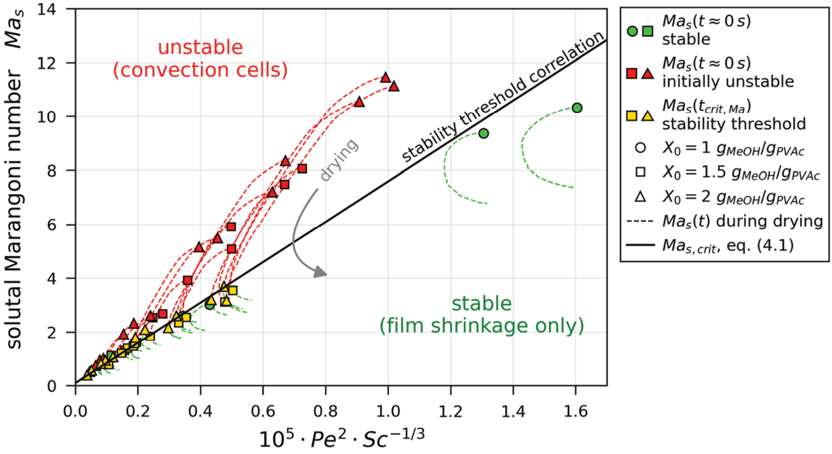

Figure 4.19: Solutal Marangoni numbers extracted from non-isothermal simulations (matched to 3D-µPTV experiments) and plotted over the combined parameter $Pe^2 \cdot Sc^{-1/3}$ from the found power-law correlation equation (4.1). The correlation, denoting a functional relation between the critical solutal Marangoni number and the Péclet and Schmidt numbers can account for the initial (in)stability as well as the stability threshold during drying. (Tönsmann et al. 2021b)[16]

The comparison becomes clearer when plotting the found values of the solutal Marangoni number over the combined parameter $Pe^2 \cdot Sc^{-1/3}$, as done in Figure 4.19. The transient course of Ma_s is given as dashed lines in addition to the discrete values. The newly found correlation equation (4.1) clearly separates convectively unstable regions (red markers and curves) from convectively stable regions (green markers and curves). The values extracted at the stability threshold during drying (yellow markers) coincide well with the correlation with an average deviation of 9.0 %. It has to be noted that the small intercept of 0.1 in the proposed correlation is supported by the found $Ma_{s,crit}$ values. In addition, considering the limiting value of $Pe^2 \cdot Sc^{-1/3} \rightarrow 0$ would imply either an infinitely large viscosity $\eta \rightarrow \infty$ or a drying velocity approaching zero $v_{int} \rightarrow 0$. A correlation with zero intercept would imply that films with any of these limiting cases would be exactly at the stability threshold, which is unlikely to be correct. Therefore, the introduction of the small intercept value of 0.1 in the correlation of this work appears reasonable.

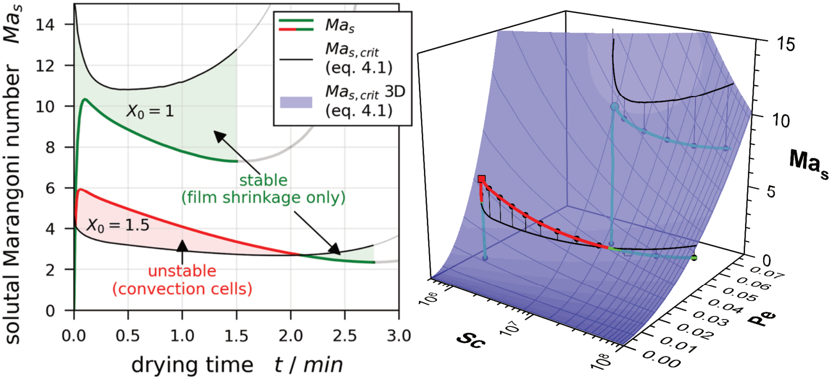

Figure 4.20: Transient solutal Marangoni number during drying of two selected films, one being entirely stable and one initially exhibiting Bénard-Marangoni convection cells. Ma_s values from the stable film reside entirely below the transient critical threshold $Ma_{s,crit}$ from correlation equation (4.1), whereas Ma_s from the initially unstable film undercuts the critical value during drying at $t_{crit,Ma}$. Left: Plotted over drying time. Right: Plotted over Pe and Sc. The black markers and vertical anchor lines denote $\Delta t = 15\ s$ steps. (Tönsmann et al. 2021b)[16]

The transient course of the solutal Marangoni number during drying is exemplarily shown in Figure 4.20 for two selected experiments, one being entirely stable and one being initially convectively unstable. The colored lines indicate the transient solutal Marangoni number, whereas the black lines denote the corresponding transient critical solutal Marangoni number, changing with Pe and Sc during drying. The Ma_s values from the entirely stable film resides below $Ma_{s,crit}$ during the entire course of drying, whereas the initially convectively unstable film undercuts $Ma_{s,crit}$ during drying. It can be concluded that the found correlation unifies the initial (in)stability as well as the stop of convection cells during drying. The dependence of $Ma_{s,crit}$ on the Péclet and Schmidt numbers also explains the alleged hysteresis found in Figure 4.16. This finding confirms the research hypothesis that the onset and stop of convective instabilities can be described with a unified critical Marangoni number, but only when accounting for the dependency on the Péclet and Schmidt numbers.

4.5.4 Findings in Dimensional Properties

In order to gain a better understanding of the implications of the found correlation, it can be converted back to dimensional properties. Since all material properties are changing during drying, an isolated discussion of individual material properties may be misleading (see Appendix D.1). Therefore, it is better to utilize the drying simulation results for further analysis. Figure 4.21 shows the duration of short-scale Marangoni instabilities in the form of the critical drying time $t_{crit,Ma}$ over the initial film thickness. The colored markers are experimental results already presented and discussed in section 4.5.1. The empty markers denote the calculated data from the drying simulations matched to the experimental results in combination with the correlation equation (4.1). The average and standard deviation between experimentally derived and simulated $t_{crit,Ma}$ is $0.7 \pm 10.9\ s$, showing a moderate distribution but a good representation of the general trends: From left to right the initial solvent content increases and so does the duration of the instability. It can also be seen that an increase in initial film thickness increases the occurrence and duration of the instability, as already discussed in section 4.5.1. A variation of the drying speed is beyond the experimental scope of this work. However, the combination of non-isothermal drying simulations and the critical solutal Marangoni number correlation allows for a prediction of the impact of increased drying rates. Therefore, a parameter variation was conducted with $\alpha_{top} = 1.5$, 1.7, 2.0, and $5.0\ W/(m^2K)$. The resulting instability duration is given in Figure 4.21 as lines. It can be seen that an increase in drying rate, represented by α_{top}, predicts a shorter duration of the instability. For an initial solvent content of $X_0 = 1.0\ g_{MeOH}/g_{PVAc}$, the instability ceases entirely when increasing α_{top} from 1.5 to $1.7\ W/(m^2K)$, whereas for $X_0 = 1.5$ and $2.0\ W/(m^2K)$ the instability ceases between 2.0 and $5.0\ W/(m^2K)$. This implies that an increase in drying speed results in a more stable film, but has yet to be validated experimentally in future work. In addition, this trend may vary with different concentration dependency of the material properties from different material systems.

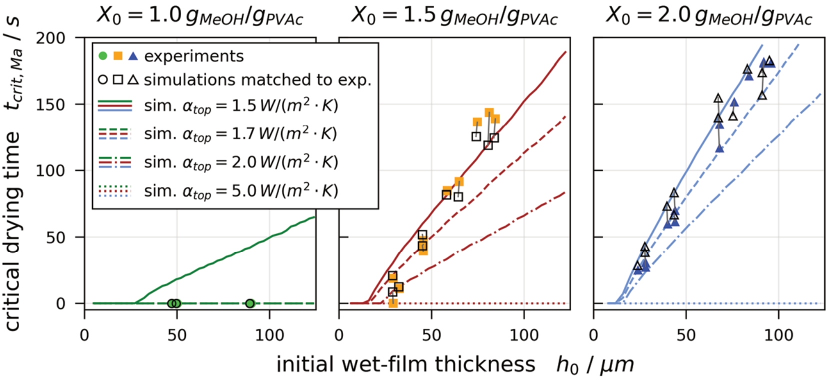

Figure 4.21: Instability duration $t_{crit,Ma}$ over the initial wet-film thickness h_0 from 3D-µPTV experiments, and drying simulations in combination with correlation equation (4.1). The non-isothermal simulations were conducted with $\alpha_{bottom} = 50\, W/(m^2K)$ under variation of the initial film thickness and the drying speed in the form of α_{top} (section 4.4).

4.6 Additional Considerations

The non-isothermal simulation in combination with concentration- and temperature-dependent material properties allows the calculation of several additional relevant dimensionless numbers. The Bond number (equation (3.1)) was found to be $1.1 \cdot 10^{-5} \leq Bo \leq 3.3 \cdot 10^{-3} \ll 1$ for all experiments presented in this chapter and decreases during drying. This confirms in hindsight that the found convective instabilities are not buoyancy induced Rayleigh-Bénard convection, but surface tension induced Marangoni convection cells. This is in line with the already discussed finding that the largest flow velocity occurs laterally (see section 4.1.1).

Regarding possible surface deformations and perturbation leveling, the capillary length (equation (1.2)) was found to be $1.6\, mm < l_{capillary} < 1.9\, mm$, whereas the lateral length scale of the observed convection cells was significantly smaller

($d_{cells} \approx 80$ to $140\ \mu m$, see Figure 4.9). This implies that the leveling mechanism due to capillarity may be relevant. In line with the finding that solutal effects are dominating, the dimensionless Capillary number was calculated using equation (3.6). It was found to be $6 \cdot 10^{-5} < Ca < 1.6 \cdot 10^{-3}$ for $0\,s \leq t \leq t_{crit,Ma}$. The very small upper limit implies that surface deformations during the convective instability are unlikely to occur. After $t_{crit,Ma}$ the Capillary number further increases up to $\widehat{Ca} < 2.8 \cdot 10^{-2}$ due to the continuous viscosity increase. It has to be noted that the latter limit was calculated by extrapolating the viscosity data to lower solvent concentrations, which was not validated by experiments. The actual viscosity increase is likely to be even larger. This is discussed in Appendix B.9. Hence, all values calculated with the fit equation (3.10) extrapolated to lower methanol concentrations are denoted with either $\widehat{\ }$ or $\widecheck{\ }$, indicating whether the true value is likely to be larger or smaller, respectively.

According to De Gennes et al. (2010) the characteristic time constant for the leveling of capillary waves can be calculated using equation (3.8). Assuming a lateral length scale of $\lambda = 200\ \mu m$ (data in Figure 4.9 suggest $\lambda \leq 170\ \mu m$), the resulting characteristic leveling time is $\tau_{capillary}(0\ s \leq t \leq t_{crit,Ma}.) \leq 1.3 \cdot 10^{-2}\ s$ for all experiments presented in this chapter. It has to be noted that De Gennes et al. derived equation (3.8), assuming two-dimensional sinusoidal height perturbations and not 3D convection cell patterns as found in this work. Therefore, this assessment has to be regarded as qualitative. Nevertheless, it suggests that a surface deformation is unlikely while the convective instability is active. After reaching $t_{crit,Ma}$, the characteristic leveling time constant increases due to the continued film shrinkage and viscosity increase. At the end of the constant-rate period, an upper limit of $\hat{\tau}_{capillary} \leq 9.5\ s$ was assessed, using extrapolated values for the viscosity at low solvent concentrations. The actual value might be even larger.

In addition, $\tau_{capillary}$ strongly depends on the lateral length scale (λ^{-4}). Cavadini et al. (2013) found secondary surface deformations evolving during the drying of a PVAc-MeOH film ($X_0 = 2\ g_{MeOH}/g_{PVAc}$, $h_0 \approx 150\ \mu m$) on a temperature controlled substrate with a partial Teflon inlay (see Figure 1.9). The secondary deformations had a lateral length scale of $\approx 1\ mm$ and were later attributed to short-scale convective instabilities (Cavadini et al. 2015). While the drying conditions were slightly different (higher substrate temperature and faster drying), an implicit mechanism of surface deformations due to short-scale Marangoni instabilities may still be possible: It was clearly demonstrated in this dissertation that a lateral transport of the polymer during short-scale instabilities occurs ($u_{lateral} > 0$, see section 4.1). Therefore, it is a possibility that the lateral area density of the polymer is not uniform after the convective instability stops. The lateral characteristic length of such undulations may then be a multiple of the characteristic lateral wavelength of the short-scale instabilities. In addition, the viscosity further increases during drying even after $t_{crit,Ma}$ is reached. The characteristic timescale of capillary leveling at the end of the constant rate period, assuming $\lambda = 1\,mm$ and extrapolating the concentration-dependent viscosity values beyond the experimentally validated lower solvent concentration limit, results in $\hat{\tau}_{capillary}(\lambda = 1\,mm, t_{crit,CRP}) \leq 10\,min$. This implies that surface deformations may still occur, but they evolve after the short-scale Bénard-Marangoni convection has stopped, due to a possible inhomogeneous lateral polymer distribution induced by the earlier Marangoni convection. It would also explain the observation by Cavadini et al. (2013) that the secondary deformations occurred only after $\approx 40\,s$ of drying ($t_{crit,CRP} \approx 50\,s$). Regarding industrial film drying process design, these findings imply that surface deformations cannot be avoided by allowing for surface leveling at late stages of drying, since the leveling time significantly increases with increasing viscosity. Hence, short-scale Marangoni instabilities have to be avoided altogether in order to inhibit lateral polymer transport.

4.7 Summary

In this chapter, film drying experiments with poly(vinyl acetate)-methanol were investigated with 3D-µPTV, which allows the measurement of transient three-dimensional flow fields over the entire film height and drying time. It was found that films with an initial solvent content of $X_0 = 1\ g_{MeOH}/g_{PVAc}$ and an initial film thickness of $h_0 \leq 90\,\mu m$, drying at $T_{substrate} = 20\,°C$ and otherwise ambient conditions do not exhibit convective instabilities. Increasing the initial solvent load to $X_0 \geq 1.5\ g_{MeOH}/g_{PVAc}$ results in an initial convective instability in the form of short-scale Marangoni convection cells. The drying time at which the instability stops during drying $t_{crit,Ma}$ increases with increasing initial solvent load and increasing initial film thickness h_0. This demonstrates that 3D-µPTV is well suited to investigate convective instabilities in thin drying polymer films quantitatively. It was found that the lateral flow velocity at the surface of the films is larger than the vertical one, and that the overall flow velocity decreases with decreasing initial solvent content.

Furthermore, it was shown that 1D non-isothermal drying simulations can be used, despite the 3D short-scale instabilities, to derive transient Marangoni numbers during drying, based on realistic concentration- and temperature-dependent material properties. It was found that solutally induced Marangoni convection is dominating and that the onset and end of instabilities can be accounted for by a critical solutal Marangoni number, depending on the Péclet and Schmidt number, which confirms the first research hypothesis of this dissertation. Utilizing this correlation beyond the experimentally validated drying rates predicts a stabilizing effect of an increased drying rate.

Finally, an assessment of capillary wave leveling indicates that surface deformations are unlikely to occur during the convective instability, but may evolve after the instability stopped due to the lateral transport of polymer. This finding implies that in industrial process design the occurrence of short-scale Marangoni convection needs to be avoided altogether, since a leveling at later stages of drying is unlikely to occur due to the strong viscosity increase. A possible strategy would be to use a ternary polymer-solvent-solvent solution, such as PEG-methanol-water, where the surface tension of the pure solvents resides below and above the free surface energy of the pure polymer, respectively (Appendix B.8). With appropriate process design (e.g. drying air pre-loaded with solvent), it may be possible to ensure a drying path along a contour line of constant surface tension (e.g. dashed black line with $\sigma = 40\ mN/m$ in Figure A.17). Doing so would avoid solutally induced surface tension gradients and therefore short-scale convective instabilities.

5 Long-Scale Instabilities in Drying Polymer Films

In the previous chapter, short-scale Bénard-Marangoni convection cells have been investigated. As pointed out in section 1.1, several experimental conditions may induce additional lateral inhomogeneities in drying conditions. In section 1.2.1 (Figure 1.7) it was summarized that long-scale Marangoni instabilities are always associated with free surface deformations and have a lower critical Marangoni number than short-scale instabilities. For the limiting case of zero wavenumber $k = 0$ or infinite wavelength $\lambda \rightarrow \infty$, the film is always convectively unstable, if gravity wave leveling is neglected. Due to the leveling mechanisms of gravity waves, the stability of the film may increase, but the leveling affinity strongly decreases with increasing viscosity, as intrinsic for polymer film drying. Hence, the second research hypothesis is that long-scale Marangoni instabilities in drying polymer films, induced by laterally inhomogeneous drying conditions, have no stability limit. In order to test this hypothesis, film-drying experiments were conducted with half of the film partially covered as depicted in Figure 5.1.

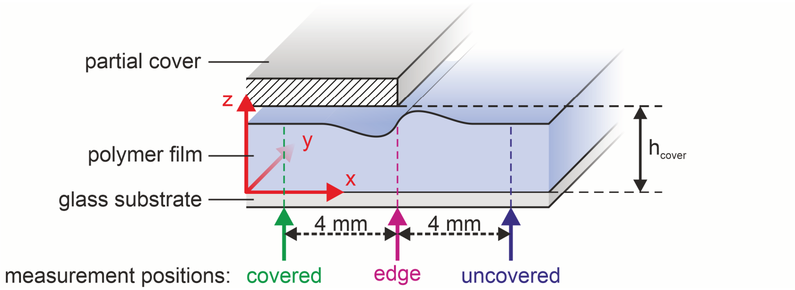

Figure 5.1: Schematic drawing of a partially covered drying experiment including the cover height h_{cover} and the different lateral measurement positions. 3D-µPTV measurements were conducted at the *edge* position (below the edge of the partial cover) and IMRS measurements were conducted at all three measurement positions.

The partial cover encloses an air gap between the surface of the film and the underside of the cover. Experiments with an initial solvent load identical to the uncovered experiments ($X_0 = 1$, 1.5, and 2 g_{MeOH}/g_{PVAc}) and a coating gap $h_{gap} = 100\,\mu m$ were conducted. In addition, two different cover distances $h_{cover} = 0.5$ and $1.5\,mm$ were investigated. The remaining conditions were identical to the uncovered drying experiments (section 3.1).

During drying, the air in the gap between film and partial cover starts to saturate with solvent vapor, resulting in a lower drying rate of the covered portion of the film due to the reduced concentration difference for mass transfer. The uncovered portion of the film dries faster, the solvent concentration decreases faster and therefore the surface tension increases faster during drying (see Figure 3.6), compared to the covered portion of the film (for material systems with increasing surface tension during drying, as MeOH-PVAc). Therefore, a lateral long-scale Marangoni flow from the covered towards the uncovered area is expected. This was already shown in qualitative experiments reported by Cavadini et al. (2015).

Flow field measurements were conducted using the 3D-µPTV setup with an observation volume set to be below the edge of the partial cover (see Figure 5.1). In order to quantify the expected lateral surface tension gradient, IMRS measurements were conducted at a lateral measurement position below the edge of the partial cover, as well as at a position under the cover and in the uncovered portion of the film with a total lateral distance of 8 mm (4 mm left and right of the partial cover edge), as indicated in Figure 5.1. Note that the lateral positioning accuracy of the cover edge was approximately $\pm 0.5\,mm$.

First, the results from 3D-µPTV drying experiments are presented (section 5.1), followed by the corresponding IMRS drying experiments (section 5.2) and an assessment of the resulting lateral Marangoni numbers (section 5.3). Additional aspects regarding potential surface deformations are discussed in section 5.4.

5.1 Transient 3D Flow Fields

The three-dimensional tracer particle trajectories measured with 3D-µPTV in two partially covered drying films ($h_{gap} = 100\,\mu m$ and $h_{cover} = 1.5\,mm$) are depicted in Figure 5.2. At an initial solvent load of $X_0 = 1.5\ g_{MeOH}/g_{PVAc}$ (top), the flow field is governed by a lateral flow in x-direction, perpendicular to the cover edge. The corresponding transient vertical tracer particle positions are given in Figure 5.3.

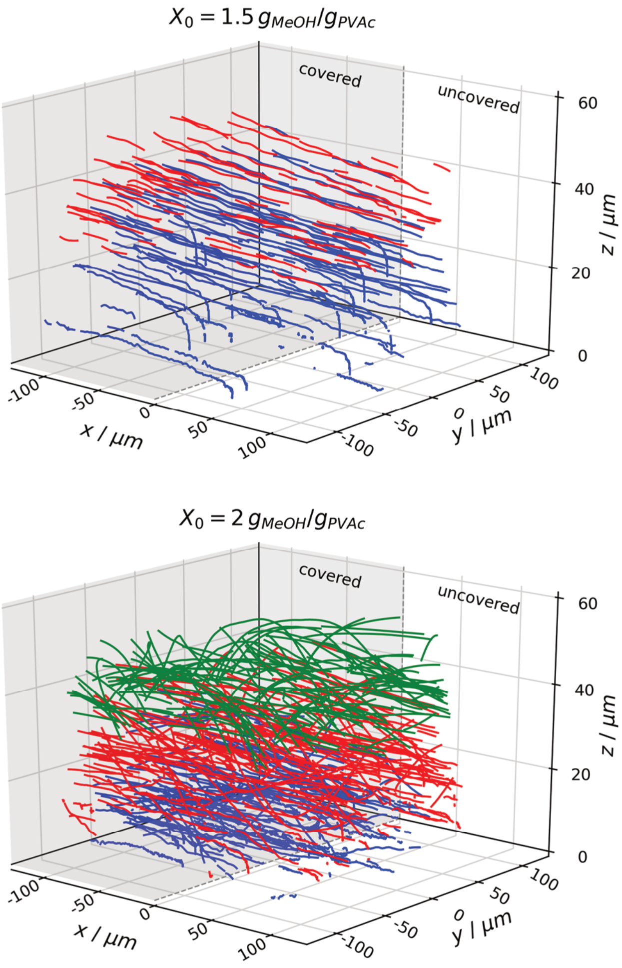

Figure 5.2: Three-dimensional tracer particle trajectories derived by 3D-μPTV in partially covered poly(vinyl acetate)-methanol films with a partial cover distance $h_{cover} = 1.5\ mm$. The different colors denote the three different recording cameras. The initial solvent load was $X_0 = 1.5\ g_{MeOH}/g_{PVAc}$ (top) and $2\ g_{MeOH}/g_{PVAc}$ (bottom).

In the first ≈ 3 minutes of drying, several short trajectories can be observed with noticeable interruptions. This is a result of the lateral flow since tracer particles continuously enter and exit the observation volume. In order to assess the duration and magnitude of the lateral flow, the velocity in x-direction is also shown as solid orange line in Figure 5.3. As expected, the lateral flow occurs in positive x-direction from the covered towards the uncovered area of the film due to a lateral surface tension gradient. The flow velocity decreases during drying until the lateral flow stops at a critical drying time $t_{crit,Ma,lateral} = 2.9\ min$. The corresponding experiments with identical coating gap and solvent load but without partial cover exhibited short-scale Bénard-Marangoni convection cells until $t_{crit,Ma,cells} = 44 \pm 4\ s$ (see section 4.1.1). In the experiment with the partially covered film, however, such short-scale instabilities were not observed. This can be seen by the lack of vertically upward moving particles and very low flow velocity magnitudes in vertical z- as well as lateral y-direction, perpendicular to the dominant lateral flow, given in Figure 5.3 as dash-dotted and dashed orange lines, respectively.

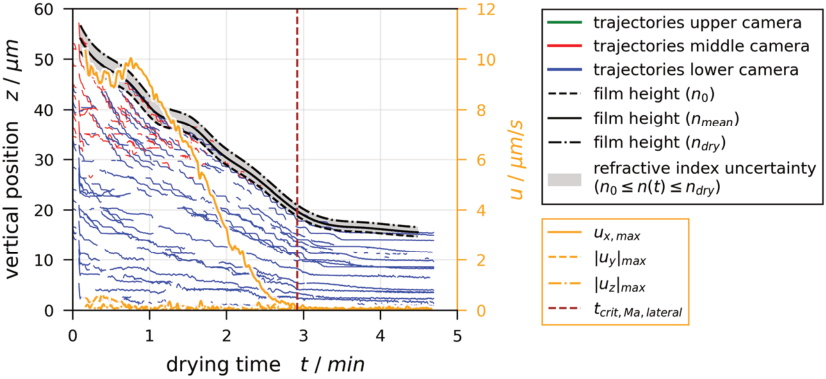

Figure 5.3: Transient vertical tracer particle positions and flow velocities in a partially covered drying poly(vinyl acetate)-methanol film with $X_0 = 1.5\ g_{MeOH}/g_{PVAc}$ and $h_{cover} = 1.5\ mm$. At early stages of drying, several short trajectories can be observed since particles laterally enter and exit the observation volume. The critical drying time denoting the end of the lateral flow $t_{crit,Ma,lateral}$ was extracted from the maximal flow velocity in x-direction $u_{x,max}$.

Increasing the initial solvent load to $X_0 = 2\ g_{MeOH}/g_{PVAc}$ results in perturbed particle trajectories (Figure 5.2 bottom). Many trajectories exhibit a lateral flow in x-direction but several trajectories, especially near the film surface (green) are curved and exhibit additional movement in y- and z-direction. The corresponding plot with transient vertical tracer particle positions is given in Figure 5.4. At early stage of drying, simultaneous upward and downward flow, similar to the short-scale instability in uncovered films, can be observed. At the same time, the lateral velocity $u_{x,max}$ (orange solid line) indicates a flow from the covered to the uncovered portion of the film. At $t_{crit,Ma,cells} = 81\ s$, the upward movement stops and the magnitude of the vertical velocity $|u_z|_{max}$ as well as the lateral velocity $|u_y|_{max}$ perpendicular to the main flow (orange dashed and dash-dotted lines) have decreased from $\approx 15\ \mu m/s$ to less than $1\ \mu m/s$. The dominant lateral flow in positive x-direction, however, decelerates but remains active until $t_{crit,Ma,lateral} = 3.8\ min$.

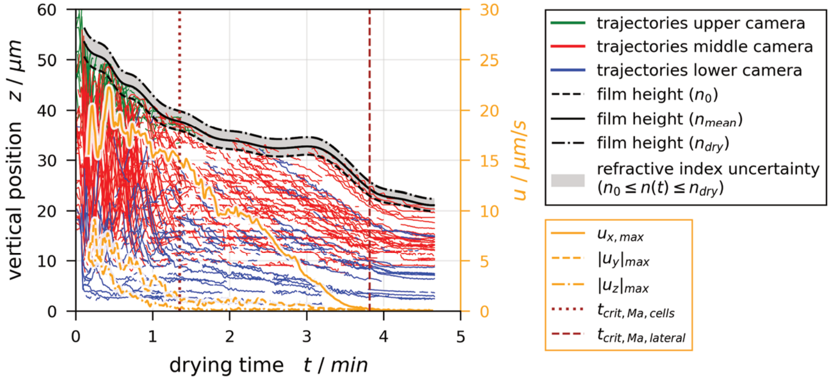

Figure 5.4: Transient vertical tracer particle positions and flow velocities in a partially covered drying poly(vinyl acetate)-methanol film with $X_0 = 2\ g_{MeOH}/g_{PVAc}$ and $h_{cover} = 1.5\ mm$. At early stages of drying, strong vertical particle movements indicate the existence of short-scale Marangoni convection cells. The critical drying time denoting the end of the lateral flow $t_{crit,Ma,lateral}$ was extracted from the maximal flow velocity in x-direction $u_{x,max}$ and the end of the short-scale convection cells $t_{crit,Ma,cells}$ was derived likewise from $|u_y|_{max}$ and $|u_z|_{max}$.

An additional observation can be made when considering the extracted drying curves, denoting the transient film height. For $X_0 = 1.5\ g_{MeOH}/g_{PVAc}$ (Figure

5.3), the drying curve shows some minor perturbations but generally exhibits the trend of one-dimensional film drying with a constant rate period, followed by a transition to a diffusion-limited regime. The film with $X_0 = 2\ g_{MeOH}/g_{PVAc}$ (Figure 5.4), however, exhibits an intermediate plateau-like constant film height during 2 and 3 minutes of drying time, differing significantly from one-dimensional film drying, followed by a short intermediate constant rate period and subsequent transition to the diffusion-limited regime.

The transient velocity distribution found in the partially covered drying films was derived similarly as in the uncovered films: At several characteristic drying times, the tracer particle velocities were averaged laterally and in slices of $\Delta z = 4\ \mu m$. In contrast to the uncovered experiments, a dominant lateral flow from the covered towards the uncovered area of the film was found. Consequently, the lateral velocity distribution is not given as $u_{lateral} = \sqrt{u_x^2 + u_y^2}$, as done for the uncovered films, but was calculated in x- and y-direction independently.

Figure 5.5 shows the results for $X_0 = 1.5\ g_{MeOH}/g_{PVAc}$ (same as Figure 5.2 top and Figure 5.3) exhibiting a dominant flow in positive x-direction but no perpendicular flow. It can be seen that the x-velocity profiles over the film height are perfectly linear with the highest velocity u_x occurring at the surface of the film ($u_x \leq 11\ \mu m/s$). This velocity profile is well known from fluids between two parallel walls moving with different velocities (Couette flow). The difference here is that there is no rigid upper wall but a free liquid surface with a Marangoni flow inducing the equivalent shear force[18] from covered towards uncovered area of the film. The slope of the u_x profile remains constant at early stages of drying (red and blue markers) followed by deceleration until at $t_{crit,Ma,lateral}$ the lateral flow in x-direction stops (green markers). The lateral flow perpendicular to the dominant Marangoni driven flow (y-direction) shows some mild initial perturbations over the film height (red blue and yellow markers) but is very small compared to the dominant x-flow ($|u_y| \leq 0.5\ \mu m/s$). The perturbations decrease

---

[18] The shear stress $\tau = \eta \cdot \partial u_x/\partial z$ from the lateral flow at early stages of drying can be estimated using the shear rate $\partial u_x/\partial z = 0.2\ s^{-1}$ from the x-velocity data in Figure 5.5 left at $t = 15\ s$, and the viscosity of the coating solution $\eta_0(X_0 = 1.5\ g_{MeOH}/g_{PVAc}, T = 20\ °C) = 0.44\ Pa\ s$ (equation (3.10)). This results in a shear stress of $\tau \approx 88\ mPa$.

with increasing drying time. A similar observation can be seen regarding the vertical velocity magnitude $|u_z|$ but at $t_{crit,Ma,lateral}$ it is slightly larger than $|u_y|$, indicating slow but noticeable film shrinkage.

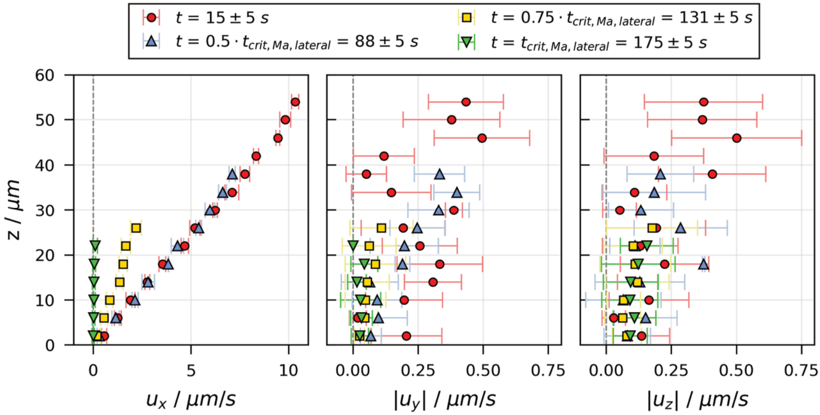

Figure 5.5: Velocity distribution in a poly(vinyl acetate)-methanol film ($X_0 = 1.5\ g_{MeOH}/g_{PVAc}$ and $h_{gap} = 100\ \mu m$) with a partial cover ($h_{cover} = 1.5\ mm$). The flow field is governed by a dominant lateral flow in x-direction from covered towards uncovered regions of the film (left) in the form of a Couette flow (linear velocity increase with vertical position).

The same evaluation for the film with $X_0 = 2\ g_{MeOH}/g_{PVAc}$ (same as Figure 5.2 bottom and Figure 5.4), which exhibited noticeable initial vertical particle movements in addition to a dominant flow from covered towards uncovered regions, is given in Figure 5.6. The x-velocity distribution shows again the Couette-like linear velocity profiles, but with a noticeably larger lateral surface velocity ($u_x \leq 19\ \mu m/s$). The y- and z-velocity distribution, however, differ noticeably. Instead of small perturbations, the velocity profiles initially exhibit the same shape as found for uncovered drying experiments with short-scale Marangoni convection cells (red and blue markers, see section 4.1.1): The lateral y-velocity perpendicular to the dominant lateral flow has its maximum at the film surface, a local minimum at approximately two-thirds of the film height and a local maximum at about one third of the film height. The vertical velocity magnitude shows a maximum at approximately two thirds of the film height. Considering only $|u_y|$ and $|u_z|$, the highest velocity occurs laterally at the film surface ($|u_y| \leq 10\ \mu m/s$)

but is noticeably smaller than the dominant x-velocity. As the velocity distribution in y- and z-direction strongly resembles the one from the experiments without partial cover (chapter 4), it is reasonable to assume that the same argumentation regarding Marangoni convection as the driving force, due to the highest velocity being tangential at the surface, also holds for the experiment presented here. After the convection cells stop at a critical drying time of $t_{crit,Ma,cells} = 81\ s$, the y- and z-velocities becomes very small ($< 1\ \mu m/s$, yellow and green markers) and appear to be uniform over the film height while the lateral flow continues (compare yellow markers).

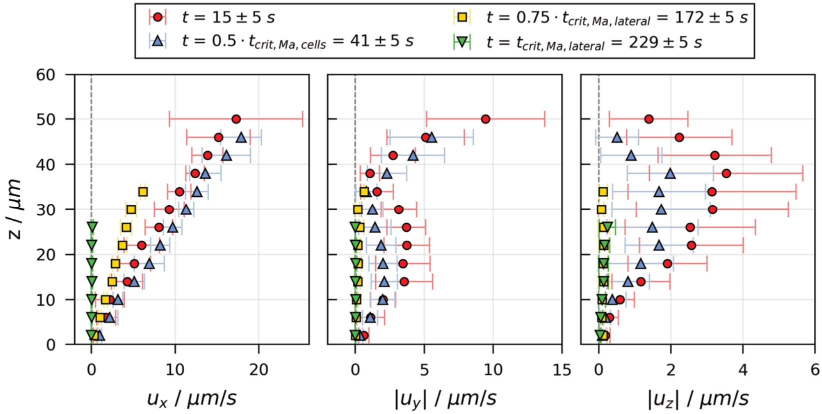

Figure 5.6: Velocity distribution in a poly(vinyl acetate)-methanol film ($X_0 = 2\ g_{MeOH}/g_{PVAc}$ and $h_{gap} = 100\ \mu m$) with a partial cover (cover height $h_{cover} = 1.5\ mm$). The flow field is governed by a dominant lateral flow in x-direction from covered towards uncovered regions of the film. In addition, short scale convection cells occur perpendicular to the dominant x-flow but stop at earlier drying times.

A total of six different parameter combinations ($X_0 = 1, 1.5, 2\ g_{MeOH}/g_{PVAc}$ and $h_{cover} = 0.5,\ 1.5\ mm$) were investigated. The results of the two partially covered drying experiments presented up to this point give a good representation of all found flow field characteristics. Partially covered drying films with an initial solvent load of $X_0 = 1$ and $1.5\ g_{MeOH}/g_{PVAc}$ exhibited only a long-scale lateral flow from covered to uncovered area of the film for both cover distances with varying critical drying times $t_{crit,Ma,lateral}$ denoting the end of the lateral flow.

Films with $X_0 = 2\ g_{MeOH}/g_{PVAc}$ additionally showed initial short-scale convection cells occurring perpendicular to the dominant lateral flow, which stopped at critical drying times $t_{crit,Ma,cells} < t_{crit,Ma,lateral}$ significantly before the lateral flow stopped.

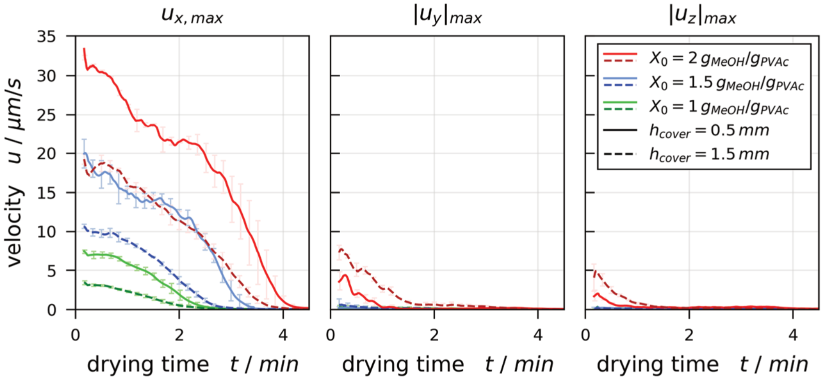

Figure 5.7: Transient evolution of Cartesian velocity components, accounting for the highest tenth fraction of 3D-µPTV derived tracer particle data in drying partially covered poly(vinyl acetate)-methanol films with varying initial solvent content X_0 (different colors) and varying cover distance h_{cover} (solid vs. dashed lines of same color). Since films with $X_0 \leq 1.5\ g_{MeOH}/g_{PVAc}$ (blue and green lines) did not exhibit short-scale convection cells perpendicular to the dominant lateral x-flow (left), the y- and z-velocities (middle and right) are very small ($< 1\ \mu m/s$). Considering $X_0 = 2\ g_{MeOH}/g_{PVAc}$ (red lines), the dominant lateral x-velcity (left) is larger for a small cover distance (solid red line) compared to the large cover distance (dashed red line). This behavior reverses for the short-scale cell velocities in y- and z-direction (middle and right).

Figure 5.7 shows the transient course of the maximum velocities in all three Cartesian directions of all six parameter combinations. It can be seen that the dominant lateral flow $u_{x,max}$, induced by the partial cover, increases with initial solvent load X_0 (different colored lines) most likely due to the lower initial viscosity of the coating solution. In addition, it can be seen that for a constant initial solvent load (same color), $u_{x,max}$ is faster in drying experiments with a small cover distance (solid lines) compared to the large cover distance (dashed lines). This is plausible since a decrease in cover distance increases the difference in drying rates between the covered and uncovered portion of the film, resulting in an increased lateral surface tension gradient. Surprisingly, in partially covered drying films with $X_0 = 2\ g_{MeOH}/g_{PVAc}$, which initially exhibit additional short-scale convection cells perpendicular to the dominant lateral flow, the cell flow velocities $|u_y|_{max}$ as well as $|u_z|_{max}$ shows an opposite trend regarding the cover distance. The cell velocities (Figure 5.7 middle and right) are faster for the large cover distance (dashed red lines) compared to the small cover distance (solid red lines). In line with the finding that partially covered films with $X_0 = 1.5\ g_{MeOH}/g_{PVAc}$ did not exhibit additional short scale instabilities, whereas uncovered experiments with otherwise identical conditions did exhibit initial short-scale convection cells, these observations indicates that the lateral long-scale flow mitigates the occurrence of short-scale instabilities.

In order to confirm the shape of the found short-scale convection cells perpendicular to the dominant lateral flow, Figure 5.8 shows the vector projections from a partially covered drying film with vertical particle movement ($X_0 = 2\ g_{MeOH}/g_{PVAc}$, $h_{cover} = 1.5\ mm$) at a drying time of $t = 10\ s$. Similar to the results presented in Figure 4.8 for uncovered drying experiments, the top view is given with colored areas denoting the height-averaged vertical velocity, where green areas denote upward moving flow and brown areas downward moving flow. The black arrows indicate the lateral surface velocity. In addition, the vertical vector projections are provided. The yz-projection (right) clearly confirms short-scale vertical convection cells perpendicular to the dominant lateral flow in x-direction. This implies that tracer particles as well as the surrounding coating solution exhibit a helical flow in x-direction while simultaneously rotating in the perpendicular plane.

Similar to the uncovered experiments (section 4.1.2), some limited information regarding the lateral length scale of the found convection cells can be extracted by analyzing the white areas of the top view denoting areas of zero height-averaged vertical velocity ($\bar{u}_z = 0\ \mu m/s$). Due to the dominant lateral flow, the cell size was extracted using lines (red dashed lines in Figure 5.8) rather than circles as done for the uncovered experiments. The limited data, which could be extracted, are compared to the cell size of uncovered drying experiments in Figure 5.9. It can be seen that some larger fluctuations in lateral cell size occur for partially covered films, especially for $h_{cover} = 0.5\ mm$ (red triangles), but the data for $h_{cover} = 1.5\ mm$ (yellow circles) compare reasonably with the data extracted from uncovered drying experiments (blue empty squares).

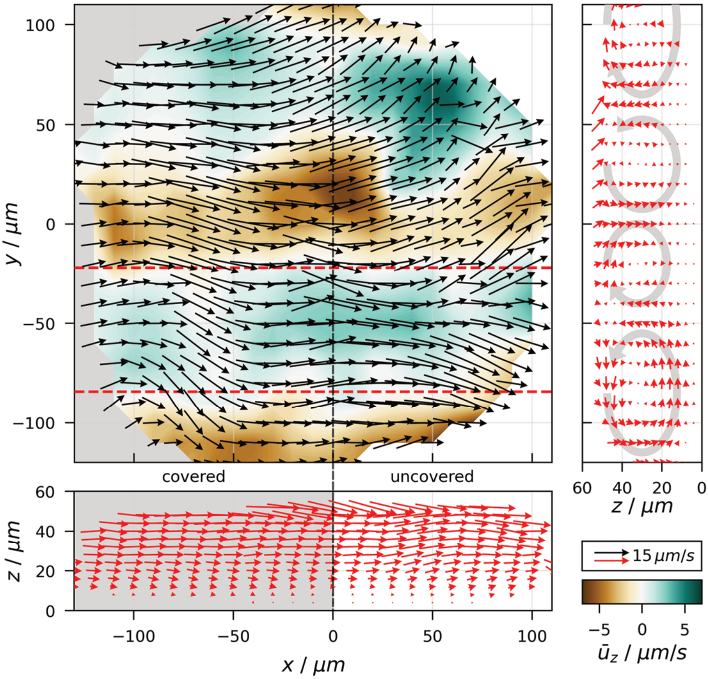

Figure 5.8: Top view and vertical vector projections of the flow field in a partially covered poly(vinyl acetate)-methanol film at early stages of drying ($t = 10\ s$, $X_0 = 2\ g_{MeOH}/g_{PVAc}$, $h_{gap} = 100\ \mu m$, $h_{cover} = 1.5\ mm$). The colored background denotes the height-averaged vertical velocity and the black arrows denote the lateral surface flow. The discrete tracer data were interpolated on a regular grid for better visualization. The red dashed lines were fitted to the white areas, indicating regions with zero height-averaged vertical flow velocity, as a measure for the lateral cell size of convection cells perpendicular to the dominant flow in x-direction.

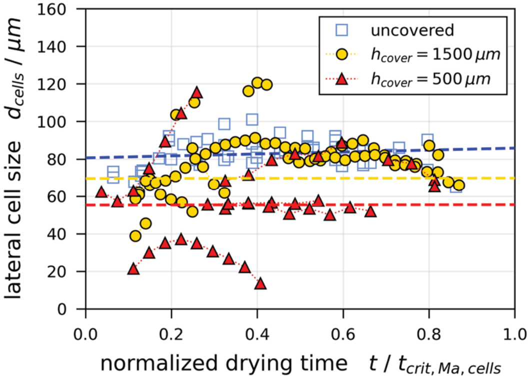

Figure 5.9: Lateral convection cell size from poly(vinyl acetate)-methanol films with an initial solvent load of $X_0 = 2\ g_{PVAc}/g_{MeOH}$, a coating gap of $h_{gap} = 100\ \mu m$, and different cover distance h_{cover} in comparison with the results from uncovered experiments. Each marker set denotes experimental results of a single cell perpendicular to the dominant flow in x-direction (see Figure 5.8, red dashed lines) and the dashed lines represent the respective linear fits.

Table 5.1 summarizes the found critical drying times, denoting the end of convective instabilities in form of a long-scale lateral flow $t_{crit,Ma,lateral}$ and short-scale vertical convection cells $t_{crit,Ma,cells}$. In line with the already reported course of maximum velocities, $t_{crit,Ma,lateral}$ increases with increasing X_0 but no clear trend regarding the impact of h_{cover} on the threshold of the lateral flow was found. In addition, partially covered films with $X_0 = 1\ g_{MeOH}/g_{PVAc}$ exhibit no initial vertical convection cells, same as uncovered films, whereas partially covered films with $X_0 = 2\ g_{MeOH}/g_{PVAc}$ exhibit vertical convection cells with similar threshold times compared to uncovered films. Films with an initial solvent load of $X_0 = 1.5\ g_{MeOH}/g_{PVAc}$, however, do not exhibit vertical convection cells when drying with a partial cover, whereas uncovered films do initially exhibit such cells. Furthermore, the threshold time of the lateral flow is significantly larger than the threshold time of vertical convection cells, clearly showing that a possible stability threshold of long-scale lateral flows must be smaller.

Table 5.1: Summary of critical threshold times denoting the end of the lateral flow and perpendicular short-scale convection cells in comparison with results from uncovered experiments ($h_{gap} = 100\ \mu m$).

	partially covered			uncovered
X_0	h_{cover}	$t_{crit,Ma,lateral}$	$t_{crit,Ma,cells}$	$t_{crit,Ma,cells}$
g_{MeOH}/g_{PVAc}	μm	s	s	s
1	500	147 ± 7	–	–
	1500	155 ± 8	–	
1.5	500	174 ± 6	–	44 ± 4
	1500	204 ± 6	–	
2	500	250 ± 14	44 ± 9	64 ± 5
	1500	238 ± 8	85 ± 7	

5.2 Raman Drying Experiments

With the intention to quantify the driving force of the long-scale lateral flow in partially covered drying experiments, additional experiments under close to identical drying conditions have been conducted using the IMRS measurement setup. In order to assess the lateral surface tension gradient driving such long-scale lateral flows, IMRS measurements have been conducted not only below the edge of the partial cover, as done during the 3D-µPTV experiments, but additionally at two lateral points under the cover and in the uncovered area of the film, as sketched in Figure 5.1.

Exemplarily, Figure 5.10 shows the results from all three lateral measurement positions for a drying film with an initial solvent load $X_0 = 1.5\ g_{MeOH}/g_{PVAc}$ and a partial cover distance $h_{cover} = 1.5\ mm$. The markers denote experimental IMRS results and the solid colored lines were derived by averaging and smoothing the results. It can be seen that at the uncovered measurement position (blue), $\bar{X}$ as well as h show a transient course almost identical to one-dimensional film drying with a constant rate period followed by a transition to the diffusion-limited plateau. The IMRS measurements under the film cover (green), however, initially show a delayed solvent load decrease, followed by an intermediate constant rate period when the uncovered portion of the film is already in the diffusion-limited regime. The measurement under the edge of the partial cover (purple) shows a similar but less pronounced behavior with the height averaged solvent load $\bar{X}$ residing between the results from the uncovered and covered measurement positions. From the height-averaged solvent load $\bar{X}$, derived from IMRS measurements, it is possible to assess the occurrence and end of an (intermediate) constant rate period, as indicated by the additional black dashed lines and colored dotted lines in Figure 5.10 (left), respectively.

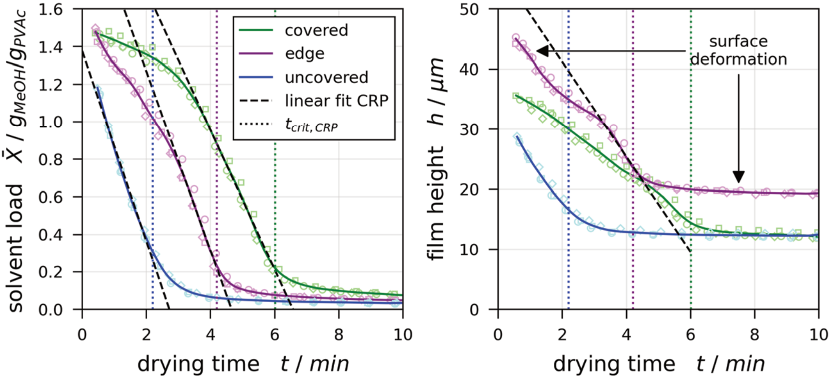

Figure 5.10: IMRS results during drying of a partially covered poly(vinyl acetate)-methanol film ($X_0 = 1.5\ g_{MeOH}/g_{PVAc}$, $h_{gap} = 100\ \mu m$, $h_{cover} = 1.5\ mm$) at different lateral measurement positions (covered, edge, uncovered) being 4 mm apart (see Figure 5.1).

When comparing the transient film height at the laterally different measurement positions (Figure 5.10 right), it can be seen that the film shrinkage under the partial cover (green solid line) is delayed compared to the uncovered portion of the film (blue solid line), but the film height in the subsequent diffusion-limited regime is identical. This observation implies that the lateral zone of influence affected by surface deformation is smaller than the distance between these measurement positions ($l_{deformation} < 8\ mm$). The results under the edge of the partial cover show a noticeably different course. Even at the first acquired measurement point ($t \approx 0.6\ min$) the film height under the edge is already elevated, followed by a nonlinear decrease of the film height. In the diffusion limited regime ($t \geq 7\ min$) the film exhibits a significantly larger height below the cover edge, compared to the (un)covered measurement positions. This clearly shows a surface deformation below the partial cover edge, which persists in the dry film.

The surface elevation under the cover edge for all parameter combinations is summarized in Table 5.2, with the film thickness being 36 to 57 % larger compared to the adjacent (un)covered measurement positions. The data show no clear trend regarding the impact of the initial solvent load X_0, but all experiments with $h_{cover} = 1.5\ mm$ exibit a larger surface deformation compared to the corresponding experiments with same X_0 and $h_{cover} = 0.5\ mm$. This appears contradictory to the flow field results presented in section 5.1, where it was shown that the lateral velocity was larger for the narrower cover distance, assuming that a larger lateral flow velocity should also produce larger surface deformations. It has to be noted that the IMRS measurements are one-dimensional. Therefore, it is a possibility that the highest elevation of the free surface does not occur exactly at the measurement position, and the lateral position of the highest elevation may be affected by the cover distance. This would explain the latter observation that the surface deformation is more pronounced during experiments with $h_{cover} = 1.5\ mm$.

Table 5.2: Film surface elevation under the partial cover edge at the diffusion plateau derived by IMRS measurements.

	$\boldsymbol{h_{cover} = 0.5\ mm}$	$\boldsymbol{h_{cover} = 1.5\ mm}$
$\boldsymbol{X_0\ /\ g_{MeOH}/g_{PVAc}}$	$(\mathbf{h}_{\mathbf{edge}}/\boldsymbol{h_{(un)covered}} - 1)\ /\ \%$	
1	35.9	49.4
1.5	52.0	56.3
2	43.3	57.0

Since the available one-dimensional simulation model cannot account for lateral flows, using the model as an elaborated fit (as done for the uncovered drying experiments in chapter 4) is not applicable to the partially covered experiments presented in this chapter. Hence, the drying curves from IMRS and 3D-µPTV experiments have to be compared directly (see Appendix D.2). A reasonable agreement was found utilizing the normalized drying time $t/t_{crit,CRP}$.

The critical drying times, denoting the end of short-scale and lateral long-scale Marangoni convection during partially covered experiments derived by 3D-µPTV (provided in Table 5.1), can also be given in terms of the normalized drying time. The resulting values are provided in Table 5.3. It can be seen that the long-scale lateral flow, induced by the partial cover, stops close to the end of the constant rate period, with an average value of the normalized critical threshold time of $t_{crit,Ma,lateral}/t_{crit,CRP} = 0.99 \pm 0.14$. The lowest local solvent load at the end of the constant rate period, extracted from IMRS experiments, was $X(t_{crit,CRP}) \geq 0.19\, g_{MeOH}/g_{PVAc}$ ($x_{MeOH} \geq 0.16$), indicating that a possible glass transition may occur only after the lateral long-scale flow stopped. Comparing the normalized threshold time of short-scale convection cells between partially covered (this chapter) and uncovered (chapter 4) experiments with $X_0 = 2\, g_{MeOH}/g_{PVAc}$ indicates that the convection cells stop earlier when a dominant lateral long-scale flow is present (Table 5.3). This would also explain the absence of short-scale convection cells in partially covered drying experiments with $X_0 = 1.5\, g_{MeOH}/g_{PVAc}$, whereas the uncovered experiments exhibited such instabilities. In addition, the finding that a dominant lateral flow weakens perpendicular short-scale instabilities is in line with previously presented flow field results. It would explain why the y-velocity is smaller when the x-velocity is larger, as found for films with $X_0 = 2\, g_{MeOH}/g_{PVAc}$ and h_{cover} variation, depicted in Figure 5.7. It has to be noted, however, that the effect of initially delayed drying under the partial cover edge may also affect the lifetime of short-scale convection cells.

Table 5.3: Summary of normalized critical threshold times denoting the end of the lateral flow and perpendicular short-scale convection cells in comparison with results from uncovered experiments.

	partially covered			uncovered
X_0	h_{cover}	$\frac{t_{crit,Ma,lateral}}{t_{crit,CRP}}$	$\frac{t_{crit,Ma,cells}}{t_{crit,CRP}}$	$\frac{t_{crit,Ma,cells}}{t_{crit,CRP}}$
g_{MeOH}/g_{PVAc}	mm	–	–	–
1	0.5	0.91 ± 0.04	–	–
	1.5	1.11 ± 0.06	–	–
1.5	0.5	0.83 ± 0.03	–	0.38 ± 0.03
	1.5	1.20 ± 0.04	–	
2	0.5	0.95 ± 0.05	0.17 ± 0.03	0.49 ± 0.04
	1.5	0.94 ± 0.03	0.34 ± 0.03	

5.3 Transient Marangoni Numbers

In chapter 4, the transient thermal and solutal Marangoni numbers were derived from 1D non-isothermal drying simulations matched to 3D-µPTV results. Due to the one-dimensional nature of the simulation model, it cannot account for long-scale lateral flows and accompanying surface deformations. Hence, the transient solutal Marangoni number during partially covered drying experiments was calculated directly from the IMRS results. Since it was found in the last section (and in section 4.4) that the drying rate during 3D-µPTV experiments is slightly larger compared to IMRS experiments, the following comparison of transient Marangoni numbers is of qualitative nature. Nevertheless, some interesting insights can be gained.

In theory, it should be possible to calculate the transient short-scale (vertical) solutal Marangoni number directly from the IMRS results obtained under the partial cover edge, by extracting the local concentrations near the bottom and surface of the films from the vertical concentration profiles. Unfortunately, it was found that due to the small drying rate, the difference between bottom and surface concentration is smaller than the fluctuations of IMRS results within one vertical profile. Without the smoothening effect from a simulation model (as done for the uncovered experiments in chapter 4), the resulting transient vertical Marangoni number exhibits large unrealistic fluctuations. Therefore, a comparison of the vertical solutal Marangoni number with the correlation derived in section 4.5.3 from uncovered drying experiments is not possible.

The lateral Marangoni numbers (equations (3.4) and (3.5)), however, can be calculated using the solvent load at the surface from the (un)covered IMRS measurement positions for the calculation of the linearized lateral surface tension gradient $\Delta\sigma_{lateral}/\Delta L$, with $\Delta L = 8\,mm$ being the lateral distance between the measurement positions[19] (see Figure 5.1). The remaining properties in equations

---

[19] As pointed out in section 5.2, the lateral zone of influence regarding surface deformations observed in this work is $l_{deformation} < 8\,mm$. Therefore, it is possible that the true lateral surface tension gradient is slightly larger than estimated by the linearization. Investigating this would require a large additional IMRS experiments at various lateral measurement positions, beyond the scope of this work.

(3.4) and (3.5) were calculated from the IMRS experiment under the cover edge. In lack of a non-isothermal simulation model accounting for lateral convection providing a more detailed film temperature evolution, the averaged temperature was assumed constant $\bar{T} = 20\,°C$, being the set substrate temperature. For the temperature induced lateral surface tension difference $\Delta\sigma(\bar{X}, T)_{lateral} = \sigma(\bar{X}, T_{uncovered}) - \sigma(\bar{X}, T_{covered})$, a worst-case estimate of the lateral temperature difference was made by assuming lab temperature under the partial cover $T_{covered} = 22.5\,°C$ and $T_{uncovered} = 18.8\,°C$ from the thermal imaging results provided in Appendix C.2. It was found that for all partially covered experiments, the thermal lateral Marangoni number did not exceed $\widetilde{Ma}_{T,lateral} \leq 3.3 \cdot 10^{-3}$ during the entire course of drying.

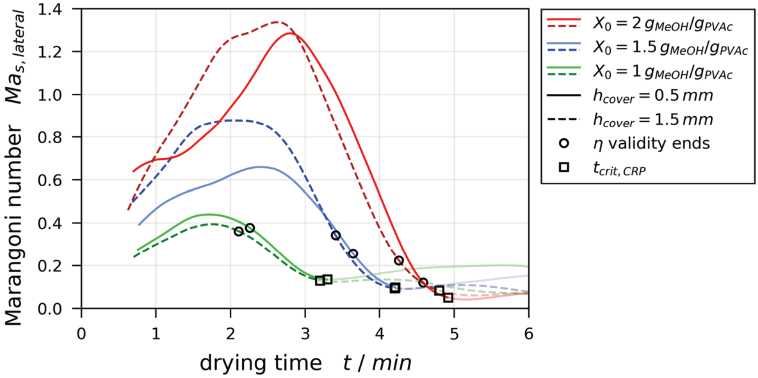

Figure 5.11: Transient solutal Marangoni numbers for the lateral flow derived from partially covered IMRS drying experiments.

The found transient course of the solutal lateral Marangoni number is given in Figure 5.11. The resulting solutal Marangoni numbers are significantly larger than the upper limit estimate of the thermal one, clearly showing that the thermal effect on the lateral Marangoni flow is negligible. This is in line with the findings from the uncovered drying experiments, from which it was deduced that the observed short-scale convection is also dominated by a solutally induced Marangoni flow. The transient course of the solutal lateral Marangoni number is qualitatively identical for all parameter combinations (X_0, h_{cover}) presented in this chapter, exhibiting a maximum during the constant rate period. Initially, the value rises because the lateral surface tension difference increases, induced by the unhindered drying of the uncovered portion of the film, compared to the delayed drying under the partial cover. The subsequent decrease is dominated by the drying induced film shrinkage and viscosity increase under the cover edge. After the end of the constant rate period (black squares), the Marangoni number mildly increases due to the strong diffusion coefficient decrease for very low solvent concentrations (lines with dim colors).

The overall magnitude of the Marangoni number increases with initial solvent load (different colored lines in Figure 5.11). This is in good agreement with the found trend of increasing lateral velocity u_x, measured with 3D-μPTV, with increasing initial solvent load, reported in Figure 5.7. There is, however, no clear trend regarding the impact of the partial cover distance h_{cover} on the Marangoni number (solid and dashed lines of same color in Figure 5.11), while the lateral velocity was distinctly larger for the smaller cover distance (Figure 5.7). In addition, the maximum of the transient lateral Marangoni numbers occurs at approximately $t_{crit,CRP}/2$, whereas the lateral velocity is highest at the beginning of drying. Whether this implies that the magnitude of Marangoni number does not correlate with the resulting flow velocity or if the qualitative nature of the comparison of the different measurement techniques contributes to this discrepancy, could not be finally resolved.

From the 3D-μPTV experiments, it was found that the lateral flow stops close to the end of the constant rate period (Table 5.3). Based on the corresponding IMRS experiments, it can be seen that the solutal lateral Marangoni number at $t_{crit,CRP}$ ranges between 0.14 and 0.05 (black squares in Figure 5.11, see also Table 5.4). At these points, the solvent concentration is already lower than the lower limit of experimentally validated viscosity data (Figure 3.2). The points beyond which the viscosity was extrapolated from the fitted mixing rule equation is given as black circles. Since extrapolating the viscosity from the employed fit equation is likely to underpredict the viscosity values at low methanol concentrations (see Appendix B.9), the resulting Marangoni numbers in Figure 5.11 are possibly slightly smaller after the validity of the viscosity fit ends (black circles). The values of $\widetilde{Ma}_{s,lateral}(t_{crit,CRP})$ derived from IMRS experiments are summarized in Table 5.4.

Table 5.4: Summary of IMRS derived solutal lateral Marangoni numbers (eq. (3.5)) from partially covered drying experiments in comparison with short-scale instabilities and corresponding critical Marangoni numbers (eq. (3.3)) of uncovered experiments.

	partially covered $Ma_{s,lateral}$			**uncovered** $Ma_{s,cells}$	
X_0	h_{cover}	Ma_{max}	$\widetilde{Ma}(t_{crit,CRP})$	Ma_{max}	Ma_{crit}
g_{MeOH}/g_{PVAc}	mm	$-$	$-$	$-$	$-$
1	0.5	0.4	0.14	2.9	stable
	1.5	0.4	0.13		
1.5	0.5	0.7	0.10	2.6	1.5
	1.5	0.9	0.09		
2	0.5	1.3	0.05	2.3	0.9
	1.5	1.3	0.08		

The viscosity extrapolation and the discussed difference between the drying rate of IMRS and 3D-µPTV experiments, makes the assessment of a potential stability threshold in form of a critical solutal lateral Marangoni number qualitative. Nevertheless, the found small values of the Marangoni number still imply that a potential stability threshold would be very low or non-existent for a long-scale lateral Marangoni flow in drying poly(vinyl acetate)-methanol films. This means that a lateral Marangoni flow induced by laterally inhomogeneous drying conditions only stops at the end of the constant rate period where the polymer film becomes highly viscous.

5.4 Additional Considerations

The capillary length (equation (1.2)) is independent of the viscosity and was found to be in the range of $1.6\,mm < l_{capillary} < 1.8\,mm$. Regarding the possibility of short-scale surface deformations ($\lambda \ll l_{capillary}$), the readers are reffered to the discussion in section 4.6, which is also qualitatively valid for the experiments presented in this chapter. A free surface deformation due to the long-scale lateral flow was clearly confirmed from the IMRS results presented in section 5.2. This is in line with theoretic findings, which indicate that surface deformability is a necessary requirement for lateral long-scale instabilities. A possible leveling due to gravity can be assessed by calculating the solutal dimensionless Galileo number with equation (3.7), and the characteristic time-constant for gravity waves to level using equation (3.9). The film height was averaged from IMRS results using all three laterally different measurement positions, whereas the material properties were calculated from the IMRS measurement position under the partial cover edge. The smaller the Galileo number the weaker the leveling effect of gravity waves (see Figure 1.7). Since the end of the lateral flow exclusively occurs at lower solvent concentrations than the lower limit of viscosity measurements, the accents $\frown$ and $\smile$ denote whether the true values are likely to be larger or smaller due to the underpredicted viscosity values at low solvent concentrations, respectively (see Appendix B.9).

Table 5.5: Values of Galileo number at the first measurement point of partially covered IMRS experiments and at $t_{crit,CRP}$. The values decrease during drying.

$X_0/(g_{MeOH}/g_{PVAc})$	$h_{cover} = 500\,\mu m$	$h_{cover} = 1500\,\mu m$
1	$0.3 \rightarrow \overset{\smile}{2.7} \cdot 10^{-2}$	$0.3 \rightarrow \overset{\smile}{2.4} \cdot 10^{-2}$
1.5	$0.7 \rightarrow \overset{\smile}{1.3} \cdot 10^{-2}$	$0.7 \rightarrow \overset{\smile}{1.1} \cdot 10^{-2}$
2	$1.8 \rightarrow \overset{\smile}{0.4} \cdot 10^{-2}$	$1.9 \rightarrow \overset{\smile}{0.6} \cdot 10^{-2}$

Table 5.5 summarizes the resulting values of Ga at the first measurement point and at $t_{crit,CRP}$. It can be seen that Ga decreases during drying, indicating that the leveling effect due to gravity weakens due to the drying induced film shrinkage and viscosity increase. In addition, the initial values of Ga are largest for $X_0 = 2\ g_{MeOH}/g_{PVAc}$ as these films have the lowest initial viscosity. This finding could also explain why no clear trend regarding the strength of the surface elevation with changing initial solvent load was found (see Table 5.2). While films with with $X_0 = 2\ g_{MeOH}/g_{PVAc}$ exhibited the largest lateral velocity, they also possess the strongest affinity to gravity wave leveling at early stages of drying.

This finding is also reflected in the characteristic time constant of gravity wave leveling, assuming a small characteristic lateral length of $\lambda = 2\,mm$ ($\tau_{gravity} \sim \lambda^2$, see equation (3.9)). $\tau_{gravity}$ data at the first IMRS measurement point ($t \approx 0.6\,min$) are summarized in Table 5.6. Since $\tau_{gravity}$ is proportional to the viscosity and h^{-3}, the characteristic leveling time significantly increases during drying. At $t_{crit,CRP}/2$ the lowest value from all partially covered experiments is already as high as $\tau_{gravity} \geq 22\ min$ and at the end of the constant rate period the lower limit is $\hat{\tau}_{gravity} \geq 5.6\ days$. From the IMRS results, it was found that the free surface under the partial cover edge was already significantly elevated at the first measurement point (Figure 5.10) and the calculations presented in this section indicate that the strength of gravity wave leveling is significantly decreasing during drying. This implies that surface deformations induced by long-scale lateral Marangoni convection cannot be avoided unless a lateral Marangoni flow is inhibited in the first place. It further implies that the observed long-scale lateral flow has no stability limit, since the only force resisting a purely lateral Marangoni flow is the leveling of accompanying surface deformations, as indicated by the discussed literature in section 1.2.1. This is also reflected by the finding that the lateral flow stops only at the end of the constant rate period and confirms the second research hypothesis of this dissertation.

Table 5.6: Characteristic time constant of gravity wave leveling at the first measurement point ($t \approx 0.6\ min$) of partially covered IMRS drying experiments, assuming $\lambda = 2\ mm$.

$X_0/(g_{MeOH}/g_{PVAc})$	$h_{cover} = 0.5\ mm$	$h_{cover} = 1.5\ mm$
1	$2563\ s$	$2433\ s$
1.5	$654\ s$	$685\ s$
2	$193\ s$	$190\ s$

5.5 Summary

In this chapter, the impact of laterally inhomogeneous drying conditions on the occurrence and strength of lateral long-scale Marangoni instabilities in drying films of poly(vinyl acetate)-methanol were investigated. The coating gap during film preparation was kept constant at $h_{gap} = 100\ \mu m$, resulting in an initial wet film thickness of $h_0 \approx 50\ \mu m$. The lateral inhomogeneity in experimental drying conditions was induced by partially covering the film. The distance between the partial cover and substrate was varied using $h_{cover} = 0.5$ and $1.5\ mm$, and the initial solvent load was varied using $X_0 = 1$, 1.5, and 2 g_{MeOH}/g_{PVAc}.

All films under investigation exhibited a lateral long-scale Marangoni flow from the covered towards the uncovered portion of the film measured with 3D-µPTV. The flow stopped near the end of the constant rate period of drying. The lateral flow velocity increased with increasing initial solvent load and decreasing cover distance. Furthermore, only films with $X_0 = 2\ g_{MeOH}/g_{PVAc}$ exhibited additional short-scale convection cells perpendicular to the dominant lateral flow. The convection cells stopped significantly earlier than the long-scale lateral flow. In addition, the convection cells stopped earlier when the lateral flow velocity was larger, and partially covered films with $X_0 = 1.5\ g_{MeOH}/g_{PVAc}$ did not exhibit convection cells, whereas the uncovered experiments, presented in chapter 4, did initially show such cells. These findings indicate that the occurrence of short-scale Marangoni convection cells is mitigated by the long-scale lateral flow.

The IMRS drying experiments under close to identical conditions revealed a strong elevation of the film's free surface under the edge of the partial cover. They gave access to transient solutal lateral Marangoni numbers during drying. A comparison of lateral thermal and solutal Marangoni numbers showed the dominance of solutally induced instabilities. Albeit the slightly higher drying rate during 3D-µPTV experiments, the results indicate a significantly lower stability threshold limit for long-scale lateral Marangoni instabilities, compared to short-scale instabilities. An assessment of the characteristic time constant of gravity wave leveling showed that due to the strong viscosity increase, a leveling of surface deformations induced by long-scale Marangoni instabilities is unlikely to occur. Hence, lateral Marangoni convection has to be avoided altogether, if surface deformations shall be avoided.

6 Conclusion

6.1 Summary

The aim of this dissertation was to gain a better understanding of the impact of drying conditions on the occurrence and lifetime of convective instabilities in thin drying polymer solution films. This was achieved by further developing the 3D-µPTV experimental setup and by investigating two research hypotheses.

A rigorous calibration, automation and postprocessing routine was developed for a three-dimensional micro particle tracking velocimetry (3D-µPTV) setup. The setup utilizes the "off-focus imaging" approach proposed by Speidel et al. (2003), which allows for the extraction of line-of-sight particle positions by analyzing the diffraction rings occurring when fluorescent tracer particles are not in the focus plane of the observing camera. In order to extend the vertical observation volume, the 3D-µPTV setup combines this approach with multifocal microscopy, using multiple cameras with different vertical focus plane positions. It was found that the setup is well suited for the quantitative investigation of 3D convective instabilities in drying films.

The first research hypothesis was that the onset and end of short-scale convective Marangoni instabilities during drying can be described by a unified critical threshold in Marangoni numbers. Hence, film drying experiments without a deliberate lateral inhomogeneity in drying conditions were conducted using the model system poly(vinyl acetate)-methanol. It was found that 3D-µPTV derived flow field mappings combined with 1D IMRS experiments and drying simulations allows for a quantitative assessment of stability thresholds in the form of dimensionless Marangoni numbers. For this approach, a large amount of concentration- and temperature-dependent material properties is required, and a special emphasis was laid on utilizing realistic experimentally validated properties. Therefore, the surface tension of several polymer solutions was investigated in detail. The observed instabilities occurring during drying were dominated by solutally induced Marangoni convection, and from drying experiments without deliberate laterally inhomogeneous drying conditions, a new empiric power-law correlation for the critical solutal Marangoni number $Ma_{s,crit} \sim Pe^2 \cdot Sc^{-1/3}$ was found. The correlation accounts for the initial (in)stability as well as the stop of short-scale Marangoni convection cells during the constant rate period of drying and thereby verifies the first research hypothesis. An assessment of the characteristic leveling time of capillary wave (short-scale) surface deformations indicates that deformations are unlikely to occur while the short-scale convection cells are still active. They may, however, be a result of lateral polymer transport due to the instability and evolve during drying after the instability has already stopped. Due to the strong viscosity increase during drying, a leveling at later stages of drying appears unlikely.

The second research hypothesis was that long-scale Marangoni instabilities, induced by laterally inhomogeneous drying conditions, have no stability threshold. Hence, deliberately inhomogeneous drying conditions were induced by partially covering the drying poly(vinyl acetate)-methanol films. It was found that the resulting long-scale lateral Marangoni flow was accompanied by strong surface deformations, starting at early stages of drying. The lateral flow stopped only near the end of the constant rate period of drying, having a significantly longer lifetime than short-scale instabilities. In addition, films from diluted solutions exhibited simultaneous long-scale flow and perpendicular short-scale convection cells. The results indicate that the long-scale flow mitigates the occurrence of short-scale instabilities. A qualitative assessment of Marangoni numbers at the end of the constant rate period implies that a potential stability threshold are very low or non-existent for a long-scale lateral Marangoni flow in drying poly(vinyl acetate)-methanol films. Furthermore, the assessment of the characteristic time constant of gravity wave (long-scale) surface deformation leveling indicates that a leveling of surface deformations induced by long-scale lateral Marangoni convection during drying is not possible.

6.2 Outlook

The 3D-µPTV setup grants unique insights into the three-dimensional flow field of drying polymer solution films subject to convective instabilities. A procedure how to avoid the remaining systematic discrepancy in vertical tracer particle position reconstruction was proposed, but it requires a large amount of calibration samples and is computationally intensive. Since this only mildly affects the vertical positions and velocities derived by the camera with the upmost vertical focus position, the occurrence and lifetime of convective instabilities was successfully investigated despite this remaining inaccuracy. Hence, the correction of this discrepancy is of minor importance.

Due to the optical access from below, through a transparent glass substrate, the setup allows for varying convective airflow conditions above the film during drying. Hence, different forced convective airflows, for example lateral channel flow or an impinging jet and an increased drying rate can be investigated in the future. It has to be noted, however, that due to the lens opening, the lateral uniformity of substrate temperature control is affected. Increasing the drying rate would induce a stronger evaporative cooling effect and therefore enhance the lateral inhomogeneity in temperature control. Therefore, the most important aspect, which should be addressed in the future, is a more uniform temperature control of the substrate. This may be realized by different methods: *First*, it was found that the air temperature surrounding the microscope could not be controlled independently of the temperature of the solid substrate support. Hence, the substrate support including the opening should be redesigned so that an independent temperature control is possible. This way the air temperature surrounding the lens could be set higher than the solid support temperature, with the intention that the steady-state temperature of the film during the constant rate period of drying would coincide with the support temperature. *Second*, it was also found that the lateral inhomogeneity in substrate temperature control was smaller during IMRS experiments because IMRS utilizes immersion oil between the lens and the bottom of the glass substrate, acting as a heat conducting liquid bridge. Hence, it should be tested whether introducing an immersion liquid during 3D-µPTV experiments is feasible. Since 3D-µPTV evaluation relies on an asymmetric point spread function (PSF), this has to be ensured and could be assessed via PSF simulations under various non-design conditions. The non-design conditions, however, are likely to require using a microscope lens with an immersion liquid it was not designed for (e.g. air lens with oil immersion). Hence, it has to be conferred with the lens manufacturer, which combination is possible. If a suitable “non-design” combination of lens and immersion liquid can be found, it has to be noted that devices for microscope lens temperature control exist, which may help to improve the uniformity of substrate temperature control.

The stability assessment employed in this work requires a large amount of concentration- and temperature-dependent material properties of the coating solution. Especially the diffusion coefficient in the solution, the phase equilibrium, the viscosity and the surface tension are of major importance, since they show a strong non-ideal concentration dependency. This, and the aforementioned substrate temperature control, explain in hindsight why the experiments in this dissertation were limited to a single polymer solution system and very low drying rates. If these shortcomings are addressed in future work, variations of the drying rate and temperature, as well as material systems should be investigated, as well as different types of forced convective airflow. Based on this, the validity of the found power law correlation for different higher drying rates and different material systems should be investigated.

The results for poly(vinyl acetate)-methanol, presented in this dissertation, imply that the solutal effect on Marangoni instabilities is dominating the occurrence of convective instabilities. It was further deduced that surface deformations can only be avoided by inhibiting Marangoni instabilities altogether. Hence, material systems with different concentration dependencies of the surface tension should be prioritized in future investigations. The system poly(ethylene glycol)-methanol-water, investigated in terms of surface tension, appears to be a well-suited candidate, because the binary subsystems PEG-water and PEG-methanol are complementary regarding their concentration dependency. However, the solutions suffer from phase-separation below $30\ ^\circ C$ and therefore require the substrate temperature control to be addressed first. Furthermore, the ternary data of PEG-methanol-water indicate that suitable drying conditions (along the $\sigma = 40\ mN/m$ contour line in Figure A.17) could exclude the effect of concentration dependency of the surface tension altogether. This may be achieved by preloading the drying air with solvent. The required conditions for such a drying behavior could be assessed using the 1D simulation model, which is also available for ternary polymer-solvent-solvent systems.

References

Abbasian, A.; Ghaffarian, S.R.; Mohammadi, N.; Khosroshahi, M.R.; Fathollahi, M. (**2004**): *Study on different planforms of paint's solvents and the effect of surfactants (on them)*. In *Progress in Organic Coatings* 49 (3), pp. 229–235. DOI: 10.1016/j.porgcoat.2003.09.020.

Afik, E.; Steinberg, V. (**2017**): *On the role of initial velocities in pair dispersion in a microfluidic chaotic flow*. In *Nat Commun* 8 (1), p. 468. DOI: 10.1038/s41467-017-00389-8.

Al-Fariss, T.; Al-Zahrani, S. (**1993**): *Rheological Behaviour of Some Dilute Polymer Solutions*. In *JKAU: Eng Sci* 5 (1), pp. 95–109. DOI: 10.4197/Eng.5-1.7.

Arya, R. K.; Tewari, K.; Shukla, S. (**2016**): *Non-Fickian drying of binary polymeric coatings: Depth profiling study using confocal Raman spectroscopy*. In *Progress in Organic Coatings* 95, pp. 8–19. DOI: 10.1016/j.porgcoat.2016.02.004.

Babaie, A.; Stoeber, B. (**2015**): *Concentration Field Evolution during the Drying of a Thin Polymer Solution Film near the Contact Line*. In *Langmuir* 31 (33), pp. 9033–9040. DOI: 10.1021/acs.langmuir.5b01960.

Baesch, S. (**2017**): *Influence of the Drying Conditions on the Particle Distribution in Polymer Matrix Composites: Drying Regime Maps - Approach for Facilitated Industrial Applicability*. Doctoral Thesis. Karlsruhe Institute of Technology (KIT), Karlsruhe.

Bahloul, A.; Delahaye, R.; Vasseur, P.; Robillard, L. (**2003**): *Effect of surface tension on convection in a binary fluid layer under a zero gravity environment*. In *Int J Heat Mass Transf* 46 (10), pp. 1759–1771. DOI: 10.1016/S0017-9310(02)00480-5.

Bassou, N.; Rharbi, Y. (**2009**): *Role of Bénard-Marangoni instabilities during solvent evaporation in polymer surface corrugations*. In *Langmuir* 25 (1), pp. 624–632. DOI: 10.1021/la802979a.

Baumgärtel, M.; Willenbacher, N. (**1996**): *The relaxation of concentrated polymer solutions*. In *Rheol Acta* 35 (2), pp. 168–185. DOI: 10.1007/BF00396044.

Bénard, H. (**1900**): *Étude expérimentale des courants de convection dans une nappe liquide. — Régime permanent : tourbillons cellulaires*. In *J. Phys. Theor. Appl.* 9 (1), pp. 513–524. DOI: 10.1051/jphystap:019000090051300.

Bénard, H. (**1901**): *Les tourbillons cellulaires dans une nappe liquide. - Méthodes optiques d'observation et d'enregistrement*. In *J. Phys. Theor. Appl.* 10 (1), pp. 254–266. DOI: 10.1051/jphystap:0190100100025400.

Berg, J. C.; Acrivos, A.; Boudart, M. (**1966**): *Evaporative Convection*. In: Drew, T. B.; Hoopes, J. W.; Vermeulen, T. (Eds.). *Advances in Chemical Engineering, vol.* 6. New York: Academic Press, pp. 61–123. ISBN: 9780120085064.

Bernardo, G. (**2013**): *Diffusivity of alcohols in amorphous polystyrene*. In *J. Appl. Polym. Sci.* 127 (3), pp. 1803–1811. DOI: 10.1002/app.37918.

Berry, G. C.; Fox, T.G. (**1968**): *The viscosity of polymers and their concentrated solutions*. In: Cantow, H.-J.; Dall'Asta, G.; Ferry, J. D.; Kern, W.; Natta, G.; Okamura, S. et al. (Eds.). *Advances in Polymer Science: Fortschritte der Hochpolymeren-Forschung*. Berlin: Springer, pp. 261–357. ISBN: 978-3-540-35769-8.

Bestehorn, M.; Pototsky, A.; Thiele, U. (**2003**): *3D Large scale Marangoni convection in liquid films*. In *Eur Phys J E Soft Matter* 33 (4), pp. 457–467. DOI: 10.1140/epjb/e2003-00186-3.

Bhattacharya, A.; Ray, P. (**2004**): *Studies on surface tension of poly(vinyl alcohol): Effect of concentration, temperature, and addition of chaotropic agents*. In *J. Appl. Polym. Sci.* 93 (1), pp. 122–130. DOI: 10.1002/app.20436.

Birnie, D. P. (**2001**): *Rational solvent selection strategies to combat striation formation during spin coating of thin films*. In *J. Mater. Res.* 16 (4), pp. 1145–1154. DOI: 10.1557/JMR.2001.0158.

Birnie, D. P. (**2013**): *A model for drying control cosolvent selection for spin-coating uniformity: the thin film limit*. In *Langmuir* 29 (29), pp. 9072–9078. DOI: 10.1021/la401106z.

Block, M. J. (**1956**): *Surface Tension as the Cause of Bénard Cells and Surface Deformation in a Liquid Film*. In *Nature* 178 (4534), pp. 650–651. DOI: 10.1038/178650a0.

Bormashenko, E.; Balter, S.; Pogreb, R.; Bormashenko, Y.; Gendelman, O.; Aurbach, D. (**2010**): *On the mechanism of patterning in rapidly evaporated polymer solutions: is temperature-gradient-driven Marangoni instability responsible for the large-scale patterning?* In *J Colloid Interface Sci* 343 (2), pp. 602–607. DOI: 10.1016/j.jcis.2009.12.005.

Bormashenko, E.; Pogreb, R.; Musin, A.; Stanevsky, O.; Bormashenko, Y.; Whyman, G.; Gendelman, O.; Barkay, Z. (**2006**): *Self-assembly in evaporated polymer solutions: influence of the solution concentration*. In *J Colloid Interface Sci* 297 (2), pp. 534–540. DOI: 10.1016/j.jcis.2005.11.025.

Boyer, H. C.; Bzdek, B. R.; Reid, J. P.; Dutcher, C. S. (**2017**): *Statistical Thermodynamic Model for Surface Tension of Organic and Inorganic Aqueous Mixtures*. In *The journal of physical chemistry. A* 121 (1), pp. 198–205. DOI: 10.1021/acs.jpca.6b10057.

Bradski, G. (**2000**): *The OpenCV Library*. In *Dr Dobb's J. Software Tools*. Available online at https://opencv.org.

Buckley, A. (Ed.) (**2013**): *Organic light-emitting diodes (OLEDs): Materials, devices and applications*. Oxford: Woodhead Publishing (Woodhead Publishing Series in Electronic and Optical Materials, No. 36). ISBN: 978-0-85709-425-4.

Cammenga, H.K.; Schreiber, D.; Barnes, G.T.; Hunter, D.S. (**1984**): *On Marangoni convection during the evaporation of water*. In *J Colloid Interface Sci* 98 (2), pp. 585–586. DOI: 10.1016/0021-9797(84)90187-5.

Cavadini, P.; Erz, J.; Sachsenheimer, D.; Kowalczyk, A.; Willenbacher, N.; Scharfer, P.; Schabel, W. (**2015**): *Investigation of the flow field in thin polymer films due to inhomogeneous drying*. In *J Coat Technol Res* 12 (5), pp. 921–926. DOI: 10.1007/s11998-015-9725-9.

Cavadini, P.; Krenn, J.; Scharfer, P.; Schabel, W. (**2013**): *Investigation of surface deformation during drying of thin polymer films due to Marangoni convection*. In *Chem Eng Process* 64, pp. 24–30. DOI: 10.1016/j.cep.2012.11.008.

Cavadini, P.; Weinhold, H.; Tönsmann, M.; Chilingaryan, S.; Kopmann, A.; Lewkowicz, A.; Miao, C.; Scharfer, P.; Schabel, W. (**2018**): *Investigation of the flow structure in thin polymer films using 3D µPTV enhanced by GPU*. In *Exp Fluids* 59 (4), p. 370. DOI: 10.1007/s00348-017-2482-z.

Cerisier, P.; Perez-Garcia, C.; Jamond, C.; Pantaloni J. (**1987**): *Wavelength selection in Bénard-Marangoni convection*. In *Physical review. A, General physics* 35 (4), pp. 1949–1952. DOI: 10.1103/physreva.35.1949.

Chai, A.-T.; Zhang, N. (**1998**): *Experimental study of Marangoni-Benard convection in a liquid layer induced by evaporation*. In *Exp Heat Transfer* 11 (3), pp. 187–205. DOI: 10.1080/08916159808946561.

Chauvet, F.; Dehaeck, S.; Colinet, P. (**2012**): *Threshold of Bénard-Marangoni instability in drying liquid films*. In *Europhys Lett* 99 (3), p. 34001. DOI: 10.1209/0295-5075/99/34001.

Chen, J.-J.; Lin, J.-D. (**2000**): *Thermocapillary effect on drying of a polymer solution under non-uniform radiant heating*. In *International Journal of Heat and Mass Transfer* 43 (12), pp. 2155–2175. DOI: 10.1016/S0017-9310(99)00277-X.

Chmelař, J.; Mrazek, J.; Dusankova, M.; Novotny, J.; Velebny, V. (**2019**): *Convective Patterns in Solution-Casted Films from Acylated Hyaluronan*. In *Macromol. Chem. Phys.* 220 (5), p. 1800515. DOI: 10.1002/macp.201800515.

Chow, T. S. (**1980**): *Molecular Interpretation of the Glass Transition Temperature of Polymer-Diluent Systems*. In *Macromolecules* 13 (2), pp. 362–364. DOI: 10.1021/ma60074a029.

Cierpka, C.; Kähler, C. J. (**2012**): *Particle imaging techniques for volumetric three-component (3D3C) velocity measurements in microfluidics*. In *J Vis* 15 (1), pp. 1–31. DOI: 10.1007/s12650-011-0107-9.

Craster, R. V.; Matar, O. K. (**2009**): *Dynamics and stability of thin liquid films*. In *Rev Mod Phys* 81 (3), pp. 1131–1198. DOI: 10.1103/RevModPhys.81.1131.

Crawford, H.; Van Winkle, M. (**1959**): *Composition Determines Surface Tension and Density of Ternary Systems at Normal Boiling Point*. In *Ind. Eng. Chem.* 51 (4), pp. 601–606. DOI: 10.1021/ie50592a054.

Cröll, A.; Müller-Sebert, W.; Nitsche, R. (**1989**): *The critical marangoni number for the onset of time-dependent convection in silicon*. In *Materials Research Bulletin* 24 (8), pp. 995–1004. DOI: 10.1016/0025-5408(89)90184-0.

Cross, M. C.; Hohenberg, P. C. (**1993**): *Pattern formation outside of equilibrium*. In *Rev Mod Phys* 65 (3), pp. 851–1112. DOI: 10.1103/RevModPhys.65.851.

Curak, M.; Saranjam, N.; Chandra, S. (**2018**): *Motion Of Pigments In Thin Paint Films*. In: Czekanski, A. (Ed.). *Progress in Canadian Mechanical Engineering: Proceedings of The Canadian Society for Mechanical Engineering International Congress 2018.* CSME International Congress. Toronto, 27-30 May 2018. York: York University Libraries. ISBN: 9781773550237.

Daviaud, F.; Vince, J. M. (**1993**): *Traveling waves in a fluid layer subjected to a horizontal temperature gradient*. In *Phys. Rev. E* 48 (6), pp. 4432–4436. DOI: 10.1103/physreve.48.4432.

Davis, S. H. (**1969**): *Buoyancy-surface tension instability by the method of energy*. In *J Fluid Mech* 39 (2), pp. 347–359. DOI: 10.1017/S0022112069002217.

Davis, S. H. (**1987**): *Thermocapillary Instabilities*. In *Annu Rev Fluid Mech* 19 (1), pp. 403–435. DOI: 10.1146/annurev.fl.19.010187.002155.

De Gennes, P. G. (**2001**): *Instabilities during the evaporation of a film: Non-glassy polymer + volatile solvent*. In *The European physical journal. E, Soft matter* 6 (5), pp. 421–424. DOI: 10.1007/s10189-001-8055-3.

De Gennes, P. G. (**2002**): *Solvent evaporation of spin cast films: “crust” effects*. In *Eur. Phys. J. E* 7 (1), pp. 31–34. DOI: 10.1140/epje/i200101169.

De Gennes, P. G.; Brochard-Wyart, F.; Quéré, D. (**2010**): *Capillarity and wetting phenomena: Drops, bubbles, pearls, waves*. New York, NY: Springer. ISBN: 978-0-387-21656-0.

Di Nicola, G.; Pierantozzi, M. (**2013**): *Surface tension prediction for refrigerant binary systems*. In *International Journal of Refrigeration* 36 (2), pp. 562–566. DOI: 10.1016/j.ijrefrig.2012.10.004.

Douglas, K.; Babcock, H. (**2018**): *MicroscPSF-Py*. Available online at https://github.com/MicroscPSF/MicroscPSF-Py.

Doumenc, F.; Boeck, T.; Guerrier, B.; Rossi, M. (**2010**): *Transient Rayleigh–Bénard–Marangoni convection due to evaporation: A linear non-normal stability analysis*. In *J Fluid Mech* 648, p. 521. DOI: 10.1017/S0022112009993417.

Doumenc, F.; Chénier, E.; Trouette, B.; Boeck, T.; Delcarte, C.; Guerrier, B.; Rossi, M. (**2013**): *Free convection in drying binary mixtures: Solutal versus thermal instabilities*. In *Int J Heat Mass Transf* 63, pp. 336–350. DOI: 10.1016/j.ijheatmasstransfer.2013.03.070.

Eckert, K.; Bestehorn, M.; Thess, A. (**1998**): *Square cells in surface-tension-driven Bénard convection: experiment and theory*. In *J Fluid Mech* 356, pp. 155–197. DOI: 10.1017/S0022112097007842.

Eötvös, R. (**1886**): *Ueber den Zusammenhang der Oberflächenspannung der Flüssigkeiten mit ihrem Molecularvolumen*. In *Ann. Phys. Chem.* 263 (3), pp. 448–459. DOI: 10.1002/andp.18862630309.

Erz, J. (**2014**): *In-situ Visualisierung von Oberflächendeformationen aufgrund von Marangoni-Konvektion während der Filmtrocknung*. Doctoral Thesis at Karlsruhe Institute of Technology (KIT). Karlsruhe: KIT Scientific Publishing. ISBN: 978-3-7315-0148-0.

Foglarová, M.; Chmelař, J.; Huerta-Angeles, G.; Vágnerová, H.; Kulhánek, J.; Bartoň Tománková, K.; Minařík, A.; Velebný, V. (**2016**): *Water-insoluble thin films from palmitoyl hyaluronan with tunable properties*. In *Carbohydrate Polymers* 144, pp. 68–75. DOI: 10.1016/j.carbpol.2016.02.027.

Gaines, G. L. (**1969**): *Surface tension of polymer solutions. I. Solutions of poly(dimethylsiloxanes)*. In *J. Phys. Chem.* 73 (9), pp. 3143–3150. DOI: 10.1021/j100843a060.

Gambaryan-Roisman, T. (**2010**): *Marangoni convection, evaporation and interface deformation in liquid films on heated substrates with non-uniform thermal conductivity*. In *Int J Heat Mass Transf* 53 (1-3), pp. 390–402. DOI: 10.1016/j.ijheatmasstransfer.2009.09.017.

Gambaryan-Roisman, T. (**2015**): *Modulation of Marangoni convection in liquid films: Reinhard Miller, Honorary Issue*. In *Adv Colloid Interface Sci* 222, pp. 319–331. DOI: 10.1016/j.cis.2015.02.003.

Gans, P.; Gill, J. B. (**1983**): *Examination of the Convolution Method for Numerical Smoothing and Differentiation of Spectroscopic Data in Theory and in Practice*. In *Appl Spectrosc* 37 (6), pp. 515–520. DOI: 10.1366/0003702834634712.

Gibson, S. F.; Lanni, F. (**1992**): *Experimental test of an analytical model of aberration in an oil-immersion objective lens used in three-dimensional light microscopy*. In *J Opt Soc Am A* 9 (1), p. 154. DOI: 10.1364/JOSAA.9.000154.

Golovin, A. A.; Nepomnyashchy, A. A.; Pismen, L. M. (**1995**): *Pattern formation in large-scale Marangoni convection with deformable interface*. In *Physica D* 81 (1-2), pp. 117–147. DOI: 10.1016/0167-2789(94)00184-R.

Grabowski, C. A.; Mukhopadhyay, A. (**2008**): *Diffusion of Polystyrene Chains and Fluorescent Dye Molecules in Semidilute and Concentrated Polymer Solutions*. In *Macromolecules* 41 (16), pp. 6191–6194. DOI: 10.1021/ma801035n.

Gutoff, E. B.; Cohen, E. D.; Kheboian, G. I. (**2010**): *Coating and drying defects: Troubleshooting operating problems*. 2nd ed. Hoboken, N.J: Wiley-Interscience. ISBN: 0-471-71368-6.

Haas, D. E.; Birnie, I. D. P.I.I. (**2002**): *Evaluation of thermocapillary driving forces in the development of striations during the spin coating process*. In *Journal of Materials Science* 37 (10), pp. 2109–2116. DOI: 10.1023/A:1015250120963.

Hennessy, M. G.; Munch, A. (**2014**): *Dynamics of a slowly evaporating solvent-polymer mixture with a deformable upper surface*. In *IMA Journal of Applied Mathematics* 79 (4), pp. 681–720. DOI: 10.1093/imamat/hxu024.

Hiemenz, P. C.; Lodge, T. P.; Lodge, T. (**2007**): *Polymer Chemistry*. 2nd ed. Boca Raton, FL: CRC Press. ISBN: 978-1-57444-779-8.

Janes, D. W.; Katzenstein, J. M.; Shanmuganathan, K.; Ellison, C. J. (**2013**): *Directing convection to pattern thin polymer films*. In *J. Polym. Sci. B Polym. Phys.* 51 (7), pp. 535–545. DOI: 10.1002/polb.23262.

Jeffreys, H. (**1926**): *LXXVI. The stability of a layer of fluid heated below*. In *Philosophical Magazine Series 6* 2 (10), pp. 833–844. DOI: 10.1080/14786442608564114.

Kaelble, D. H. (**1970**): *Dispersion-Polar Surface Tension Properties of Organic Solids*. In *The Journal of Adhesion* 2 (2), pp. 66–81. DOI: 10.1080/0021846708544582.

Kang, Q.; Zhang, J. F.; Hu, L.; Duan, L. (**2003**): *Experimental study on Benard-Marangoni convection by PIV and TCL*. In *Proc SPIE 5058*, p. 155. DOI: 10.1117/12.509534.

Karbalaei, A.; Kumar, R.; Cho, H. J. (**2016**): *Thermocapillarity in Microfluidics - A Review*. In *Micromachines* 7 (1). DOI: 10.3390/mi7010013.

Kistler, S. F.; Schweizer, P. M. (Eds.) (**1997**): *Liquid Film Coating*. Dordrecht: Springer. ISBN: 978-94-010-6246-6.

Koide, N. (Ed.) (**2014**): *The Liquid Crystal Display Story: 50 Years of Liquid Crystal R&D that lead The Way to the Future*. Tokyo: Springer. ISBN: 978-4-431-54859-1.

Koschmieder, E. L. (**1974**): *Bénard Convection*. In: Prigogine, I.; Rice, S. A. (Eds.). *Advances in Chemical Physics, Volume 26*. New York: John Wiley and Sons, pp. 177–212. ISBN: 9780470143780.

Koschmieder, E. L.; Biggerstaff, M. I. (**1986**): *Onset of surface-tension-driven Bénard convection*. In *J Fluid Mech* 167, p. 49. DOI: 10.1017/S0022112086002720.

Koschmieder, E. L.; Switzer, D. W. (**1992**): *The wavenumbers of supercritical surface-tension-driven Bénard convection*. In *J Fluid Mech* 240 (-1), p. 533. DOI: 10.1017/S0022112092000181.

Krenn, J.; Scharfer, P.; Schabel, W. (**2011**): *Visualization of surface deformations during thin film drying using a Digital-Image-Correlation method*. In *Chem Eng Process* 50 (5-6), pp. 569–573. DOI: 10.1016/j.cep.2010.10.005.

Kriesten, E.; Voda, M. A.; Bardow, A.; Göke, V.; Casanova, F.; Blümich, B.; Koss, H.-J.; Marquardt, W. (**2009**): *Direct determination of the concentration dependence of diffusivities using combined model-based Raman and NMR experiments*. In *Fluid Phase Equilibria* 277 (2), pp. 96–106. DOI: 10.1016/j.fluid.2008.10.012.

Ku, H.-C.; Wang, C.-C.; Tu, C.-H. (**2008**): *Densities, Viscosities, Refractive Indexes, and Surface Tensions for Binary and Ternary Mixtures of Tetrahydofuran, 2-Propanol, and 2,2,4-Trimethylpentane*. In *J Chem Eng Data* 53 (2), pp. 566–573. DOI: 10.1021/je700626v.

Kumacheva, E.; Li, L.; Winnik, M. A.; Shinozaki, D. M.; Cheng, P. C. (**1997**): *Direct Imaging of Surface and Bulk Structures in Solvent Cast Polymer Blend Films*. In *Langmuir* 13 (9), pp. 2483–2489. DOI: 10.1021/la961089i.

Kumberg, J.; Baunach, M.; Eser, J. C.; Altvater, A.; Scharfer, P.; Schabel, W. (**2020**): *Investigation of Drying Curves of Lithium-Ion Battery Electrodes with a New Gravimetrical Double-Side Batch Dryer Concept Including Setup Characterization and Model Simulations*. In *Energy Technol.*, p. 2000889. DOI: 10.1002/ente.202000889.

Langhe, D.; Ponting, M. (**2016**): *Manufacturing and Novel Applications of Multilayer Polymer Films*. Amsterdam: William Andrew / Elsevier (Plastics Design Library (PDL) Handbook Series). ISBN: 978-0-323-37125-4.

Li, C.; Wang, W.; Wang, Z. (**2000a**): *A surface tension model for liquid mixtures based on the Wilson equation*. In *Fluid Phase Equilibria* 175 (1-2), pp. 185–196. DOI: 10.1016/S0378-3812(00)00447-7.

Li, J.; Xue, F.; Blu, T. (**2017**): *Fast and accurate three-dimensional point spread function computation for fluorescence microscopy*. In *J Opt Soc Am A* 34 (6), pp. 1029–1034. DOI: 10.1364/JOSAA.34.001029.

Li, M.; Xu, S.; Kumacheva, E. (**2000b**): *Convection in Polymeric Fluids Subjected to Vertical Temperature Gradients*. In *Macromolecules* 33 (13), pp. 4972–4978. DOI: 10.1021/ma992156t.

Li, Z.; Lu, B. C.-Y. (**2001a**): *On the prediction of surface tension for multicomponent mixtures*. In *The Canadian Journal of Chemical Engineering* 79 (3), pp. 402–411. DOI: 10.1002/cjce.5450790313.

Li, Z.; Lu, B. C.-Y. (**2001b**): *Surface tension of aqueous electrolyte solutions at high concentrations — representation and prediction*. In *Chemical Engineering Science* 56 (8), pp. 2879–2888. DOI: 10.1016/S0009-2509(00)00525-X.

Lindken, R.; Rossi, M.; Grosse, S.; Westerweel, J. (**2009**): *Micro-Particle Image Velocimetry (microPIV): recent developments, applications, and guidelines*. In *Lab Chip* 9 (17), pp. 2551–2567. DOI: 10.1039/b906558j.

Luo, S.-C.; Craciun, V.; Douglas, E. P. (**2005**): *Instabilities during the formation of electroactive polymer thin films*. In *Langmuir* 21 (7), pp. 2881–2886. DOI: 10.1021/la047702c.

Machrafi, H.; Rednikov, A.; Colinet, P.; Dauby, P. (**2010**): *Bénard instabilities in a binary-liquid layer evaporating into an inert gas*. In *Journal of Colloid and Interface Science* 349 (1), pp. 331–353. DOI: 10.1016/j.jcis.2010.04.043.

Macleod, D. B. (**1923**): *On a relation between surface tension and density*. In *Trans. Faraday Soc.* 19 (July), p. 38. DOI: 10.1039/TF9231900038.

Mamaliga, I.; Schabel, W.; Kind, M. (**2004**): *Measurements of sorption isotherms and diffusion coefficients by means of a magnetic suspension balance*. In *Chem Eng Process* 43 (6), pp. 753–763. DOI: 10.1016/S0255-2701(03)00077-1.

Mancini, H.; Maza, D. (**2004**): *Pattern formation without heating in an evaporative convection experiment*. In *EPL* 66 (6), pp. 812–818. DOI: 10.1209/epl/i2003-10266-0.

McTaggart, C. L. (**1983**): *Convection driven by concentration- and temperature-dependent surface tension*. Journal of Fluid Mechanics, 134(-1), 301. In *J Fluid Mech* 134, pp. 301–310. DOI: 10.1017/S0022112083003377.

Merklein, L.; Eser, J. C.; Börnhorst, T.; Könnecke, N.; Scharfer, P.; Schabel, W. (**2021**): *Different dominating mass transport mechanisms for drying and sorption of toluene-PMMA films – Visualized with Raman spectroscopy*. In *Polymer* 222, p. 123640. DOI: 10.1016/j.polymer.2021.123640.

Merkt, D.; Bestehorn, M. (**2003**): *Bénard–Marangoni convection in a strongly evaporating fluid*. In *Physica D* 185 (3-4), pp. 196–208. DOI: 10.1016/S0167-2789(03)00234-3.

Mueller, F.; Krueger, K.-M.; Sadowski, G. (**2012**): *Non-Fickian Diffusion of Toluene in Polystyrene in the Vicinity of the Glass-Transition Temperature*. In *Macromolecules* 45 (2), pp. 926–932. DOI: 10.1021/ma202283e.

Müller, M. (**2013**): *Zum Stofftransport schwer flüchtiger Additive in Polymerbeschichtungen: Untersuchungen mit Hilfe der konvokalen Mikro-Raman-Spektroskopie*. Doctoral Thesis at Karlsruhe Institute of Technology (KIT). Karlsruhe: KIT Scientific Publishing. ISBN: 978-3-86644-997-8.

Naseri, A. T.; Cetindag, E.; Bilgili, E.; Davé, R. N. (**2019**): *A predictive transport model for convective drying of polymer strip films loaded with a BCS Class II drug*. In *Eur J Pharm Biopharm* 137, pp. 164–174. DOI: 10.1016/j.ejpb.2019.02.023.

Nepomnyashchy, A. A.; Velarde, M. G.; Colinet, P. (**2001**): *Interfacial Phenomena and Convection*. Boca Raton, FL: Chapman and Hall/CRC. ISBN: 9781482296303.

Nield, D. A. (**1964**): *Surface tension and buoyancy effects in cellular convection*. In *J Fluid Mech* 19 (03), p. 341. DOI: 10.1017/S0022112064000763.

Ober, R.; Paz, L.; Taupin, C.; Pincus, P.; Boileau, S. (**1983**): *Study of the surface tension of polymer solutions: theory and experiments. Good solvent conditions*. In *Macromolecules* 16 (1), pp. 50–55. DOI: 10.1021/ma00235a010.

Ohring, M. (**2002**): *Materials science of thin films: Deposition and structure*. 2nd ed. San Diego, CA: Academic Press. ISBN: 0-12-524975-6.

Oliphant, T. E. (**2006**): *A guide to numpy*. USA: Trelgol Publishing. Available online at http://www.numpy.org/.

Oron, A.; Davis, S. H.; Bankoff, S. G. (**1997**): *Long-scale evolution of thin liquid films*. In *Rev Mod Phys* 69 (3), pp. 931–980. DOI: 10.1103/RevModPhys.69.931.

Owens, D. K.; Wendt, R. C. (**1969**): *Estimation of the surface free energy of polymers*. In *J. Appl. Polym. Sci.* 13 (8), pp. 1741–1747. DOI: 10.1002/app.1969.070130815.

Palmer, H. J.; Berg, J. C. (**1971**): *Convective instability in liquid pools heated from below*. In *Journal of Fluid Mechanics* 47 (4), pp. 779–787. DOI: 10.1017/S0022112071001368.

Park, J. S.; Choi, C. K.; Kihm, K. D. (**2005**): *Temperature measurement for a nanoparticle suspension by detecting the Brownian motion using optical serial sectioning microscopy (OSSM)*. In *Meas Sci Technol* 16 (7), pp. 1418–1429. DOI: 10.1088/0957-0233/16/7/003.

Park, J. S.; Kihm, K. D. (**2006**): *Three-dimensional micro-PTV using deconvolution microscopy*. r. In *Exp Fluids* 40 (3), pp. 491–499. DOI: 10.1007/s00348-005-0090-9.

Pearson, J. R. A. (**1958**): *On convection cells induced by surface tension*. In *J Fluid Mech* 4 (05), p. 489. DOI: 10.1017/S0022112058000616.

Poling, B. E.; Prausnitz, J. M.; O'Connell, J. P. (**2001**): *The properties of gases and liquids*. 5th ed. New York: McGraw-Hill. ISBN: 0-07-011682-2.

Rabel, W. (**1971**): *Einige Aspekte der Benetzungstheorie und ihre Anwendung auf die Untersuchung und Veränderung der Oberflächeneigenschaften von Polymeren*. In *Farbe und Lack* 77 (10).

Raffel, M.; Willert, C. E.; Kompenhans, J. (**1998**): *Particle Image Velocimetry: A Practical Guide*. Berlin: Springer. ISBN: 978-3-662-03639-6.

Rahal, S.; Cerisier, P.; Azuma, H. (**2007**): *Bénard–Marangoni convection in a small circular container: influence of the Biot and Prandtl numbers on pattern dynamics and free surface deformation*. In *Exp Fluids* 43 (4), pp. 547–554. DOI: 10.1007/s00348-007-0323-1.

Ramesh, N.; Duda, J. L. (**2000**): *Diffusion in polymers below the glass transition temperature: Comparison of two approaches based on free volume* *concepts*. In *Korean J. Chem. Eng.* 17 (3), pp. 310–317. DOI: 10.1007/BF02699046.

Rastogi, A. K.; St. Pierre, L. E. (**1971**): *Interfacial phenomena in macromolecular systems*. In *J Colloid Interface Sci* 35 (1), pp. 16–22. DOI: 10.1016/0021-9797(71)90179-2.

Raupp, S. M.; Siebel, D. K.; Kitz, P. G.; Scharfer, P.; Schabel, W. (**2017**): *Interdiffusion in Polymeric Multilayer Systems Studied by Inverse Micro-Raman Spectroscopy*. In *Macromolecules* 50 (17), pp. 6819–6828. DOI: 10.1021/acs.macromol.7b01037.

Lord **Rayleigh**, O.M. F.R.S. (**1916**): *LIX. On convection currents in a horizontal layer of fluid, when the higher temperature is on the under side*. In *Philosophical Magazine Series 6* 32 (192), pp. 529–546. DOI: 10.1080/14786441608635602.

Redlich, O.; Kister, A. T. (**1948**): *Algebraic Representation of Thermodynamic Properties and the Classification of Solutions*. In *Ind. Eng. Chem.* 40 (2), pp. 345–348. DOI: 10.1021/ie50458a036.

Riley, R. J.; Neitzel, G. P. (**1998**): *Instability of thermocapillary–buoyancy convection in shallow layers. Part 1. Characterization of steady and oscillatory instabilities*. In *J Fluid Mech* 359, pp. 143–164. DOI: 10.1017/S0022112097008343.

Roe, R.-J. (**1968**): *Surface tension of polymer liquids*. In *J. Phys. Chem.* 72 (6), pp. 2013–2017. DOI: 10.1021/j100852a025.

Romdhane, I. H.; Price, P. E.; Miller, C. A.; Benson, P. T.; Wang, S. (**2001**): *Drying of Glassy Polymer Films*. In *Ind. Eng. Chem. Res.* 40 (14), pp. 3065–3075. DOI: 10.1021/ie001110h.

Sakurai, S.; Furukawa, C.; Okutsu, A.; Miyoshi, A.; Nomura, S. (**2002**): *Control of mesh pattern of surface corrugation via rate of solvent evaporation in solution casting of polymer film in the presence of convection*. In *Polymer* 43 (11), pp. 3359–3364. DOI: 10.1016/S0032-3861(02)00156-8.

Sankaran, A.; Yarin, A. L. (**2018**): *Evaporation-driven thermocapillary Marangoni convection in liquid layers of different depths*. In *Int J Heat Mass Transf* 122, pp. 504–514. DOI: 10.1016/j.ijheatmasstransfer.2018.01.136.

Santos, B.M.S.; Ferreira, A.G.M.; Fonseca, I.M.A. (**2003**): *Surface and interfacial tensions of the systems water + n-butyl acetate + methanol and water + n-pentyl acetate + methanol at 303.15 K*. In *Fluid Phase Equilibria* 208 (1-2), pp. 1–21. DOI: 10.1016/S0378-3812(02)00320-5.

Saranjam, N.; Chandra, S.; Mostaghimi, J.; Fan, H.; Simmer, J. (**2016**): *Orange peel formation due to surface tension-driven flows within drying paint films*. In *J Coat Technol Res* 13 (3), pp. 413–426. DOI: 10.1007/s11998-015-9752-6.

Savitzky, A.; Golay, M. J. E. (**1964**): *Smoothing and Differentiation of Data by Simplified Least Squares Procedures*. In *Anal Chem* 36 (8), pp. 1627–1639. DOI: 10.1021/ac60214a047.

Schabel, W. (**2004a**): *Trocknung von Polymerfilmen: Messung von Konzentrationsprofilen mit der Inversen-Mikro-Raman-Spektroskopie*. Doctoral Thesis at University of Karlsruhe. Aachen: Shaker. ISBN: 978-3-8322-2997-9.

Schabel, W. (**2005**): *Inverse Mikro-Raman-Spektroskopie - Eine neue Messmethode zur Untersuchung lokaler Stofftransportvorgänge in dünnen Filmen, Folien und Membranen*. In *Chemie Ingenieur Technik* 77 (12), pp. 1915–1926. DOI: 10.1002/cite.200500060.

Schabel, W.; Ludwig, I.; Kind, M. (**2004b**): *Measurements of Concentration Profiles in Polymeric Solvent Coatings by Means of an Inverse Confocal Micro Raman Spectrometer—Initial Results*. In *Drying Technology* 22 (1-2), pp. 285–294. DOI: 10.1081/DRT-120028234.

Schabel, W.; Scharfer, P.; Kind, M.; Mamaliga, I. (**2007**): *Sorption and diffusion measurements in ternary polymer–solvent–solvent systems by means of a magnetic suspension balance—Experimental methods and correlations with a modified Flory–Huggins and free-volume theory*. In *Chemical Engineering Science* 62 (8), pp. 2254–2266. DOI: 10.1016/j.ces.2006.12.062.

Scharfer, P. (**2009**): *Zum Stofftransport in Brennstoffzellenmembranen: Untersuchungen mit Hilfe der konfokalen Mikro-Raman-Spektroskopie*. Doctoral Thesis at Karlsruhe Institute of Technology (KIT). Karlsruhe: KIT Scientific Publishing. ISBN: 978-3-86644-432-4.

Scharfer, P.; Schabel, W.; Kind, M. (**2008**): *Modelling of alcohol and water diffusion in fuel cell membranes—Experimental validation by means of in* *situ Raman spectroscopy*. In *Chemical Engineering Science* 63 (19), pp. 4676–4684. DOI: 10.1016/j.ces.2008.03.014.

Schatz, M. F.; Neitzel, G. P. (**2001**): *Experiments on Thermocapillary Instabilities*. In *Annu Rev Fluid Mech* 33 (1), pp. 93–127. DOI: 10.1146/annurev.fluid.33.1.93.

Schatz, M. F.; VanHook, S. J.; McCormick, W. D.; Swift, J. B.; Swinney, H. L. (**1995**): *Onset of Surface-Tension-Driven Bénard Convection*. In *Physical review letters* 75 (10), pp. 1938–1941. DOI: 10.1103/PhysRevLett.75.1938.

Schnell, M.; Wolf, B. A. (**2001**): *Excess viscosity and glass transition*. In *Polymer* 42 (21), pp. 8599–8605. DOI: 10.1016/S0032-3861(01)00372-X.

SCHOTT GmbH (Ed.) (**2021a**): *BOROFLOAT® 33 – Mechanical Properties*. Available online at https://www.schott.com/d/borofloat/723d30c8-cca0-4159-ad40-31e658dbf588/1.8/borofloat33_mech_eng_web_09_2020.pdf, checked on 2/3/2021.

SCHOTT GmbH (Ed.) (**2021b**): *BOROFLOAT® 33 – Thermal Properties*. Available online at https://www.schott.com/d/borofloat/4d03b8f4-0583-4139-9841-952114e60dee/1.0/schott-data-sheet-thermal-properties-borofloat-english-23112018.pdf, checked on 2/3/2021.

Schwabe, D.; Scharmann, A. (**1979**): *Some evidence for the existence and magnitude of a critical marangoni number for the onset of oscillatory flow in crystal growth melts*. In *Journal of Crystal Growth* 46 (1), pp. 125–131. DOI: 10.1016/0022-0248(79)90119-2.

Schweizer, P. M. (**1997**): *Experimental Methods*. In: Kistler, S. F.; Schweizer, P. M. (Eds.). *Liquid Film Coating*. Dordrecht: Springer. ISBN: 978-94-010-6246-6.

Scriven, L. E.; Sternling, C. V. (**1964**): *On cellular convection driven by surface-tension gradients: effects of mean surface tension and surface viscosity*. In *J Fluid Mech* 19 (3), pp. 321–340. DOI: 10.1017/S0022112064000751.

Serpetsi, S. K.; Yiantsios, S. G. (**2012**): *Stability characteristics of solutocapillary Marangoni motion in evaporating thin films*. In *Physics of Fluids (1994-present)* 24 (12), p. 122104. DOI: 10.1063/1.4771903.

Sharma, J.; Arya, R. K.; Verros, G. D. (**2019**): *A unified model for the drying of glassy polymer coatings*. In *Progress in Organic Coatings* 134, pp. 219–225. DOI: 10.1016/j.porgcoat.2019.04.067.

Sharma, J.; Tewari, K.; Arya, R. K. (**2017**): *Diffusion in polymeric systems–A review on free volume theory*. In *Progress in Organic Coatings* 111, pp. 83–92. DOI: 10.1016/j.porgcoat.2017.05.004.

Siebel, D.; Schabel, W.; Scharfer, P. (**2017a**): *Diffusion in quaternary polymer solutions—Model development and validation*. In *Progress in Organic Coatings* 110, pp. 187–194. DOI: 10.1016/j.porgcoat.2017.05.002.

Siebel, D.; Scharfer, P.; Schabel, W. (**2015**): *Determination of Concentration-Dependent Diffusion Coefficients in Polymer-Solvent Systems: Analysis of Concentration Profiles Measured by Raman Spectroscopy during Single Drying Experiments Excluding Boundary Conditions and Phase Equilibrium*. In *Macromolecules* 48 (23), pp. 8608–8614. DOI: 10.1021/acs.macromol.5b02144.

Siebel, D.; Scharfer, P.; Schabel, W. (**2016**): *Prediction of diffusion in a ternary solvent–solvent–polymer blend by means of binary diffusion data: Comparison of experimental data and simulative results*. In *Journal of Applied Polymer Science* 133 (36). DOI: 10.1002/app.43899.

Siebel, D. K. (**2017b**): *Zur Mehrkomponentendiffusion in Polymer-Lösemittel-Systemen: Untersuchungen im Kontext der Polymerfilmtrocknung mittels inverser Mikro-Raman-Spektroskopie*. Doctoral Thesis at Karlsruhe Institute of Technology (KIT). München: Verlag Dr. Hut. ISBN: 978-3-8439-3190-8.

Siow, K. S.; Patterson, D. (**1973**): *Surface thermodynamics of polymer solutions*. In *J. Phys. Chem.* 77 (3), pp. 356–365. DOI: 10.1021/j100622a012.

Smith, K. A. (**1966**): *On convective instability induced by surface-tension gradients*. In *J Fluid Mech* 24 (02), p. 401. DOI: 10.1017/S0022112066000727.

Smith, M. K.; Davis, S. H. (**1983**): *Instabilities of dynamic thermocapillary liquid layers. Part 2. Surface-wave instabilities*. In *J Fluid Mech* 132, pp. 145–162. DOI: 10.1017/S0022112083001524.

Speidel, M.; Jonáš, A.; Florin, E.-L. (**2003**): *Three-dimensional tracking of fluorescent nanoparticles with subnanometer precision by use of off-focus imaging*. In *Opt Lett* 28 (2), p. 69. DOI: 10.1364/OL.28.000069.

Sprow, F. B.; Prausnitz, J. M. (**1966**): *Surface tensions of simple liquid mixtures*. In *Trans. Faraday Soc.* 62, p. 1105. DOI: 10.1039/TF9666201105.

Strawhecker, K. E.; Kumar, S. K.; Douglas, J. F.; Karim, A. (**2001**): *The Critical Role of Solvent Evaporation on the Roughness of Spin-Cast Polymer Films*. In *Macromolecules* 34 (14), pp. 4669–4672. DOI: 10.1021/ma001440d.

Sugden, S. (**1924**): *CXLII.—A relation between surface tension, density, and chemical composition*. In *J. Chem. Soc., Trans.* 125 (0), pp. 1177–1189. DOI: 10.1039/CT9242501177.

Sultan, E.; Boudaoud, A.; Amar, M. B. (**2005**): *Evaporation of a thin film: Diffusion of the vapour and Marangoni instabilities*. In *J Fluid Mech* 543 (-1), p. 183. DOI: 10.1017/S0022112005006348.

Takashima, M. (**1981**): *Surface Tension Driven Instability in a Horizontal Liquid Layer with a Deformable Free Surface. II. Overstability*. In *J. Phys. Soc. Jpn.* 50 (8), pp. 2751–2756. DOI: 10.1143/JPSJ.50.2751.

Taylor, J. R. (**1997**): *An Introduction to Error Analysis: The Study of Uncertainties in Physical Measurements*. 2nd ed. Sausalito, CA: University Science Books. ISBN: 978-0935702422.

Thomson, J. (**1855**): *XLII. On certain curious motions observable at the surfaces of wine and other alcoholic liquors*. In *Philosophical Magazine Series 6* 10 (67), pp. 330–333. DOI: 10.1080/14786445508641982.

Tönsmann, M.; Ewald, D. T.; Scharfer, P.; Schabel, W. (**2021a**): *Surface tension of binary and ternary polymer solutions: Experimental data of poly(vinyl acetate), poly(vinyl alcohol) and polyethylene glycol solutions and mixing rule evaluation over the entire concentration range*. In *Surfaces and Interfaces* 26, p. 101352. DOI: 10.1016/j.surfin.2021.101352.

Tönsmann, M.; Kröhl, F.; Cavadini, P.; Scharfer, P.; Schabel, W. (**2019**): *Calibration Routine for Quantitative Three-Dimensional Flow Field Measurements in Drying Polymer Solutions Subject to Marangoni Convection*. In *Colloids and Interfaces* 3 (1), p. 39. DOI: 10.3390/colloids3010039.

Tönsmann, M.; Scharfer, P.; Schabel, W. (**2021b**): *Critical Solutal Marangoni Number Correlation for Short-Scale Convective Instabilities in Drying Poly(vinyl acetate)-Methanol Thin Films*. In *Polymers* 13 (17). DOI: 10.3390/polym13172955.

Tönsmann, M.; Scharfer, P.; Schabel, W. (**2021c**): *Transient Three-Dimensional Flow Field Measurements by Means of 3D µPTV in Drying Poly(Vinyl Acetate)-Methanol Thin Films Subject to Short-Scale Marangoni Instabilities*. In *Polymers* 13 (8), p. 1223. DOI: 10.3390/polym13081223.

Topping, D. O.; McFiggans, G. B.; Kiss, G.; Varga, Z.; Facchini, M. C.; Decesari, S.; Mircea, M. (**2007**): *Surface tensions of multi-component mixed inorganic/organic aqueous systems of atmospheric significance: measurements, model predictions and importance for cloud activation predictions*. In *Atmos. Chem. Phys.* 7 (9), pp. 2371–2398. DOI: 10.5194/acp-7-2371-2007.

Torres, M. A.; Aimoli, C. G.; Beppu, M. M.; Frejlich, J. (**2005**): *Chitosan membrane with patterned surface obtained through solution drying*. In *Colloids and Surfaces A: Physicochemical and Engineering Aspects* 268 (1), pp. 175–179. DOI: 10.1016/j.colsurfa.2005.07.009.

Touazi, O.; Chénier, E.; Doumenc, F.; Guerrier, B. (**2010**): *Simulation of transient Rayleigh–Bénard–Marangoni convection induced by evaporation*. In *International Journal of Heat and Mass Transfer* 53 (4), pp. 656–664. DOI: 10.1016/j.ijheatmasstransfer.2009.10.029.

Toussaint, G.; Bodiguel, H.; Doumenc, F.; Guerrier, B.; Allain, C. (**2008**): *Experimental characterization of buoyancy- and surface tension-driven convection during the drying of a polymer solution*. In *Int J Heat Mass Transf* 51 (17-18), pp. 4228–4237. DOI: 10.1016/j.ijheatmasstransfer.2008.02.006.

Trouette, B.; Chénier, E.; Doumenc, F.; Delcarte, C.; Guerrier, B. (**2012**): *Transient Rayleigh-Bénard-Marangoni solutal convection*. In *Physics of Fluids (1994-present)* 24 (7), p. 74108. DOI: 10.1063/1.4733439.

Uyama, Y.; Inoue, H.; Ito, K.; Kishida, A.; Ikada, Y. (**1991**): *Comparison of different methods for contact angle measurement*. In *J Colloid Interface Sci* 141 (1), pp. 275–279. DOI: 10.1016/0021-9797(91)90322-Y.

Van Krevelen, D. W.; Nijenhuis, K. t. (**2009**): *Properties of polymers: Their correlation with chemical structure ; their numerical estimation and prediction from additive group contributions*. 4th ed. Amsterdam: Elsevier. ISBN: 978-0-08-054819-7.

Van Oss, C. J.; Chaudhury, M. K.; Good, R. J. (**1987**): *Monopolar surfaces*. In *Adv Colloid Interface Sci* 28, pp. 35–64. DOI: 10.1016/0001-8686(87)80008-8.

VanHook, S. J.; Schatz, M. F.; McCormick, W. D.; Swift, J. B.; Swinney, H. L. (**1995**): *Long-wavelength instability in surface-tension-driven Bénard convection*. In *Physical review letters* 75 (24), pp. 4397–4400. DOI: 10.1103/PhysRevLett.75.4397.

VanHook, S. J.; Schatz, M. F.; Swift, J. B.; McCormick, W. D.; Swinney, H. L. (**1997**): *Long-wavelength surface-tension-driven Bénard convection: Experiment and theory*. In *J Fluid Mech* 345, pp. 45–78. DOI: 10.1017/S0022112097006101.

Vazquez, G.; Alvarez, E.; Navaza, J. M. (**1995**): *Surface Tension of Alcohol Water + Water from 20 to 50.degree.C*. In *J Chem Eng Data* 40 (3), pp. 611–614. DOI: 10.1021/je00019a016.

VDI e.V. (Ed.) (**2013**): *VDI-Wärmeatlas*. 11th ed. Berlin: Springer Vieweg. ISBN: 978-3-642-19980-6.

Venerus, D. C.; Nieto Simavilla, D. (**2015**): *Tears of wine: new insights on an old phenomenon*. In *Sci Rep* 5 (1), p. 16162. DOI: 10.1038/srep16162.

Villers, D.; Platten, J. K. (**1992**): *Coupled buoyancy and Marangoni convection in acetone: experiments and comparison with numerical simulations*. In *J Fluid Mech* 234 (-1), p. 487. DOI: 10.1017/S0022112092000880.

Virtanen, P.; Gommers, R.; Oliphant, T. E.; Haberland, M.; Reddy, T.; Cournapeau, D.; Burovski, E.; Peterson, P.; Weckesser, W.; Bright, J.; Van der Walt, S. J.; Brett, M.; Wilson, J.; Millman, K. J.; Mayorov, N.; Nelson, A. R. J.; Jones, E.; Kern, R.; Larson, E.; Carey, C. J.; Polat, İ.; Feng, Y.;

Moore, E. W.; VanderPlas, J.; Laxalde, D.; Perktold, J.; Cimrman, R.; Henriksen, I.; Quintero, E. A.; Harris, C. R.; Archibald, A. M.; Ribeiro, A. H.; Pedregosa, F.; Van Mulbregt, P. (**2020**): *SciPy 1.0: fundamental algorithms for scientific computing in Python*. In *Nat Methods* 17 (3), pp. 261–272. DOI: 10.1038/s41592-019-0686-2.

Wanchoo, R. K.; Narayan, J. (**1992**): *Excess Properties of (Methanol + Toluene Or p -xylene) Binary Liquid Mixture*. In *Physics and Chemistry of Liquids* 25 (1), pp. 15–26. DOI: 10.1080/00319109208027283.

Wang, J.-m.; Liu, G.-h.; Fang, Y.-l.; Li, W.-k. (**2016**): *Marangoni effect in nonequilibrium multiphase system of material processing*. In *Rev Chem Eng* 32 (5), p. 2. DOI: 10.1515/revce-2015-0067.

Weh, L. (**2005**): *Surface Structures in Thin Polymer Layers Caused by Coupling of Diffusion-Controlled Marangoni Instability and Local Horizontal Temperature Gradient*. In *Macromol. Mater. Eng.* 290 (10), pp. 976–986. DOI: 10.1002/mame.200500165.

Wengeler, L. (**2014**): *Coating and drying processes for functional films in polymer solar cells - from laboratory to pilot scale*. Doctoral Thesis at Karlsruhe Institute of Technology (KIT). Karlsruhe: KIT Scientific Publishing. ISBN: 978-3-7315-0201-2.

Wereley, S. T.; Meinhart, C. D. (**2010**): *Recent Advances in Micro-Particle Image Velocimetry*. In *Annu Rev Fluid Mech* 42 (1), pp. 557–576. DOI: 10.1146/annurev-fluid-121108-145427.

Wiley, R. H.; Brauer, G. M. (**1949**): *Specific refractivity-temperature data for polyvinyl acetate and polybutyl acrylate*. In *J. Polym. Sci.* 4 (3), pp. 351–357. DOI: 10.1002/pol.1949.120040310.

Williams, M. L.; Landel, R. F.; Ferry, J. D. (**1955**): *The Temperature Dependence of Relaxation Mechanisms in Amorphous Polymers and Other Glass-forming Liquids*. In *J. Am. Chem. Soc.* 77 (14), pp. 3701–3707. DOI: 10.1021/ja01619a008.

Wohlfarth, C.; Lechner, M. D. (Eds.) (**2016**): *Surface Tension of Pure Liquids and Binary Liquid Mixtures*. Berlin: Springer. ISBN: 978-3-662-48335-0.

Wu, K.-H.; Lu, S.-Y.; Chen, H.-L.; Chen, Y.-Y. (**2008**): *Two-Dimensional Marangoni-Instability-Induced Periodic Patterns of Polymer Blend Films Cast on Tilted Substrates*. In *Macromol. Chem. Phys.* 209 (6), pp. 615–624. DOI: 10.1002/macp.200700471.

Wu, S. (**1969**): *Surface and interfacial tensions of polymer melts*. In *J Colloid Interface Sci* 31 (2), pp. 153–161. DOI: 10.1016/0021-9797(69)90321-X.

Xu, S.; Li, M.; Mitov, Z.; Kumacheva, E. (**2003**): *Surface textures induced by convection in thin films of polymeric and polymerizable fluids*. In *Progress in Organic Coatings* 48 (2), pp. 227–235. DOI: 10.1016/j.porgcoat.2003.02.001.

Xue, L.; Zhang, J.; Han, Y. (**2012**): *Phase separation induced ordered patterns in thin polymer blend films*. In *Progress in Polymer Science* 37 (4), pp. 564–594. DOI: 10.1016/j.progpolymsci.2011.09.001.

Zhang, N.; Chao, D. F. (**1999**): *Mechanisms of convection instability in thin liquid layers induced by evaporation*. In *International Communications in Heat and Mass Transfer* 26 (8), pp. 1069–1080. DOI: 10.1016/S0735-1933(99)00098-6.

Ziegler, H. (**1981**): *Properties of Digital Smoothing Polynomial (DISPO) Filters*. In *Appl Spectrosc* 35 (1), pp. 88–92. DOI: 10.1366/0003702814731798.

Zisman, W.A. (**1964**): *Relation of the Equilibrium Contact Angle to Liquid and Solid Constitution*. In: Fowkes, F. M. (Ed.). *Contact Angle, Wettability and Adhesion*. Washington, D.C.: American Chemical Society (Advances in Chemistry, vol. 43), pp. 1–51. ISBN: 0-8412-0044-0.

Appendix

A Additional 3D-µPTV-related Information

A.1 Magnification Template Matching and Lateral Offset

In order to accurately determine the lateral magnification of the 3D-µPTV setup as well as the lateral offset between multiple camera recordings, a template matching routine was implemented in *python*. The *OpenCV* library for image processing comprises a function for template matching (Bradski 2000). This function finds the best lateral matching position of a template image in a camera image. However, the function does not account for variations of the scale or rotation of the template. To find the scale, position and rotation of the micrometer scale in lateral calibration images (see section 2.2.1), an idealized template image of the micrometer scale was created in a vector image program (*CorelDraw*). Since the available template matching function does not account for variations in scale and rotation, two nested loops iterating over coarse steps of the scale and rotation of the template image were employed, and for each of the value pairs the best matching lateral position of the template in the camera image was found using the available *OpenCV* function. As this approach is computationally intensive, it was applied to downscaled camera calibration images. The resulting coarse best match is shown in Figure A.1, left. As a second step, the matching was further optimized by minimizing the sum of squared residuals between the grayscale values of the full resolution camera image and the template under variation of the lateral position, the scale and the rotation of the template image. This was implemented using the *minimize* function from the *scipy* library (Virtanen et al. 2020). The resulting optimized template match is shown in Figure A.1, right.

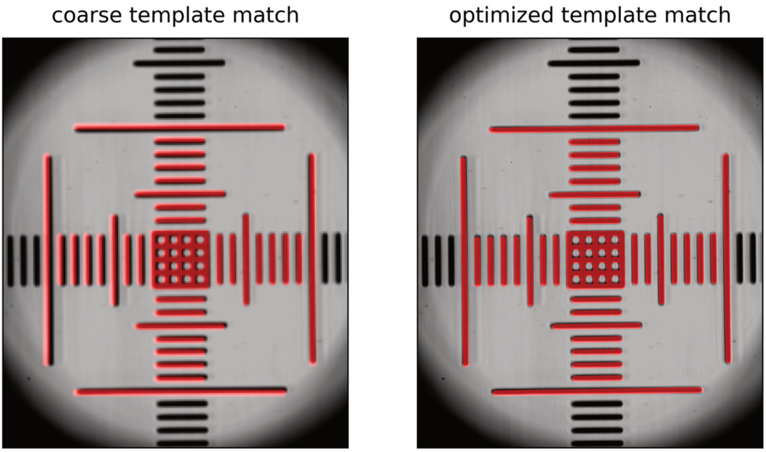

Figure A.1: Template matching of a micrometer scale for the accurate determination of the lateral magnification and lateral offset between multiple cameras as a function of the motorized lens position s_{axis}. The grayscale images are camera recordings, whereas the red overlay denotes the matched idealized template of the micrometer scale. Left: Coarse inital template match using the *OpenCV* function in two nested loops for scale and rotation variation. Right: Optimized template match after least-square minimization.

The template matching routine was applied to all lateral calibration images acquired for all three cameras of the 3D-µPTV setup utilized in drying experiments under variation of the motorized lens positions s_{axis} of each camera. The found lateral magnification of the camera with the upmost vertical focus position (backport camera without motorized lens system) was $M = 54.1$ and the values for the other two cameras are given in Figure A.2. The found lateral offset, using the upper (backport) camera as reference, is provided in Figure A.3. The angular offset was found to be $< 1°$ and was not corrected due to the small value.

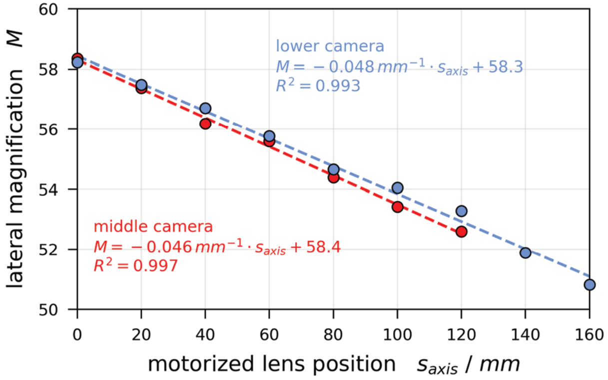

Figure A.2: Lateral magnification as a function of the motorized lens position s_{axis} of the cameras with middle and lowest position of the vertical focal plane used in drying experiments.

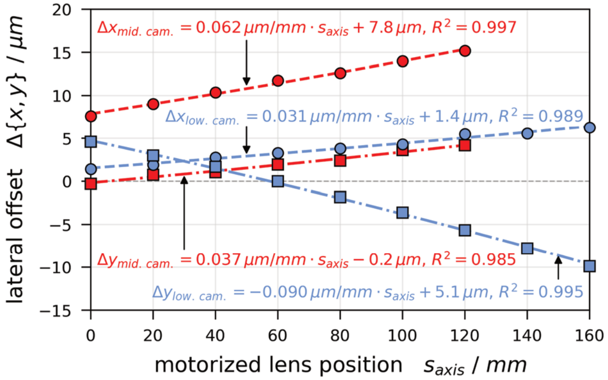

Figure A.3: Lateral offset between multiple cameras using the upmost camera (backport) as a reference.

A.2 Point Spread Function Simulation Input Parameters

Table A.1: Comprehensive list of optical input parameters for fast point spread function (PSF) simulations based on (Li et al. 2017).

Quantity	Value	Description
z_p	$0 - 200\ \mu m$	Vertical particle position
n_s	$1.0 - 1.6$	Refractive index of sample
NA	0.95	Numerical aperture of microscope lens
t_g^*	$110 - 230\ \mu m$	Design cover-glass thickness (adjustable with correction collar at lens)
t_g	$140 - 150\ \mu m$	Actual cover-glass thickness
n_g^*	1.526	Design refractive index of cover glass
n_g	1.526 ± 0.002	Actual refractive index of cover glass
t_i^*	$110 - 210\ \mu m$	Design immersion layer thickness (lens working distance)
n_i^*	1.00	Design refractive index of immersion medium (air)
n_i	1.00	Actual refractive index of immersion medium (air)

A.3 Additional Details Regarding Correction Factor f_r

The values of the correction factor f_r, introduced in section 2.2.5 and utilized in Figure 2.13, is shown in Figure A.4. It can be seen that for air as calibration sample medium (red), the correction factor is independent of the vertical particle layer position $\tilde{z}_{focus,p}$. This is expected behavior since in this case the refractive index of the sample and the immersion are identical. There is, however, a clear impact of the motorized lens position s_{axis} (different marker shapes) on the correction factor. Considering the sample media water and tesa (green and blue), the correction factor is additionally dependent on the vertical particle layer position within the calibration samples, showing a decreasing f_r value with increasing $\tilde{z}_{focus,p}$. It can further be seen that this dependency is similar for water and tesa (compare blue and green data sets with identical marker shape). As the transition between a sample refractive index of $n_s = 1.0$ and $n_s \geq 1.3$ is unlikely to be a step change, additional calibration samples with an intermediate refractive index would be required in order to understand the functional relation between f_r and n_s. Furthermore, the limited number of calibration samples makes it impossible to interpret to what extent the differences between water and tesa data are measurement uncertainties or an impact of the sample refractive index beyond $n_s \geq 1.3$. Hence, more reproductions and a finer graduation of vertical particle layer positions would be required. Since the correction factor f_r has additional shortcomings regarding experiment evaluation (discussed in section 2.3.3), the strategy of preparing and measuring additional calibration samples was discarded.

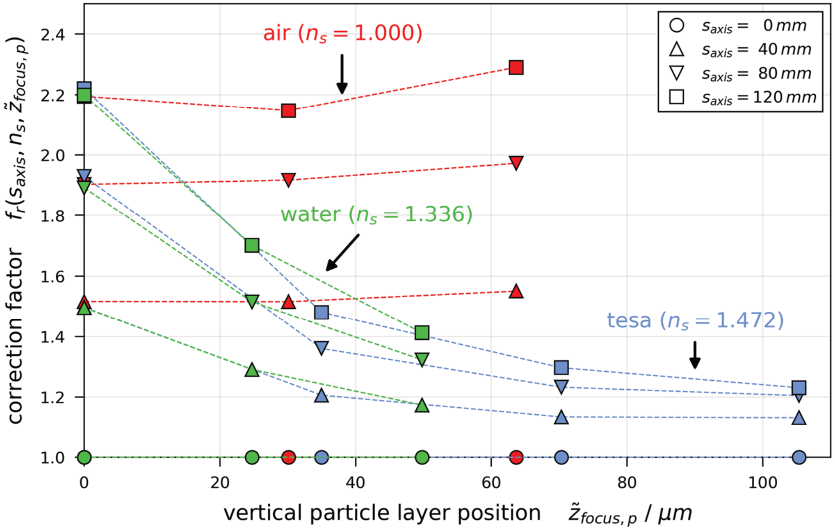

Figure A.4: Correction factor f_r, introduced in section 2.3.3, as function of vertical particle layer position in lens coordinates $\tilde{z}_{focus,p}$, calibration sample refractive index n_s, and motorized lens position s_{axis}.

A.4 Finding the Vertical Origin prior to Experiments

In order to find the vertical origin (top surface of the glass substrate) prior to drying experiments, two procedures have been tested but discarded. For the first approach, the micrometer scale used for lateral magnification calibration (see section 2.2.1) was placed on top of the glass substrate with the imprinted scale facing downwards, acting as a visual aid to find the substrate surface. Then, the vertical microscope lens position was manually adjusted until the camera with the upmost vertical focus plane position ($s_{axis} = 0\,mm$) showed a clear undistorted image of the micrometer scale, indicating that the scale was in focus. This vertical position was set to be the origin of $\tilde{z}_{piezo}$. Subsequently, the micrometer scale was removed, and the vertical lens position was set to the desired measurement position, using the piezo actuator. Afterwards, the sample film was coated and 3D-µPTV measurement was performed. Unfortunately, it was found that pressing down the knife coater on the glass substrate during coating, changes the vertical position of the glass substrate in the order of $10\,\mu m$, whereas the films under investigation had an initial wet-film thickness in the range of approximately 20 to $100\,\mu m$. This means that the change of the vertical origin during coating was large compared to the film thickness. Consequently, this procedure to find the vertical origin was not nearly precise enough for accurate experiment evaluation.

For the second approach to accurately detect the surface of the glass substrate, a small amount of tracer particle suspension was deposited and dried on the glass substrate prior to experiments, acting as an indicator of the upper substrate surface. Subsequently, the sample film was coated and a 3D-µPTV measurement was performed. Since the deposited particles were left on the substrate during experiments, their vertical position could be used as a precise indicator for the substrate surface during the postprocessing. Unfortunately, it was found that depositing tracer particles from the suspension resulted in laterally uneven distributed particles, with areas where no particle could be found and areas where large amounts of clusters or agglomerates formed during deposition. Even when not in focus, the fluorescent tracer particle clusters introduced a significant amount of background glow, which significantly deteriorated the detection of diffraction rings, using the GPU-accelerated algorithm. Therefore, this approach was also deemed unfeasible. It has to be noted that tracer particle deposition from suspension was also used for calibration sample preparation, also introducing lateral areas of many particle clusters and a resulting background glow. This was compensated by using significantly larger exposure times during camera recordings ($\approx 1\,s$) of the stationary particles in the samples. During drying experiments, however, the dynamics of the flow field require significantly smaller exposure times ($\approx 0.05\,s$). Hence, increasing the exposure time during the experiments in order to compensate the introduced background glow from particles deposited on the surface of the substrate is not a viable option.

A.5 Qualitative Error Propagation Assessment due to $s_{axis} > 0\ mm$ Correction

The error, resulting from the simplified vertical stitching procedure of multiple observation volumes (section 2.3.3) is a complex interplay between the impact of the motorized lens position on the vertical focus position of each camera (section 2.2.4) and the assumption that the observed tracer particles with lowest vertical position are likely to be very close to the substrate $z_{p,min} \approx 0.5\ \mu m$ (section 2.3.2). This is shown qualitatively in Figure A.5 left. The colored lines indicate lookup polynomials $z_p = P_4(r_{ring})$ for three cameras having three different vertical focus plane positions, with red, green and blue colors denoting the uncorrected polynomials directly obtained from PSF simulations (see Figure 2.14), the likely true course of the polynomials accounting for correction factor f_r, and the polynomials resulting from the simplified correction procedure using f_z, respectively. The correction factors are larger than unity for a motorized lens position of $s_{axis} > 0\ mm$, hence the lookup polynomials of the middle and lower camera have to be corrected. This results in a different slope of the lookup polynomials. The camera with the upmost focus position ($s_{axis} = 0\ mm$) remains uncorrected since the ring data coincide well with the simulated data (see Figure 2.12). Nevertheless, the correction procedure still affects the lookup polynomial of the upmost camera, which will be qualitatively explained in the following.

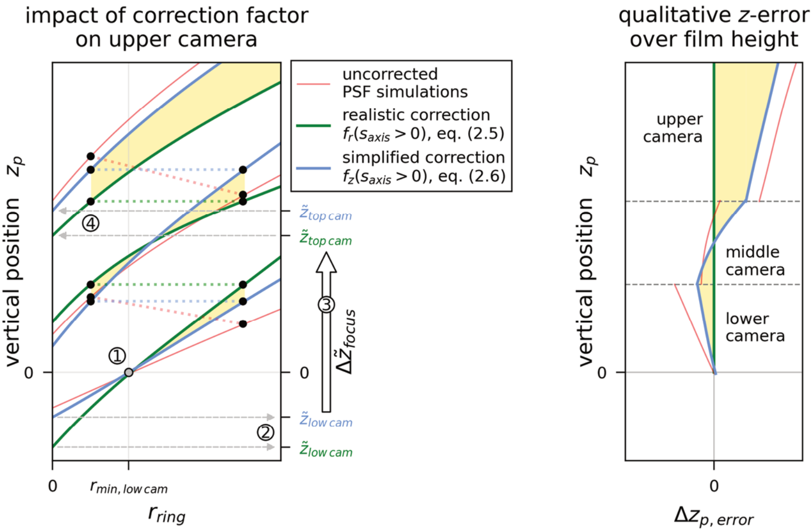

Figure A.5: Qualitative error assessment associated with the different correction procedures, accounting for the discrepancy in diffraction ring diameter when $s_{axis} > 0\,mm$. Left: Impact of the correction on the upper camera ($s_{axis} = 0\,mm$). Right: Error of reconstructed vertical particle positions for uncorrected lookup polynomials (red) and simply corrected polynomials (blue) in comparison with true positions (green).

In Figure A.5, the gray circle (1) indicates a particle observed with the lowest camera and having the smallest detected diffraction ring. Since it was assumed that such a particle is likely to be very close to the surface of the substrate, it serves as the vertical origin of the vertical lens coordinate $\tilde{z}$ as well as the true vertical position z_p. Due to the different slopes of the lookup polynomials, resulting from the different correction procedures, the correction affects the attributed vertical focus position in lens coordinates of the lowest camera $\tilde{z}_{low\ cam}$ (2). It was experimentally validated that the vertical shift in focus plane positions with the motorized lens positon is independent of the sample refractive index as well as the true vertical particle positions (see Figure 2.7) and can be calculated using equation (2.2) and (2.3). The correction procedure therefore also affects the attributed vertical focus position in lens coordinates $\tilde{z}_{top\ cam}$ of the upper cameras (3). Even though the lookup polynomial for the upmost camera needs no correction ($s_{axis} = 0\,mm$), the magnitude of $\tilde{z}_{top\ cam}$ still affects the choice of polynomial from the lookup table (4) (see also Figure 2.14b/c). The resulting qualitative error in the reconstructed vertical particle positions is shown in Figure A.5 right, resulting from the discrepancy between the uncorrected (red) or the simply corrected (blue) lookup polynomial in comparison with the assumed realistic course of the polynomials (green) in Figure A.5 left. The error made using the uncorrected polynomials is large for the lower and upper camera. The error is also discontinuous between adjacent observation volumes (different cameras) as shown exemplarily in Figure 2.17 as well as in Figure A.5 left and indicated by two connected markers. The simplified correction procedure, accounting for f_z, ensures vertical continuity (marker pairs having the same vertical position in Figure A.5 left) but it also affects the choice of the lookup polynomial for the upper camera as discussed earlier. The resulting qualitative error in vertical position reconstruction (blue line and yellow areas in Figure A.5 right) is noticeably smaller compared to the uncorrected use of polynomials derived from PSF-simulation, but it is largest in the upmost observation volume and increasing with increasing particle position. This explains the systematic discrepancy found by comparing 3D-µPTV derived drying curves and matched simulations in section 4.3.

A.6 Error Assessment

The approach to combine “off-focus imaging”, using the diffraction ring diameter to reconstruct the vertical tracer particle positions in combination with multifocal microscopy is new and unique to this dissertation. Hence, a detailed error analysis in form of worst-case errors is provided in this section.

Lateral Particle Position and Velocity

Based on superimposing detected diffraction rings over the recorded camera images, a worst case of 5 px discrepancy in ring radius and lateral ring center was estimated, which corresponds to ≈ 1 % of the lateral image resolution when using 4 × 4 pixel binning. Note that in the original publication of the ring detection algorithm, the matching error was found to be $< 1\ px$ (Cavadini et al. 2018).

The lateral position uncertainty of a single particle detection $\Delta\{x,y\}_{\mu m,single}$ can be calculated using

$$\Delta\{x,y\}_{\mu m,single} = \Delta\{x,y\}_{px} \cdot B \cdot d_{px}/M\ , \qquad \text{(A.1)}$$

where $B = 4$ is the utilized camera pixel binning and $d_{px} = 6.483\ \mu m/px$ the physical size of a camera sensor pixel, calculated from the overall dimension and resolution given in the camera data sheet. A maximal possible motorized lens position of $s_{axis} = 160\ mm$ entered in equation (2.1), results in a minimal lateral magnification of $M_{min} = 49$. With equation (A.1), this results in a maximal lateral position uncertainty of $\Delta\{x, y\}_{\mu m,single} \leq 2.65\ \mu m$ for an individual particle detection.

The found positions are smoothened using Savitsky-Golay filtering. With a minimum filtering interval of $\Delta t = 2\ s$ and a recording framerate of at least $10\ fps$, this results in a filtering window length of $N_{SG} \geq 21$ (next larger odd value). The resulting uncertainty due to filtering with a polynomial degree of 2 is given in (A.2) (Ziegler 1981; Gans and Gill 1983).

$$\Delta = \sqrt{\frac{3(3N_{SG}^2 - 7)}{4N_{SG}(N_{SG}^2 - 4)}}\Delta_{single} \tag{A.2}$$

This results in a lateral position uncertainty after filtering of $\Delta\{x, y\}_{\mu m} \leq 0.87\ \mu m$.

The velocity is calculated from particle positions at two different times, resulting in an individual uncertainty of $\Delta u_{lateral,single} \leq 2 \cdot \Delta\{x, y\}_{\mu m,single}/\Delta t = 2.65\ \mu m/s$, which reduces to $\Delta u_{lateral} \leq 0.87\ \mu m/s$ due to Savitsky-Golay filtering. The reported velocities have been additionally averaged over a large number of occurrences N_{av} in the reported velocity distributions. The error after averaging over several multiple occurrences reduces by a factor of $\sqrt{N_{av}}^{-1}$, for unidirectional statistical errors (Taylor 1997). With $N_{av} \geq 10$ this results in a lateral velocity error of $\Delta u_{lateral,av.} = \Delta u_{lateral}/\sqrt{N_{av}} \leq 0.28\ \mu m/s$. With increasing N_{av}, the error reduces significantly. Note that in the velocity distributions reported in this work N_{av} is in the order of 10^2 to 10^3, which would imply $\Delta u_{lateral,av.} \leq 0.1\ \mu m/s$.

Lateral Camera Stitching

The lateral offset correction between multiple cameras relies on identifying an arbitrary chosen reference point on the micrometer scale used for lateral magnification calibration reported in section 2.2.1 and Appendix A.1. The distance between the dashes on the micrometer scale (Figure 2.4) is 5 μm. It appears reasonable to assume that detecting a fifth of this distance is easily possible, resulting in a lateral stitching error of 1 μm. A possible angular displacement of the individual cameras was considered while using the template-matching approach detailed in Appendix A.1, but not corrected during experiment evaluation. It was found that the angular displacement is $\leq 1°$. The worst-case assumption would be, that the rotation centers have a maximal lateral distance equaling the lateral extent of the observation volume, which is approximately $250\ \mu m$. This results in a maximal lateral offset between two camera recordings of $\sin 1° \cdot 250\ \mu m = 4.3\ \mu m$. It can be concluded that the worst-case error due to lateral observation volume stitching is $\Delta\{x, y\}_{cam-stitching} \leq 4.3\ \mu m$.

Vertical Particle Position and Velocity

The reconstructed vertical particle positions are strongly influenced by the correction procedure, accounting for the discrepancy between simulated and experimentally derived diffraction ring sizes for motorized lens positions $s_{axis} > 0\ mm$. Hence, a rigorous error propagation analysis is unfeasible. Instead, several aspects are considered independently.

First, the impact of inaccurate ring detection is assessed. Assuming a maximum error of $\Delta r_{ring,px} \leq 5\ px$ converted to micrometer using equation (A.1) results in a worst-case error of $\Delta r_{ring,\mu m} \leq 2.65\ \mu m$. The impact of conversion to vertical particle position was considered by extracting the maximum (average) slope of simulated PSF lookup polynomials $3.2\ \mu m_z/\mu m_{r,ring}$ ($1.7\ \mu m_z/\mu m_{r,ring}$) multiplied by the maximum (average) correction factor $f_{z,max} = 2$ (1.4). The resulting error can then be calculated using

$$\Delta z_{p,max} = slope_{max} \cdot f_{z,max} \cdot \Delta r_{ring,\mu m} = 16.9\ \mu m\ . \tag{A.3}$$

Since this combination only occurs in rare occasions, the error was additionally calculated using averaged values for the lookup polynomial slope and correction factor. This results in $\Delta z_p = 6.3\ \mu m$. Resulting values based on the average slope are provided in parentheses. The application of Savitsky-Golay smoothing and averaging of velocity distributions discussed during the lateral error assessment is also valid for the vertical particle position and velocity. The resulting maximum (average slope and correction) errors after smoothing are $\Delta z_{p,SG} \leq 5.6\ \mu m$ ($2.1\ \mu m$).

The vertical velocity errors (see lateral error for calculation) are $\Delta u_{z,single} \leq 16.9\ \mu m/s$ ($6.3\ \mu m/s$) before and $\Delta u_z \leq 5.6\ \mu m/s$ ($2.1\ \mu m/s$) after Savitsky-Golay smoothing. Averaging over at least $N_{av} = 10$ particles further reduces the error to $\Delta u_{z,av} \leq 1.8\ \mu m/s$ ($0.7\ \mu m/s$). Note that in the velocity distributions reported in this work N_{av} is in the order of 10^2 to 10^3, which would imply $\Delta u_{z,av} \leq 0.6\ \mu m/s$ ($0.3\ \mu m/s$).

Vertical Camera Stitching

The aforementioned worst-case vertical position and velocity errors are only valid for individual observation volumes. Due to the complex error propagation associated with the correction procedure, qualitatively discussed in Appendix A.5, a rigorous error propagation analysis is unfeasible. Instead, the error associated with vertical stitching is assessed from experimental results. In section 4.3 (Figure 4.14), it was found that there is a systematic discrepancy between one-dimensional simulations and 3D-µPTV measurements regarding the transient film thickness for larger films, which is in accordance with the discussion in Appendix A.5. The relative error for large film thicknesses can be derived by comparing the initial wet film thickness of matched 1D simulations with 3D-µPTV results (Figure A.21, other factors are discussed in Appendix C). The largest systematic error of the initial wet film thickness was $\leq +16\ \%$ ($\leq +11\ \mu m$) for a film thickness in the range of approximately $65\ \mu m$ to $90\ \mu m$. For films with $h \leq 50\ \mu m$ it was $\leq +10.4\ \%$ ($\leq +4.8\ \mu m$). The dry film thickness resulting from 3D-µPTV evaluation was validated using a physical measuring probe (Appendix C.1). The resulting relative error for a dry film thickness in the range of $h_{dry} = 22.4$ to $39.5\ \mu m$ was $\Delta h_{dry}/h_{dry} \leq 4.5\ \%$.

Particle Sedimentation, Inertia and Brownian Motion

The effect of particle sedimentation, inertia and Brownian Motion were addressed in Tönsmann et al. (2019). Here, only the summarized results are presented. Assuming the highest initial solvent load $X_0 = 2\ g_{MeOH}/g_{PVAc}$ and therefore lowest viscosity in combination with Stoke's law (Raffel et al. 1998), results in a maximum sedimentation velocity of $u_s \leq 0.96\ \mu m/h$. Due to the exponential viscosity increase during drying (Figure 3.2), the sedimentation velocity will be orders of magnitude smaller during drying. It can be concluded that sedimentation is negligible.

The effect of tracer particles, lagging behind the flow of the surrounding liquid due to inertia can be assessed by calculating the time constant of an exponential relaxation law assuming a step change in liquid velocity (Raffel et al. 1998). The time constant was found to be $\tau \leq 2 \cdot 10^{-10}\ s$, clearly showing that inertia is not relevant and that the tracer particles faithfully follow the surrounding liquid (Tönsmann et al. 2019).

Due to the small diameter of the tracer particles ($d_p = 0.5\ \mu m$), particle diffusion and Brownian motion may introduce an error on the particle velocities. It was assessed that for $X_0 = 2\ g_{MeOH}/g_{PVAc}$ the resulting velocity is $\leq 1\ \mu m/s$, significantly decreasing with increasing viscosity during drying (Tönsmann et al. 2019). Savitsky-Golay smoothing and averaging for reported velocity distribution further reduces the impact of Brownian motion ($u_{BM,SG} \leq 0.4\ \mu m/s$, $u_{BM,av} \leq 0.1\ \mu m/s$). Hence, the effect is also negligible.

Summary Error Assessment

Table A.2 summarizes the heretofore-discussed worst-case errors. The realistic values are likely to be even smaller due to the large number of detected particles averaged and due to the worst-case assumption of 5 px uncertainty in ring detection, whereas the original publication indicates sub pixel accuracy (Cavadini et al. 2018).

Table A.2: Summary of the values derived by worst-case error assessment.

Property	Uncertainty	Details
$\Delta\{x, y\}$	$\leq 0.87\ \mu m$	Errors due to inaccurate ring detection. The velocity errors denote the maximum error in reported velocity distributions.
Δz_p	$\leq 2.1\ \ \mu m$	
$\Delta u_{lateral}$	$\leq 0.1\ \mu m/s$	
$\Delta u_{z,av}$	$\leq 0.3\ \mu m/s$	
$\lvert u_{z,s} \rvert$	$\leq 1\ \ \mu m/h$	Sedimentation
$\tau_{inertia}$	$\leq 2 \cdot 10^{-10}\ s$	Time constant of inertia relaxation.
u_{BM}	$\leq 0.1\ \mu m/s$	Brownian motion
$\Delta\{x, y\}_{stitching}$	$\leq 4.3\ \mu m$	Error due to observation volume stitching.
$(\Delta h/h)_{stitching}$	$\leq +16\ \%$	

B Material Properties

Densities and refractive indices have been measured using DMA 4100 M (Anton Paar) and Abbemat (Dr. Kernchen), respectively.

B.1 Methanol

Refractive Index

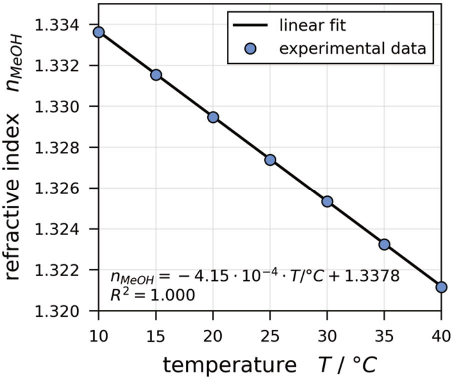

Figure A.6: Refractive index of methanol. Own measurement data and linear fit.

Table A.3: Tabulated measurement data of the refractive index of methanol.

Temperature / °C	Value
10	1.3336
15	1.3315
20	1.3295
25	1.3274
30	1.3253
35	1.3232
40	1.3212

Properties from Literature

Table A.4: Additional properties of pure methanol taken from VDI e.V. (2013).

Property	Unit	Value	T / °C
M	g/mol	32.04	–
λ	$W/(m \cdot K)$	0.20	10 to 30
c_p	$J/(kg \cdot K)$	2508	20
Δh_v	kJ/kg	1178.362	20
p^*	$mbar$	$10^{8.1974-\frac{1574.99}{\vartheta+238.86}}$	0 to 100

B.2 Poly(vinyl acetate)

According to the supplier the molar mass of the utilized PVAc is in the range of $M_w = 55 - 70\ kg/mol$.

Refractive Index

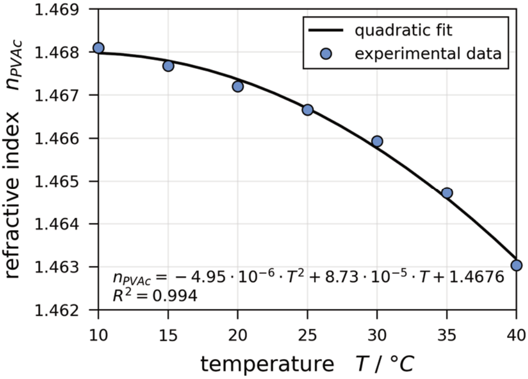

Figure A.7: Refractive index of poly(vinyl acetate). Own measurement data and quadratic fit.

Table A.5: Tabulated measurement data of the refractive index of poly(vinyl acetate).

Temperature / °C	Value
10	1.4681
15	1.4677
20	1.4672
25	1.4667
30	1.4659
35	1.4647
40	1.4630

Properties from Literature

Table A.6: Additional properties of pure poly(vinyl acetate) taken from Van Krevelen and Nijenhuis (2009).

Property	Unit	Value	T / $°C$
λ	$W/(m \cdot K)$	0.159	≈ 20
c_p	$J/(kg \cdot K)$	1449	20

B.3 Poly(vinyl acetate)-Methanol Solution

Density

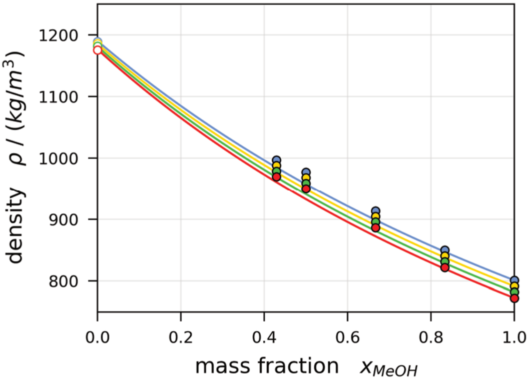

Figure A.8: Density of poly(vinyl acetate)-methanol at $T = 10, 20, 30$ and $40\ °C$. Filled values denote own measurement data, empty values for pure PVAc were taken from Wiley and Brauer (1949) and lines denote ideal mixing rule (eq. (A.4)).

Table A.7: Density of poly(vinyl acetate)-methanol in kg/m^3. Values for pure PVAc were taken from Wiley and Brauer (1949).

x_{MeOH}	$10\ °C$	$20\ °C$	$30\ °C$	$40\ °C$
1.000	800.8	791.5	782.0	772.5
0.833	850.1	840.8	831.4	821.9
0.667	913.8	904.7	895.6	886.3
0.500	977.3	968.3	959.1	949.9
0.429	997.0	988.0	978.9	969.8
0.000	1189.4	1186.3	1181.7	1175.8

Ideal mixing rule for the density of solutions (VDI e.V. 2013):

$$\rho = \left(\sum_i x_i \cdot \rho_i^{-1} \right)^{-1} \tag{A.4}$$

Flory-Huggins Interaction Parameter

Fit to experimental data between 20 $°C$ and 40 $°C$, taken from Schabel (2004a):

$$\chi = 1.1 \cdot \varphi_{MeOH}^2 - 1.9 \cdot \varphi_{MeOH} + 1.3 \tag{A.5}$$

Diffusion Coefficient

Fit to experimental data between 20 $°C$ and 60 $°C$, taken from Siebel (2017b):

$$D_{MeOH,PVAc}(T_{ref} = 20\,°C, X) = \exp\left(-\frac{30.39 + 111.17 \cdot X}{1 + 5.57 \cdot X}\right) m^2/s$$

$$D_{MeOH,PVAc}(T, X) = D_{MeOH,PVAc}(T_{ref}, X) \cdot \exp\left(-\frac{E_A}{\tilde{R}} \cdot \left(\frac{1}{T} - \frac{1}{T_{ref}}\right)\right) \tag{A.6}$$

$$E_A = \frac{70130.82 + 140655.58 \cdot X}{1 + 10.30 \cdot X}$$

Viscosity

The shear-rate-dependent measurement data are provided in Figure A.9 to Figure A.12, and the found zero-shear viscosity is summarized in table Table A.8.

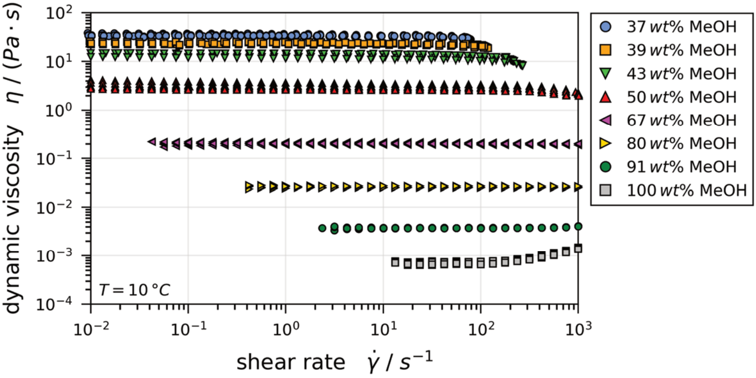

Figure A.9: Shear-rate-dependent measurement data of the dynamic viscosity of poly(vinyl acetate)-methanol solutions at $T = 10\,°C$.

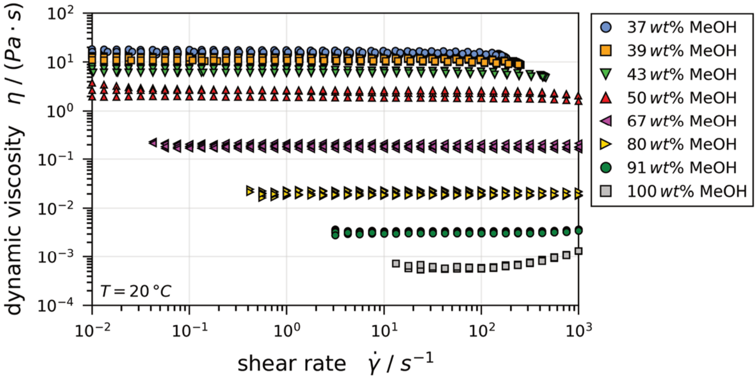

Figure A.10: Shear-rate-dependent measurement data of the dynamic viscosity of poly(vinyl acetate)-methanol solutions at $T = 20\ °C$.

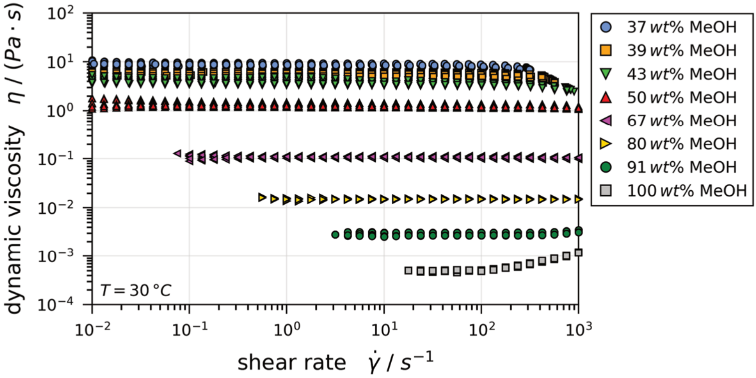

Figure A.11: Shear-rate-dependent measurement data of the dynamic viscosity of poly(vinyl acetate)-methanol solutions at $T = 30\ °C$.

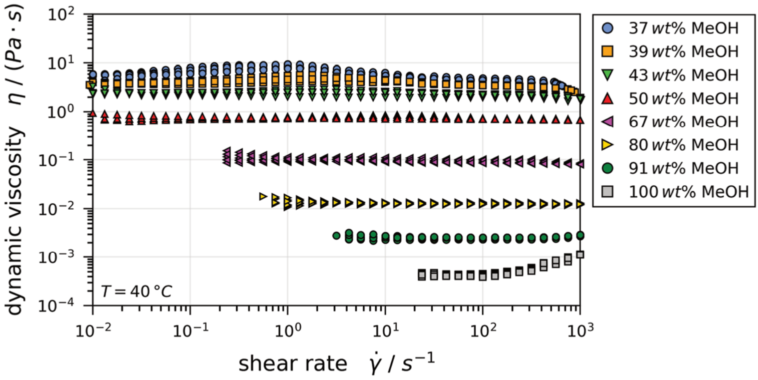

Figure A.12: Shear-rate-dependent measurement data of the dynamic viscosity of poly(vinyl acetate)-methanol solutions at $T = 40\,°C$.

Table A.8: Own experimental data for the zero-shear viscosity of poly(vinyl acetate)-methanol in $Pa \cdot s$.

x_{MeOH}	**10 °C**	**20 °C**	**30 °C**	**40 °C**
0.375	3.43E+01	1.61E+01	8.96E+00	6.66E+00
0.394	2.38E+01	1.16E+01	5.78E+00	4.18E+00
0.429	1.16E+01	6.70E+00	3.86E+00	2.35E+00
0.500	3.05E+00	2.20E+00	1.31E+00	7.45E-01
0.667	2.02E-01	1.78E-01	1.08E-01	1.03E-01
0.800	2.59E-02	1.99E-02	1.49E-02	1.30E-02
0.909	3.79E-03	3.23E-03	2.95E-03	2.55E-03
1.000	8.47E-04	7.27E-04	6.54E-04	5.75E-04

Fit parameters using equation (3.10) on own data in Table A.8:

$$
\begin{aligned}
A &= 4.2407 \cdot 10^{-8}\ Pa \cdot s \\
B &= 7533.73\ K \\
C_0 &= -38.870 \\
C_1 &= 0.07827\ K^{-1}
\end{aligned}
\tag{A.7}
$$

A qualitative discussion regarding lower methanol concentrations is provided in Appendix B.9.

Ideal Mixing Rule Equations for additional Properties

Table A.9: List of additional mixing rule equations used in this work.

Property	Mixing Rule Equation	Source
n	$\sum_i \varphi_i \cdot n_i$	Schabel (2004a)
λ	$\sum_i \sum_j \frac{2\varphi_i \varphi_j}{\lambda_i^{-1} + \lambda_j^{-1}}$	VDI e.V. (2013)
c_p	$\sum_i x_i \cdot c_p$	VDI e.V. (2013)

B.4 Borosilicate Glass Substrate

Table A.10: Thermal properties of glass substrates used in IMRS and 3D-μPTV experiments. Sources: SCHOTT GmbH (2021a) and SCHOTT GmbH (2021b).

Property	Unit	Value	T / °C
ρ	kg/m^3	2230	25
λ	$W/(m \cdot K)$	1.2	90
c_p	$J/(kg \cdot K)$	830	20 to 100

B.5 Raman Spectra and Calibration

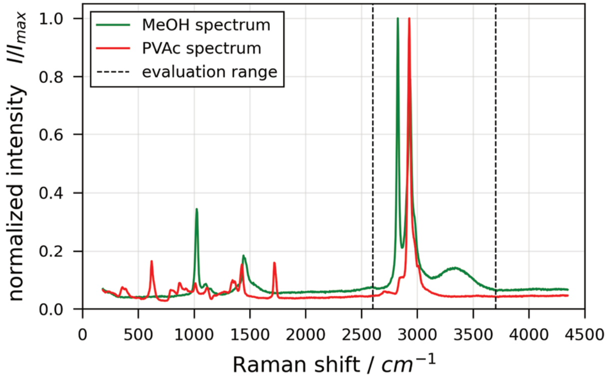

Figure A.13: Normalized Raman spectra of pure poly(vinyl acetate) and methanol used for IMRS experiment evaluation.

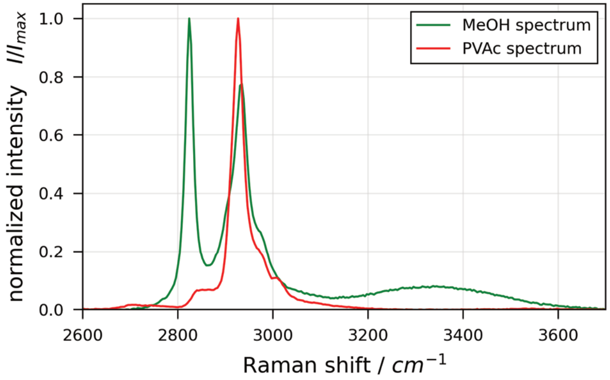

Figure A.14: Normalized Raman spectra of pure poly(vinyl acetate) and methanol in the evaluation range used for IMRS experiment evaluation.

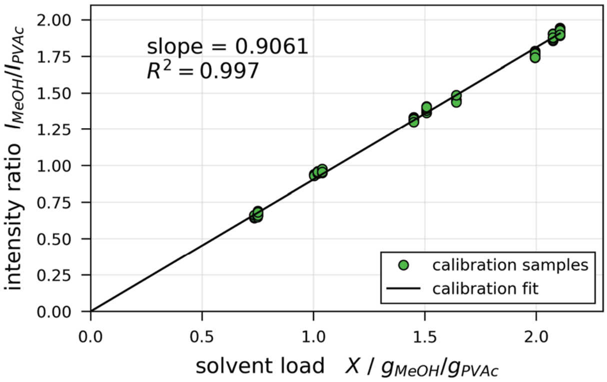

Figure A.15: Calibration curve of binary poly(vinyl acetate)-methanol solutions for IMRS experiment evaluation. Each marker denotes a calibration sample with known composition. The slope of the linear fit represents the calibration constant, necessary for IMRS experiment evaluation as proposed by Schabel (2005).

B.6 Solution Preparation for additional Surface Tension Measurements

The materials for additional surface tension measurements of polymer solutions were double-distilled water (3478.1, Carl Roth), toluene (7346.1, Carl Roth), 2-propanol (7343.2, Carl Roth), partially hydrolyzed poly(vinyl alcohol) (PVA, Poval LM-22, Kuraray) and polyethylene glycol (PEG, 0263.2, Carl Roth). All solutions were prepared by weight and mixed on a roll mixer, except for PEG solutions, which were stored at 40 $°C$ for several days until dissolution was complete.

B.7 Surface Energy of Polymers

Table A.11: Surface energy of polymers.

Polymer	$\sigma\ /\ mN/m$	Source
PVAc	$-0.066 \cdot T/°C + 36.5$	Wu (1969)
PVA	42	Van Oss et al. (1987)
PEG	$-0.101 \cdot T/°C + 42.4$	Rastogi and St. Pierre (1971)

B.8 Surface Tension of Ternary Polymer-Solvent-Solvent Mixtures

Regarding the surface tension of ternary mixtures ($N = 3$), some available mixing rule equations (e.g. eq. (3.12), section 3.7.4) comprise fit parameters of binary origin and therefore offer the possibility to predict the surface tension of ternary mixtures, based on the parameters fitted to the binary subsystems. In addition, all equations of excess type can be predicted using

$$\sigma_{123}^{E} = \sigma_{12}^{E} + \sigma_{13}^{E} + \sigma_{23}^{E} + \sigma_{T}^{E} \tag{A.8}$$

in combination with one of six equations for σ_{123}^{E}, compiled by Ku et al. (2008). Equation (A.9) denotes one of such relations. A total of six ternary predictive equations were tested (Tönsmann et al. 2021a).

$$\begin{aligned}\sigma_{123}^{E} = {} & \frac{4x_1x_2}{1-(x_1-x_2)^2}\sigma_{12}^{E}\left(\frac{1+x_1-x_2}{2},\frac{1-x_1+x_2}{2}\right) \\ & + \frac{4x_1x_3}{1-(x_1-x_3)^2}\sigma_{13}^{E}\left(\frac{1+x_1-x_3}{2},\frac{1-x_1+x_3}{2}\right) \\ & + \frac{4x_2x_3}{1-(x_2-x_3)^2}\sigma_{23}^{E}\left(\frac{1+x_2-x_3}{2},\frac{1-x_2+x_3}{2}\right)\end{aligned} \tag{A.9}$$

Alternatively, three different fit equations for σ_{T}^{E} in equation (A.8) were found, accounting for the non-ideality of ternary surface tension data (Redlich and Kister 1948; Santos et al. 2003; Ku et al. 2008). Equation (A.10) denotes the best matching equation for the ternary contribution to the excess surface tension.

$$\sigma_{T}^{E} = x_1x_2x_3\sum_{i=0}^{2}\sum_{j=0}^{2-i} C_{ij}x_1^{i}\,x_2^{j} \tag{A.10}$$

A possible strategy to avoid Marangoni-induced convective instabilities during polymer film drying is to avoid concentration-gradient-induced surface tension changes altogether. This may be achieved by utilizing a solvent with the same surface tension as the pure polymer. As it might be challenging to find such a matching polymer-solvent pair, an alternative approach could be to use solutions with two solvents, one having a higher surface tension than the pure polymer, and the other solvent having a lower surface tension than the pure polymer. In such a ternary polymer-solvent-solvent solution, a contour line with varying concentration but constant surface tension should exist. Therefore, the surface tension of two ternary polymer-solvent-solvent solutions has been investigated as well, while corresponding film drying experiments are reserved for future work. The ternary solution data were predicted by using the derived fit parameters of the respective binary subsystems in combination with equation (A.9) for the ternary excess surface tension σ_{123}^{E}. Alternatively, the ternary data were fitted using equations (3.11), (3.13) and (A.8) in combination with a ternary fit equation (A.10).

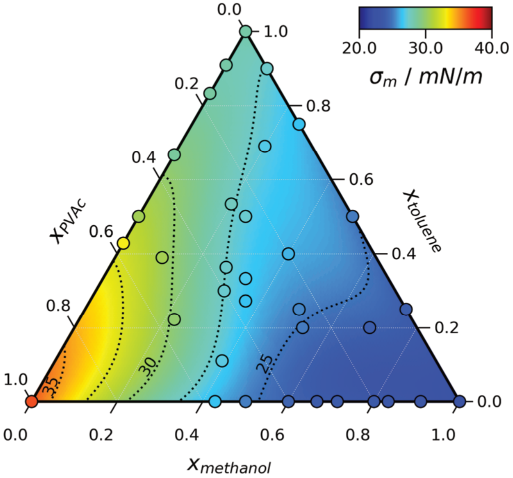

Figure A.16: Surface tension of ternary PVAc-methanol-toluene solution at 20 $°C$. Markers indicate experimental values and background denotes the best ternary fit using equations (3.11), (3.13), (A.8) and (A.10) ($AAD_{ternary,only}$ = 0.47 %, AAD_{all} = 0.61 %). The dotted lines indicate regions of constant surface tension. Comparing the color within the markers with the surrounding background color gives a visual impression of fit quality. *Reprint from Tönsmann et al. (2021a) with permission from Elsevier.*

Regarding fits to ternary surface tension data of poly(vinyl acetate)-toluene-methanol and poly(ethylene glycol)-methanol-water, equation (A.10) resulted in the best match with $AAD_{ternary,only}$ as little as 0.47 % and 0.79 %, respectively (Tönsmann et al. 2021a). The experimental data as well as fitted equation values are shown in Figure A.16and Figure A.17, respectively. Note that the marker colors denote the experimental values whereas the background color denotes the fitted mixing equation. A color comparison between marker and background indicates local differences.

Predicting the ternary data from fits to binary subsystems, however, revealed ambiguous results. For the strongly non-ideal poly(ethylene glycol)-methanol-water solutions, none of the predictive approaches revealed good agreement with experimental values ($AAD_{ternary,only} \geq 3.31\,\%$). Whereas the ternary surface tension of poly(vinyl acetate)-toluene-methanol could be predicted reasonably with an accuracy of $AAD_{ternary,only} = 1.36\,\%$, combining equations (3.11), (3.13), (A.8) and (A.9) (Tönsmann et al. 2021a).

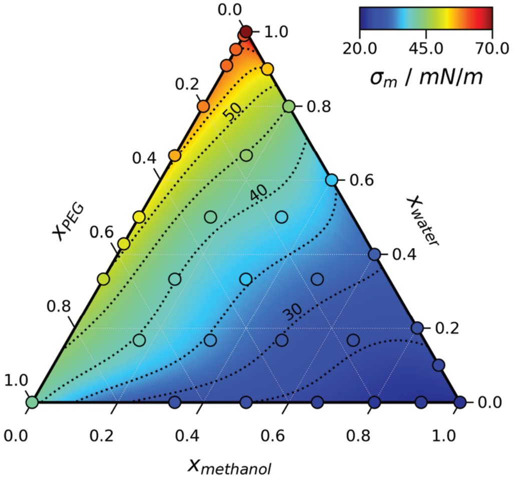

Figure A.17: Surface tension of ternary PEG-methanol-water solution at 30 °C. Markers indicate experimental values and background denotes the best ternary fit using equations (3.11), (3.13), (A.8) and (A.10) ($AAD_{ternary,only} = 0.79\,\%$, $AAD_{all} = 0.73\,\%$). The dotted lines indicate regions of constant surface tension. Comparing the color within the markers with the surrounding background color gives a visual impression of fit quality. *Reprint from Tönsmann et al. (2021a) with permission from Elsevier.*

B.9 Glass Transition and Viscosity at Lower Solvent Concentrations

The viscosity of poly(vinyl acetate)-methanol solutions was measured down to $x_{MeOH} \geq 0.37$ (see data in Appendix B.3). At lower concentrations, the measurement with the rheometer became challenging due to the high viscosity of the solution and continued evaporation of methanol. Hence, the lower concentration limit of the experimental data results. The obtained experimental data show excellent agreement with the fit equation (3.10), denoting an exponential dependency on concentration and an Arrhenius-like temperature dependency. With lower solvent concentrations, the glass transition temperature increases, which increasingly affects the rheology of the solution.

The glass transition temperature of pure PVAc is $T_g \approx 31 \pm 2\,°C$ (Schabel 2004a) and the added methanol acts as a plasticizer, significantly reducing T_g. Several equations are available to predict the concentration-dependent glass transition temperature from the pure components T_g. The glass transition temperature of pure methanol is $T_g \approx -163\,°C$ (Van Krevelen and Nijenhuis 2009). One popular equation is the Fox-Equation (e.g. Hiemenz et al. 2007)

$$\frac{1}{T_g} = \frac{x_{MeOH}}{T_{g,MeOH}} + \frac{1 - x_{MeOH}}{T_{g,PVAc}} \; . \qquad \text{(A.11)}$$

A different equation was suggested by Van Krevelen and Nijenhuis (2009)

$$T_g = \frac{T_{g,PVAc} + \left(K \cdot T_{g,MeOH} - T_{g,PVAc}\right) \cdot \varphi_{MeOH}}{1 + (K - 1) \cdot \varphi_{MeOH}} \; , \qquad \text{(A.12)}$$

with φ_{MeOH} being the volume fraction of methanol and K an adjustable parameter, which according to Van Krevelen and Nijenhuis is typically in the range of 1 to 3. Figure A.18 shows the most likely course of T_g with an increasing methanol concentration. At a drying temperature of $T \approx 20\,°C = T_g$ the corresponding methanol concentration is likely to be in the range of $x_{MeOH} = 1.3 - 3.8\,wt\%$. This is in reasonable agreement with experimental data of Schabel (2004a), who reported $T_g(x_{MeOH} = 4\,wt\%) \approx 15 \pm 6\,°C$.

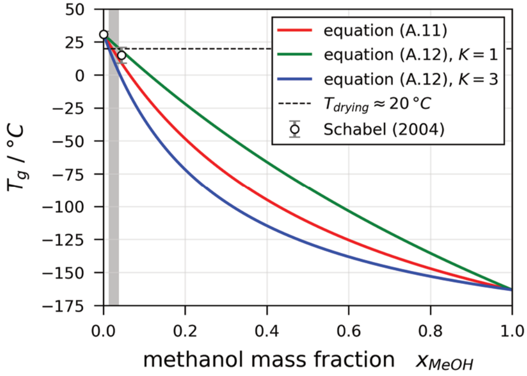

Figure A.18: Predicted concentration dependency of the glass transition temperature of poly(vinyl acetate)-methanol solutions. The grey area denotes the likely concentration range at which T_g equals the drying temperature employed in this dissertation.

The results of the convectively instable films presented in chapter 4 and 5 show that the end of Marangoni convection occurs before the glass transition temperature exceeds the drying temperature. It is known, however, that the rheological behavior changes when approaching the glass transition temperature, even if it is not reached (e.g. Baumgärtel and Willenbacher 1996; Van Krevelen and Nijenhuis 2009). The temperature dependency of the zero-shear viscosity, for example, is commonly described with an Arrhenius-like equation (as done in this work for fit equation (3.10)) for diluted solutions and when $T \gg T_g$ (Van Krevelen and Nijenhuis 2009). For concentrated polymer solutions and $T > T_g$, the Williams-Landel-Ferry (WLF) temperature-dependency is established (Williams et al. 1955).

A similar discrimination between diluted and concentrated solutions has to be considered when it comes to the concentration-dependent viscosity. Baumgärtel and Willenbacher (1996), as well as Van Krevelen and Nijenhuis (2009) propose different methods to predict the zero-shear viscosity of concentrated polymer solutions from pure polymer melt data. Both methods also include a dependency on the molar mass of the polymer. Since for PVAc utilized in this dissertation, only a range of $M_w = 55 - 70\ kg/mol$ is known, the following discussion is limited to the qualitative course of the zero-shear viscosity of concentrated polymer solutions. Figure A.19 shows the experimental data of the zero-shear viscosity (markers) and the utilized fit equation (3.10) (solid lines) in comparison with the qualitative course of concentrated polymer solutions (dashed lines) inferred from data of polystyrene-ethylenebenzene by Baumgärtel and Willenbacher (1996). It can be seen that extrapolating the utilized fit equation to lower methanol concentrations is likely to underpredict the true zero-shear viscosity.

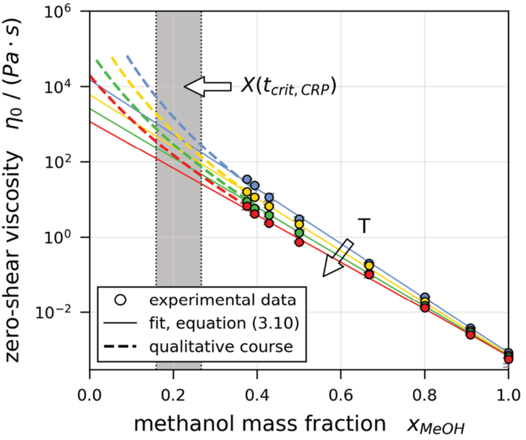

Figure A.19: Qualitative course of the zero-shear viscosity of concentrated polymer solutions (dashed lines) in comparison with experimental data (makers) and the fitted equation used in this work (solid lines). $T = 10, 20, 30, \text{and } 40\ °C$. The grey area denotes the concentration range at the end of the constant rate period from partially covered IMRS drying experiments reported in chapter 5.

C Additional Aspects Regarding the Comparability of 3D-µPTV Experiments and Drying Simulations

In Figure 4.14, it was shown that there is a systematic discrepancy between 3D-µPTV derived and simulated drying curves for larger film thicknesses and early drying times. Several aspects, which could account for this discrepancy, are discussed in the following subsection in detail.

C.1 Vertical Tracer Particle Distribution

Using an upper envelope curve on the transient vertical particle positions measured with 3D-µPTV with the intention to derive the transient film height requires that the tracer particles during 3D-µPTV experiments are distributed over the entire film height. Baesch (2017) investigated the impact of drying conditions on vertical particle distributions in polymer composite films. The coating solutions consisted of poly(vinyl alcohol)-water solutions and dispersed silica spheres with a diameter of $1\ \mu m$. She identified different drying regimes, where the suspended particles either accumulated at the bottom of the dry film, were evenly distributed over the film height, or accumulated at the surface of the dry film (evaporation regime). Among other results, she provided CryoSEM pictures of the vertical cross sections of two partially dried films from the evaporation regime. The micrographs revealed that the particles indeed accumulated near the film's free surface during drying but she also found that a particle-depleted top layer of approximately $5\ \mu m$ in a $\approx 250\ \mu m$ thick polymer film emerged during drying. This finding was attributed to a possible phase-separation of the polymer-solution during drying but no further investigation was undertaken.

The formation of such a particle depleted surface layer could explain the discrepancy in drying curves because this would imply that the dry-film thickness measured with 3D-µPTV does not reflect the actual dry-film thickness of the polymer film. If this was true, the matching drying simulations should be pinned to the initial wet-film thickness instead using the alleged dry-film thickness as input for the simulations.

This effect was investigated in this dissertation by performing additional drying experiments and using several methods to obtain the dry-film thickness. In order to exclude the possible effect of lateral temperature-control inhomogeneities, discussed in the next section, the films were dried on identical glass substrates as used for all experiments. These were attached to temperature-controlled substrate supports without a lens opening. The addition of fluorescent tracer particles is required for 3D-µPTV measurements, but the fluorescence signal makes Raman spectroscopy based IMRS measurements impossible. As a consequence, measuring the dry-film thickness of the identical film with 3D-µPTV and IMRS is not possible. The dry film thickness was therefore additionally measured using a physical probe (ID-H 543-561D, Mitutoyo). Films with tracer particles were prepared using an initial solvent load $X_0 = 1$ and 2 g_{MeOH}/g_{PVAc} and a coating gap of $h_{gap} = 200\ \mu m$ and were dried for at least two hours. The resulting dry-film thickness was measured using 3D-µPTV at three laterally different points. In addition, the thickness of all films was measured using the physical probe. The results are summarized in Table A.12.

Table A.12: Comparison of dry film thicknesses measured with 3D-µPTV and a physical measuring probe.

$X_0/(g_{MeOH}/g_{PVAc})$	$h_{dry,\mu PTV}/\mu m$	$h_{dry,probe}/\mu m$	$\Delta h_{dry}/\mu m$
1	40.2 ± 2.0	39.5 ± 1.7	$\mathbf{0.7 \pm 3.7}$
2	23.4 ± 1.6	22.4 ± 1.4	$\mathbf{1.0 \pm 3.0}$

It can be seen that the values are in good agreement, validating the dry-film thickness derived from 3D-µPTV measurements. Hence, it can be concluded that the effect of a particle depleted surface layer reported by Baesch (2017) does not occur during the experiments presented in this dissertation and that pinning the simulations to the experimentally derived dry-film thickness is legitimate.

C.2 Lateral Marangoni Flow

In section 4.2, it was confirmed that the transient film height of IMRS experiments and drying simulations are in excellent agreement, whereas a discrepancy between 3D-µPTV experiments and simulations was found. The experimental drying conditions were close to identical, but there was a small but possibly relevant difference: IMRS measurements require the presence of immersion oil between the microscope lens and the bottom of the glass substrate in order to ensure high spatial resolution, whereas 3D-µPTV uses no immersion medium in order to ensure an asymmetric PSF and unambiguous diffraction rings for vertical position reconstruction. This difference may affect the substrate temperature control at the lens opening. As summarized in the introduction (section 1.2.4), Cavadini et al. (2013) found that a partial Teflon inlay in a temperature-controlled metallic substrate support resulted in a different drying rate over the inlay, which induced a solutally driven lateral long-scale Marangoni flow. The good agreement between IMRS experiments and one-dimensional drying simulations shows that no such lateral flow occurs during IMRS experiments. It may, however, occur during 3D-µPTV experiments due to the lack of immersion oil.

In order to assess the lateral uniformity of substrate temperature control, additional drying experiments have been performed using glass substrates coated with a thin layer of black spray varnish prior to the polymer film drying experiments. The substrates were placed on either the IMRS setup with immersion oil or 3D-µPTV setup without immersion oil. The lateral temperature distribution during polymer film drying was observed with a thermal imaging camera (T530, FLIR) from top view. The top view configuration requires that the covering boxes, intended to mitigate the impact of lab air ventilation cannot be used during these experiments. Therefore, it is likely that the resulting drying rate and effect of evaporative cooling is slightly larger during these experiments, compared to those presented in the main text.

Exemplarily, Figure A.20 shows the measured lateral temperature during the constant rate period of drying on the IMRS setup (left) and the 3D-µPTV setup (right). The horizontal stripes in both images are the drying films and the dashed circle indicate the positions of the respective lens openings. It can be clearly seen that the film temperature above the opening is lower compared to the portion of the film above the metallic substrate support and this effect is more pronounced for the 3D-µPTV setup. The lateral temperature difference at the IMRS setup was $\Delta T_{lateral} = T_{solid} - T_{opening} \approx 0.3 \pm 0.2\ °C$ and the 3D-µPTV setup resulted in $\Delta T_{lateral} = 1.2 \pm 0.1\ °C$. In order to mitigate this effect, the set temperature of the airflow surrounding the 3D-µPTV objective was increased. Unfortunately, it turned out that with the current geometry of the 3D-µPTV support, the solid substrate temperature and opening temperature cannot be controlled independently.

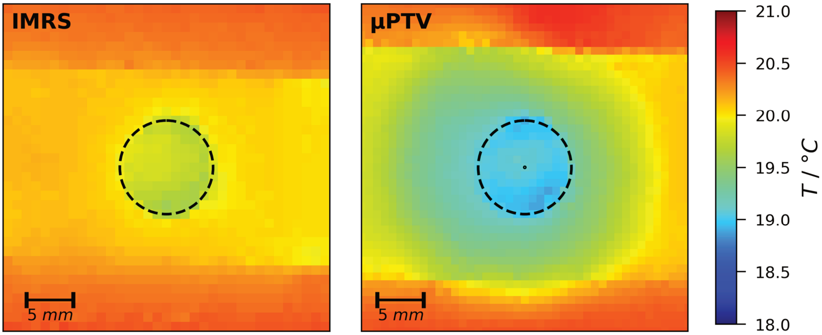

Figure A.20: Thermal images of the lateral temperature control during IMRS (left) and 3D-µPTV (right) drying experiments. The horizontal stripe is the drying film and the dashed circle indicates the lens opening. The tiny circle (right) provides a size comparison of the lateral extent of the observation volume during 3D-µPTV experiments.

Although the found temperature difference is still reasonably small, from these results alone a lateral long-scale Marangoni flow away from the opening cannot be excluded. In the following, three arguments will be presented, which contradict the possibility of a lateral Marangoni flow.

First, the initial discrepancy in 3D-µPTV-derived and simulated drying curves also occurs for $X_0 = 1\ g_{MeOH}/g_{PVAc}$ and $h_{gap} = 200\ \mu m$ (upper left curves in Figure 4.14). The flow field of this experiment, however, shows only very small initial lateral velocities $u_{lateral} \leq 0.4\ \mu m/s$ (Figure 4.4 left) and almost no tracer particles laterally exiting the observation volume (Figure 4.1 left). For a long-scale lateral Marangoni flow, higher values would be expected, as shown in section 5.1.

Second, Cerisier et al. (1987) investigated the lateral cell size of short-scale BM instabilities and found that the cell size increased with increasing aspect ratio $\Gamma = L_{lateral}/h$ until at $\Gamma \geq 70$ the cell size remained at a constant size. The authors concluded that films with a large aspect ratio > 70 are unaffected of lateral bounds and may be treated as infinitely extended films (see section 1.2.1). The lateral diameter of the lens opening $d_{opening} = 10\ mm$ combined with the initial wet-film thickness $h_0 \approx 20$ to $100\ \mu m$ results in an aspect ratio of $\Gamma \geq 100$ to 500, further increasing during drying-induced film shrinkage. Hence, the lateral temperature due to the lens opening is unlikely to affect the flow field above the center of the opening (see Figure A.20 right for size comparison).

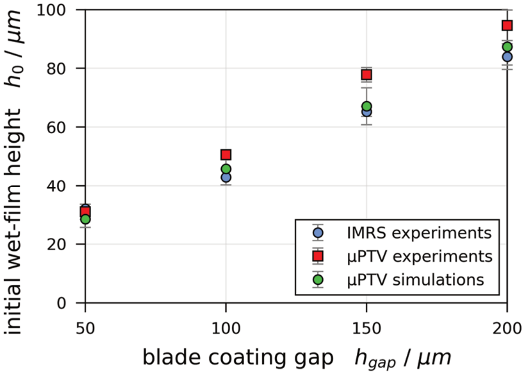

Figure A.21: Comparison of the initial wet film thickness between IMRS experiments, 3D-µPTV experiments and 1D simulations matched to the dry film thickness of 3D-µPTV experiments. (Tönsmann et al. 2021b, License: CC-BY 4.0)

Third, even if the drying film would be affected by a lateral Marangoni flow, the initial wet-film thickness h_0 is solely a result of the blade-coating process. Blade coating is a self-metered coating technique, and the coaters were manually operated (moved by hand). Therefore, small variations in h_0 may occur. Assuming that a lateral flow away from the lens opening does occur, it would be expected that the initial wet-film thickness derived from 3D-µPTV and IMRS experiments would coincide due to the same coating technique. Since the one-dimensional simulation cannot account for a lateral flow, it would further be expected that h_0 from the simulations would be smaller than the 3D-µPTV and IMRS derived wet-film thicknesses, because it was pinned to the in the last section independently validated dry-film thickness of 3D-µPTV experiments. This comparison is shown in Figure A.21, where the red markers denote h_0 extrapolated from 3D-µPTV derived drying curves to $t = 0\ s$, the blue markers denote h_0 from IMRS experiments and the green markers denote h_0 from drying simulations matched to the 3D-µPTV derived dry-film thickness. In contrast to the expectation when a lateral flow would be present, the results show a systematic discrepancy between h_0 from 3D-µPTV experiments and IMRS experiments. In addition, h_0 derived from IMRS experiments is in very good agreement with h_0 from the drying simulations, matched to the 3D-µPTV dry-film thickness. This finding clearly shows that the initial discrepancy between the simulated and 3D-µPTV drying curves cannot be a result of a lateral flow due to the imperfect lateral substrate-temperature control. On the contrary, it confirms that the simulations are indeed a good representation of the 3D-µPTV drying experiments.

C.3 Impact of Simplified 3D-µPTV Camera Stitching

In the last two sections, it was confirmed that the tracer particles are indeed distributed over the entire film height by validating the measured dry-film thickness. This justifies using the upper envelope curve derived from the highest vertical particle positions from 3D-µPTV evaluation as representation of the transient film thickness. In addition, it was found that no lateral flow away from the opening occurs, despite a small imperfection of lateral temperature control due to the lens opening and absence of immersion oil. Hence, a remaining issue in vertical particle position reconstruction is likely to be the cause of the discrepancy between 3D-µPTV-derived and simulated drying curves, presented in Figure 4.14. The discrepancy almost exclusively occurs for larger film thicknesses and when the experimental drying curves were derived from data of the upmost observation volume, having a motorized lens position of $s_{axis} = 0\ mm$. The latter appears contradictory to the findings during 3D-µPTV diffraction-ring calibration. As in section 2.2.5 (Figure 2.12), it was found that for a motorized lens position $s_{axis} = 0\ mm$, the observed diffraction rings coincide well with the PSF simulation results and need no correction. This can be explained when accounting for the complex interplay of identifying the bottom of the film and the simplified vertical camera stitching procedure during postprocessing, presented in 2.3.3. A qualitative but detailed discussion of this interplay is provided in Appendix A.5.

D Additional Aspects of Drying Experiments

D.1 Interpretation of the Correlation Equation

Entering the definition of Pe and Sc in the correlation, found for experiments presented in chapter 4, results in equation (A.13).

$$Ma_{s,crit} \sim \frac{v_{int}^2 \cdot h^2}{\eta^{1/3} \cdot \delta_{s,p}^{5/3}} \tag{A.13}$$

This can be set in relation to the definition of the Marangoni number (eqn. (3.3)):

$$\frac{Ma_s}{Ma_{s,crit}} \sim \frac{\Delta\sigma \cdot \delta_{s,p}^{2/3}}{h \cdot \eta^{\,2/3} \cdot v_{int}^2} \tag{A.14}$$

From equation (A.14), it can be seen that an increase of the initial solvent content (implying a decreases of the viscosity in the denominator, and an increase of the diffusion coefficient in the numerator) results in a larger ratio of $Ma_s/Ma_{s,crit}$, making the film less stable. This may also affect the vertical surface tension difference $\Delta\sigma$. However, as both the viscosity and the diffusion coefficient show an exponential dependency (in opposite directions) on the solvent content (see section 3.6) the impact of these two properties on the film stability is much stronger. This is in line with the results presented earlier (Figure 4.16).

Not all influences can be easily inferred by this method. On first glance, an increase of the film thickness h, being in the denominator of equation (A.14), would decrease the ratio of $Ma_s/Ma_{s,crit}$, making the film more stable. This, however, is in contradiction to the previously reported findings. The reason for this is that an increase in film thickness also increases the vertical concentration gradient during drying, and therefore the vertical surface tension difference $\Delta\sigma$. The same challenge arises for an increase in drying speed (represented by v_{int}), since faster drying affects the rate change of all other properties.

D.2 Drying Curve Comparison for Partially Covered Experiments

The 3D-µPTV and IMRS results (sections 5.1 and 5.2) have to be compared directly, as shown in Figure A.22 for the film height under the edge of the partial cover. The grey areas, denoting the transient film height from 3D-µPTV experiments including refractive index uncertainty, and the IMRS results (violet lines) show noticeable differences.

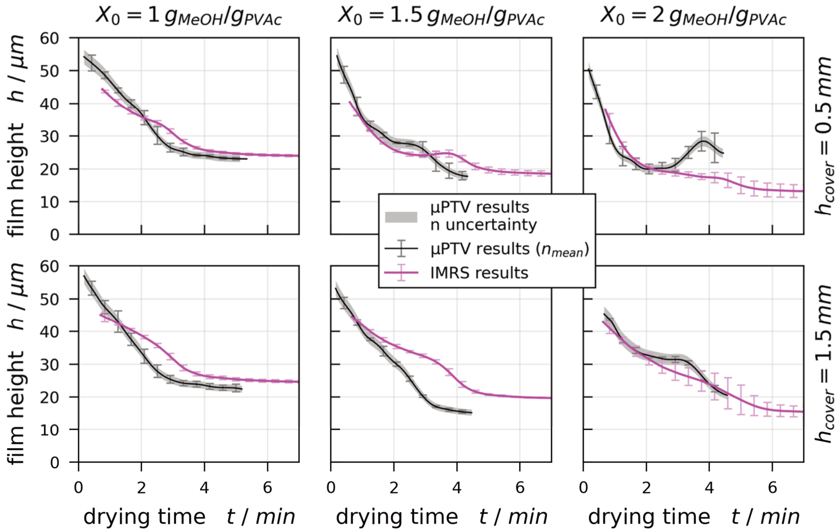

Figure A.22: Comparison of drying curves from IMRS and 3D-µPTV drying experiments under the cover edge.

Several aspects may cause this discrepancy: *First*, the comparison of 1D simulated drying curves with the 3D-µPTV derived film height of uncovered drying experiments already revealed that there is a still unresolved issue with the vertical position reconstruction from diffraction rings for larger film thicknesses (see Figure 4.14 and Appendix C.3). *Second*, it was already discussed that the drying rate of IMRS and 3D-µPTV measurements is slightly different due to different lab conditions and possible methanol accumulation in the gas phase because of the ambient drying conditions without forced air convection (section 4.3). This results in mildly faster drying rates during 3D-µPTV experiments. This would explain the slightly larger initial slope of the 3D-µPTV results, compared to the IMRS results in Figure A.22 as well as the observation that the diffusion-controlled regime (flat end of the drying curves) occurs earlier in 3D-µPTV experiments. *Third*, the lateral positioning of the partial cover edge may vary slightly, as stated at the beginning of this chapter ($\pm 0.5\, mm$).

A better feature comparison can be achieved by plotting the same data over the normalized drying time $t/t_{crit,CRP}$. This eliminates the aspect of different drying rates for IMRS and 3D-µPTV experiments. While the end of the constant rate period $t_{crit,CRP}$ can easily be extracted from the IMRS derived height-averaged solvent load as already discussed (Figure 5.10 left, dashed black and colored dotted lines), the intermediate constant rate period is less apparent from the transient film height. However, it is still possible to find a linear portion of the curve before the diffusion-controlled regime. This is indicated by a black dashed line in Figure 5.10 (right). Similarly, $t_{crit,CRP}$ has been extracted from 3D-µPTV derived height hullcurves.

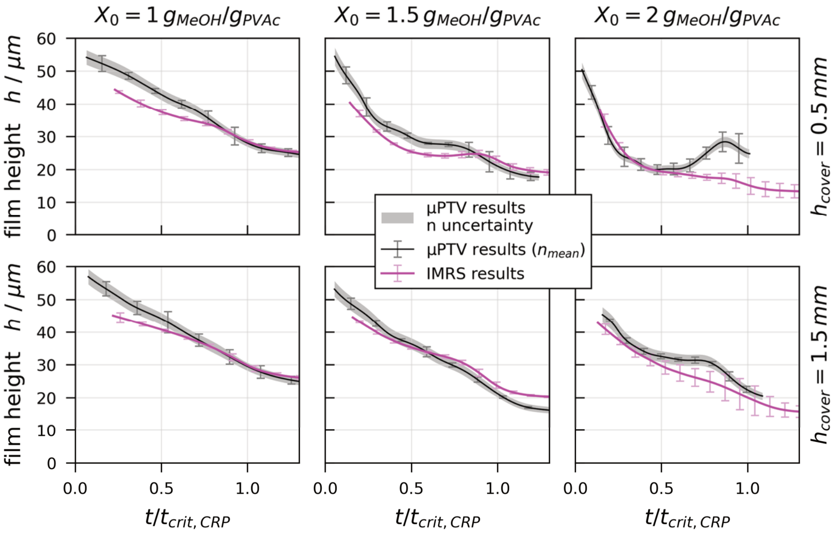

Figure A.23: Comparison of drying curves from IMRS and 3D-µPTV drying experiments under the cover edge, plotted over the normalized drying time.

The drying curve comparison over the normalized drying time is provided in Figure A.23, resulting in a much better agreement of IMRS and 3D-µPTV results. The small initial discrepancy for film drying experiments with $X_0 = 1\, g_{MeOH}/g_{PVAc}$ (left column) is likely to be caused by the deviation in vertical 3D-µPTV position calibration for larger film thicknesses. For films with $X_0 = 1.5\, g_{MeOH}/g_{PVAc}$ (middle column), the intermediate plateau-like curve shape aligns well between the two measurement techniques. Only for $X_0 =$

$2\ g_{MeOH}/g_{PVAc}$ a slightly larger discrepancy remains at approximately 0.8 normalized drying time. These data also show the largest error bars, indicating reproducibility fluctuations. A likely explanation would be that the surface elevation might have a very small lateral extent. In combination with the lateral positioning uncertainty of the cover edge, this would explain the noticeable deviation as well as the larger reproducibility uncertainty. In addition, the IMRS measurements have a lateral extent of $\approx 1\ \mu m$, whereas the lateral 3D-µPTV observation volume is $\approx 250\ \mu m$. Therefore, 3D-µPTV may capture surface deformations not in the measurement region of IMRS experiments. It may also be possible that the lower viscosity (largest initial solvent load) makes the film surface more sensitive to naturally occurring local fluctuations affecting the reproducibility.

It can be concluded that the IMRS and 3D-µPTV experiments are in reasonable agreement with the sole exception for slightly faster drying rates during 3D-µPTV experiments due to the drying under ambient conditions without forced convective airflow and therefore possible lab airflow impact.